# Hybrid Additive Manufacture and Deformation Processing for Large Scale Near-Net Shape Manufacture of Titanium Aerospace Components

A thesis submitted to The University of Manchester for the degree of Doctor of Philosophy in the Faculty of Engineering and Physical Sciences

2016

Jack Marsden Donoghue

School of Materials

# Contents

Word Count: 66,895

# List of Abbreviations

ALM – Additive Layer Manufacture

AM – Additive Manufacture

bcc – Body Centred Cubic

BOR – Burgers' Orientation Relationship

DSC – Differential Scanning Calorimetry

SEBM – Scanning Electron Beam Melted

EBSD – Electron Backscatter Diffraction

EDM – Electrical Discharge Machine

EM – Electron Microscopy

ETMT – Electro-Thermal Mechanical Testing

FIB – Focused Ion Beam

hcp – Hexagonal Close Packed

LBP – Laser Blown Powder

LENS – Laser Engineered Net Shaping

MIG – Metal Inert Gas

SEM – Scanning Electron Microscopy

SLM – Selective Laser Melted

TEM – Transmission Electron Microscopy

TIG – Tungsten Inert Gas

TKD – Transmission Kikuchi Diffraction

UIT – Ultrasonic Impact Treatment

WAAM – Wire Arc Additive Manufacture

# List of Figures

# Hybrid Additive Manufacture and Deformation Processing for Large Scale Near-Net Shape Manufacture of Titanium Aerospace Components

*A thesis submitted to The University of Manchester for the degree of Doctor of Philosophy*
*in the Faculty of Engineering and Physical Sciences*

2016

Jack Donoghue, School of Materials
University of Manchester

## Abstract

The titanium alloy Ti-6Al-4V has been favoured by the aerospace industry for the past several decades due to its good combination of specific mechanical properties, alongside corrosion and fatigue resistance. Titanium alloys are naturally suited to the near net shape processing technique of Additive Manufacture (AM) due to both the inherent high cost of the raw materials, and the difficulties associated with machining the alloys. Unfortunately, the combination of Ti-6Al-4V with AM has been found to lead to undesirable microstructures with respect to large columnar prior β grains being found to grow potentially across the entire height of builds. This microstructure has been shown to lead to property anisotropy and poor fatigue resistance. However, it has recently been found that the integration of an additional process step that lightly deforms the deposited material between added layers leads to the refinement of this undesirable microstructure.

This work characterises the effect that two different deformation processing techniques have on two different additive manufacturing processes; the effect of peening on a laser-powder AM technique, and the effect of rolling on an electric arc – wire AM technique. In both cases far more randomly textured prior β grains were found with an average grain size of > 100 µm rather than mm long columnar grains with a common <100> growth direction formed in the non-deformed builds. The refined β microstructure was found to lead to a reduction in texture of the room temperature α phase. The low stains involved (>10%) indicated that the refined grain structures did not form by traditional recrystallisation mechanisms.

In-situ EBSD measurements at temperatures spanning the α → β phase transformation have been used to observe the growth of new β orientations from crystallographic twins in the deformed microstructure that may explain the origin of the refined grains. New β orientations were observed to grow from twinned α colonies and from between α laths, where the new β is found to grow sharing a twinning relationship with the residual β. Simulation of both of the individual processing steps under laboratory conditions has been found to successfully replicate the refinement observed in process. Orientation analysis suggests that twinning of the residual β could lead to the texture observed in the refined grains. It is therefore suggested that the refined grains are formed from β twinned regions in the deformed material growing under the α → β phase transformation, as the material is heated by the next added layer during AM.

# Declaration

No portion of the work referred to in the thesis has been submitted in support of an application for another degree or qualification of this or any other university or other institute of learning.

# Copyright

i. The author of this thesis (including any appendices and/or schedules to this thesis) owns certain copyright or related rights in it (the "Copyright") and s/he has given The University of Manchester certain rights to use such Copyright, including for administrative purposes.

ii. Copies of this thesis, either in full or in extracts and whether in hard or electronic copy, may be made only in accordance with the Copyright, Designs and Patents Act 1988 (as amended) and regulations issued under it or, where appropriate, in accordance with licensing agreements which the University has from time to time. This page must form part of any such copies made.

iii. The ownership of certain Copyright, patents, designs, trademarks and other intellectual property (the "Intellectual Property") and any reproductions of copyright works in the thesis, for example graphs and tables ("Reproductions"), which may be described in this thesis, may not be owned by the author and may be owned by third parties. Such Intellectual Property and Reproductions cannot and must not be made available for use without the prior written permission of the owner(s) of the relevant Intellectual Property and/or Reproductions.

iv. Further information on the conditions under which disclosure, publication and commercialisation of this thesis, the Copyright and any Intellectual Property and/or Reproductions described in it may take place is available in the University IP Policy (see http://documents.manchester.ac.uk/DocuInfo.aspx?DocID=487), in any relevant Thesis restriction declarations deposited in the University Library, The University Library's regulations (see http://www.manchester.ac.uk/library/aboutus/regulations) and in The University's policy on presentation of theses.

# Acknowledgements

First of all I am thankful to all those that allowed this PhD study to exist in the first place, to Prof. Phil Prangnell of the University of Manchester and Prof. Stuart Williams of Cranfield University who conceptualised the project, and the various organisations that funded both myself and the work, as well as allowing me to present it at international conferences: the University of Manchester, Airbus, EPSRC, and LATEST2.

Particular thanks to my supervisors; Prof. Phil Prangnell who has always trusted me enough to get on with my own work, but has always made himself available should I need to talk to him; and Dr. João Quinta da Fonseca, whose conversations have always been fruitful.

I feel indebted to take note of all the technicians, experimental officers and researchers that look after and manage the equipment, and without whom the research at university would grind to halt. With particular acknowledgement for this study of Ken Gyves for assistance with metallography, Dr. Marc Shmidt with differential scanning calorimetry, and Michael Faulkner and Ali Gholinia for scanning electron microscopy.

I have to thank all of my fellow students of the Manchester materials department for the numerous conversations both work related and not, that have respectively furthered my understanding of my subject and maintained my sanity. I will always look back at my time being a part of the (now defunct) C7 office community with fondness. Of the students, my particular thanks go to Alister JW Garner MSc and Chris Daniel for their assistance with the high resolution orientation mapping and electro-thermal mechanical testing experiments respectively, and to Samuel Edward Tammas-Williams, to whom I hope I was as useful a sounding board as he was to me.

Finally, I am thankful to my family. To my mother Sarah Marsden, who at the beginning of my PhD was in Musgrove Park hospital learning to walk and talk again, and who wouldn’t hear of me staying home to help look after her. To my sister Polly Donoghue, who did stay home, and allowed me to continue my studies. And to my girlfriend Kirsty Marsh who has put up with me every step of the way. I love you all.

# 1. Introduction

Despite being a relatively new family of processing technologies, Additive Manufacture (AM) has rapidly caught the imagination of designers and engineers due to its ability to manufacture geometrically complex components near-net shape out of a large range of materials. Commonly referred to in the media as ‘3D-Printing’, additive manufacture consists of a large family of processes that all share the principle concept of using a moving heat source in a controlled pattern to consolidate a material feedstock to build up a component layer-by-layer. The ability to manufacture near-net shape is particularly beneficial where the raw material costs are high and where traditional processing routes are difficult. Therefore, titanium alloys are particularly well suited to additive manufacture due to both the difficulties associated with machining them, and the inherent high cost of the raw material.

A significant proportion of global titanium metal production is concerned with the aerospace industry, so it is of no surprise that there has been heavy investment by the industry to further AM technologies. Particular focus has initially been put on improving the understanding of additive manufacture with Ti-6Al-4V, an alloy favoured by the aerospace industry for the past several decades due to its good specific mechanical properties at moderate elevated temperatures, excellent corrosion resistance, and well understood fatigue resistance [1].

Figure 1:1. Entire demonstrator winglets built by Wire-Arc Additive Manufacture (WAAM), adapted from [2].

Unfortunately, the combination of Ti-6Al-4V with AM has been found to lead to undesirable microstructures where large columnar prior β grains are found to grow across many added layers, and potentially across the entire height of the build. These columnar grains are found to grow with a common <100> growth direction, leading to a textured build [3]. Texture is partially inherited through a phase transformation to predominantly α phase at room and operating temperatures due to an orientation relationship maintained through the phase transformation. This microstructure has been found to influence mechanical property anisotropy and is expected to lead to other undesirable properties such as poor fatigue resistance [4].

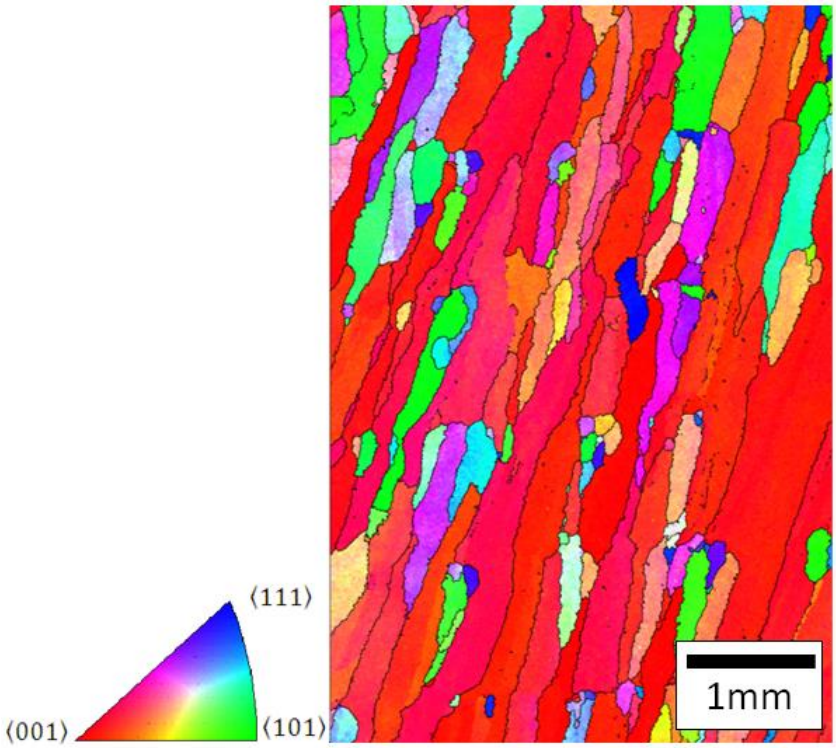

Figure 1:2. Example of the highly textured prior-β columnar microstructure observed in the AM of Ti-6Al-4V; adapted from [5].

However, it has recently been found that the incorporation of an additional process step that lightly deforms the material between every added layer breaks up or refines this undesirable microstructure replacing it with a far finer, seemingly equiaxed prior-β grains [6]. Prior to this study the mechanism, which leads to the formation of this refined microstructure, was not understood as the low strains involved (>10%) indicate that the refined grain structure does not form by traditional recrystallisation.

It was the aim of this study to characterise, and understand the mechanisms behind the formation of the refined microstructure that is created when additive manufacture is combined with deformation processing. The work included in this thesis has been born out of LATEST2, a collaboration between academia and industry to understand and develop Light Alloys Towards Environmentally Sustainable Transport.

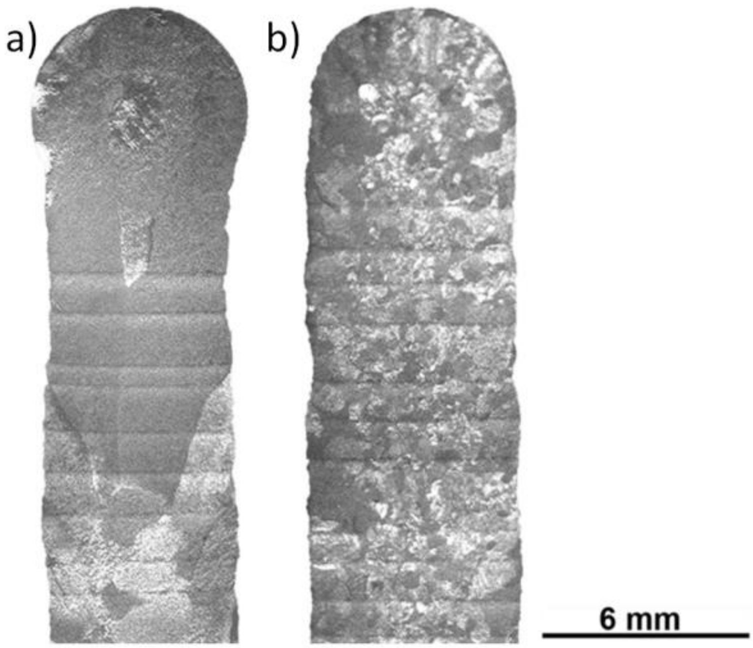

Figure 1:3. Examples of etched micrographs of the cross section of Ti-6Al-4V AM walls showing in (a) the conventional coarse columnar prior β structure of an as built wall, and in (b) the high level of prior β refinement achieved by rolling between layers of deposition; adapted from [6].

This work characterises the effect that two different deformation processing techniques have on two different additive manufacturing processes; namely the effect of peening on a laser-powder AM technique, and the effect of rolling on an electric arc – wire AM technique. This study makes extensive use of Electron Backscattered Diffraction (EBSD) to measure the orientation of α grains in various Ti-6Al-4V structures built by hybrid AM and deformation processing techniques. The α EBSD measurements were not only used to measure the effect the added deformation has on texture, but also to reconstruct the high temperature prior-β grain structure.

The β refinement mechanism was investigated by two experimental techniques; the direct observation of the phase transformation in-situ by EBSD at temperatures over the α→β phase transformation, and by simulating both the deformation processing step and the thermal cycle of an AM layer addition under laboratory conditions in order to replicate the refinement process.

The intended outcome of this study was to better understand the mechanism by which the refined β microstructure is developed so that it can be better exploited in the future, and potentially extended to other processes.

The structure of this thesis is as follows; after a literature review and a section on the experimental techniques used, the main body of the thesis is presented in an alternative format, being comprised of four paper manuscripts with a further traditional chapter of additional results given before the final concluding chapter.

The literature review provides a background understanding of AM, titanium alloys, and the two in combination, and summarises current knowledge in the field. The experimental section gives a background and justification to the experimental techniques used, with details of the experimental parameters adopted provided in the relevant manuscripts themselves. Rather than being placed in order of publication, the manuscripts are arranged in an order to give a more coherent story to the study. The first two manuscripts characterise the effect on the microstructure that different deformation processes have on separate AM techniques, and the following two manuscripts proposing mechanisms to explain those observations. Two of the manuscripts (Manuscripts 1 & 3) have undergone peer review and have been published in global conference proceedings, one of the paper manuscripts (Manuscript 2) was recently published in the peer reviewed journal ‘Materials Characterization’, and the final manuscript is in draft form and will be submitted in the near future. The additional chapter of results presented after the manuscripts contains numerous experiments that although do not warrant publication in themselves, do further the narrative and add to the discussion from the papers, as well as corroborate some of the earlier findings. The final section of this document is intended to summarise the key points of the manuscripts and tie them together with mutual conclusions and comments on suggested future work.

# 2. Literature Review

The following literature review is structured in such a way that the first three sections give a general introduction to additive manufacture, deformation of metallic systems, and titanium alloys in that order. The subsequent literature review sections build on the introductory ones, and focus in more depth on the topics with the most relevance to this thesis, firstly by going into greater detail on the titanium alloy investigated, Ti-6Al-4V, before discussing it in combination with additive manufacture and deformation processing. Finally a brief summary is given, putting the reviewed literature into context with the study.

## 2.1. Additive Manufacture

### *2.1.1. Introduction*

Additive manufacture is a term that is used to describe a relatively new family of processes that are able to fabricate near-net shape components from wire, or powder, feedstock by the motion of a focused heat source, to build up a part layer by layer. Due to the relatively recent development of AM, several alternate terms for the technology are still present in the literature and in common vernacular, these include: Rapid Prototyping (RP) [7], reflecting the history behind the processes, Additive Layer Manufacture (ALM) [8], due to the layered nature of the process, and 3D Printing (3DP), a terminology much used by the media as it enables a laymen to better understand the concept [9].

AM has been used to process a range of material feed stocks from polymers [10], to ceramics [11], and composite structures [12], but due to the scope of this project, the rest of this discussion will be focused on metallic AM techniques.

#### Basic Principles of Additive Manufacture

The term additive manufacture covers a relatively diverse family of processes, an overview of which will be given in §2.1.2. However, they can all be simplified to consisting of the following steps, summarised in Figure 2:1.

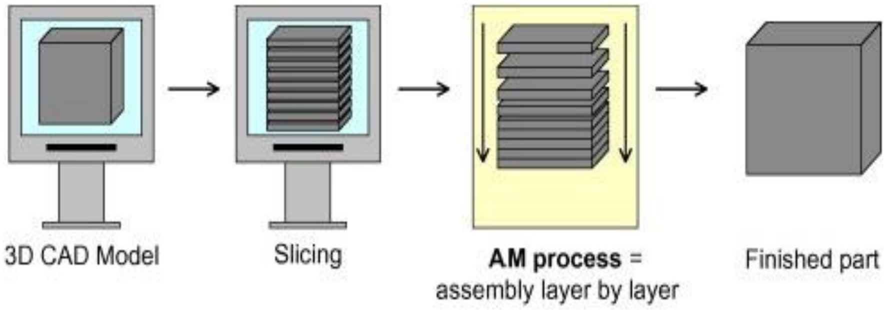

Figure 2:1. Schematic showing the four key steps common to all additive manufacturing techniques [13].

### *Step 1: CAD Model*

All AM parts start off as a 3D computer model that fully describes the geometry of the desired part. This is generally made using Computer Aided Design (CAD) software. Alternatively, the computer model can also be generated by reverse engineering from an actual object by, for example, laser scanning [14].

### *Step 2: Conversion to Layers*

In order for the 3D design to be built by the AM machine it is necessary for it to be divided into layers that the AM machine can then build up one after the other in order to build up the 3D component. The development and an adoption of a standard file type by both the CAD software developers and the AM machine producers has simplified this process [15] .

### *Step 3: Build*

The material is deposited and fused in layers to build up the desired component. This step is usually the least labour intensive as most machines are fully automated [9].

### *Step 4: Removal and Post-processing*

The majority of AM processes will leave the finished part attached to a baseplate that, depending on the part design, may need to be removed, as well as sacrificial structures added to support overhanging elements [9]. Additional post-processing heat treatments may include: Hot Isotactic Pressing (HIP) in order to reduce the porosity [16], machining for specific surface finishes [17], and heat treatments [18].

## Benefits of Additive Manufacture

Each of the AM processes have their own advantages and disadvantages. However, there are some general statements that are true across all AM processes.

Advantages include:

- AM is able to fabricate parts very close to the desired dimensions (near-net shape) usually requiring only minimal post-process machining to achieve the desired dimensions and surface finish [9].
- AM is an additive process rather than a subtractive one, unlike traditional techniques such as machining, which leads to considerably less wastage. A commonly used measure of the manufacturing efficiency by the aerospace industry is the Buy:Fly ratio, which is simply the ratio of the weight of the material used to the weight of the component fabricated from it. AM is potentially able to fabricate components with a Buy:Fly ratio of 2-3:1 as opposed to traditional methods that can have Buy:Fly ratios of upwards of 20:1 [19].
- The use of AM can dramatically improve the development cycle when designing new parts by reducing both the associated cost and lead time in the fabrication of tooling required in traditional manufacture techniques, such as forging and die-casting [20].

- With most AM techniques it is possible to manufacture complex shapes that would be difficult or impossible to fabricate with traditional techniques, for example, creating a component with an internal cellular structure [21].
- AM also has the potential benefit of being able to fabricate functionally graded components. This could be achieved either by varying density in the build [22] or grading the material [23].

Disadvantages of AM processes can include: low productivity relative to traditional manufacture, a high initial cost outlay, and the high cost of feedstock material. However, the relative scale of these drawbacks are more linked to the deposition technique being used, and so will be discussed more in the following section.

### *2.1.2. Additive Manufacture Techniques*

There are a range of AM techniques that have been developed by various companies and institutes. This has led to the trademarking of methods by these individuals. However, the AM techniques can generally all be classified by nature of the material feedstock (powder or wire) and by the heat source used to melt it (electron beam, laser beam or electric-arc). This section gives a brief description of the most common techniques before weighing up their relative advantages.

#### Powder based techniques

Powder based AM techniques are further subdivided into two further families of techniques: powder bed and blown powder. Powder bed incorporates a bed of powder and a focused heat source that traces over it in a pattern dictated by the CAD model, in order to fuse the powder in each layer. After the layer is complete, a new thin layer of the powder is redistributed over the fused layer so a subsequent layer can be added. In the blown powder techniques the powder is fed straight into the melt pool created by the directed heat source via an inert carrier gas.

The powder bed techniques can use either an electron beam (selective electron beam melting – SEBM) or laser beam (selective laser melting – SLM) as a heat source. A schematic of the laser process is given in Figure 2:2, the basic SEBM set up is very similar to this with the exception of the heat source.

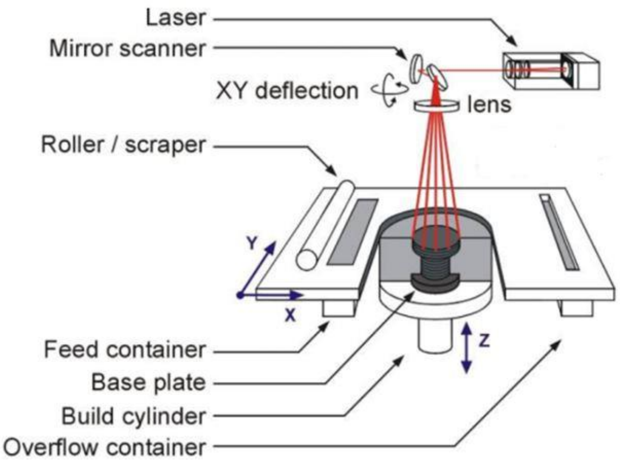

Figure 2:2. Schematic of a laser based powder bed additive manufacture machine [24]

A controlled atmosphere is required when using a powder bed system. A vacuum is required for SEBM in order to avoid scattering of the electron beam by gas atoms as well as preventing oxidation [9]. SLM in comparison does not require a vacuum, but a protective atmosphere of inert gas is still required to prevent oxidation with most materials [24].

Blown powder techniques are limited to using a laser as a heat source due to the inability to operate in a vacuum, which rules out the use of an electron beam. Several terminologies exist including Laser Engineered Net Shaping (LENS) [25] and Laser Additive Manufacture (LAM) [26]. However, these techniques generally all include the same elements as shown in Figure 2:3.

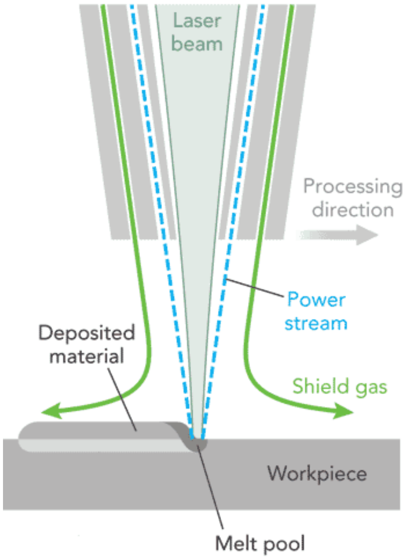

Figure 2:3. Diagram showing the basic set up of blown powder AM techniques; adapted from [27].

This process functions by focusing a laser beam on the substrate surface to create a melt pool. The powder is then propelled by an inert carrier gas, and injected into the melt pool via a nozzle to create a deposition track. An inert shield gas is often required in order to protect the high temperature deposition from oxidation. Spatial control of the deposition is either managed by manipulation of the work piece under the fixed laser beam [28] or by manipulation of the tool head around the work piece [29].

### Wire based techniques

The electron beam and laser heat sources can also be used to melt a wire feed stock [17,30], but it is more common to use an electric arc torch, with possible heat sources including both tungsten inert gas welding (TIG) [31], metal inert gas arc welding (MIG), and plasma arc [32]. The TIG set up is shown in Figure 2:4, though the principle is similar for all three processes, with the directed heat source simultaneously creating a melt pool and melting the wire being fed into it. The only exception is the MIG torch, where the feedstock wire is used as a consumable electrode in the creation of the arc that generates the melt pool [32].

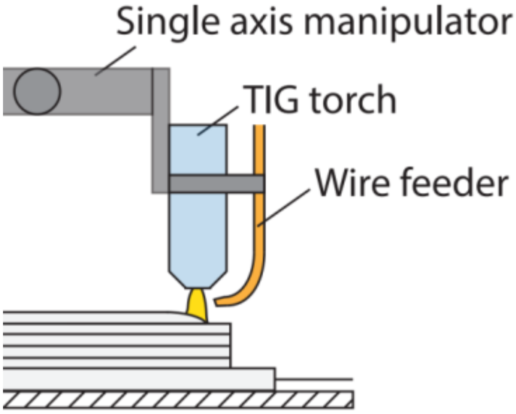

Figure 2:4. Schematic of a TIG based wire AM technique; adapted from [33].

Although the use of a controlled inert atmosphere is desirable for the arc based processes in order to avoid oxidation, it has been found that minimal oxygen uptake occurs with the use of an efficient trailing gas shroud [34]. As with SEBM, a vacuum chamber is required with the use of an electron beam heat source [17].

### *2.1.3. Comparison of AM techniques*

Table 2:1 gives an overview of the maximum capabilities of the different AM techniques, though it should be noted that these only give an indication of what the equipment can achieve when pushed to extremes. It would be impossible to achieve both the maximum build resolution and deposition rate as stated in Table 2:1 simultaneously, with the deposition rate and layer height understandably falling when attempting to build finer features. The relationship between resolution and build rate for the beam based technologies is shown in Figure 2:5, and this trade-off is seen across all AM technologies.

Table 2:1. Maximum achievable parameters of the different AM platforms. Data taken from catalogues of commercially available equipment where available.

| Heat Source | Feedstock | Resolution* (cm) | Build Rate ($cm^3$/h) | Component Size (mm) | References |
|---|---|---|---|---|---|
| Electron Beam | Powder Bed | 0.010 | 80 | Ø 350 x 380 | [35,36] |
| | Wire Feed | 0.250 | 2500 | 300 x 300 x 150 | [17,37] |
| Laser Beam | Powder Bed | 0.015 | 100 | 500 x 365 x 280 | [38–40] |
| | Powder Feed | 0.025 | 110 | 900 x 1500 x 900 | [41] |
| Arc | Wire Feed | 3.000 | 270 | 1000 x 1000 x1500 | [42,43] |

** Often quoted 'minimum feature size', approximately akin to melt pool diameter.*

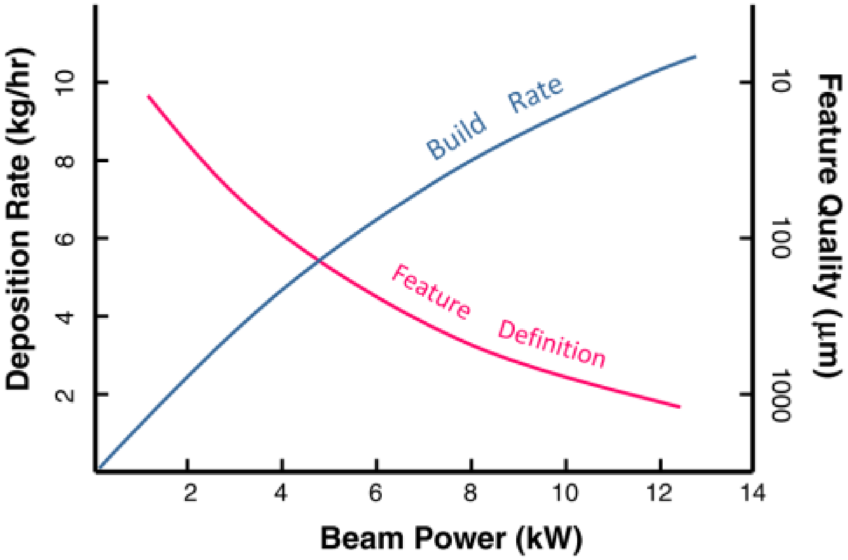

Figure 2:5. Schematic figure demonstrating the general relationship between deposition rate and resolution for different beam powers [44].

Due to the small melt pool size, the use of a powder bed allows for the highest dimensional accuracy of all the AM techniques, and leads to the ability to fabricate highly complex shapes with a good surface finish and good utilisation of the powder [45]. There is a certain amount of overlap in the capabilities of the laser and electron beam heat sources in terms of the build rate and resolution; however, it is generally the case that the SEBM can achieve a higher deposition rate for the same resolution than SLM [38]. Other advantages for the SEBM process include greater power efficiency, due to the greater efficiency of the electron gun compared to lasers [9], and no issues with reflectivity of the powder leading to a greater absorption of the beam energy [3]. The laser based systems benefit from the simpler construction of a chamber to provide an inert atmosphere compared to a vacuum chamber, allowing for larger builds and cheaper systems [9].

The use of blown powder systems sacrifice the ability to go to quite as high resolutions as the powder bed systems, but allow deposition on 3D surfaces enabling the use of the technology for repair purposes [46]. However, there is often lower feedstock utilisation due to difficulties of powder capture by the melt pool, and the processes also tends to lead to a high surface roughness, as semi-molten powder adheres to the surfaces [30]. The semi-molten powder can also lead to high build porosity unless parameters, such as powder feed angle, are selected carefully [7].

The wire based techniques, though not as suitable for creating fine detail as those using a powder feedstock, benefit greatly from a much higher deposition rate. Wire based techniques also benefit from using a cheaper feedstock, as the fabrication of good quality metallic powders is an expensive process, and have much greater material utilisation, with close to 100% of the feedstock ending up in the wall of the component [30]. Wire + Arc Additive Manufacture (WAAM) techniques have the lowest resolution of all the AM techniques and are thus limited to large structural parts, but benefit from high build rates, lower initial investment, and from the relative simplicity of the process [43]. As sufficient oxygen protection can often be provided by a gas shroud, there is no need for a controlled atmosphere like with other AM techniques, allowing for a virtually limitless build size that is only dependent on travel of the robot that directs the deposition torch.

The work contained within this thesis is concerned with combining additive manufacture with an added deformation step. The basic descriptions of the different AM techniques given above were for the benefit of the reader and it should be noted that the majority of the techniques would be unsuitable for incorporation with a deformation step. For example, it is unlikely that the SEBM process would be combined with a deformation step due to the cost implications associated with the fabrication of larger vacuum chambers to encompass an additional piece of equipment. By the same token, the disruption caused to a bed full of loose powder by any deformation step would also prevent these AM systems being combined with a deformation step. Therefore, the AM platforms that are most easily combined with a deformation step are laser blown powder and wire based additive manufacture methods. It is these methods that are the subject of this investigation and are covered in further detail throughout the rest of this thesis.

### *2.1.4. Deformation Processing in AM*

Deformation is utilised in metallurgical processing for two purposes: firstly, to shape the component to desired dimensions, and secondly, to improve the mechanical properties. As AM is a family of near net shape fabrication techniques, the ability to shape the component by deformation processing is mostly redundant. Therefore, the benefits that can be garnered by the addition of a deformation step to AM are largely associated with an improvement to mechanical properties as a result of modifying the microstructure and texture and this aspect will be discussed in greater detail in the following chapters. The discussion of deformation processing is limited in this section to the deformation techniques that can be successfully combined with AM.

### Rolling

Rolling is most commonly carried out between two rollers during processes such as sheet production, however this would be near impossible to achieve with AM deposits. It is more feasible to run a single roller across the top of a deposited layer, as has previously been applied to welds in order to reduce residual stresses [47,48]. Rolling has been applied to wire based AM techniques with steel [33] and titanium alloys [42], to reduce residual stresses. In the case of the titanium, an unexpectedly well refined microstructures was also found in addition to the reduction in residual stress. The refined microstructure will be described more fully in §2.5.3. In both of these studies the wall was a single track wide straight wall as it is substantially easier to apply rolling in AM to simple geometries, due to inevitable inhomogeneity in the distribution of the deformation with more complex geometries. However a recent study by Xie et al. [49] has investigated what they have termed a ‘metamorphic’ rolling system with steel deposition, that adjusts the rollers in contact with the build depending on the geometry, as shown in Figure 2:6, in order to improve mechanical properties and geometrical accuracy.

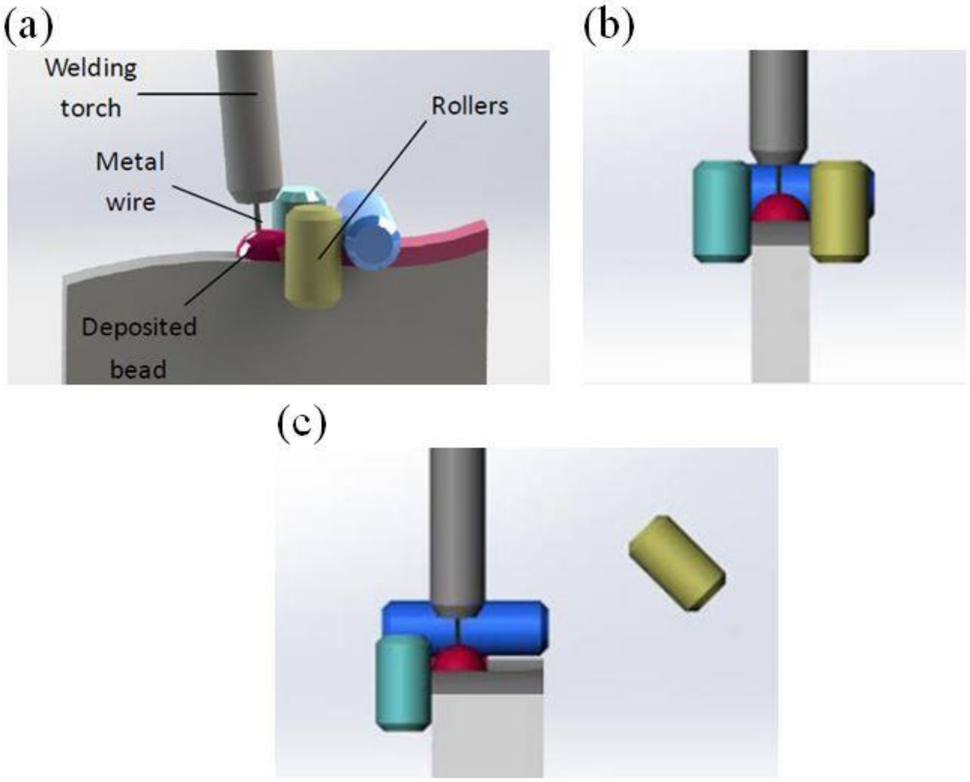

Figure 2:6. (a) Schematic of the ‘metamorphic’ rolling system developed by[49] with plan views of how it adapts for single (b), and multi-pass deposits (c); adapted from [49].

### Peening

Peening is a commonly used technique for plastically deforming the surface of a component. One of the most common ways to do this is via ‘shot peening’, where many small spherical particles of a hard material are projected at the surface of a component with sufficient force to deform it. This would not be practical to combine with additive manufacture due the time it would take to set up, peen, and recover shot between the addition of every layer during the process. In contrast, Ultrasonic Impact Treatment (UIT) is a reasonably recent variation of peening that does not have this difficulty. In UIT, an ultrasonic transducer is coupled with hard pins that are held in place but free to oscillate along their axis. The pins have a normalised wavelength with respect to the carrier frequency and are therefore excited by it. The pins are put in contact with the component surface and deform it by many ultrasonic impacts [50]. In the literature, UIT has not been previously combined with AM. However, several studies have reported the benefits of UIT for extending the fatigue life of welds, over more traditional peening methods [51–53].

### Forging

Both rolling and peening have the potential to be integrated in to an additive manufacture technique at any stage of the process, for example, between every layer of deposition. However a third technique developed by Alcoa includes a forging deformation step as the final stage in the process as shown in Figure 2:7.

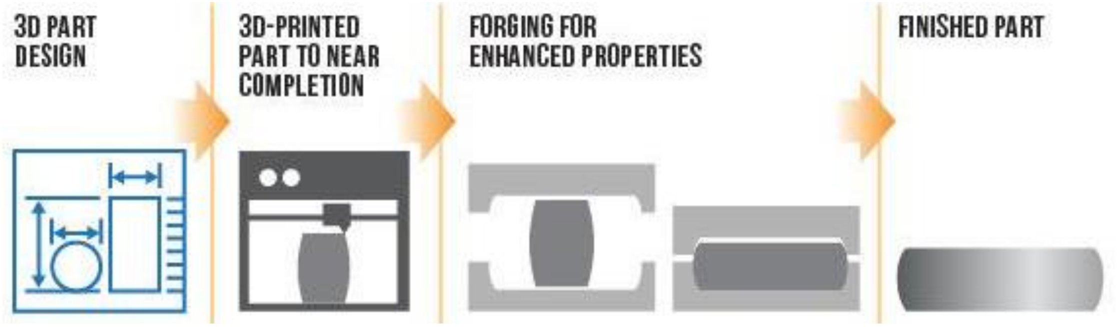

Figure 2:7. Schematic of the major stages of the Ampliforge$^{TM}$ Process developed by Alcoa [54].

Alcoa has named this process ‘Ampliforge’ and states that the addition of the forging stage leads to improved mechanical properties [55]. However the necessity for a specific die for each part negates two of the greatest advantages of AM, flexibility and a short lead time.

## 2.2. Deformation Mechanisms

In order to understand the potential benefits that a deformation step can add, it is important to have some understanding of the mechanisms by which metallic crystals accommodate deformation. The following discussion gives a brief general introduction and overview of the main deformation mechanisms, as well as the effect it can have on microstructure and mechanical performance in the general case. Deformation in combination with Ti-6Al-4V and AM will be discussed in more detail in §0 and §2.5.3 respectively.

### 2.2.1. Crystallographic Slip

Slip is the most common mechanism by which metal crystals deform. Slip can only occur on specific slip systems, involving a combination of a particular slip plane and slip direction; this is usually on the close packed planes in the close packed directions. For example, in face-centred cubic (fcc) metals slip primarily occurs on the close packed {111} octahedral planes in the <110> close packed directions [56]. For slip to occur, a shear stress is required.

The shear stress, $\tau$, is the Resolved Shear Stress (RSS) on the slip plane in the slip direction given by

$$\tau = \frac{F}{A}\cos\phi\cos\lambda$$

Equation 1

where $\lambda$ is the angle between the load applied, $F$, and the slip direction, making '$F\cos\Theta$' the component of force in the slip direction. And $\phi$ is the angle between $F$ and the slip plane normal, making '$A/\cos\phi$' the area over which this acts. This can be visualised with figure 2:8.

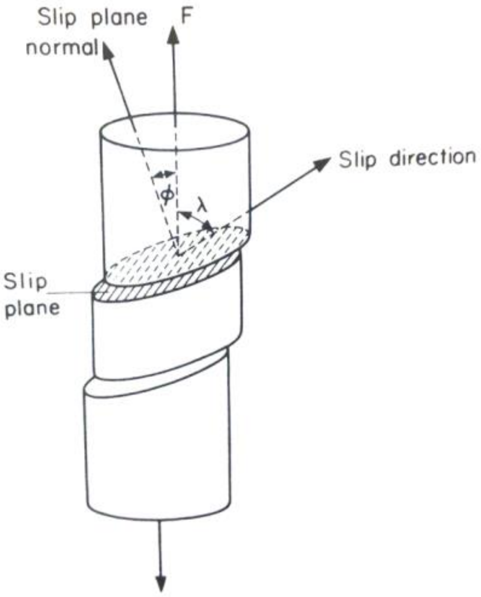

Figure 2:8. Illustration of the geometry of slip within a single crystal [57].

The quantity '$\cos\phi\cos\lambda$' is known as the Schmidt factor. Schmidt and others found that a slip system will only become active when the RSS reaches a critical value, $\tau_c$, otherwise known as the Critical Resolved Shear Stress (CRSS) [58]. $\tau_c$ is independent of crystal orientation and slip will primarily occur on the slip system with the highest Schmidt factor.

Von Mises determined that there have to be 5 impendent slip systems active in order to accommodate a general shape change during deformation [59]. In fcc crystals this criterion is usually easily satisfied as the structure is highly symmetrical. With other less symmetric crystal structures, such as hexagonally close packed (hcp), it can be more difficult to find 5 independent slip systems. In situations where slip is not favourable, other deformation mechanisms, such as twinning, are required to accommodate a shape change.

### *2.2.2. Dislocation Theory*

The stress that would be required to simultaneously move an entire plane of atoms past another would be enormous; and the mechanism that allows slip to occur at a much lower CRSS is the movement of crystallographic defects known as dislocations.

Dislocations are line defects that exist in two main types; edge and screw. The pictorial representation of an edge dislocation in figure 2:9 demonstrates how the movement of a dislocation can occur and how it can lead to the net deformation by slip of the crystal.

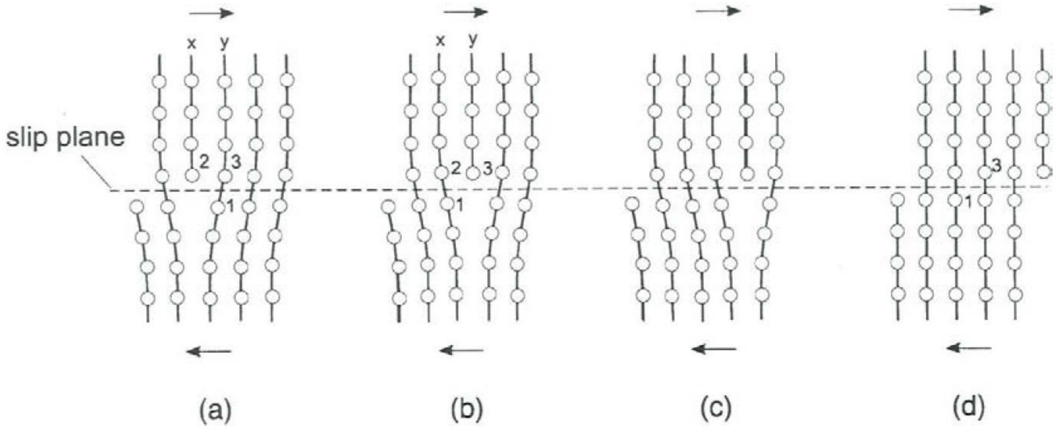

Figure 2:9. The movement of an edge dislocation under a shear stress through a lattice [57].

The edge dislocation is essentially a defect caused by an extra half plane of atoms that terminates halfway through the crystal lattice. Only a small change in position is required by relatively few atoms close to the defect for the dislocation to move. Figure 2:9 also highlights the importance of the ‘Burgers vector’ when discussing dislocations. The Burgers vector represents the magnitude and direction of the lattice distortion caused by a dislocation in a crystal lattice and can be visualised as the difference between a circuit made around a perfect part of the lattice and one containing a dislocation as shown in figure 2:10. This can be related to figure 2:9 as adjacent atoms across the slip plane are displaced by a burgers vector by the passing of a dislocation. Therefore the slip direction is parallel to the burgers vector. Screw dislocations differ from edge in that the Burgers vector is parallel to the line defect, rather than normal to it, however slip is still parallel to the burgers vector.

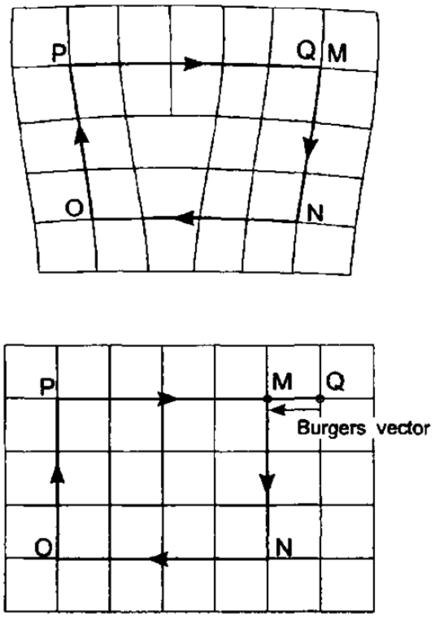

Figure 2:10. Burgers circuit around an edge dislocation and the same circuit in a perfect crystal, where M to Q is displaced by the Burgers vector [57].

### 2.2.3. Twinning

Twinning consists of the sudden coordinated movement of atoms within a crystal under shear to symmetrically recreate the crystal structure at a different orientation, but with retained shared lattice points with the parent crystal. This is shown schematically in figure 2:11.

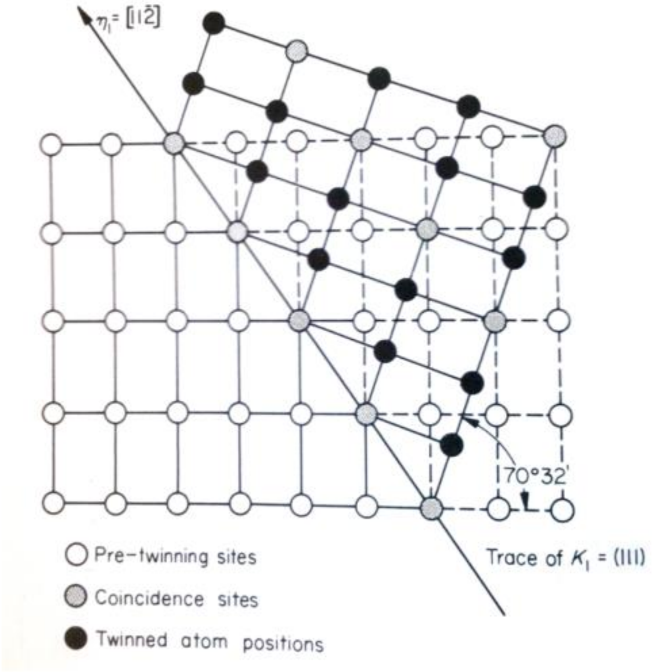

Figure 2:11. An example of the geometry of twinning for an FCC lattice; adapted from [60].

Deformation twins tend to form lens shaped structures across their parent grain. The twin transformation can be considered to occur in three stages: nucleation, propagation and growth. Nucleation tends to occur at grain boundaries, as the they provide a stress concentration and a heterogeneous site for nucleation to occur [61]. Twin propagation occurs very rapidly until impingement at a grain boundary, although twins have been observed to propagate across boundaries of similarly orientated grains [62].

The resolved shear stress required to initiate a twin transformation is generally greater than that required for slip, but if there is a limited number of possible slip systems (as with HCP metals) and the crystal is orientated so that these are unfavourable (i.e. with a low RSS), then the crystal is more likely to deform by twinning. As the shear stress required for twinning is still significantly less than would be required to simultaneously move all of the atoms within the twinned region, it is apparent that twinning is also facilitated by dislocations [56]. The dislocations that allow twinning to occur are generally more complex than those considered above with slip, and will not be described in detail here, but often involve a dislocation splitting into several partial dislocations, to define a twinned region spanning several planes known as a ‘zonal dislocation’ [61].

The propensity for twinning is sensitive to grain size with it generally found that twinning occurs more easily with larger grains [63,64]. However, below a certain grain size, it is found that the critical stress needed to activate deformation twinning drops dramatically, as shown schematically in Figure 2:12 [64]. The cause of this behaviour is believed to be due to the reduced probability of the presence of defects in a nanoscale-volume of material to act as a dislocation sources to facilitate slip [64,65]. This behaviour has most commonly been observed in fcc materials [64,66], although it has recently been confirmed to also be present in nano-grained bcc structures [65].

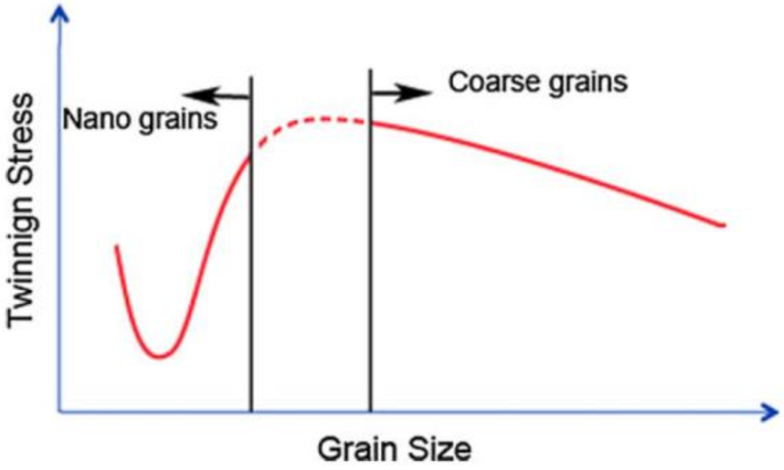

Figure 2:12. Schematic description of the effect of grain size on the critical stress needed to activate deformation twinning; adapted from [64].

### *2.2.4. Effect of Deformation on Crystallographic Orientation*

Both slip and twinning are associated with creating an orientation change in the crystal being deformed. For every slip system there is an associated rotation of the lattice with respect to the loading direction. This rotation can cause the Schmidt factor on the active slip system to change to a point where another slip system is orientated preferentially for slip. Single active slip system deformation only really occurs in unconstrained circumstances (i.e. single crystals). In polycrystalline systems, where grains are constrained by their neighbours, multiple slip systems can be active and the lattice rotation is a resultant of the displacement of these slip systems. As a grain is not constrained equally across its volume, different parts of the lattice may have different slip systems active, causing different rotations and grains to split into deformation bands. The lattice can accommodate these ‘misorientations’ via ‘geometrically necessary’ dislocations [57].

Twinning can be seen as a short cut to orientation change as it rapidly transforms a part of the lattice to completely different orientation. In comparison the shear strain required to achieve this same orientation change by slip would be far greater.

### *2.2.5. Effect of Deformation on Texture*

The spread of crystallographic orientations in a polycrystalline material is rarely random due to the propensity for one or more orientation to develop preferentially, either after solidification or a thermomechanical process. This preferred orientation is known as texture. The presence of texture in a material has been shown to affect numerous material properties causing anisotropy in strength, ductility and toughness, especially in materials with a more anisotropic crystal structures, such as hexagonally close packed metals [67].

As both slip and twinning are associated with an orientation change for the crystal being deformed, deformation causes a change in texture of polycrystalline materials. Deformation can lead to a weakening of texture as the preferentially orientated grains are deformed and rotated away from their previous orientation. Alternatively, under constant deformation conditions, textures can be strengthened as non-aligned grains are rotated towards a preferential direction. The change in texture achieved is dependent on the direction and extent of the deformation, as well as the starting texture. The stating texture is important as it is the initial orientation of the grains with respect to the loading direction determines which deformation systems will be active first [68].

### *2.2.6. Stored Energy, Recovery and Recrystallisation*

During the deformation of a polycrystalline material, 99% of the work put into the material is expended as heat; however, the remaining energy is stored within the material as dislocations and other defects [69]. Deformation increases the number of dislocations by the trapping of existing dislocations and the generation of new ones.

These dislocations are the origin of the work hardening effect of deformation. As the density of dislocation density increases, so does the number of dislocation interactions. If dislocations lie on the same slip plane then they can annihilate each other if they are oppositely orientated, essentially restoring the lattice locally. If the dislocations are similarly orientated within the lattice then they will repel each other due to the interaction of their associated strain fields repelling each other, making slip by dislocation movement more difficult, and the material stronger. However, greater material strengthening is achieved by dislocations on different slip planes cutting across each other. Dislocations intersecting each other will result in a small section of each dislocation line becoming shifted onto a different atomic plane, known as a 'jog'. If the jog is no longer on the slip plane then it is considered 'sessile' and is unable to glide, increasing strain hardening. Heating to approximately one third of the melting point of a metal gives the dislocations enough mobility to climb crystallographic planes and reorder themselves in a process known as recovery [69]. Recovery causes some dislocations to annihilate with each other and the others to assume a more stable orientation, increasing material ductility at the cost of strength.

Recrystallisation can also occur, where grains free of dislocations are grown from the deformed lattice creating a new microstructure. The driving force for this change is the difference between the stored energy within the grains. Recrystallisation can either occur on subsequent heating after deformation, or while deformation is occurring, which is termed dynamic recrystallisation. The resultant microstructure will have a different grain size and texture to that prior to recrystallisation [69].

The recrystallised grain size achieved is highly dependent on the parameters of the deformation, reheating, and the starting microstructure. However, the final grain size is often desired to be as fine as possible to increase strength by the Hall-Petch relationship which states that the yield stress of a material, $\sigma_y$, is related to the grain size, $d$, by the following relationship:

$$\sigma_y = \sigma_0 + k_y d^{-n}$$

Equation 2

Where $\sigma_0$ and $k_y$ are materials constants and $n$ has a typical value of 0.5 [70].

The grains in a recrystallised microstructure also do not tend to be randomly orientated, but have a preferred texture. The recrystallisation texture is controlled by the orientations of the recrystallised nuclei, and the relative rate at which these grains grow. A few of the major factors that can affect this include: the starting deformed microstructure, deformation temperature and the influence of a second phase [69]. Recrystallisation of titanium alloys will be covered in greater detail in §2.4.1.

## 2.3. Titanium Alloys

### 2.3.1. Introduction

The use and development of titanium alloys has been dominated over the past half a century by the aerospace industry. This is due to the alloys having many desirable properties (such as high specific strength and stiffness, as well as corrosion resistance) but applications have been limited by the high cost of the extraction and processing of titanium metal [71].

Titanium alloys are suitable for use in aerospace components as they have a high strength-to-weight ratio and provide substantial weight savings in comparison to steel. However, this does not lead to as greater a use of titanium alloys as one might expect, as the specific stiffness of titanium alloys is similar to that of high strength aluminium alloys but at a significantly higher price. Titanium finds its niche wherever volume constraints would rule out the use of thicker gauge aluminium components, or where elevated temperature becomes an issue as titanium alloys have a far higher temperature operating range [1]. Titanium alloys are also finding increasing use in the aerospace industry due to their superior compatibility with composite materials [72], as the industry drives to reduce weight by increasing the amount of composite materials used in aircraft manufacture.

This section gives a brief background to the metallurgy of titanium alloys, including their crystallography and deformation mechanisms, before focussing the discussion on the alloy that is the main focus of this work, Ti-6Al-4V. Finally, a brief discussion on the suitability of titanium alloys for processing by additive manufacture is given, leading into the following and final section of this literature review that covers the microstructure formation and mechanical properties in AM of Ti-6Al-4V.

### 2.3.2. Classification of Titanium Alloys

Pure titanium has an alpha (α) hexagonal close packed stucture (hcp) at room temperature that undergoes an allotropic phase transformation to a body centred cubic (bcc) beta (β) structure at a β-transus temperature of approximately 882°C,which stays stable up to the melting point of 1625°C [73]. These two crystal structures are shown in figure 2:13.

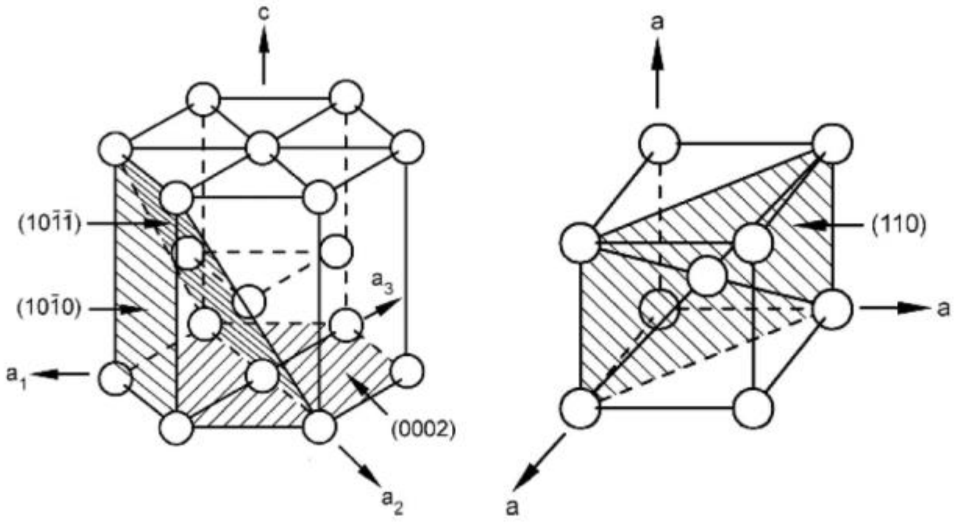

Figure 2:13. The α (hcp) and β (bcc) unit cells of titanium. Also indicated are the most closely packed planes; adapted from [74].

As titanium is a transition element with an incomplete outer shell in its electronic structure, it is able to readily alloy to form substitutional solid solutions with most transitional elements within a reasonable size difference to the titanium atom [74]. In addition, several non-metallic interstitial elements readily dissolve into titanium. These alloying additions have a profound effect on mechanical properties, in part due to the effects of solid solution strengthening, but the additions often stabilise one of the phases so that either phase, or both, are present at the operating temperature [74].

The difference in deformation behaviour between the α and β phases is largely due to the lack of symmetry in the hcp crystal system making deformation more difficult to occur. As a result, the α-phase has lower ductility than the β-phase, but has significantly higher creep resistance [74]. The α-phase also benefits from higher strength and stiffness, but is more anisotropic, for example; the Young’s modulus for an pure titanium α crystal varies from 145 GPa to 100 GPa, depending on the direction of the applied load relative to the crystal orientation [74].

Material properties other than mechanical properties also vary dependant on the phase distribution and volume fraction. The β-phase is found to be both thermally [3] and electrically [75] more conductive than the α-phase. The variation in electrical resistivity with temperature is shown in Figure 2:14, it can be seen that there is a dramatic increase in the conductivity at ~1150K as titanium transforms from α to β-phase.

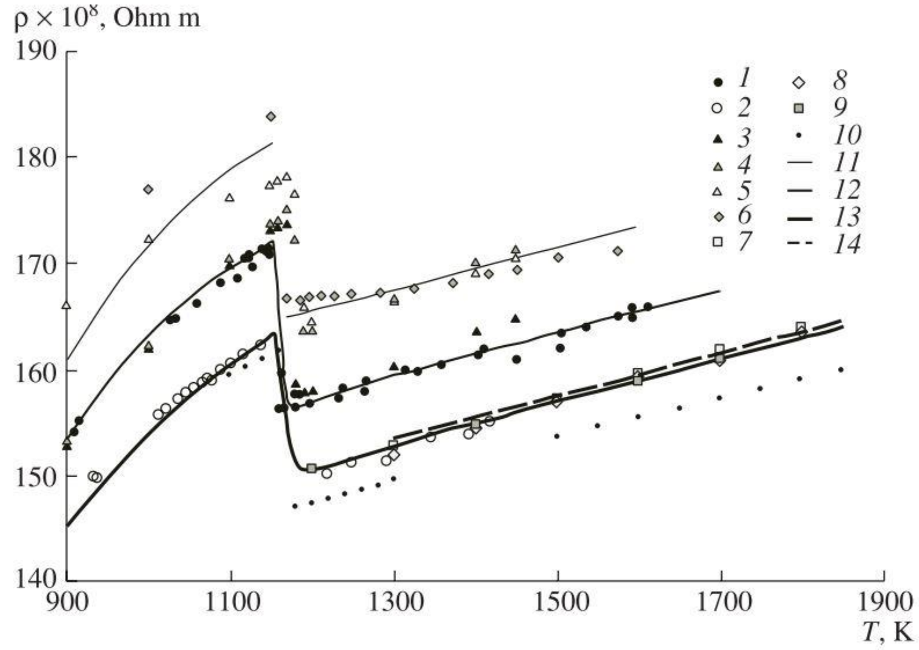

Figure 2:14. Numerous studies of the effect of temperature on the resistivity of commercially pure titanium collated by Ref[75]. The lines 11 to 14 show the influence of impurities of 0.01%, 0.1%, 0.3% and 0.5% respectively.

Due to the dual phase polymorphic nature of titanium, and the many alloying additions used in titanium alloys, there are numerous complex phase diagrams of alloy compositions. However, for convenience it is possible to simplify the effect of many of the major alloying additions down to four types, depending on the effect they have on relative phase stability. These are shown in Figure 2:15.

**Alpha stabilisers** are those that dissolve preferentially into the α-phase. These include aluminium, oxygen, nitrogen and carbon. By stabilising the α-phase they increase the β-transus temperature. Aluminium is the principle α stabiliser used and increases tensile strength by causing solid solution hardening.

**Beta stabilisers** decrease the β-transus temperature and can be split into two types, **β isomorphous stabilisers** and **β eutectoid stabilisers**. The β-isomorphous stabilisers include molybdenum and vanadium which are isomorphous with, or totally soluble in titanium. The β-eutectoid elements are those that form intermetallic compounds with titanium and include copper and nickel. However, the eutectoid reaction is generally quite slow and can usually be treated as if it does not exist [73].

The final phase diagram in figure 2:15 is a representation of the effect of tin, or zirconium when used as an alloying element. Addition of these alloying elements neither stabilises the α or β-phase and so are often referred to as **Neutral**. However, the addition of neutral alloying elements can still alter other material properties such as, for example, providing solid solution strengthening.

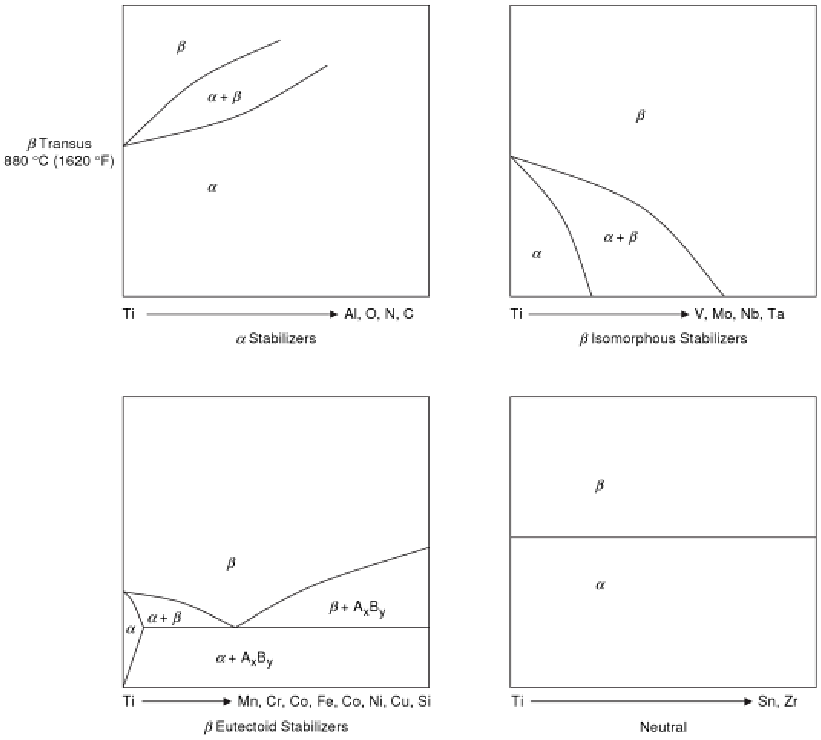

Figure 2:15. The four generic binary phase diagram types for titanium alloys showing the effect of (clockwise from top left) α stabilisers, β eutectic stabilisers, and those that have little effect on phase stability [76].

It has thus become standard practice to group the large number of titanium alloys by their phase composition. The four main classifications used are α, near-α, α+β and β alloys, roughly describing their phase compositions at room temperature.

### 2.3.3. *Titanium α → β and β → α phase transformations*

The anisotropic properties of the room temperature hcp α-phase, does not always translate into as strongly anisotropic fabricated parts as may be expected. This is because on cooling from the β-phase, it is common for many α grains to be nucleated at the β grain boundaries, generally leading to a relatively fine grained microstructure. However, there is still a texture inherited from the β phase as there is an orientation relationship that is maintained between the β and α through the transformation. Therefore the number of different α orientations that can form from each β grain is limited. Preferential α variant selection can also occur, further limiting textural weakening.

It has been confirmed that the during the polymorphic titanium phase transformation, the same orientation relationship is maintained as was first observed by Burgers for single crystals of zirconium (a metal with similar phase behaviour to titanium) [77]. The Burgers orientation relationship is given by:

$$\{110\}_\beta \parallel \{0002\}_\alpha \qquad \langle 111\rangle_\beta \parallel \langle 11\bar{2}0\rangle_\alpha$$

Equation 3

Upholding the Burgers orientation relationship ensures that there are only six possible orientation variants of β that can form from a single α grain in the α→β transformation. There are a further 12 α orientation variants that can be formed with the β→α transformation. If all of the variants mentioned in the previous two transformations form within a heat cycle that sees the material transform α→β→α, then a total of 72 variants should form with equal probability, effectively randomising the α texture [78]. If this were to occur, then the texture of material that has been through a heat treatment in the β-phase several times should have a very weak texture that bares little, if any, resemblance to the untreated material. However, there is often an apparent preference for certain variants to form relative to others, leading to a stronger texture than would be expected. Variant selection can lead to the phenomenon of 'texture memory', where the original α texture is recovered to a certain extent after a β heat treatment [79].

There are several factors that have been found to affect texture variant selection including deformation of the β-phase [80], an increased β grain size [81], and local internal strains [82]. A special case of variant selection has been seen to occur when neighbouring β grains share a (110) pole then (0002) α variants on either side of a grain boundary are selected with near identical crystallographic orientation. This was postulated by [83] and has been confirmed by others [80].

The texture memory effect can also be caused by the titanium alloy not being entirely single phase before transformation. This occurs because it is more thermodynamically favourable for a new phase to grow from a residual phase than nucleating new grains from a single phase [84]. This can occur by not fully heating into the β-phase region, meaning that there is some residual α that new grains can grow from upon cooling. This effect is particularly prevalent in two phase alloys where the β-phase is retained at room temperature and re-grows as the alloy temperature is taken towards and beyond the β-transus temperature [85].

### *2.3.4. Suitability of Titanium for AM*

As discussed in §2.1.1, one of the main advantages of additive manufacture is the ability to fabricate parts near-net shape. This is of clear benefit in use with titanium alloys where the raw material at ~20 $/Kg is significantly more expensive than other structural metals such as steel (~0.75 $/Kg) and aluminium (~1.5 $/Kg) [86]. However, the cost of the raw material is not the only cost involved with the manufacturing from titanium, as machining from titanium is more expensive than machining from other materials due to several reasons. The poor thermal conductivity of titanium leads to higher tool tip temperatures and increased tool wear. Tool wear can be negated to some extent by reducing the cutting speed, but this in turn leads to increased time of manufacture and cost [87]. Rather than achieving a continuous length of swarth of removed material, titanium tends to release removed material as individual small chips; this leads to tool wear by 'chattering'; the bouncing of the tool tip along the surface due to it springing back into place every time a chip of swarth is released [87,88]. Finally, the chemical reactive nature of titanium metal, with its strong alloying tendency, makes it difficult to machine, because it has a propensity to weld itself to the surface of the cutting tool, especially at the higher temperatures. This reduces the efficiency of the cutting edge and also increases the tool wear. Titanium has a particular affinity towards cobalt binders, which are regularly used in cutting tool materials [89].

The final way in which titanium is suited for additive manufacture is in its end use. Additive manufacture is inherently suited for smaller batch production, as the large cost outlay for bespoke dies and tooling of traditional manufacture is not split among hundreds of thousands of identical parts. This is in line with the use of titanium, the majority of which is used in the aerospace industry, where a relatively few of each part are required.

In a study in 2006 for Rolls Royce, Allen [19] found that it was already commercially viable to replace traditionally manufactured components with a buy-to-fly ratio of over 12:1 with additive manufacture, such as complex duct flanges (buy-to-fly ratio of ~20:1) as long as the performance of the part was identical. In the same study, it was projected that with maturing technology, AM should be able to replace traditional manufacture for components with a buy-to-fly ratio as low as 3:1.

## 2.4. Ti-6Al-4V

Ti-6Al-4V is the name given to the α+β alloy where 5.5 – 6.75% of the composition by weight is the α stabilising element aluminium, and 3.5 – 4.5% of the composition is the β stabilising element vanadium [90].Ti-6Al-4V is the most commonly manufactured alloy of the titanium industry, accounting for approximately 60% of all titanium metal production [1], and is the most used titanium alloy in the aerospace industry, due to its good combination of properties of high temperature strength, corrosion resistance, and good weldability [1]. It is largely for these reasons that Ti-6Al-4V has been the most extensively tested and researched titanium alloy when it comes to additive manufacture, and hence why it is the main alloy investigated in this study.

### *2.4.1. Microstructure of conventional Ti-6Al-4V products*

The microstructure of Ti-6Al-4V is highly dependent on its thermal history. The rate at which the material is cooled from the β-phase has a dramatic effect on the microstructure. On cooling slowly below the β-transus, α is nucleated at the heterogeneous sites of β grain boundaries forming a continuous grain boundary layer. Lamella α structures then proceed to grow by a diffusional process into the β grains, consuming them. At lower cooling rates these α plates tend to grow aligned, within close proximity, and with the same crystallographic orientation creating a ‘colony’ microstructure. These colonies can observed in Figure 2:16a. Faster cooling rates lead to finer α and several variants grow more intertwoven leading to a Widmanstätten or 'basket weave' microstructure [91]. In these microstructures some β is retained down to room temperature due to the growth of α enriching the β phase in vanadium to the point that the β is stable at room temperature [92]. If the cooling is so rapid as to limit the amount of diffusion possible, then martensitic structures can be formed. The most common martensite is α', similar in structure to equilibrium α but with slightly altered lattice constants due to the supersaturation of alloying elements [93]. With sufficient thermal energy for diffusion, α' laths tend to decompose into fine α plates [73]. An example of a martensitic microstructure can be seen in Figure 2:16b.

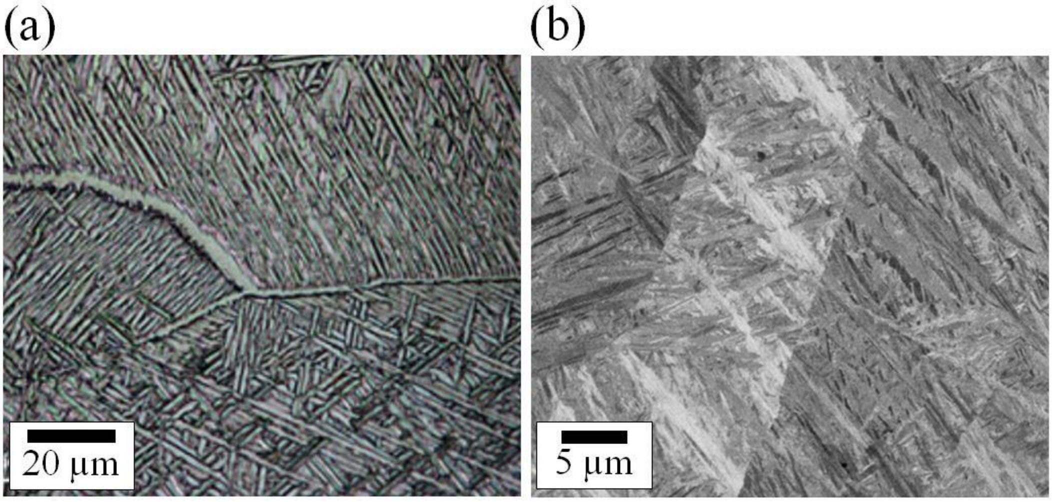

Figure 2:16. Microstructures of Ti-6Al-4V: (a) Widmanstättaen microstructure and (b) a martensitic microstructure; adapted from [94] and [95] respectively.

As will be discussed in the following section, such microstructures are not always desirable for optimum mechanical properties. Alternative Ti-6Al-4V microstructures can be achieved through more complex thermo-mechanical processing, such as that shown schematically in Figure 2:17, which can result in either a bi-modal (Figure 2:18a) or fully equiaxed structure (Figure 2:18b) depending on the cooling rate from step III of the process [74].

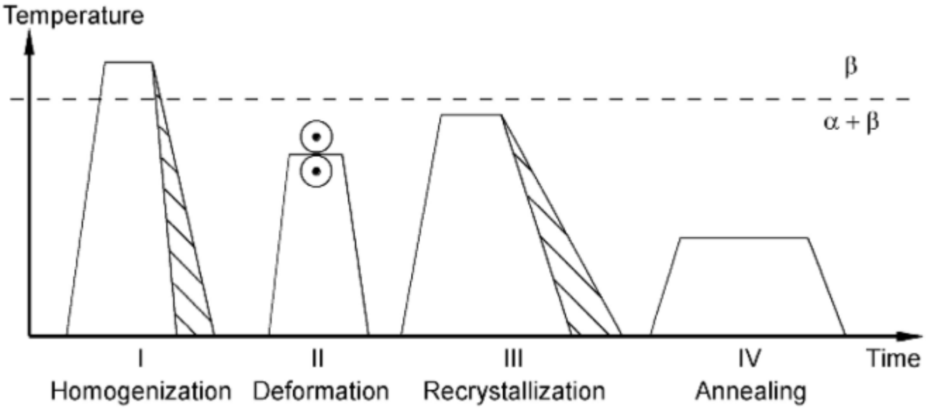

Figure 2:17. Schematic of the processing route for developing bi-modal and equiaxed Ti-6Al-4V [74].

Often hot working is initially conducted in the single β phase field to recrystallise and anneal cast material in an attempt to produce a more uniform wrought microstructure. The deformation in the β phase field refines the very coarse prior β grain structures formed on solidification by Dynamic Recrystallisation (DRX) [96,97]. As discussed in §2.2.6, DRX occurs at a critical strain if the temperature is high enough [98]. It is found that the resultant DRX grain size in Ti-6Al-4V shows good agreement with the Zener-Holloman relationship, that higher strain rates and lower temperatures lead to a finer recrystallization grain size [96]. However, the volume percentage recrystallized by DRX is reduced by these same parameters. For example, it is found that deforming at temperatures above the β transus at 1050 °C, at rates of 1 $s^{-1}$, and down to a total strain 0.7, only 3.1% of the material is found to recrystallise [97]. The recrystallised volume fraction can be increased with higher deformation temperatures, lower strain rates and higher total strains, but none of these changes are favourable from a process practicality point of view, and all will lead to an increase in the recrystallised grain size [99].

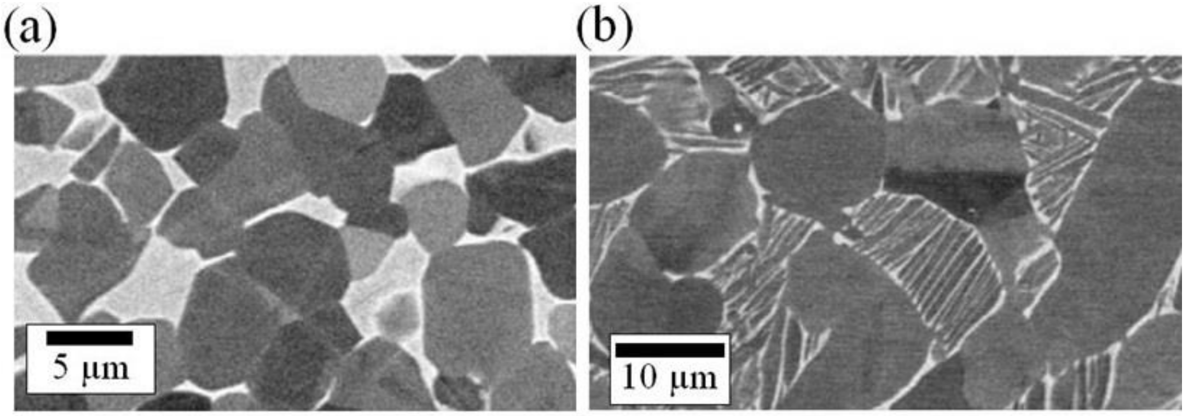

Figure 2:18. a) bi-modal and b) fully equiaxed Ti-6Al-4V microstructures obtainable via the processing route shown schematically in Figure 2:17; adapted from [100].

The α + β microstructure formed on cooling from the β phase is dependent on the cooling rate as discussed above, but if the prior β grain size is large, it is often a combination of Widmanstätten and colony α microstructures.  Deformation in the α + β phase field is used to break up this microstructure by a process known as ‘spheroidisation’ or ‘globularisation’ [101,102]. The globularisation process describes the shape changes of a lamellar structure into a globular, equiaxed, morphology. Globularisation is found to occur in a two-step process when the deformation causes intense shear bands to form across and within α plates, and the subsequent migration of interface boundaries to reduce surface energy that causes the penetration of the β phase to separate the α ‘globules’ [102,103]. High strains are found to be needed to cause globurisation, with strains of ~0.5 to ~1.5 required to initiate globularisation (dependant on the microstructure and deformation temperature) and as much as ~2.5 to get complete globularisation [104]. It is found that finer microstructures break up more easily due to the reduced α thickness [105], but the relationship with temperature is more complex due to the effect of the changing microstructure [104]. It has also been shown that after the full break-up of the grain structure, the Burgers' orientation relationship is no longer maintained between the α variants [101].

### *2.4.2. Microstructural Effects on Mechanical Properties*

The microstructure achieved in Ti-6Al-4V has a strong effect on the mechanical properties. Lütjering [106] has related the difference in mechanical properties to the 'effective slip length', equivalent to the size of the alpha laths, or colonies if present, as slip can transfer across α plate boundaries within a single colony, so that the entire colony can act as a large single grain [107]. It is found that not only does strength improve with a reduced slip length, but also fatigue life as both the nucleation and propagation can be linked to the colony size and slip length. High cycle fatigue (HCF) life is determined by the resistance to crack initiation, which is directly related to the higher yield stress of the finer microstructures, whereas low cycle fatigue (LCF) life is dominated by the resistance to crack propagation, which is also improved (at short crack lengths) by a finer microstructure [106]. Therefore, the greater the cooling rate through the β transus temperature, the greater the strength and potential fatigue performance of the alloy. These trends continue into cooling rates that produce a martensitic microstructure. However, this results a reduction in ductility [38] and creep resistance [73].

### *2.4.3. Prior β Solidification Microstructure*

As the mechanical properties of Ti-6Al-4V are determined by the α colony size, which is in turn affected by the prior β grain size (as α laths can extend across entire prior β grains) it is desirable to have as fine a prior β grain size as possible.

Large β grain sizes are common in Ti-6Al-4V solidification microstructures, this is partly due to the rapid β grain growth that takes place while above the β transus, and partly due to the nature of the solidification itself. This thesis is concerned with the refinement of this coarse β microstructure, so it is important to understand how it forms. However, as the refinement investigated in this work does not form under solidification, the topic will only be covered briefly here. More in-depth discussions of solidification can be found in textbooks such as that by Porter and Easterling [84].

As a liquid melt cools, at a certain temperature it becomes more energetically favourable to solidify as the reduction in atomic vibrational energy decreases to the point that inter-atomic bonding is favourable. However, under most conditions it is uncommon for the liquid to homogenously change phase, as any volume of solid that spontaneously forms is almost certain to re-dissolve back into the melt rather than grow. In order for these spontaneously formed nuclei to grow rather than re-dissolve, the molten liquid needs to be significantly cooler than the melting temperature. The reduced temperature of the liquid compared the freezing point is known as supercooling (also known as undercooling). Generally metals do not solidify homogenously, as heterogeneous sites such as the walls of the container (akin to sides of the meltpool), or inoculants in the melt, provide a surface for the molten material to solidify upon and thus a reduced energy barrier for nucleation. The reduced surface area, and therefore surface energy, of material solidified on heterogeneous sites, means that they can be smaller without re-dissolving, and therefore require less supercooling [84].

Under equilibrium conditions, where each element is given unlimited time for diffusion, it would be found that solidification would proceed as described by an equilibrium phase diagram, with each phase having a predicted composition at any given temperature. In the case of an alloy, the material solidifying is likely to have a different composition to the liquid. This is shown in the simplified case of a binary system in Figure 2:19 where a liquid of original global composition $X_0$ is cooled, resulting in solidification at a temperature $T_2$ of material with a composition of $X_S$ and the subsequent enrichment of alloying elements in the molten material giving a liquid of composition $X_L$. The ratio of these two compositions is known as the partition coefficient, k, and is defined in Equation 4 [84].

$$k = \frac{X_s}{X_l}$$

Equation 4

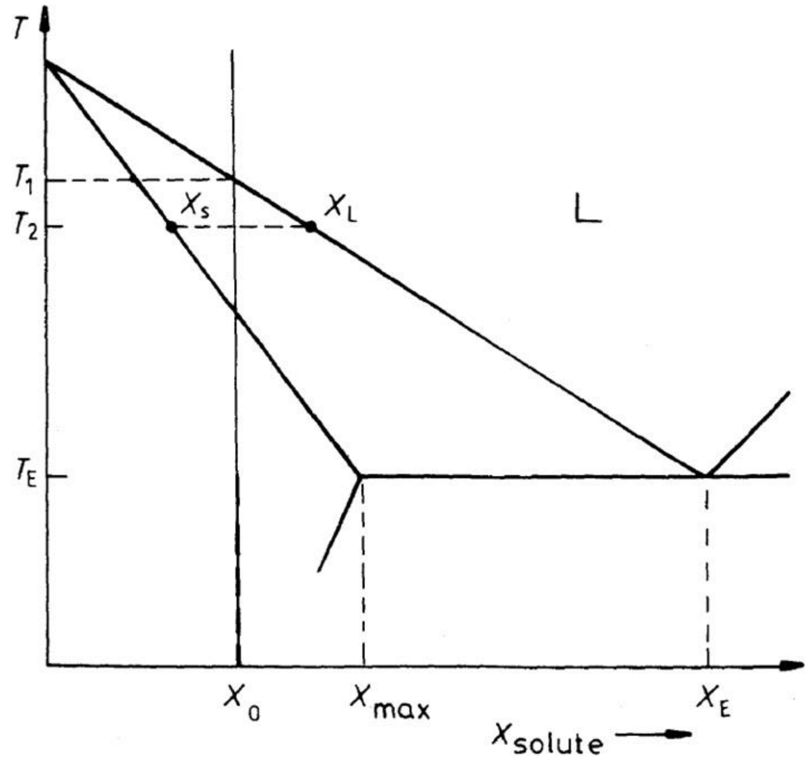

Figure 2:19. A hypothetical phase diagram demonstrating the concept of partition coefficient. Adapted from [84].

However, in most real-world conditions rapid cooling rates limit the amount of diffusion that can take place in the solid, and reduces the amount of mixing that can take place in the liquid. With minimal mixing in the liquid, the molten material immediately ahead of the solidification front becomes particularly enriched in alloying elements, altering the composition of the liquid near the interface. As the freezing point of the molten material is compositionally dependent, it is therfore possible that this enriched liquid is significantly below its freezing point to be supercooled. This is known as constitutional supercooling as it is compositionally dependent. It is therefore possible for the material ahead of the solidification front to be sufficiently supercooled to enable homogenous nucleation to take place ahead of the solidification front [84].

Unfortunately, constitutional supercooling is difficult to achieve in Ti-6Al-4V. As stated in §2.3.2, a large number of alloying elements, including Al and V, have a partition coefficients that are close to one due to their high solubility in titanium. Therefore, there is little segregation ahead of the solidification front, leading to negligible constitutional supercooling, and preventing homogenous nucleation in the melt [108].

Additions with a high partition coefficient in titanium that do segregate ahead of the solidification front have been investigated to determine their effect on the refinement of β solidification structures. These include rare earth alloying additions such as yttrium [109,110], and other elements with a low solubility in titanium such as boron [111,112]. In both cases it is found that these additions lead to heterogeneous nucleation ahead of the solidification front and lead to prior β grain refinement.

Constitutional supercooling is also one of the contributing factors towards the shape of the solidification front. When any perturbation spontaneously forms on the solidification front it can either melt back into the liquid phase to maintain a planar front, or the protrusions can grow preferentially into the liquid to create a cellular or dendritic structure as shown in Figure 2:20. Cellular and dendritic structures arise due to the enrichment of the surrounding liquid in solute during solidification. With minimal mixing in the liquid, the liquid away from the solidification is lower in solute, allowing the protrusions to grow into it. The tendency for solidification in this manner increases with greater supercooling (increased solute rejection), lower thermal gradients (prevents remelting of the cell tips), and greater growth velocities (minimising diffusion and mixing) [113]. If the conditions are extreme enough, then cells are seen to develop secondary and tertiary arms to form dendritic structures. As with the primary solidification, this occurs along crystallographically preferred directions such as (001) in cubic metals.

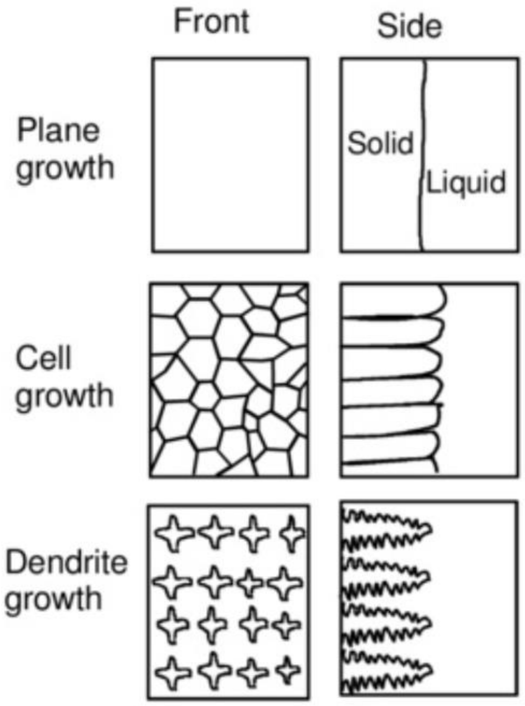

Figure 2:20. Schematic diagrams of the different morphologies the solidification front can take dependent on solidification conditions. Adapted from [84].

The formation of dendrites can also provide an additional route to refining the final grain structure during solidification, whereby the remaining molten material is agitated to the point where dendrite arms can become detached from the solidification front. If these detached dendrite fragments are above a certain size, then rather than remelting back into the molten material, they will continue to grow and can lead to a near equiaxed structure.

In the case of Ti-6Al-4V it is difficult to determine if the columnar structure solidifies by a dendritic or cellular mechanism, as any evidence of a dendritic structure will be destroyed by the subsequent $\beta \rightarrow \alpha+\beta$ transformation [113]. However, attempts to refine the microstructure through agitation of the meltpool have been found to be successful, with it reported that a refined β microstructure is generated by modulating the heat source power for both electron beam and gas-tungsten arc melted material [114,115]. Alternatively, the arc can be oscillated with an applied electro-magnetic field to generate a similar effect on the microstructure [116].

Despite reported successful attempts to refine the Ti-6Al-4V prior β microstructure by both alloying additions with a high partitioning coefficient and by perturbation of the meltpool, it has been noted that none of these techniques have found a commercial application [117]. This may be indicative of ‘reporting bias’, where only the positive results of the refined microstructure have been published. It is likely that the addition of other alloying elements has led to other undesirable properties, such as the development of brittle second phase particles. This is found to be the case with boron, where the TiB precipitates that form are found to crack under relatively small strains [118]. Likewise, it is probable that the reason that techniques with an agitated meltpool have not found an application is an unwanted consequence to the process, such as increased porosity.

Therefore, with the coarse prior β structure difficult to refine under solidification, it is left to thermomechanical processing to refine these microstructures. However, as discussed in section §2.4.1, traditional processing requires large reductions of at least 50% at high temperature in order to break up the prior β structure [101]. Not only would such a high temperature deformation process be difficult to implement with AM, but the shape change associated with these large reductions is contrary to the principle of AM.

### *2.4.4. Deformation Mechanisms*

The deformation mechanisms of Ti-6Al-4V are complex as a result of the dual phase microstructure. At room temperature the deformation behaviour is dominated by the α-phase due to it being the dominant phase making up to 95% of the volume of the alloy.

For the hexagonal phase, slip primarily occurs along the three $\langle 11\bar{2}0\rangle$ close packed directions in the <a> direction. There are 12 slip planes that this slip direction can act in (one basal (0002), three prismatic $\{10\bar{1}0\}$, and six pyramidal $\{10\bar{1}1\}$) but this is reduced to 4 independent systems due to symmetry and combinations of slip systems giving the same slip as can be achieved by another slip system [69]. This means that the von Mises criterion for five independent slip systems is not fulfilled. Therefore, a deformation mode with a component in the <c> direction is required. This can be satisfied by slip in <c + a>, or by twinning, although both of these mechanisms require a greater resolved sheer stress to be activated than pure <a> deformation [119]. There are four twinning modes that are commonly observed in hcp titanium, two that are activated by tension along the c-axis: $\{10\bar{1}2\}$ and $\{11\bar{2}1\}$, and two that are activated under compression: $\{10\bar{1}1\}$and $\{11\bar{2}2\}$ [120]. Some of the main deformation modes are shown in figure 2:21.

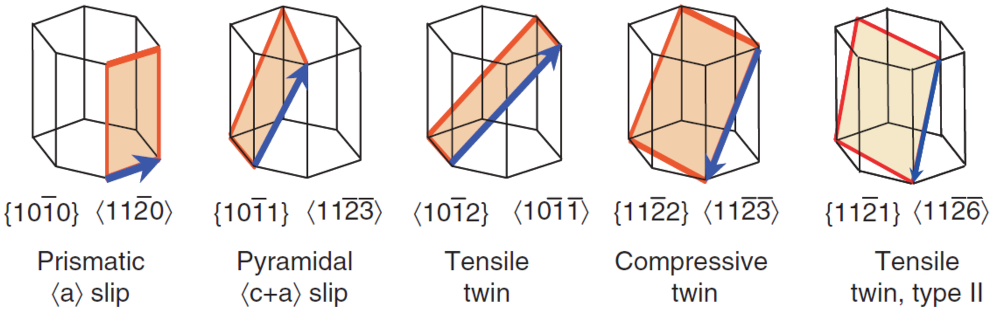

Figure 2:21. A selection of some of the main deformation mechanisms observed in titanium alloys [121].

The deformation behaviour of most hcp metals can be generalised by their c/a ratio. As α titanium has a c/a ratio below the ideal value of 1.633 slip most easily occurs on the prismatic planes, although basal and pyramidal slip can also be activated [122].

Twinning has traditionally been thought not to occur in Ti-6Al-4V unless at very high strain rates or at cryogenic temperatures, when the critically resolved stress for deformation by slip is higher [123,124]. Reasons given for this are that the high concentration of aluminium suppresses twinning [74]. However, twinning has more recently been observed at room temperature and low strain rates with deformations as small as only 6% strain [123]. The reason given for this being missed by previous studies is the difficulty in distinguishing them from similarly orientated grains. The dominating twin system observed, $\{10\bar{1}2\}\langle 10\bar{1}\bar{1}\rangle$, is shown schematically in figure 2:22.

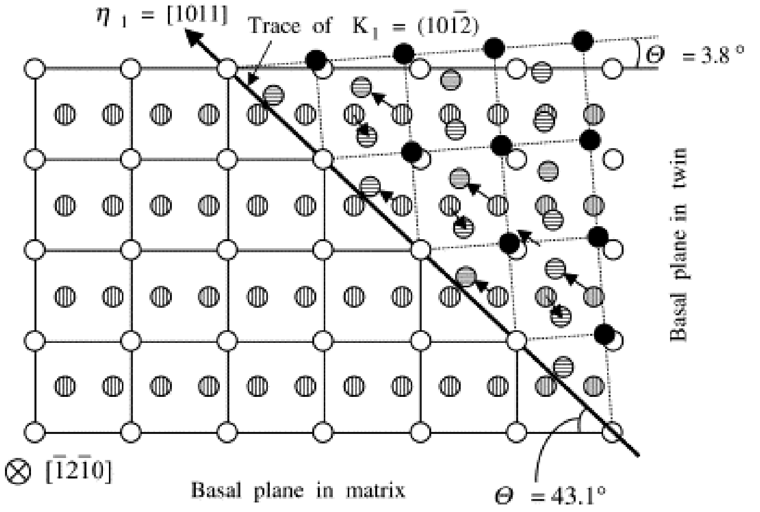

Figure 2:22. Illustration of atom movements in {10-12} twin [125].

Despite the deformation behaviour at room temperature being dominated by the deformation of the α phase in Ti-6Al4V due to the greater phase volume, deformation of the β must also be taking place. As there are no close packed planes in the bcc structure (the close packed plane of the hcp $\{0001\}$ having a packing density of ~91%, opposed to the bcc closest packed plane $\{110\}$ of the structure of only ~83%) it may be assumed that slip may be more difficult to activate in the cubic structure. However, the slip activation energy is also dependent on the length of the slip path, and it is found that the atomic shift required to recreate the crystal structure in bcc is shorter than in hcp. The shorter slip length combined with the greater number of independent slip systems (there are two close packed $\langle 111\rangle$ directions for each of the six $\{110\}$ planes, to give 12 independent slip systems), ensure that slip more readily occurs in bcc titanium [126]. Twinning is also not often observed in β titanium due to the prevalence of slip. However, two twinning systems have been observed in metastable β titanium alloys; {112}<111> and {332}<113> [127–129]. β twinning has not been previously reported in the deformation of Ti-6Al-4V, with the explanation given by Hanada et al. [129] that its composition does not lead to the formation of ω phase that is believed to facilitate twinning in metastable β alloys.

As Ti-6Al-4V has both phases present at room temperature, the deformation behaviour is influenced by the interaction of deformation mechanisms between the two phases. Due to the Burgers orientation relationship existing between the two phases, it is found that there are always three different misalignments that exist between the easy three <a> slip directions in an α grain and a ⟨111⟩ slip system in the corresponding β phase [130,131]. The closest aligned system (termed $a_1$) is only misorientated by ~0.7°, the next closest system ($a_2$) is misaligned by ~11.5°, with the third misalignment ($a_3$) by an even greater amount [131]. It is thus found that slip is most easily transferred across the well aligned slip systems, with the less aligned systems leading to dislocation pile up on the phase boundary as shown in Figure 2:23. The differing CRSS associated with slip transference for the three slip alignment conditions has been used to explain the observed deformation anisotropy of α colony microstructures [131].

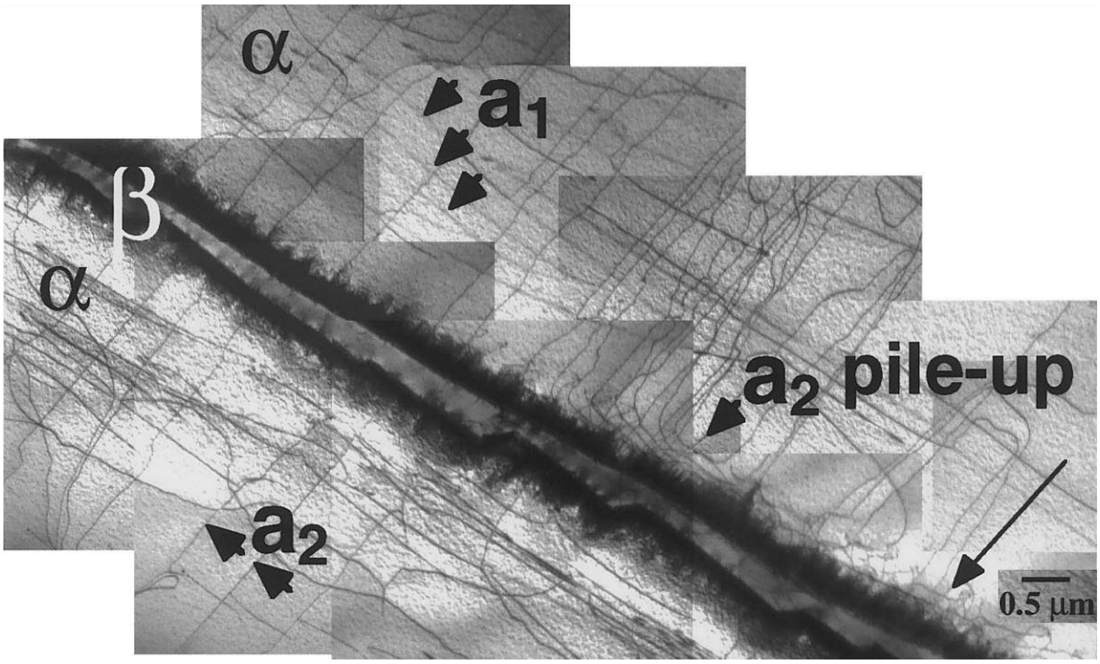

Figure 2:23. TEM micrograph of dislocation pile ups at a phase boundary within an α colony due to the slip system activated in the α colony being misaligned by ~11.5° with the closest ⟨111⟩ slip system in the β phase [130].

On the colony scale and at reasonably high strains, the deformation of the microstructure evolution is determined largely by the geometry of the imposed strain relative to the orientations of the laths. It is found that the laths (and entire colonies) will rotate with strain, with the plane normal tending to become aligned parallel to the loading axis. However, if the lamellae are aligned close to perpendicular to the compression axis then the laths tend to kink [132]. Both kinking and colony rotation can be observed in Figure 2:24 in a deformed T-6Al-4V microstructure. Also of note in the figure is the progression towards spheroidisation with increasing strain, as discussed in §2.4.1.

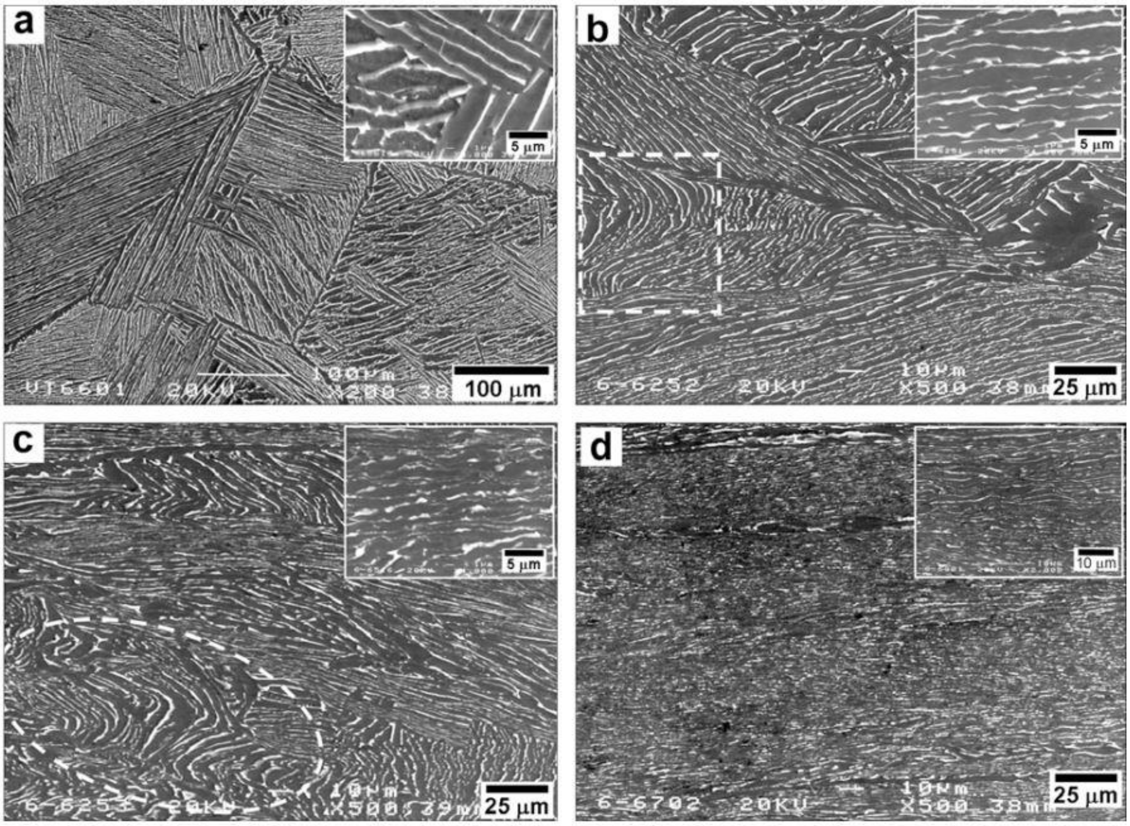

Figure 2:24. SEM images of Ti–6Al–4V microstructure (a) prior to deformation, and after height reductions of (b) 25%, (c) 50% and (d) 70%. A high- magnification image of the microstructure is shown in the top right corner of each figure (taken from [133]).

Though not reported in Ti6-Al-4V, it has been observed in other two phase titanium alloys that twins crossing α colonies can lead to a stress induced hexagonal martensite in the β phase as shown in Figure 2:25[134].

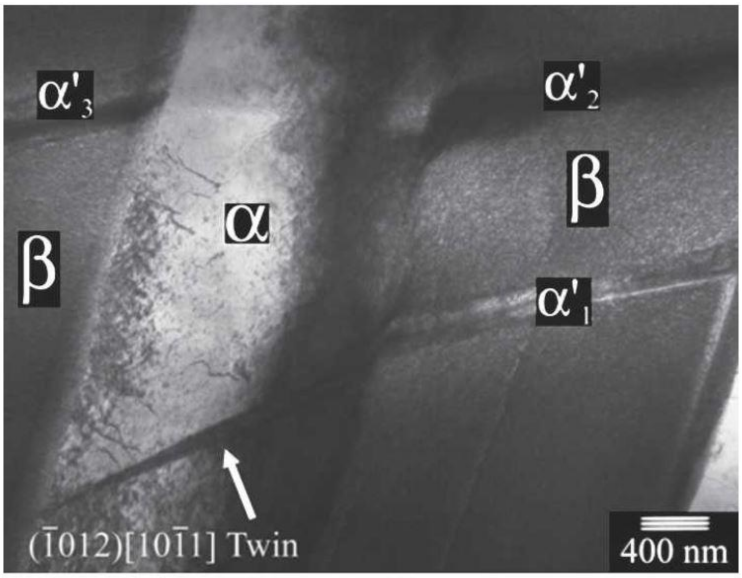

Figure 2:25. TEM micrograph of Ti-8.1V following tensile deformation showing stress-induced hexagonal martensite plates in the β phase and twins in the α phase [134].

## 2.5. Additive Manufactured Ti-6Al-4V Deposits

### 2.5.1. Microstructure of AM deposits Without a Deformation Step

#### Columnar Prior β Macrostructure

The most striking microstructure feature commonly observed in Ti-6Al-4V AM builds are large columnar prior β grains, that can be often observed by eye, and that can extend up to the entire height of the build. Columnar growth is observed with laser [26,38], electron [8,135], and arc [31] heat sources as shown in Figure 2:26.

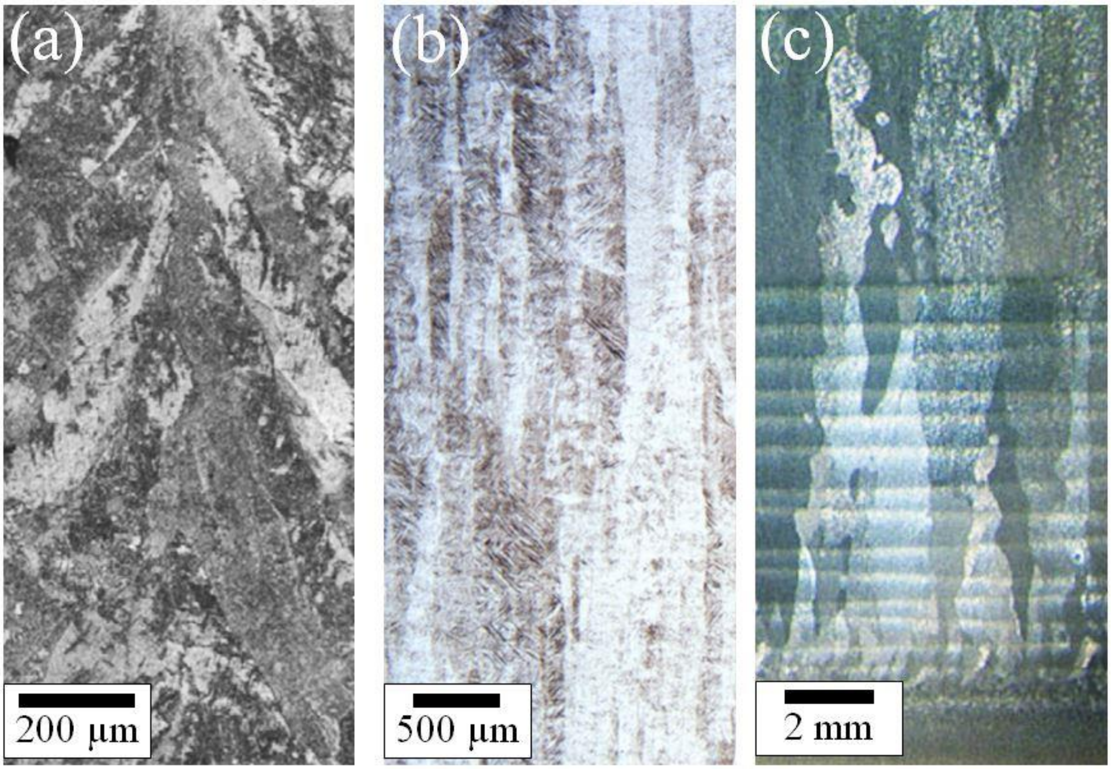

Figure 2:26. Examples of columnar prior β microstructures in: a) electron beam (SEBM), b) laser beam (SLM), and c) arc melted (WAAM) additive manufacturing processes. Taken from [136] , [95], and [94] respectively.

The large prior β grains form as a result of the AM solidification conditions when combined with the phase relationships in titanium alloys. The steps that lead to the columnar structure are shown in Figure 2:27, starting from an equiaxed prior β substrate that at room temperature is made up of an α lamella structure with retained β (Figure 2:27a). Regardless of the feedstock, the heat source not only melts the material being deposited and some of the substrate material beneath it, but to a certain depth the substrate is raised to a temperature above the β-transus, fully transforming it to the cubic β-phase (Figure 2:27c). This β phase returns to the orientation it was prior to transformation due to re-growth of the residual β retained between the laths. As the heat source moves on, and the molten material begins to cool and solidify, the high thermal gradients in the melt pool and low solute partitioning in titanium (discussed in §2.4.3) means there is insufficient supercooling ahead of the solidification front to enable nucleation ahead of the growth front [84]. In addition, owing to the high solubility of most elements including oxygen in titanium, there are few particles present in the melt for heterogeneous nuclei. Therefore the molten material solidifies epitaxially on to the β grain beneath it at the fusion boundary, continuing the grain. This cycle is repeated with each pass of the heat source as additional layers are deposited (Figure 2:27d), the thermal field returning the previously deposited material to the previous high temperature β structure, and the melt pool solidifying epitaxially upon it. As no nucleation occurs ahead of the solidification front, the coarse columnar structure develops through many layers. As the <001> growth directions are the 'easy growth directions' for bcc structures [137], these orientations are able to out compete other less well aligned orientations, and therefore come to dominate the structure [3,136]. Other than the preferred <100> orientation in the direction of the columnar growth, it is not normally expected that there should be any preference in orientation around this axis, which would result in a <100> fibre texture [3,136].

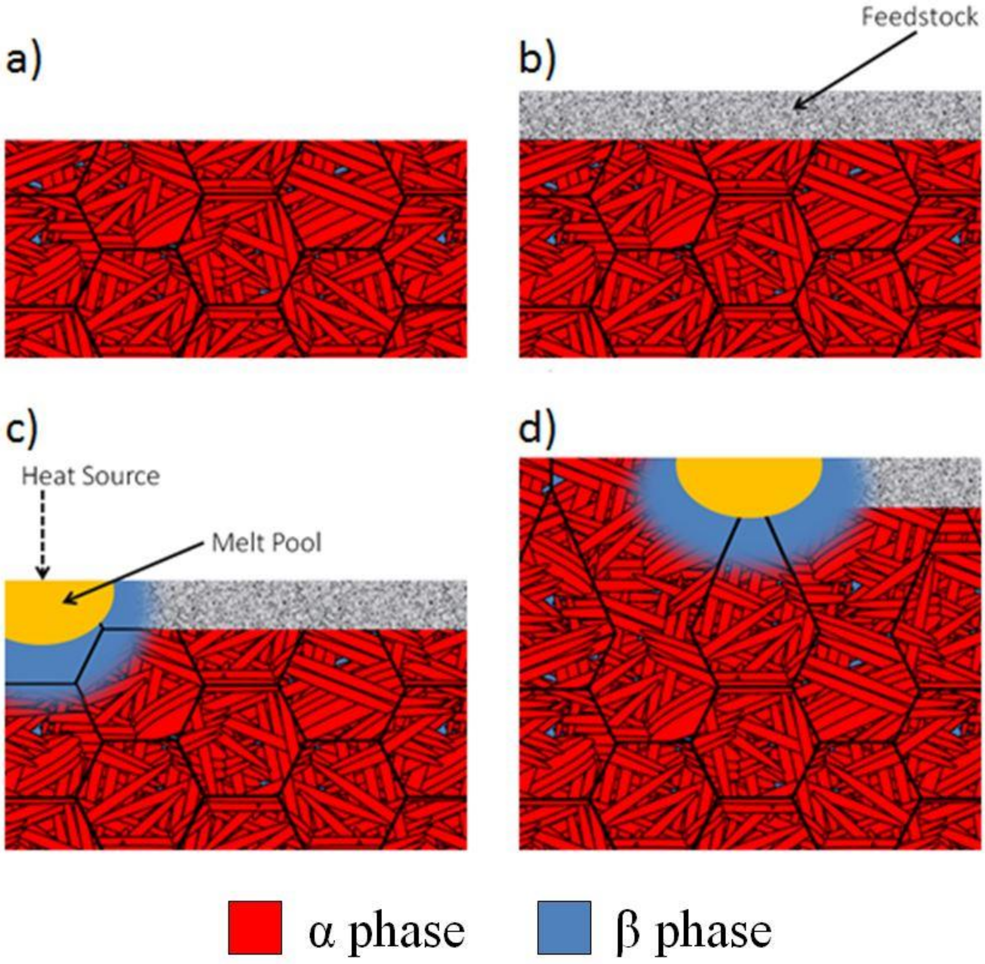

Figure 2:27. Schematic of the steps involved that lead to the coarse columnar prior β structure observed in Ti-6Al-4V AM builds.(a) - an equiaxed prior β substrate, (b) - addition of feedstock (in this case powder), (c) - the heat source that melts the feedstock and underlying material, and heats the surrounding material into the β phase, and (d) – with additional layers, prior β grains grow epitaxially through the build height, growing competitively.

### α + β lamellar microstructure

As discussed in §2.4, the microstructure of Ti-6Al-4V is highly dependent on the cooling rate through the β transus. With most AM techniques no cooling is forcibly applied, but because of the small meltpool is cooled by conduction through the substrate and previously deposited material it is sufficient to cool the material very quickly. Few measurements of the cooling rates in AM have been made, however the cooling rate at solidification has been estimated by Simoneli et al. [95] to be in the range $10^3$ to $10^5$ K/s in the EDM process, which would be sufficiently fast to expect a martensitic transformation. However, as discussed in the previous section, in all AM processes with Ti-6Al-4V the thermal field of the deposition heat source also reheats several underlying layers back above the β transus (Figure 2:28). It is the cooling rate of the material the final time it goes through the β transus that dictates the final microstructure of the build.

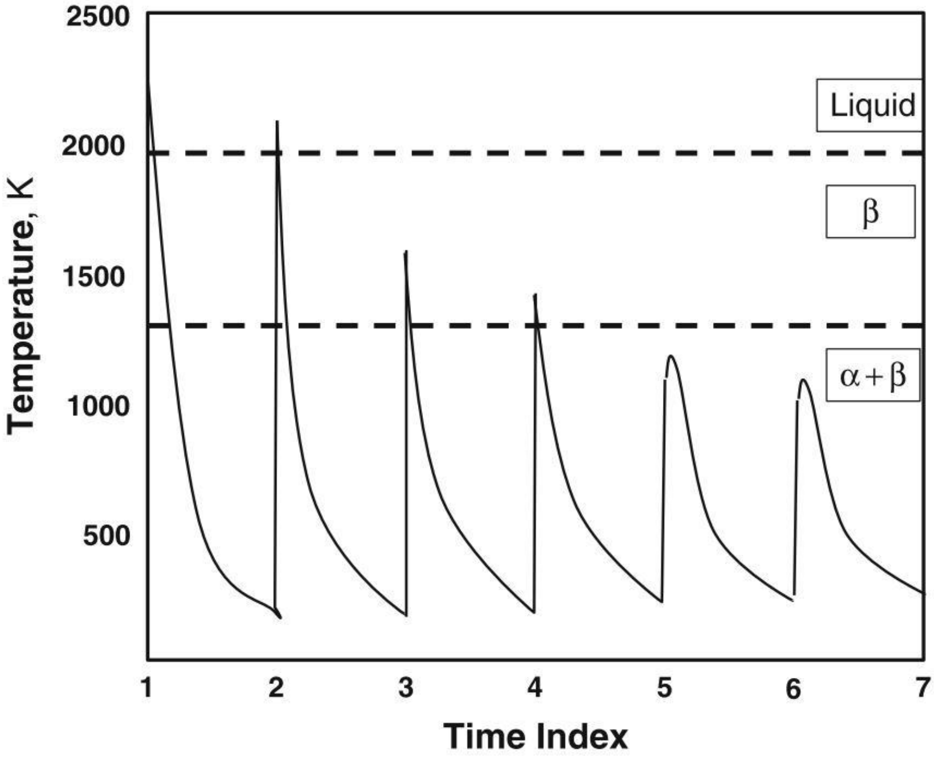

Figure 2:28. Schematic of the thermal profile of a single layer of Ti-6Al-4V during AM processing [44].

Analysis of the direct temperature measurements made during manufacture in the study by Martina et al. in [6] of Wire-arc AM indicates that the cooling rate of the material the final time it transforms through the β transus is ~70 K/s. The microstructure of this cooling rate in the WAAM process is given in Figure 2:29a, where it can be seen that the morphologies consist of grain boundary α at the prior β grain boundaries, followed by colonies of α plates forming off it, before a Widmanstätten basket weave morphology develops in the centre of the prior β grains with an average lath thickness of ~0.7 µm [6]. Similar α morphologies are reported in laser blown powder based processes, an example of which is given in Figure 2:29b with an α lath width of 1-2 µm suggesting a similar, or slightly slower, cooling rate [26]. The morphology of the microstructure when a heated powder bed is used is markedly different, as shown in Figure 2:29c of the EBM process. The different microstructure in Figure 2:29c arises from the extended time the build is held at 600-800°C EBM given sufficient time at temperature for diffusion to take place to achieve a near equilibrium volume of β [38]. Despite being held at temperatures sufficient for microstructural coarsening to take place, it is found that EBM leads to a microstructure with a comparable α lath width of ~1 µm [3,138], it can therefore be assumed that the cooling rate through the β transus is again rapid.

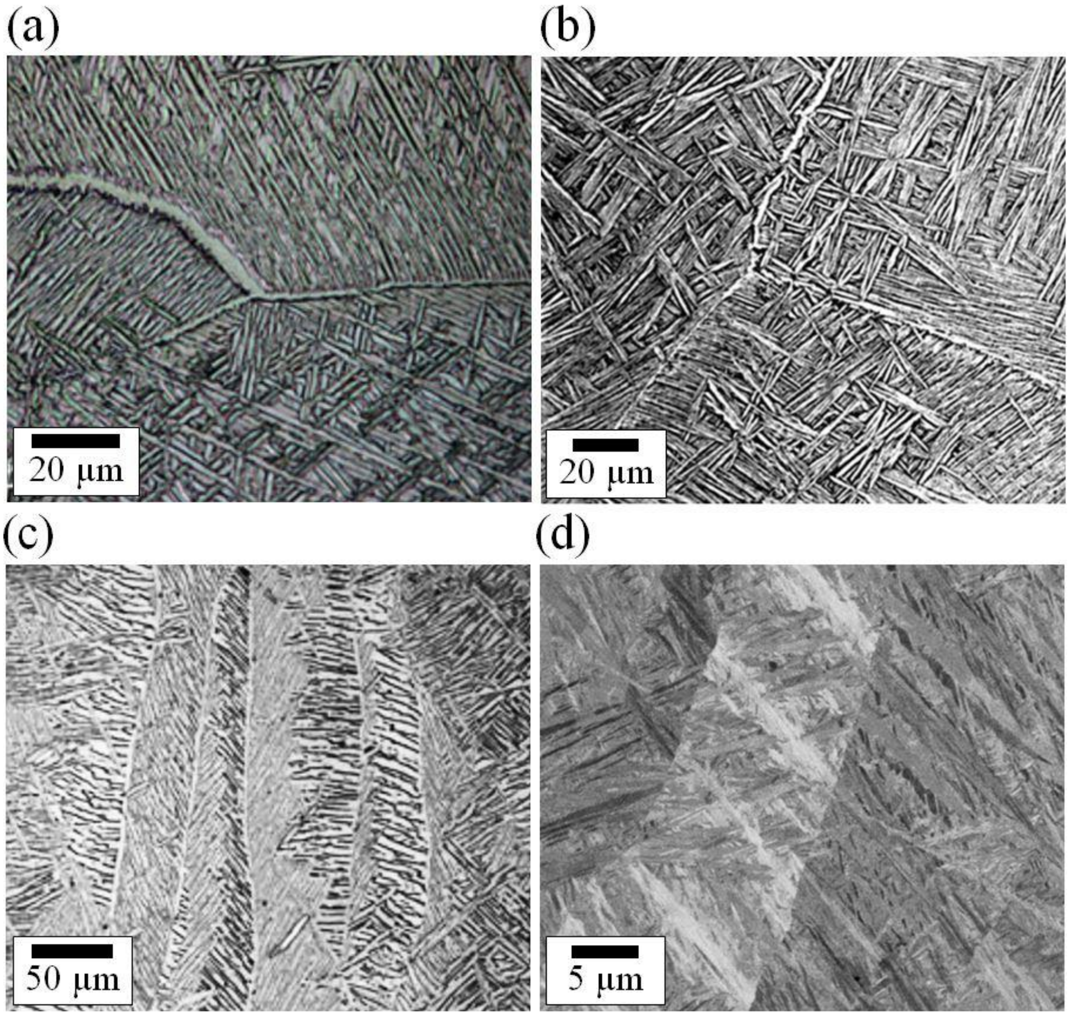

Figure 2:29. Typical Ti-6Al-4V AM microstructures. (a) & (b) are typical α+β Widmanstätten microstructures generated in arc and laser blown powder based processes respectively. A typical microstructure of a heated powder bed process is given in (c) where diffusion has allowed a greater volume of β to be retained. And (d) a martensitic microstructure generated by extreme cooling rates with SLM; adapted from [94], [26], [3], and [95] respectively.

A fine layer of α' martensite has been observed in several studies at the top of AM builds including WAAM [6] and EBM [3] resulting in the acicular sub-micron structure shown in Figure 2:29d. The formation of martensite in the top layer is not surprising as the final layer of deposition is not subsequently reheated into the β phase by the successive passes, and its cooling rate through the β transus is greater than for the rest of the build. This is shown schematically in Figure 2:28. It should be noted that the cooling rate through the β transus can be heavily affected by process parameters, such as a low heat input and/or a fast moving melt pool, resulting in a smaller thermally effected zone that will lead to both a higher initial cooling rate from solidification, and to fewer of the previously solidified layers being reheated above above the β transus and can result in a fully martensitic build. Fully martensitic microstructures are often achieved with the SLM process [95].

### Microstructural Banding

Another microstructural feature common across the various AM platforms is microstructural banding, often observable by eye after etching. Although these bands replicate the spacing of deposited layers, they do not correspond directly with the deposited material as observed by lines on the outside of the build, and no banding is observed in the top several layers [31]. An example of banding is clearly visible in the WAAM macrostructure in Figure 2:26c. The banding is thought to be due to the formation of different morphology of α forming due to the different peak temperatures reached, with the top of the uppermost band indicating the depth of the material to reach the β transus and every band beneath this showing the material taken to the β transus with every previous layer [139]. The banding is understood to correspond to a region where the material was not taken fully into the β phase, instead to a point where there was a high proportion of β phase, but still remnants of the α phase remaining; these α fragments alter the transformation kinetics upon cooling acting as nucleation sites for the transformation and leading to a different transformation microstructure [140]. The microstructural banding has been observed in arc [31] processes as well as those using electron [37] and laser based AM techniques [141]

### Texture

Few textural studies have been completed on AM Ti-6Al-4V. The only two extensive studies carried out on electron beam AM are by Al-Bermani et al. [3], and Antonysamy et al. [136]; both studies were carried out by Electron BackScattered Diffraction (EBSD) analysis, which will be described in more detail in§3.5.2. It was found in both studies that the β columnar grains do grow with a preferential <001> crystallographic direction in the direction of columnar growth as highlighted by the red colouration of the grains in the orientation maps in Figure 2:30 that are coloured with IPF colouring in the direction of columnar growth.

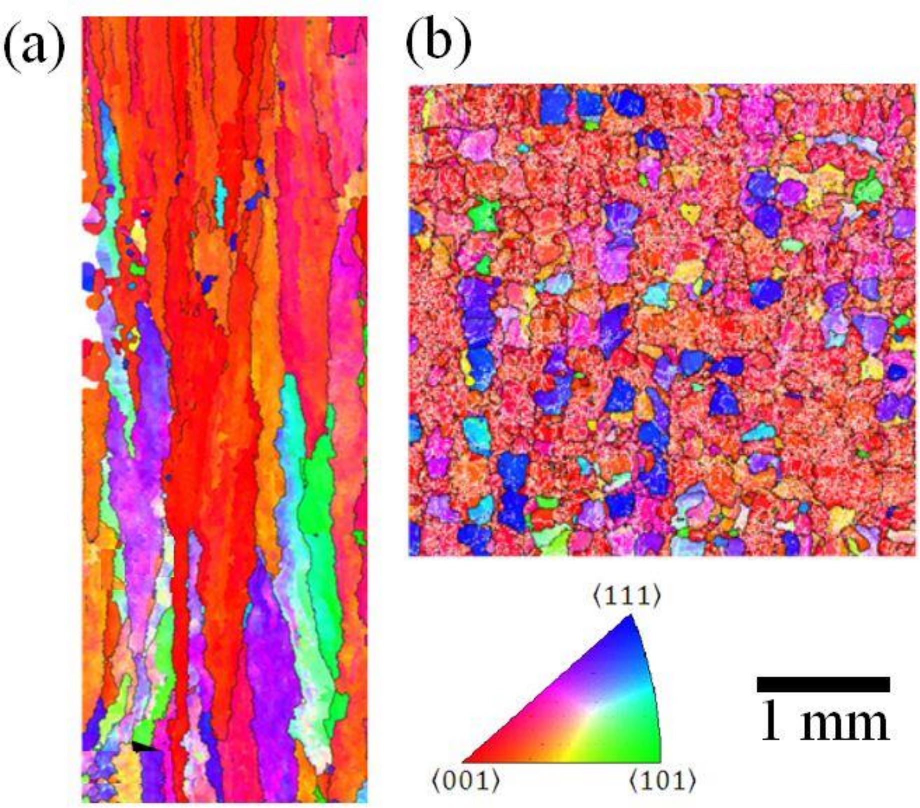

Figure 2:30. β orientation maps with IPF colouring in the primary build direction highlighting the strong <001> columnar growth observed in EBM builds. (a) show sectioning parallel to the columnar growth [136] and (b) transverse to it [3].

As expected, both studies found that the overall texture of the builds was a strong <100> fibre. This fibre texture was observed by both studies when a large number of areas of the same sample are considered (Figure 2:31 – 'Whole Build'), however, both studies individually found regions within the samples where an ill-defined cube texture was present (Figure 2:31 – 'Selected Area'). The cube texture has been found with <001> directions either parallel to the melt pool rastering directions [136] or at 45° to them [3,136]. In the case of Al-Bermani et al. the cube textures highlighted may be deceptively strong due to the low number of grains covered in these reduced areas, however they do show a tendency for a locally preferred orientation. The cube texture found in the study by Antonysamy et al. was found over a much larger area and therefore sampled many more grains. It was found by Antonysamy et al. that the cube texture was found at distinct build heights and it was proposed that this could have arisen due to the alternating, orthogonal rastering pattern taken by the melt pool encouraging the <001> easy growth direction to grow into it laterally, as it carries the solidification front along with it.

The <100> preferential growth has also been observed in a laser-powder bed process [95], but to date, no textural studies have been published on wire feedstock titanium AM processes.

| Study | Whole Build | Selected Area | Textural Strength |
|---|---|---|---|
| Al-Bermani et al. | 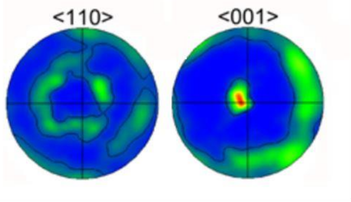 | 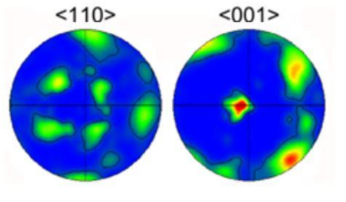 | 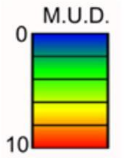 |
| Antonysamy et al. | 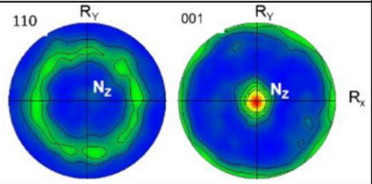 | 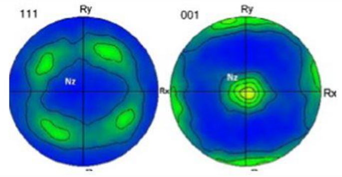 | 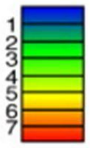 |

Figure 2:31. Summary of the two previous textural studies by Al-Bermani et al. [3], and Antonysamy et a.l [136]. with pole figures showing the β textural strength of EBM-AM.

The discussion above has been limited to the texture of the β phase, as it is this phase that forms first upon solidification, and it is this phase that leads to the continuation of the coarse columnar structure across the height of the build. However, at room and at service temperatures the majority of Ti-6Al-4V is the more anisotropic α phase, and it is the α phase that dictates the majority of the mechanical response. In the previous section it was discussed how each large prior β grain transforms to many fine α laths upon cooling below the β transus. As the Burgers' orientation relationship is maintained through the phase transformation there are 12 possible α variants that can form from each β grain. If all 12 variants are formed with equal probability, then the resultant microstructure is relatively texture free [4,136]. However, numerous factors can lead to some of the variants forming in preference to others (see §2.3.3) leading to a highly textured build. Two studies have investigated the variant selection in AM builds, Simonelli [95] found evidence of variant selection in an SLM process where it was found that half of the variants accounted for over 70% of the measured α laths, however it should be noted that the material investigated by Simonelli was entirely martensitic, and only measured the α variants in a limited number (~40) of prior β grains. Antonysamy et al. [136] considered thousands of grains in EDM material and found that there was little evidence of variant selection. The resultant weaker texture of the α phase compared to the β texture from which it transformed is highlighted in Figure 2:32.

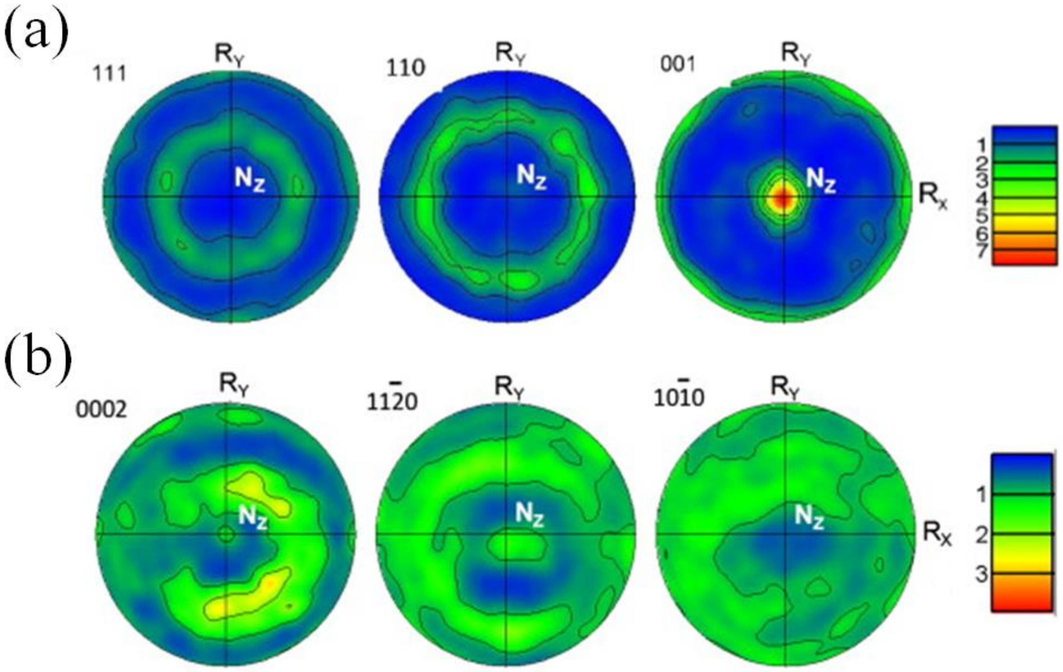

Figure 2:32. Pole figures of the coarse β grain texture (a), and the resultant α texture upon transformation; adapted from [136].

### *2.5.2. Mechanical Properties of Ti-6Al-4V AM Deposits*

There have been various studies into the mechanical properties of Ti-6Al-4V AM builds, a summary of studies that have tested in two orientations are given in Table 2:2. The orientations of the samples relative to the build direction are shown in Figure 2:33.

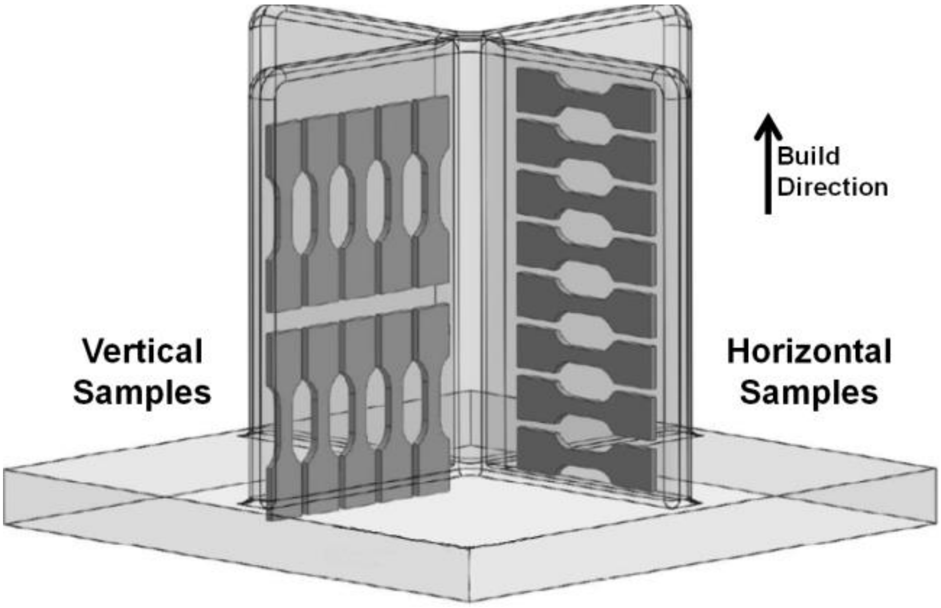

Figure 2:33. Schematic of how tensile test samples are orientated relative to the build direction as referenced in Table 2:2; adapted from [4].

For ease of interpretation, the information in Table 2:2 is also displayed graphically in Figure 2:34. It is found in general that the laser based techniques result in the highest tensile strengths, with yield strength ($\sigma_y$) ranging from ~900-1200 MPa and ultimate tensile strength ($\sigma_{UTS}$) in the range ~1050-1250 MPa; whereas the other AM techniques achieve yield strengths in the ranges of ~800-1000 MPa and ~850-1050 Mpa for $\sigma_y$ and $\sigma_{UTS}$ respectively. In all cases these values are comparable to, or exceed, the minimum values set out in standards for cast and wrought material of a $\sigma_y$ of 758 MPa and $\sigma_{UTS}$ of 860 MPa for cast material [90], and a $\sigma_y$ of 860 MPa and $\sigma_{UTS}$ of 930 MPa for wrought [142]. Rafi et al. has attributed the higher tensile properties to the greater cooling rates involved in the selective laser melting processes, which can lead to the formation of martensite. This is corroborated by the reduced elongation observed in the majority of the laser based processes as such microstructures are known to be a less ductile [38].

Table 2:2. Summary of the findings of various studies into the tensile properties of Ti-6Al-4V AM builds.

| Study | Technique | Testing Direction | Yield Strength (MPa) | UTS (MPa) | Elongation (%) |
|---|---|---|---|---|---|
| Amsterdam & Kool [143] | LENS | Horizontal | 1052 ± 27 | 1153 ± 13 | 5.3 ± 2.1 |
| | | Vertical | 1045 ± 24 | 1141 ± 15 | 9.2 ± 1.1 |
| Carroll et al. [4] | LENS | Horizontal | 960 ± 26 | 1063 ± 20 | 13.3 ± 1.8 |
| | | Vertical | 945± 13 | 1041 ± 12 | 18.7 ± 1.7 |
| Vilaro et al. [144] | SLM | Horizontal | 1137 ± 20 | 1206 ± 8 | 7.6 ± 2 |
| | | Vertical | 962 ± 47 | 1166 ± 25 | 1.7 ±0.3 |
| Rafi et al. [38] | SLM | Horizontal | 1195 ± 19 | 1269 ± 9 | 5 ± 0.5 |
| | | Vertical | 1143 ± 30 | 1219 ± 20 | 4.89 ± 0.6 |
| Edwards et al. [135] | EBM | Horizontal | 783 ± 15 | 833 ± 22 | 2.7 ± 0.4 |
| | | Vertical | 812 ± 12 | 851 ± 19 | 3.6 ± 0.9 |
| Hrabe & Quinn [138] | EBM | Horizontal | 982.9 ± 5.7 | 1029.7 ± 7.0 | 12.2 ± 0.8 |
| | | Vertical | 984.1 ± 8.5 | 1032.9 ± 12.9 | 9.0 ± 2.9 |
| Rafi et al. [38] | EBM | Horizontal | 899 ± 4.7 | 978 ± 3.2 | 9.5 ± 1.2 |
| | | Vertical | 869 ± 7.2 | 928 ± 9.8 | 9.9 ± 1.7 |
| Martina et al. [42] | WAAM | Horizontal | 860 ± 25 | 920 ± 20 | 12 ± 5.0 |
| | | Vertical | 810 ± 25 | 880 ± 10 | 21 ± 2.0 |
| Brandl et al. [145] | WLAM | Horizontal | 818 ± 31 | 885 ± 29 | 4.1 ± 0.8 |
| | | Vertical | 791 ± 15 | 870 ± 16 | 11.2 ± 3.2 |
| Brandl et al. [145] | WAAM | Horizontal | 881 ± 20 | 963 ± 24 | 7.9 ± 2.1 |
| | | Vertical | 860 ± 13 | 938 ± 22 | 16.5 ± 2.7 |

Few of the studies report on finding any tensile strength anisotropy, as within the error of the measurements, the results in each direction were not significantly different. However, though this is the case individualy, when all of the findings are considered together in Figure 2:34, it is clear that there is a general trend across all AM technologies that the tensile strength is less when tested in the build direction than normal to it, but the biggest effect is on ductility where considerably greater ductility is generally found in the build direction. Anisotropy is observed in SLM samples, the anisotropy has been attributed to irregular shaped defects caused by lack of fusion that lie in the build plane [144]. Carroll [4] dismisses the assertion that the strong texture seen for the prior β grains leads to the observed anisotropy, due to the transformation to α weakening the texture, and in contrast they argue instead that the anisotropy is due to colony α providing a preferential path to damage accumulation along prior β grain boundaries.

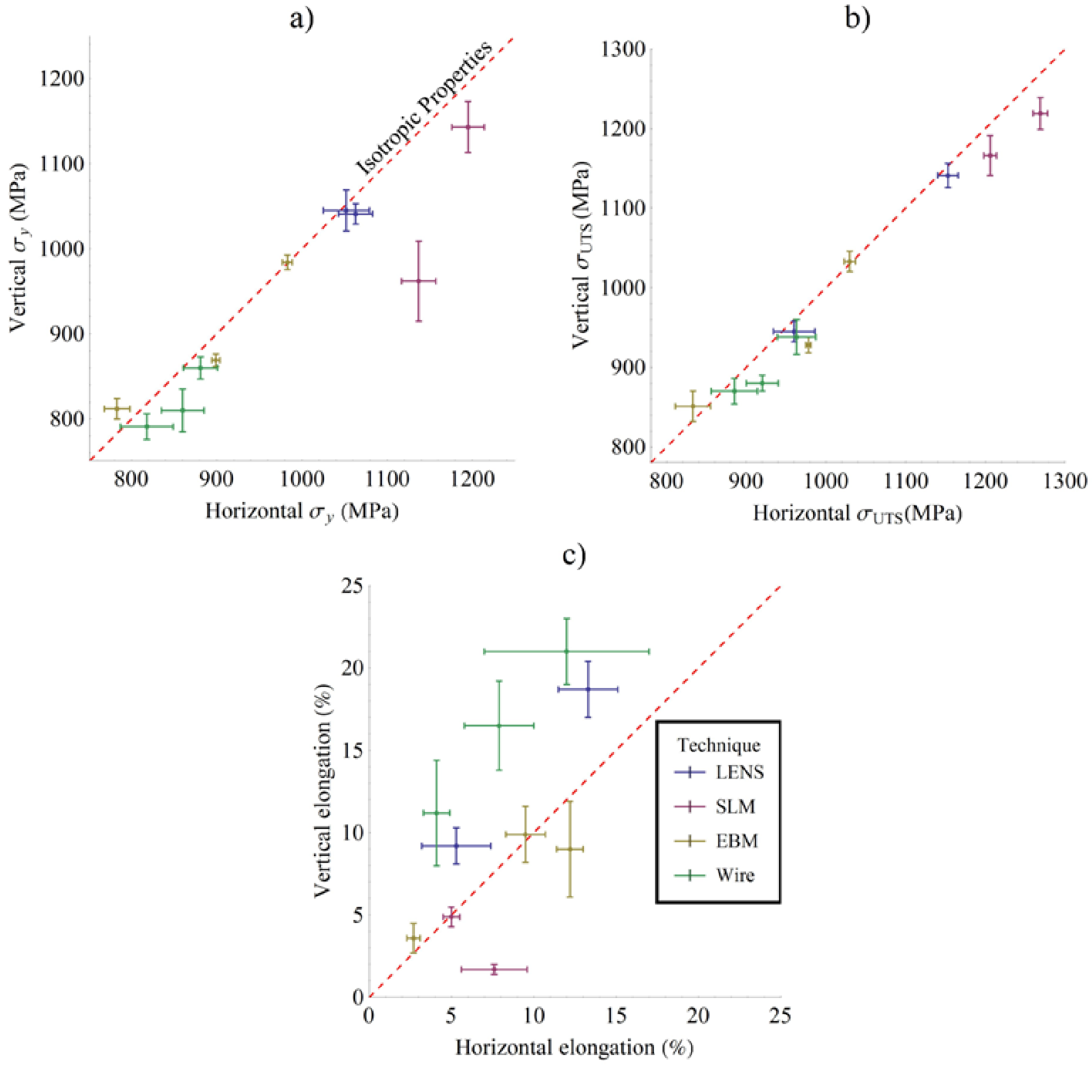

Figure 2:34. Graphical summary of data presented in Table 2:2, showing mechanical property anisotropy of Ti-6Al-4V builds in the horizontal and vertical directions for: a) yield strength, b) ultimate tensile strength, and c) elongation.

A number of the above studies have also investigated the fatigue properties of AM builds, however these were either only in one direction [38,143], or on too few samples that were too porous to be statistically relevant [135]. Where the origin of failure could not be associated with a pore or defect, the high cycle fatigue life was found to be superior to wrought material [143,145]. One study that has completes fatigue testing in two directions [145], found the material to behave anisotropically with greater dynamic strength in the horizontal direction. Anisotropic behaviour is to be expected due to crack initiation occurring at α colony boundaries (if there is no larger defect present) and the formation of large α colonies along the columnar prior β grain boundaries [38].

### 2.5.3. Effect of a Deformation Step on AM Ti-6Al-4V Deposits

Prior to the work contained within this thesis, little work has been published on the addition of a deformation step to an additive manufacture process. Only three papers have been authored by Cranfield university on the technique they have been developing on combining Wire Arc Additive Manufacture (WAAM) with rolling. In the first, Colegrove et al.-2013 [33], discusses the application of the technique to AM in steels. This was shown to be reasonably successful and resulted in reduced distortion of finished parts. In the second, Martina et al.-2013 [42], discusses extending the technique to Ti-6Al-4V, and observes not only a reduction in the build-up of residual stresses, but notes a surprising refinement of the prior β grain structure (Figure 2:35). The refinement of the prior β structure is surprising due to the low strains involved, as it is found that the refinement occurs with rolling that only results in an ~8% reduction in the height of the wall. This compares to a minimum of 50% deformation required to break up the prior β grain structure with conventional thermo-mechanical processing [101]. Alongside the refined microstructure, this work also reports more isotropic tensile properties than in samples that are not rolled. The most recently published work, Martina et al.-2015 [6], goes into more detail on the thermal history of the samples and attempts to link the refinement to the peak temperature reached within the build.

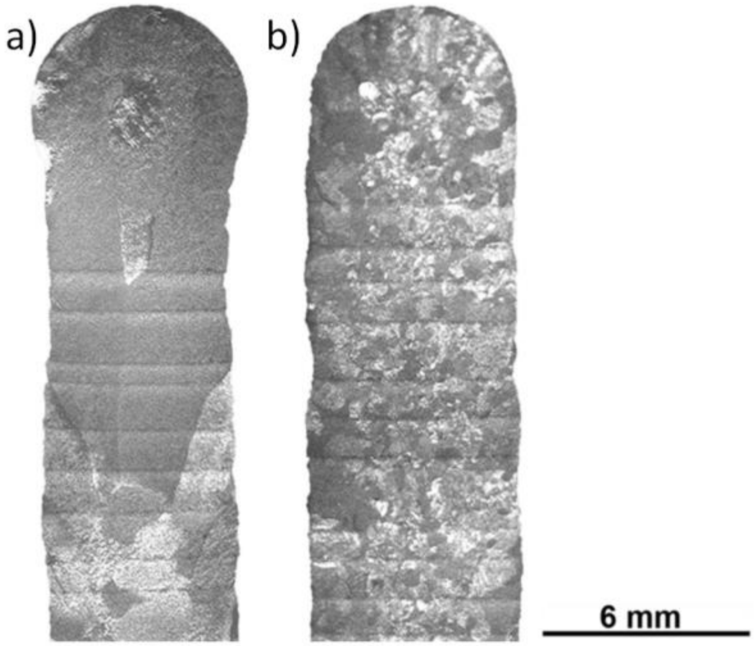

Figure 2:35. Optical microscopy of the cross section of WAAM walls showing in (a) the columnar prior β structure and banding structure of an as built wall, and in (b) the prior β refinement achieved by rolling between layers of deposition; adapted from [6].

The only attempt at an explanation of the mechanism that causes the refinement of the β when AM is combined with rolling is given in Martina et al.-2015, where the origin of the refined β grains was attributed to static recrystallization at ~780°C. However, this conjecture was based upon a direct measurement of the temperature during processing that also measured the banding in the microstructure forming at a peak temperature of ~740°C, whereas it is universally accepted in the literature that the banding is a result of material cooling from the β transus of ~1000°C [31,139]. Therefore, it is plausible that an error in the measurement of the temperature may have been made, and it is likely that temperature for the grain refinement is above the β transus. This is re-enforced by the observation that the refined grains are only found above the final white banding when the rolling is only applied to the penultimate layer (Figure 2:36). It is thus likely that the phase transformation plays an important role in the refinement mechanism.

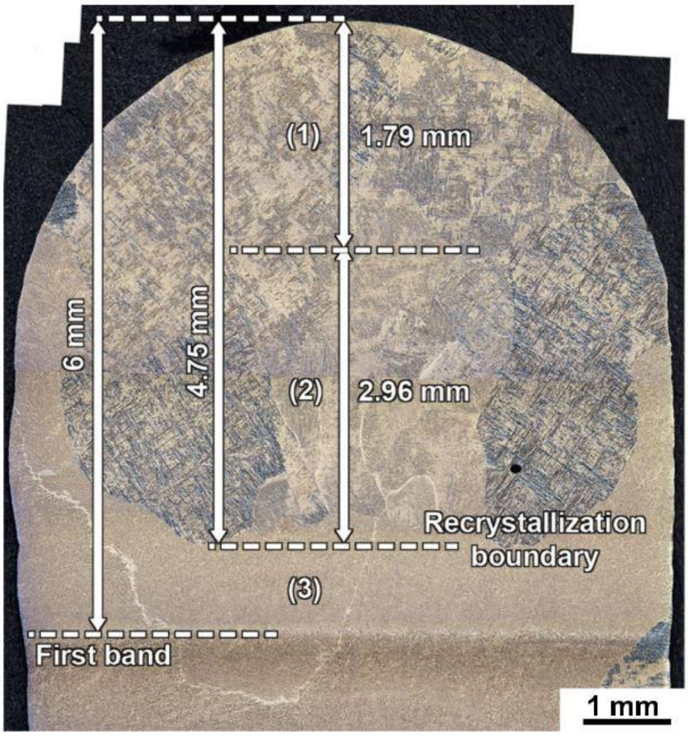

Figure 2:36. Detail of top of WAAM wall where rolling has only been applied to the penultimate layer, highlighting the refined β above the final microstructural banding; adapted from [6].

## 2.6. The Current Work

As it has been discussed in the previous chapter, the addition of an integrated rolling step is found to disrupt the formation of a highly textured, columnar prior β microstructure when producing Ti-6Al-4V components by additive manufacture. When a relatively low strain rolling deformation step is incorporated into the process it is found instead that a refined microstructure of seemingly equiaxed prior β grains is formed with manufacture. The refined microstructure is found to lead to improved material property isotropy, and the refined prior-β grain size is likely to lead to improved fatigue life improvement due to the associated smaller α colony size on cooling through the β transus. Therefore it is the purpose of this study to gain a better understanding of this refined microstructure and how it forms so that it can be better exploited in the future.

The initial work is concerned with better understanding the refined grain structure; the grain size and texture, and the distribution of these factors relative to the imparted strain by the deformation of each layer. For these purposes, a second AM technique and deformation processing technique are considered as well as the Wire + Arc AM (WAAM) and rolling method discussed in §2.5.3, in order to see how well this technique can be applied to further technologies. The second AM + deformation technique considers the effect of ultrasonic impact treatment (a form of peening) on a laser based AM technique with a powder feedstock.

The second part of the investigation is intended to attempt to understand the mechanism by which the refined grains are formed. The mechanism has been investigated by two techniques; the direct observation of the phase transformation in-situ by EBSD, and by simulating both the deformation processing and the thermal cycle of an AM layer addition step under laboratory conditions in order to replicate the refinement operation.

# 3. Experimental Methodology

This section gives a brief background of the fabrication of the samples and the various techniques used throughout this thesis, more detailed process and experimental parameters are given in the relevant manuscripts. Particular emphasis is given on electron microscopy and orientational analysis due to their prevalence throughout the work.

## 3.1. Additive Manufactured Samples

This thesis is concerned with the two separate additive manufacture techniques, and likewise two corresponding deformation techniques. The first AM technique investigated was a laser blown powder technique combined with a form of peening, and the second was a wire-arc technique combined with rolling. The characterisation of the resultant microstructures are presented in **Manuscript 1** and **Manuscript 2** respectively. The subsequent two manuscripts are focused on investigation of the mechanism that causes the observed β refinement seen in both of the techniques, but the majority of the investigation takes place on material manufactured by the wire-arc process due to a greater understanding of the process history.

### *3.1.1. Laser Blown Powder Samples*

The AM system used to produce the samples investigated was essentially a ‘home-built’ system as opposed to a commercially available system. The system was constructed by BAE Systems at their Sowerby Research Centre in Filton, Bristol, and largely by Andy Wescott, who was also responsible for the manufacture of the samples.

The system consisted of a Nd-YAG Trumpf laser and a Sulzer TWIN 10-C powder feeder delivery system mounted to an X-Y-Z motion control coordinate system. The Ti-6Al-4V feedstock powder was blown by an argon carrier gas and was injected directly into the melt pool from the directed laser beam. The entire system was fitted within an argon filled bag environment in order to prevent oxidation. The process is here after referred to as LBP (Laser Blown Powder), the terminology used to describe the technique within BAE.

The deformation of the deposited layers was carried out by Ultrasonic Impact Treatment (UIT) that was briefly described in §2.2. and is shown in Figure 3:1.

Figure 3:1. Ultrasonic Impact Treatment equipment.

UIT incorporates hard steel pins that are held in place within a tool head, but are free to oscillate along their axis. The pins are coupled to an ultrasonic transducer that causes the pins to oscillate many times per second with enough force to deform material with which the tool head is put into contact with in these experiments. The tool head was directed and manipulated manually, much as one would a hand-held drill, and it was therefore difficult to control the extent of the deformation introduced into the component surface.

It should also be noted that it is likely that the build temperature when the next layer was added was likely to be slightly higher in the undeformed wall, as the wall would not have been allowed the cooling time experienced by the other walls as they were peened. However, the temperature of the wall would still be considerably below the transformation temperature when the next layer was added, and therefore unlikely to affect the transformation kinetics significantly.

### *3.1.2. WAAM Samples*

Wire-Arc Additive Manufacture (WAAM) is a wire based additive manufacture process that has been developed by Cranfield University to the point that it is now close to being commercially available product. The WAAM process involves both multi-axis manipulators of the deposition head and the substrate in order to build complex geometries. In this study, where the deposition is combined with a rolling step, a single axis manipulator was fixed to a rigid gantry system to allow simple AM geometries to be completed consisting of single pass wide vertical walls. A schematic of the equipment is given in Figure 3:2. The axis definitions of *x*, *y* and *z* are also given in Figure 3:2, these are consistent with those used throughout AM literature, with *z* being the main build direction (normal to the plane the layers are deposited), *x* and *y* are more interchangeable but *x* is generally given to the primary deposition direction if there is one, as there is in this case with *x* being the direction of the wall. The direction '*x*' also coincided with the rolling direction when the roller was used.

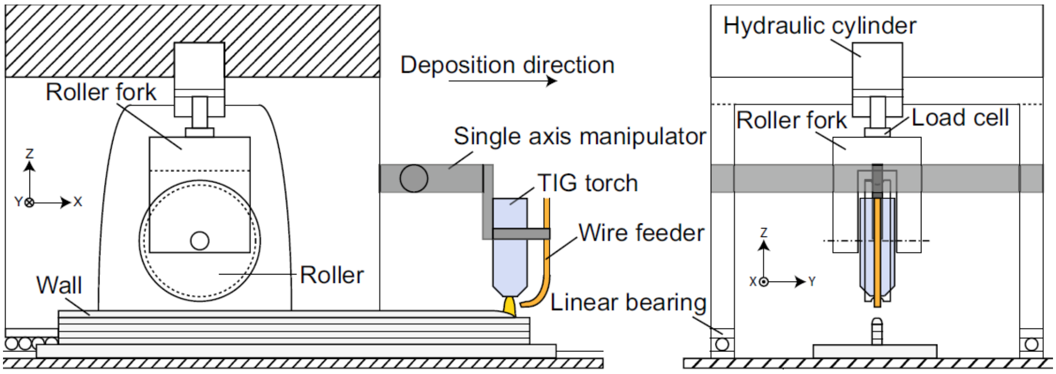

Figure 3:2. Schematic diagram of the combined WAAM rolling process [6].

The TIG torch was powered by a Lincoln Electric Invertec V310-T AC/DC TIG power supply. All of WAAM walls in this study were built with the parameters in Table 2:1

Table 3:1. WAAM deposition parameters

| | |
|---|---|
| Wire feed speed | 1.6 m/min |
| Travel speed | 4.5 mm/s |
| Peak current | 150 A |
| Background current | 70 A |
| Average current | 110 A |
| Pulse duration | 0.05 s |
| Frequency | 10 Hz |
| Gas flow rate | 10 L/min |
| Trailing shield gas flow rate | 20 L/min |
| Electrode to workpiece distance | 3.5 mm |

As shown in Figure 3:2, the roller was attached to the same ridged gantry system as the deposition torch, and followed directly behind the welding head. With this design it is technically possible to roll immediately after deposition in one process step, but for all the rolled walls in this study, the wall was allowed to cool to room temperature before rolling each layer. This also enables different rolling speeds to the deposition speed to be used. All of the rolling in this study took place at a travel speed of 3mm/s. The rolling load was applied hydraulically and controlled through a load cell. The roller contained a groove of radius 3.6 mm as shown in Figure 3:3, designed to mirror the bead profile of the top of the deposited wall.

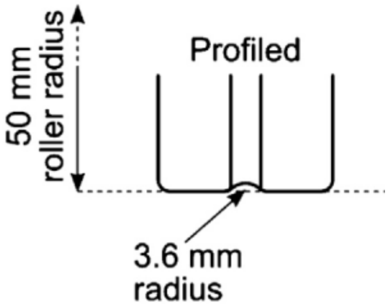

Figure 3:3. Roller design applied to the WAAM deposits [33].

Two different rolling loads were applied of 50kN and 75kN. It has been observed that while rolling results in a reduction in height in $z$, there was negligible elongation in the length of the wall in $x$, and only an increase in the width of the walls in $y$ [6]. Therefore, plane strain conditions are met as:

$$\varepsilon_y \approx -\varepsilon_z \qquad \text{and} \qquad \varepsilon_x \sim 0$$

This is due to the constraint given by the rest of the wall, resisting elongation in the rolling direction, and only allowing accommodation of the rolling strain by splaying outwards. It should be noted that this is converse to traditional rolling where it would be expected that there would be elongation in the rolling direction, with negligible strain in the transverse direction for similar reasons as sheet material effectively constrains itself in this direction [146].

As with the LBP + UIT samples, it should also be noted that it is likely that the build temperature when the next layer was added was likely to be slightly higher in the undeformed wall, as the wall would not have been allowed the cooling time experienced by the other walls as they were rolled. However, the temperature of the wall would still be significantly below the transformation temperature when the next layer was added, and therefore unlikely to affect the transformation kinetics significantly.

## 3.2. Process Simulation

For reasons that will become apparent in **Manuscript 4**, it was deemed necessary to determine the effect of the starting microstructure and texture had on grain refinement. Therefore, it was necessary to simulate both the rolling step and temperature profile of the deformed material during deposition of the subsequent layer during the WAAM process.

### *3.2.1. Deformation Simulation*

As previously stated in §3.1.2, the rolling conditions approximate plane strain conditions, therefore to simulate this, a channel compression die was fabricated out of tool steel. A schematic of this rig is shown in Figure 3:4.

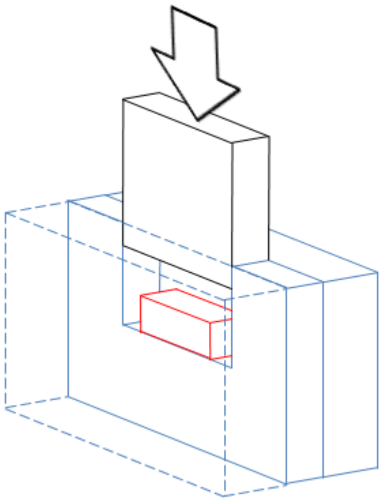

Figure 3:4. Schematic of the plane strain compression rig.

The central section determining the width of the channel was designed to 5 mm wide to enable blocks of material to be cut from sections of wall built by WAAM. The constraining plates either side of the channel were removable to allow easy access to the sample after straining and were held in place during straining by pneumatic rams. The load was applied using an Instron 5885H loading rig, compressing at a constant crosshead speed of 30mm/minute using a graphite based lubricant.

### *3.2.2. Heating Simulation*

As each new layer is added in an AM build, the rate of temperature rise of the material in the vicinity of the melt pool is dramatic [94,147]. For example, for the WAAM process it has been found to be in excess of $10^3$ K/s [6]. These rapid heating rates were replicated in the plan strain deformed samples described in the previous section by resistive heating (otherwise known as Joule heating), the phenomena of heating an electrically conductive sample by putting a current across it.

The current, and therefore temperature, was controlled by an Instron® ETMT8800 Electro-Thermal Mechanical Testing (ETMT) system. The ETMT is also designed to test samples in tension and compression as well as at temperature. The ability to manipulate the cross head allowed the tests to take place under load control enabling free thermal expansion and contraction of the sample without significant stress accumulation. The ETMT can control the temperature of the samples in two ways: current control, where the current is programmed for each moment of the test, and temperature control, where the temperature of the sample is constantly monitored and control loop feedback is used regulate the current to maintain a pre-programmed temperature profile. Temperature control is the generally preferred technique since the amount of current required to raise a sample is dependent on many variables including sample cross-section, phase composition and temperature. Regardless if it is being used to control the temperature or not, a surface spot welded thermocouple is often used to monitor the sample during a test as shown in Figure 3:5.

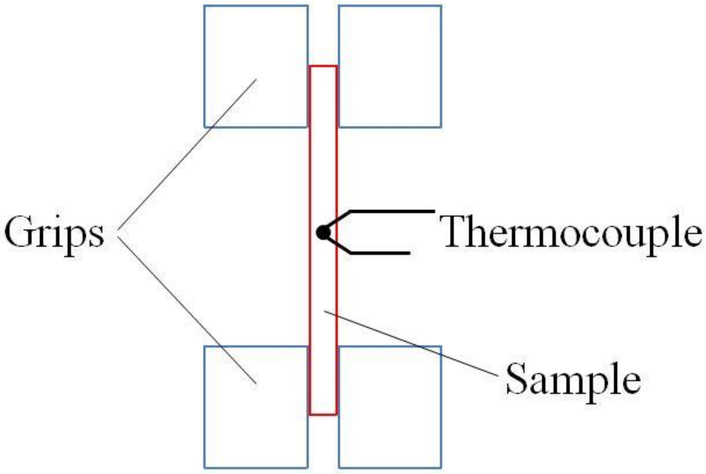

Figure 3:5. Schematic of a sample mounted in the ETMT.

The sample is limited in cross section due to the large currents that would be required to heat larger sections, and allow enable rapid cooling rates. Rapid cooling is also facilitated by water cooled grips that in addition ensure that thermal conduction to other parts of the testing rig are minimised. However, the temperature difference of the grips leads to an inevitable temperature profile across the sample that has been shown to be parabolic below 800 °C [148].

By measuring the resistance across the sample with the addition of a resistometer, as shown in Figure 3:6, it is possible to observe how the resistance of the sample changes with temperature. This is of particular interest with alloys such as titanium where the difference in the conductivity of the two phases (see §2.3.1) allows the phase transformation and the β transus temperature of the material to be directly measured.

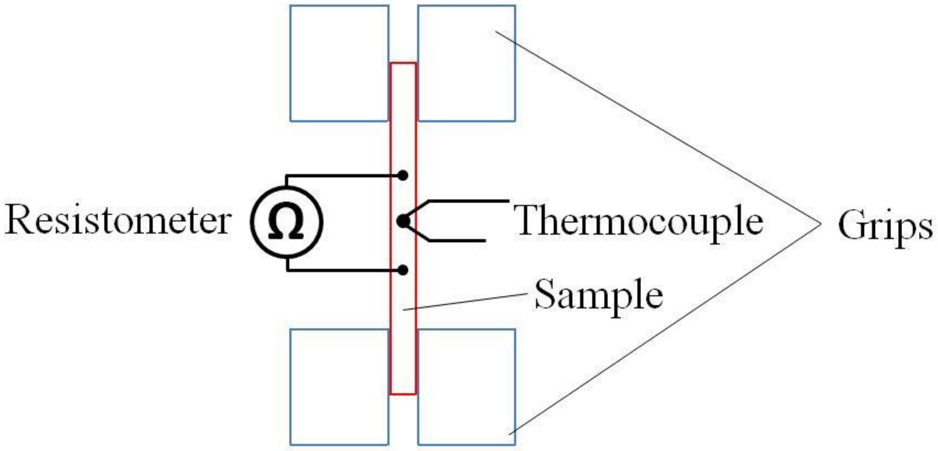

Figure 3:6. Reproduction of Figure 3:5, demonstrating how the resistivity of the sample can be measured during testing.

For the purpose of this study the ETMT 'matchstick' samples were cut to a cross section of 1.9 × 1.9 mm, as shown in Figure 3:7, from the centre of the plane strain compressed samples by electrical discharge machining (EDM) to minimise surface deformation and thermal input. The gauge length between the water cooled grips was held at 16 mm leaving ~ 4 mm at each end of the sample to be gripped and ensure a good electrical contact, as shown in Figure 3:5. R-type thermocouples (using a combination of 99.99% platinum and 87:13 wt.% platinum-rhodium wire) were spot welded to the sample surface and used to monitor and control the temperature. The thermocouple wire had a fine diameter of 0.15 mm Ø to provide a rapid response and to minimise conduction of heat from the sample. Oxidation was prevented by maintaining a constant flow of argon shielding gas over the sample.

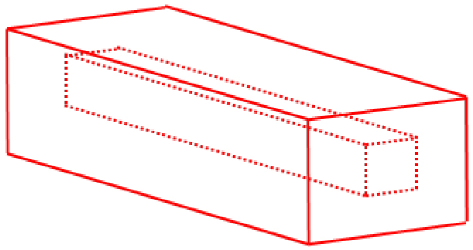

Figure 3:7. Location of ETMT sample cut from plane strain compressed sample.

In the tests where the resistance was measured, connections to the resistometer were made with the 99.99% Platinum wire, spot welded to the matchstick sample either side of the controlling thermocouple with a separation of 2 mm.

## 3.3. Sample Preparation

### 3.3.1. Metallographic Preparation

Relevant cross sections of samples were sectioned and mounted in a thermoplastic resin to enable easier manipulation of the sample during polishing and grinding. The resin used was glass filled in order to prevent it from eroding more quickly than the sample and leading to rounded edges. The samples were ground using silicon carbide paper in incremental grit sizes from #320 down to #4000, followed by a chemical-mechanical step using a mixture of colloidal silica (OP-S) and hydrogen peroxide. A mixture of four parts colloidal silica to 1 part 30% strength hydrogen peroxide was used as the final step, as it has been found that the addition of the hydrogen peroxide reduces the efficiency of the thin passivating oxide layer that forms on titanium surfaces, allowing for greater removal of material [149].

Where samples were required for scanning electron microscopy, they were carefully removed from the resin and attached to aluminium stubs with silver paint to prevent charging of the resin during analysis.

### 3.3.2. Focussed Ion Beam (FIB) sample preparation

The final part of this thesis attempts to corroborate the conclusions of the papers. As a part of this activity, a few high resolution orientation analysis techniques were used that required electron transparent samples, i.e. less than 100 nm thick. As it was required to obtain these samples from a specific location, the chosen sample preparation technique was by Focussed Ion Beam (FIB) milling. This technique is described in detail in [150], and involves the use of a focused beam of gallium ions to mill away at the sample surface to remove a thin sliver of material.

## 3.4. Optical Microscopy

The samples for optical microscopy were etched with Kroll's reagent. Optical microscopy was carried out using an Olympus BH2 microscope equipped with a Ziess camera and their AxioVision 4.8 software.

## 3.5. Electron Microscopy

Electron Microscopy is a well-established branch of analytical science, and as such has been covered well in various good textbooks such as Goodhew and Humphreys [151]. However, as electron microscopy has been used extensively in this study, a brief technical background of EM is given in the following section including a more in-depth introduction to Scanning Electron Microscopy (SEM) and the widely used phase and orientation mapping technique, Electron BackScatter Diffraction (EBSD). Also briefly covered in this section are two further analytical techniques that allow for automated orientation mapping with an increased spatial resolution compared to EBSD; Transmission Kikuchi Diffraction (TKD) and automated crystal orientation mapping in the Transmission Electron Microscope (TEM). These two high resolution orientation mapping techniques were only briefly used in this study; however they require some introduction due to their relative novelty.

### 3.5.1. Introduction

Electron microscopes come in many suits and guises. The most common two families used in analytical science are Scanning Electron Microscopes (SEM) and Transmission Electron Microscopes (TEM). Both SEMs and TEMs operate on the general principle of directing a highly focused beam of electrons at a sample and the measuring the resultant electron interactions, with the difference between the techniques being which interactions are measured, and where they are detected from, as highlighted in Figure 3:8. Scanning electron microscopes use a lower energy beam (accelerating voltages in the range of 0.5 - 30 kV) that is scanned across the surface of a bulk sample and the electron interactions measured are those back reflected towards the electron source, whereas the beam of the TEM is at a higher energy (80 -

300 kV) and uses thinner samples so the sample is largely transparent to the beam and therefore interactions are generally measured from the underside of the sample. Unfortunately, as will be discussed further later, these names become misleading as microscopes that are built as SEMs can now be used in transmission mode, and likewise, TEMs can scan the beam across the sample much the same as an SEM.

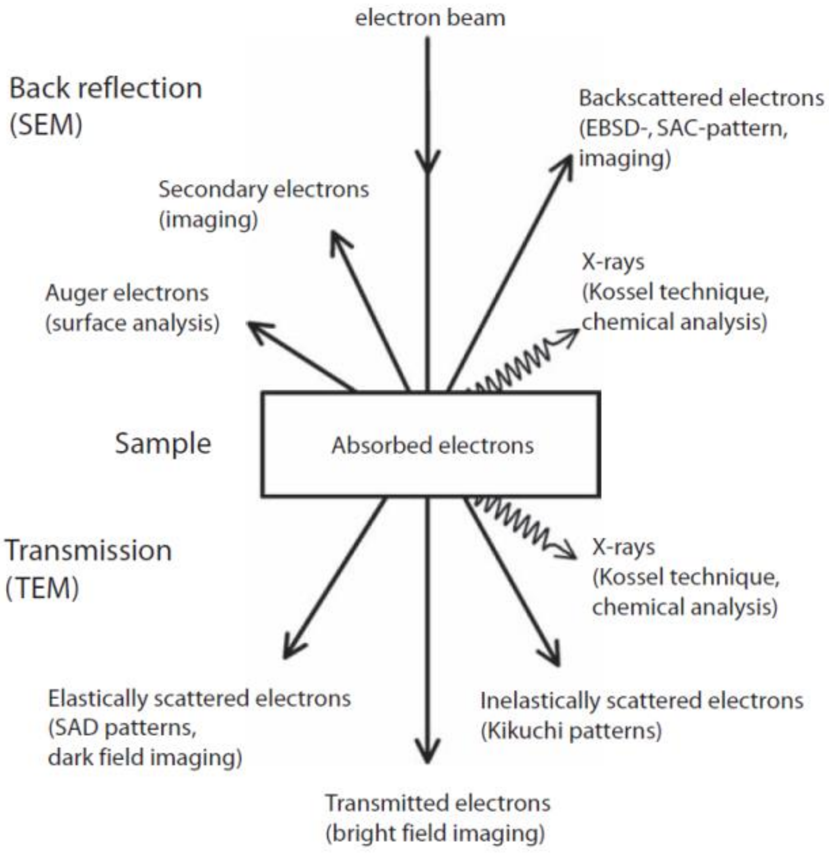

Figure 3:8. A schematic of the most common outcomes of electron interactions with crystalline matter [67].

Primary electrons entering a specimen can be scattered in two ways, elastically and inelastically. Electrons are scattered elastically when they come into close proximity to the electrostatic charge of an atom and are repelled by it, changing the path of the electron, but without losing a detectable amount of energy. The angle the electron is deflected by is generally very small and is dependent on the energy of the electron and the atomic number (Z number) of the atom that scatters the electron. The mean free path for an electron within a material before another interaction is generally quite small and the longer an electron remains within a sample the greater the chance of losing energy by an inelastic mechanism, therefore the detection of these electrons is limited to high accelerating voltages and thin samples in the TEM.

Electrons entering a specimen can lose energy in numerous ways, the two greatest in terms of energy loss are plasmons (effectively creating a wave in the ‘sea’ of electrons of metallic bonding) and phonons (loosing energy by slightly heating the solid). These inelastic interactions tend to deflect the primary electron through a greater angle than the elastic collisions and as they lose energy they become more susceptible to even greater deflections. Eventually, with the electrons losing momentum with every collision, the primary electron will either find the sample surface or will stop within the sample. The ‘random walk’ of a primary electron as it interacts with a material is shown for typical accelerating voltages in an SEM are shown in Figure 3:9. It should be noted that the effect of decreasing the accelerating voltage on the electron trajectories is similar to that of increasing the Z number of the target material.

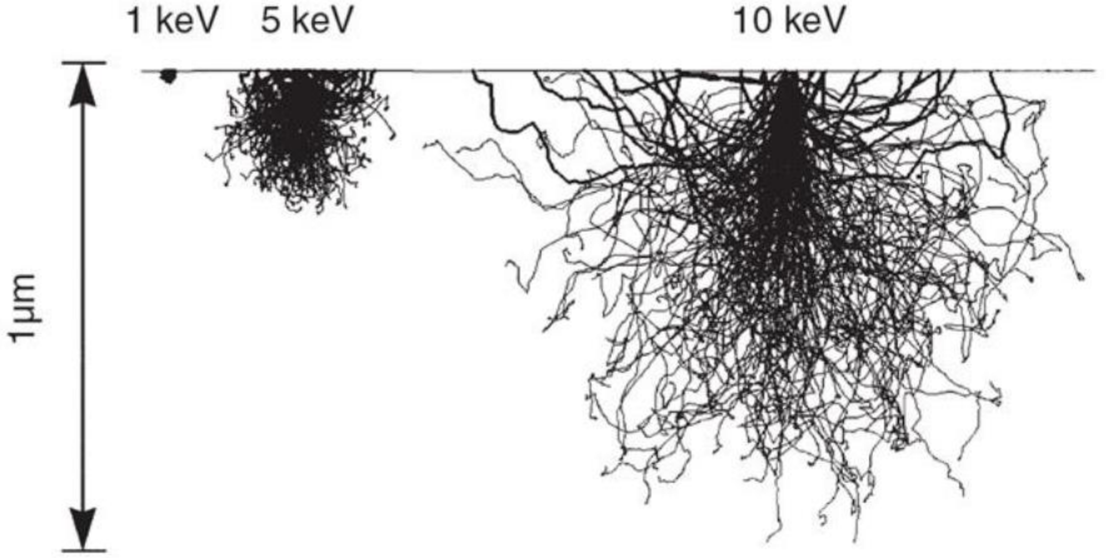

Figure 3:9 Electron trajectories in Si with accelerating voltages of 1, 5, and 10 keV, computed using Monte Carlo simulation [152].

It can be seen in Figure 3:9 that a number of the electrons find their way back to the sample surface to be emitted, and are known as backscattered electrons. These backscattered electrons tend to have only lost a negligible amount of energy relative to the incident beam and are most commonly detected by a detector sat under the pole piece. As the scattering is highly sensitive to z, imaging in this mode allows good contrast where there is chemical inhomogeneity. It is these electrons within the SEM that contribute to the diffraction patterns that allow orientation analysis, as discussed further in the next section.

Both of the inelastic scattering mechanisms mentioned above can result in the transference of a small amount of energy to electrons within the specimen. These electrons have a low amount of energy so are readily absorbed by the sample, unless located very close to a surface. When emitted from a surface these electrons are termed secondary electrons and are readily separated out from the higher energy backscattered electrons due to their lower energy. Secondary electron imaging is one of the most common forms of imaging within an SEM and is highly surface sensitive.

It should be noted that other useful inelastic electron interactions can take place, but are less common. One of the most useful of these is where the primary electron knocks the inner shell electron of an atom in to a higher energy state. At some point later the atom will relax, and as both the energy states are well defined, the quantity of energy released when this happens can be used to determine the atom involved and can be used for chemical analysis. The relaxation can either be achieved by the emission of a characteristic X-ray, or by an electron being emitted with the same excess energy known as an Auger electron.

### *3.5.2. Orientation Mapping*

#### Electron Backscattered Diffraction (EBSD)

As shown in Figure 3:9, electrons are scattered in all directions by the interaction with solid matter from a certain depth within the sample. Despite the electrons being scattered inelastically, the vast majority of the electrons backscattered out of the surface, loose very little energy relative to the incident beam and will have a similar associated wavelengths. Therefore, as long as the matter is crystalline, some of the electrons that are scattered out of the sample surface will fulfil the Bragg condition for particular crystallographic planes, leading to constructive and destructive interference and the emission of high intensity cones of scattered electrons. If a detector, such as a photoluminescent phosphor screen, is placed in such a way as to intercept these diffracted electrons then, due to the shallow Bragg angles involved, each cone appears on the phosphor screen as a set of parallel lines. These patterns are commonly termed Kikuchi patterns after Seishi Kikuchi who was one of the first to observe them in 1928 [153]. An example of a Kikuchi Pattern is given in Figure 3:10. It is possible to determine the orientation of the crystalline structure of the probed volume, with respect to the sample geometry, after identification of the bands and their relative positions. Identification of the bands can be made as the angle between bands gives the interplanar angle, and the width of the bands is related to the interplaner spacing [154]. Kikuchi patterns are very sensitive to orientation and so can give an angular resolution down to ~0.5° [155]. However, as Kikuchi patterns are diffraction based, the quality of the patterns are very sensitive to surface deformation.

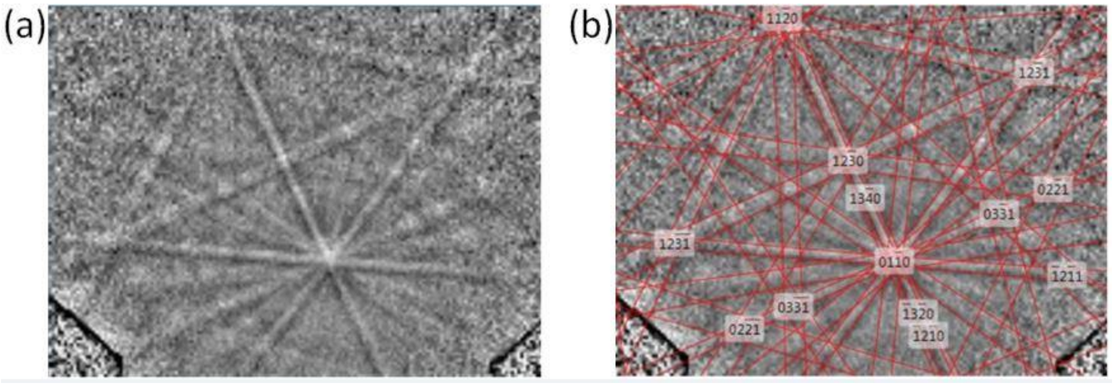

Figure 3:10. EBSD Kikuchi for hexagonal titanium pattern as imaged on a phosphor screen in (a), and as indexed by Aztec acquisition software.

Kikuchi pattern detection within an SEM is compromised as electrons are most intensely backscattered back towards the electron source, and therefore this is where the strongest Kikuchi bands would be detected. However, this is not a practical location for mounting of the phosphor screen and accompanying camera to record the patterns. Therefore, a compromise is made with the sample surface tilted until away from the electron source (a shallow incident angle of ~20° is often used) and the phosphor screen orientated roughly orthogonal to the source as shown in Figure 3:11

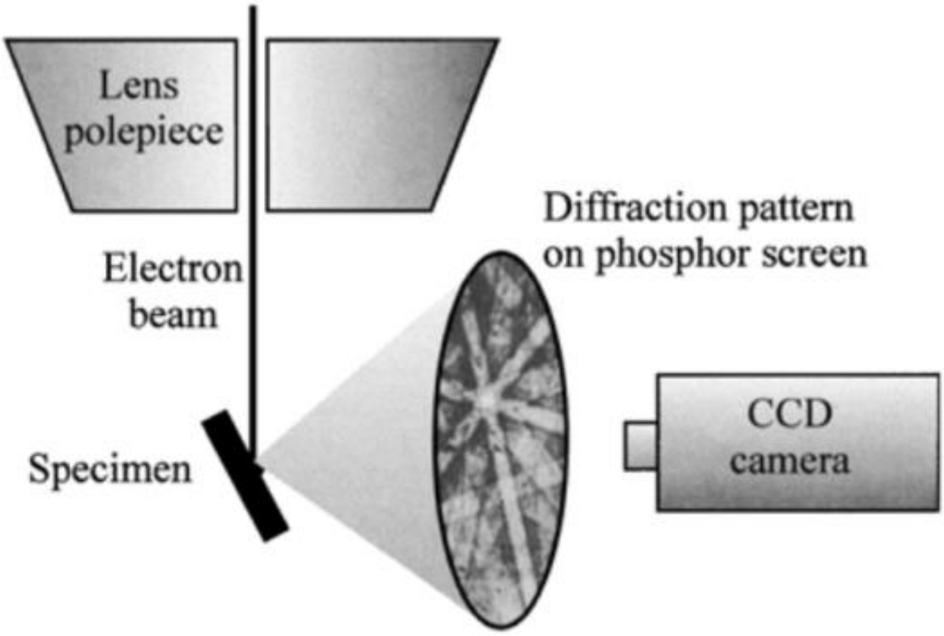

Figure 3:11. Simplified experimental set up of EBSD within an SEM; adapted from [156].

This set up necessitates large working distances, therefore larger currents are used to ensure sufficient signal than would be chosen for optimal special resolution.

Unlike other texture analysis tools, such as X-ray Diffraction, EDSD is useful as the crystallographic orientation of the probed volume is measured simultaneously with its location in the sample, therefore further analysis can be accomplished as the data is spatially corellated. The orientation of one point relative to its neighbours can be used to define points that belong to the same grain or sub-grain and to define grain boundaries, allowing analysis of grain size distributions, grain boundary misorientations, and stored energy amongst others.

It is now common for EBSD to be fully automated and mapping is achieved by the EBSD software taking control of the scanning coils and rastering the beam over the chosen area much like during imaging, albeit with a longer dwell time on each point to allow for the collection of the diffraction pattern. It is not uncommon to collect over 100 diffraction patterns per second. The patterns can be saved for analysis later, but if the crystal structure of the sample is known, modern computers are more than capable of determining the phase and orientation from the collected diffraction pattern in real time by comparing the diffraction pattern to those predicted for the crystal structure.

Additional information is also collected by the analysis software for each pattern collected, including a measure of how well the predicted pattern fits the measured diffraction pattern, and measures of the quality of the measured pattern. Two of the most common measures of pattern quality used are Band Contrast (BC) and Band Slope (BS), and both are a measure of how distinct the Kikuchi bands are within a diffraction pattern. Band contrast is effectively a measure of the peak diffracted intensity compared to the average intensity of the pattern, whereas band slope is a measure of the gradient across the peak as shown in Figure 3:12.

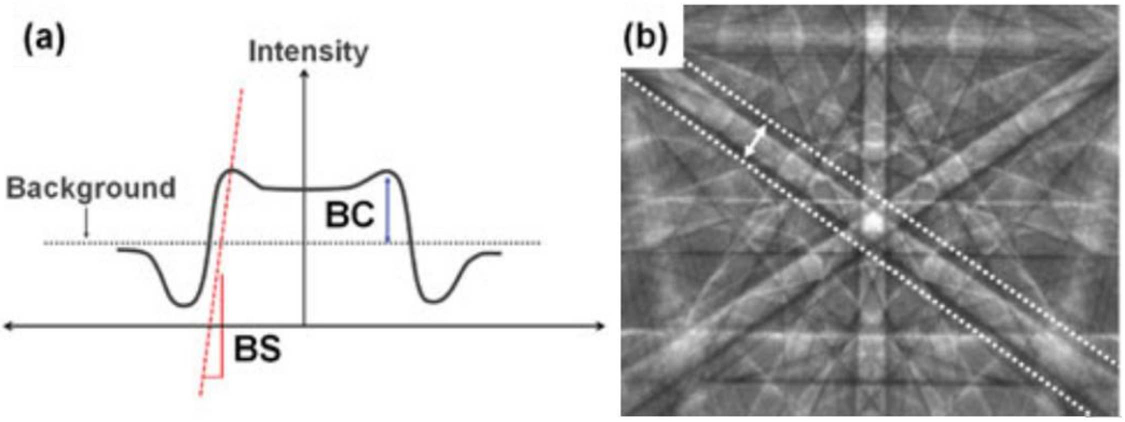

Figure 3:12. (a) Schematic showing the difference between pattern quality measurements Band Contrast (BC) and Band Slope (BS). The location of this schematic in the diffraction pattern is shown in (b); adapted from [157].

Numerous factors can affect the quality of a diffraction pattern, and include both those that are intrinsic to the sample, and those that are dependent on experimental conditions. The largest factors that can affect pattern quality that are dependent on the sample are the diffraction intensity of a phase, dislocation/crystallographic defect density, and crystallographic orientation. Experimental conditions that can affect pattern quality include the focus and alignment of the electron beam, and the quality of the surface finish on the sample. All of these factors affect both band contrast and band slope. However, each pattern quality measure is affected by the intrinsic factors by varying degrees, therefore mapping both of them yields different information. Figure 3:13 gives an example of maps made from the same diffraction patterns using the different pattern quality indicators.

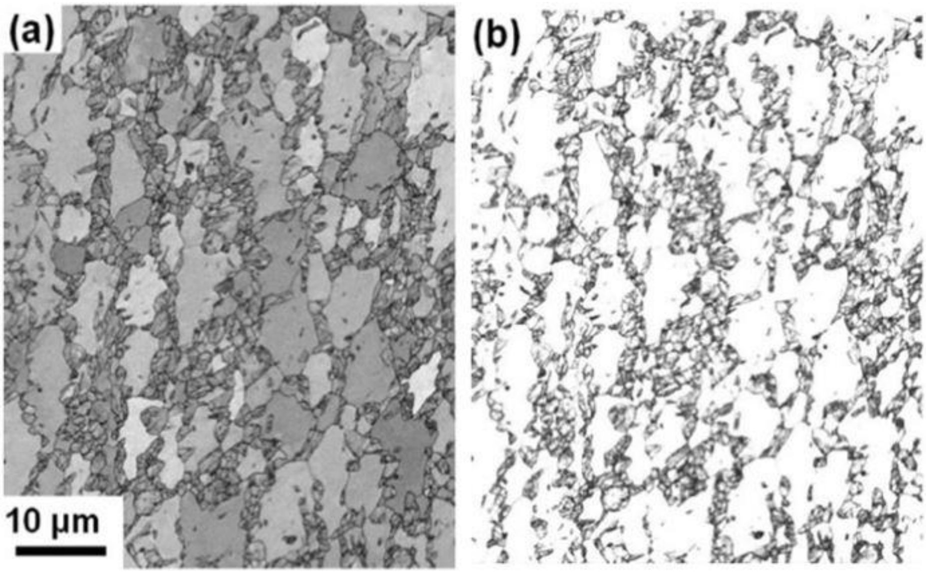

Figure 3:13. Band Contrast (a) and Band Slope maps of the same diffraction data; adapted from [157].

The band contrast map in Figure 3:13a gives a microstructural image similar to that that might be achieved by backscattered electron imaging. The contrast between grains in this case is dominated by the difference in orientation, as the intensity of a band is strongly affected by how well orientated the crystallographic planes are orientated for diffraction, with respect to the detector. Band slope is not so readily affected by orientation, with all the large grains having the same value of BS in Figure 3:13b, as even if a band's diffracted intensity is low, it can still be well defined. Therefore, BS is more sensitive to the other factors effecting diffraction, such as internal strains distorting the crystal lattice.

Several different microscopes were used throughout this study dependent on the requirements of the EBSD maps and the relative strengths of the different microscopes. High resolution mapping was carried out in a FEI Magellan 400L SEM - a microscope built around high resolution analysis, large area mapping in a CamScam Maxim – a large chamber microscope – allowing manipulation of large samples, and the in-situ heating (described further in §3.5.3) was performed in an FEI Nova 600 NanoLab due to the addition of infra-red protection on the EBSD camera. In all cases the microscopes were fitted with Oxford Instruments Nordlys EBSD detectors and the patterns were collected and analysed using their AZtec software. Details of the experimental parameters used for the individual scans are given in the relevant sections of the proceeding sections they are included in.

### Transmission Kikuchi Diffraction (TKD)

It is possible to gain increased spatial resolution within an SEM set up for EBSD, by utilising an electron transparent sample situated in close proximity to the pole piece. With a thin enough sample and a high enough accelerating voltage, Kikuchi patterns can be detected in transmission within an SEM using the standard EBSD detector in a process termed Transmission Kikuchi diffraction (TKD) [158], as shown in Figure 3:14.

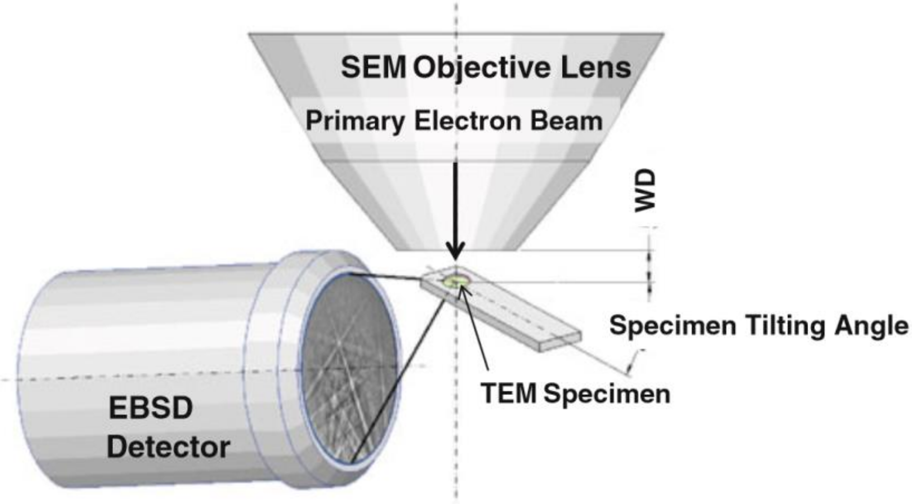

Figure 3:14. Experimental set up of Transmission Kikuchi Diffraction [159].

In this set up, the increased spatial resolution is achieved as the interaction volume of material is significantly reduced from the bulk case, as can be seen from Figure 3:15. Compared to EBSD, where a low accelerating voltage is required to achieve a greater spatial resolution through a smaller interaction volume, there is no penalty paid to spatial resolution in increasing the voltage in TKD. Not only does a higher energy e-beam have the potential to be more highly focused, but a greater proportion of a the beam will be transmitted through the sample with fewer interactions and therefore a lessened interaction volume. In reality the condition is not as perfect as shown in Figure 3:15b, as the sample requires tilting away from the detector in order to angle the diffraction patterns towards the detector which is optimally mounted for EBSD (as shown in Figure 3:14).

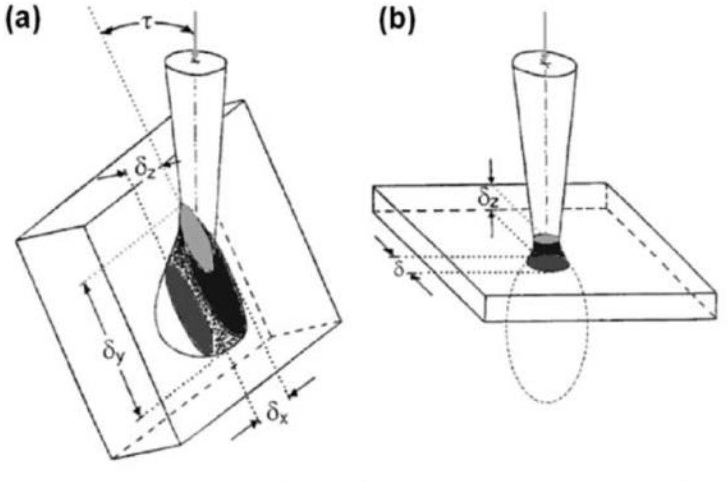

Figure 3:15. Interaction volumes, the volumes contributing to Kikuchi diffraction patterns and spatial resolution for 70° bulk sample EBSD (a) and (b) thin sample TKD; adapted from [154].

One of the factors that has led to the rapid adoption of this technique is that minimal adjustments are required to adapt the EBSD hardware and software to collect and analyse TKD patterns.

The TKD orientation mapping in this study (discussed in §5.1.1) was performed using an FEI Magellan 400L SEM, using the highest available accelerating voltage of 30kV. A low working distance of 2 mm was used in order to ensure the patterns were projected onto the detector, and the sample was tilted to 20° as this had previously been found to be an acceptable compromise between spatial resolution and pattern quality [160], leading to an interaction volume of ~ 12 nm.

### Automated Crystal Orientation Mapping in the TEM

Currently the highest spatial resolution automated orientation mapping that can be achieved is within a TEM [155]. Similar to EBSD, this technique scans the beam across the sample in a rastering pattern and captures an image of the diffraction pattern on a phosphor screen at each point, from which image recognition software attempts to determine the orientation by comparison to simulated diffraction patterns calculated for the crystal structures. The largest difference in this technique is that the diffraction patterns analysed are not the Kikuchi diffraction patterns from the initially inelastically scattered electrons from the interaction volume, but the diffraction spot patterns of elastically scattered electrons. An example of a diffraction spot pattern is shown in Figure 3:16.

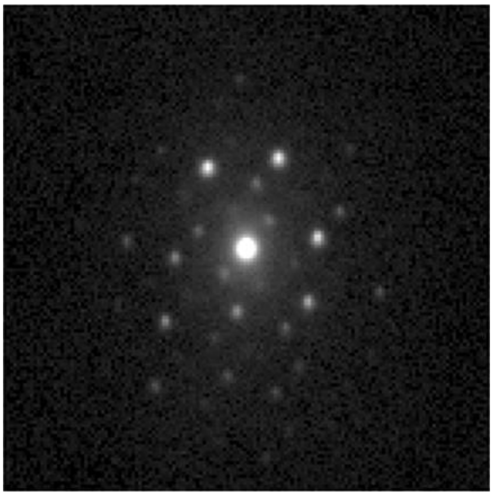

Figure 3:16. Diffraction spot pattern of α phase in Ti-6Al-4V.

Spot patterns are a result of Bragg diffraction occurring from planes which are approximately parallel to the electron beam, and therefore the planes responsible for each spot can be identified by the spacing and angles between the spots and the orientation of the crystal relative to the beam can be determined. As the effective source of Bragg scattered electrons is the fixed beam, small variations in the orientation of the crystal will not prevent fulfilment of the Bragg condition, so although the relative intensity of the diffracted spots will change, the location of the diffracted spots will remain the same on the diffraction pattern. This differs from Kikuchi diffraction where diffraction of inelastically scattered electrons, the effective source of the Bragg scattered electrons, is within the crystal itself and as such small variations in orientation will lead to a shift in the diffraction pattern. Therefore the angular resolution is sacrificed when determining orientation by diffraction spot patterns, but this is offset by the gain in spatial resolution.

When using this technique within the TEM, all efforts are made to reduce the probe size as much as possible by using the highest a voltage available combined with a thin sample to limit beam broadening by scattering events, and by using a relatively small condenser aperture to keep the beam as small and parallel as possible. The beam is precessed during scanning which involves the rotation of a slightly tilted beam around the optical axis as shown in Figure 3:17.

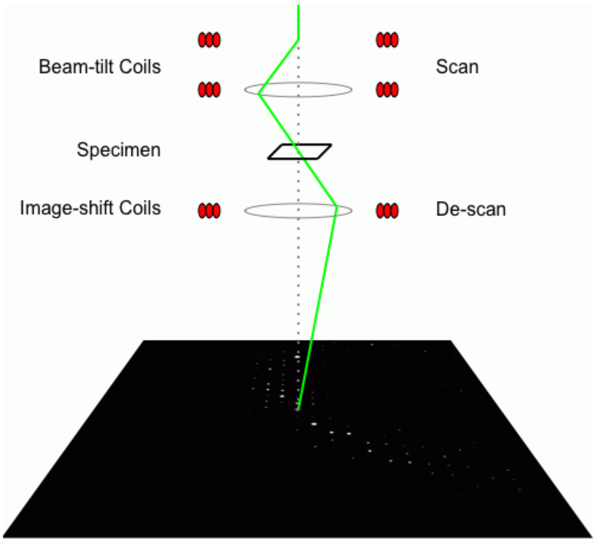

Figure 3:17. Schematic indicating beam precession within the TEM.

Precession of the beam gives a diffraction pattern at each point that is an integration of many small differences in diffraction conditions. The chief advantage of which is that the resultant diffraction pattern is less influenced to dynamic electron diffraction events, such as re-diffraction and the pattern is closer to that calculated by kinetic theory [161]. This is particularly relevant in combination with the automated orientation mapping system, as the calculated spot patterns (known as templates) from which the orientation and phase of the probed volume is determined, are largely kinematical simulations of the diffraction patterns due to the difficulty in modelling the majority of dynamic effects.

The automated crystal orientation mapping system used in this study was ASTAR developed by nanoMEGAS. ASTAR comprises of digiSTAR, a beam control unit that handles both the beam scanning and precession, and various pieces of software that individually: capture the diffraction patterns, generate templates for the known crystal systems, compare the diffraction patterns to the templates, and allow mapping of the data for orientation analysis. Unlike EBSD, pattern matching for ASTAR often takes considerably longer than the pattern acquisition due to the calculations involved and, therefore, the stored patterns tend to be indexed offline.

The TEM used in this study was an FEI Tecnai F30 FEG-TEM operating at 300keV with a 20μm condenser aperture to give a measured current of 26pA and a focused probe diameter of 3 nm. The optimal precession angle was found previously to be 0.8 ° as this increased the reliability of the indexed patterns without detrimentally affecting the resolution [160].

The sample used in this study was the same as that analysed by TKD and was therefore also prepared by FIB.

### *3.5.3. In-situ Heating*

Paper **Manuscripts 3** and **4** are concerned with determining the mechanism by which the refinement of the prior β microstructure takes place. One of the ways the mechanism was investigated was to perform EBSD analysis at temperatures approaching the β transus so that the nucleation of new β grains could be observed, and simultaneously gain information of their orientation and location relative to the deformed microstructure.

For this purpose an FEI Nova 600 NanoLab was fitted with a Gatan Model525 Murano heating stage in addition to an Oxford Instruments Nordlys EBSD detector with infra-red protection. An image of the heating stage is shown in Figure 3:18. Despite a water cooled base to protect the microscope, the heating stage is compact enough to be tilted within the SEM to allow EBSD analysis. However, the constraints of the Nova’s chamber limit this tilt to 60°, which is sub-optimal for EBSD. A 70° pre-tilted mount has recently been developed by Gatan that also fits within the chamber of the Nova, but although this allows improved interception of the diffracted Kikuchi patterns, it comes at the cost of reduced freedom to manipulate the sample within the SEM.

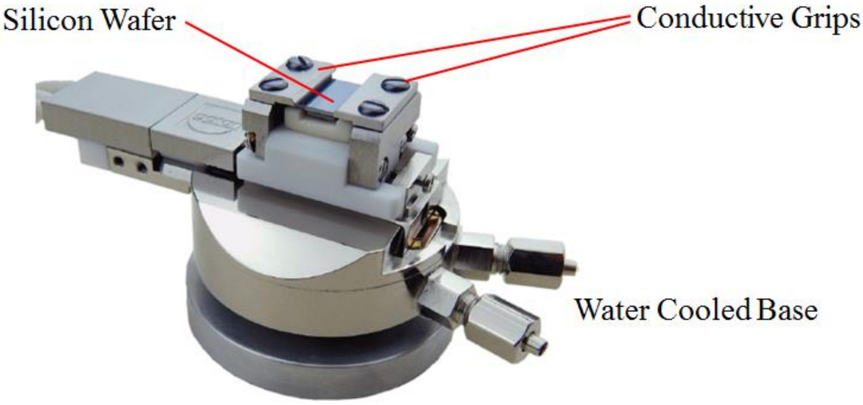

Figure 3:18. Labelled photograph of the Gatan Murano heating stage; adapted from [162].

Much like the ETMT described in §3.2.2, the Murano stage heats the sample with resistance heating. Unlike the ETMT, the sample is not heated by directly passing a current through it, but is instead heated by conduction from a silicon wafer that conducts the current. The silicon wafer can be seen in Figure 3:18 and is shown schematically in Figure 3:19. The wafers are rated to last over 100 hrs at 800°C, but the lifetime drops dramatically with temperature, and are only rated to last 10 hrs at 950°C. As with the ETMT, there is a thermocouple that measures the temperature of the wafer and adjusts the current across the wafer accordingly to reach the temperature demanded of it. The thermocouple is located on the underside of the wafer, as can be seen in Figure 3:19, and is separated from it by a soft, highly conductive graphite pad that ensures good thermal contact. The location of the sample is also shown in Figure 3:19, mounted on the upper side of the silicon wafer, and is also separated from it by a carbon pad. The carbon pad in this case serves two purposes; first, to lift the sample higher to reduce the working distance to the pole piece and EBSD detector, and secondly, to mirror the situation on the underside of the wafer, so the thermocouple gives a more accurate representation of the sample temperature.

The sample size that can be heated is fairly small, limited to 9 mm in length by the length of the silicon wafer. In width, the sample is limited to 4.5 mm which corresponds to the distance between the grips. The depth of the samples should not exceed 1.5 mm, as deeper samples may come into contact with the shroud placed over the heater assembly to protect the detectors in the SEM. Small samples are also desirable experimentally as they will have a smaller specific heat capacity and so take less energy to heat, and are more responsive to changes in temperature. The samples are affixed to the graphite (and in turn to the silicon wafer) by a water based graphite paste.

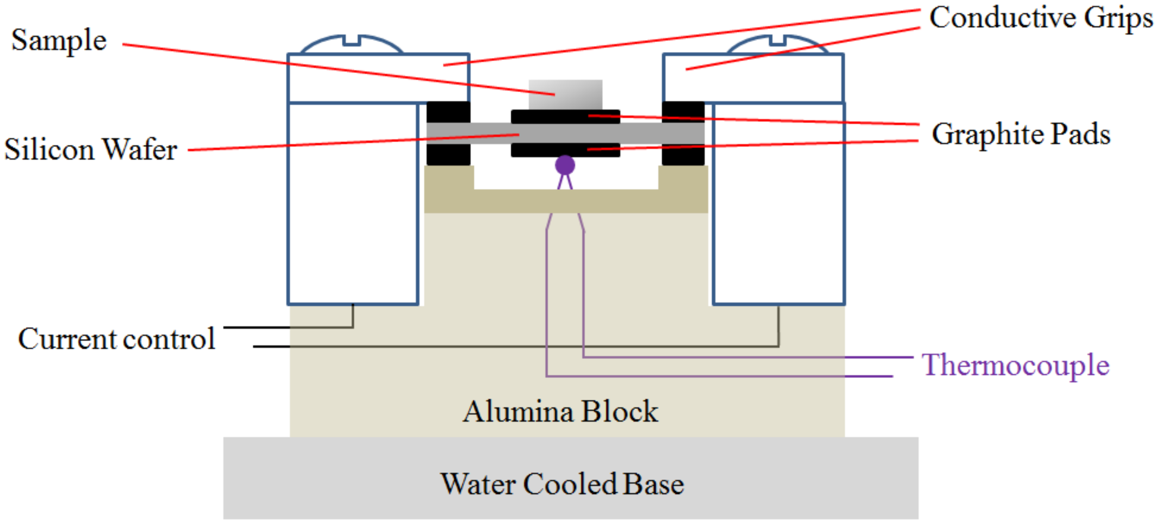

Figure 3:19. Schematic of sample mounted on the Gatan Murano heating stage.

Due to the reactivity of titanium, extensive lengths were gone to for the experiments contained within this study to limit the presence of gases within the SEM chamber. After fixing the samples to the wafers with the carbon paste, the entire heater assembly was baked at 180°C for 30 mins and allowed to cool prior to insertion into the microscope in an attempt to evaporate volatiles from the paste. No microstructural evolution is expected in Ti-6Al-4V at this temperature. Once the heating stage was mounted within the SEM, the chamber was pumped down to operating pressures ($10^{-4}$ torr) before being backfilled with nitrogen gas in an attempt to eliminate contaminant molecules from within the air. The chamber was backfilled three times before being left until the chamber reached a 'good' SEM chamber vacuum of less than $10^{-6}$ torr before beginning the heating experiment.

For all experiments run, the heating rates at lower temperatures (less than 500 °C) were reasonably high at ~1°C/s. However, the pressure in the chamber was closely monitored, and if there were any sudden jumps or significant increases in pressure due to degassing, then the heating would be paused and the sample held at temperature until a lower pressure had been re-established. No significant degassing events would be observed after ~250°C; however, the pressure within the chamber continued to rise slowly with temperature, presumably due to molecules adsorbed onto the surfaces within the SEM being excited by infra-red radiation.

The specifics of the heating rates and sample geometries used are provided in the relevant sections where the results are presented.

## 3.6. Beta Reconstruction

As this work is primarily concerned with the prior β microstructure formed in hybrid AM and deformation processing, it is important to obtain orientation maps of this phase to allow textural measurements, grain size and grain boundary analysis, as described in§3.5.2. However, the task is made challenging as this is the high temperature phase. The β transus being above the comfortable operating temperature of the heating stage described in §3.5.3 precludes mapping at temperature, and that is before thermal evolution of the microstructure is taken into account. It is possible to index the orientations directly by EBSD due to there being some residual β remaining at room temperature. However, due to the cooling rates involved in AM, the room temperature microstructure is extremely fine, and the majority of the residual β is below the resolution of the EBSD parameters used for large area mapping, and even when statistically the beam happens to fall on a thick enough region of β to acquire a diffraction pattern that can be indexed (i.e. at a triple point where α laths meet), it is unlikely that enough of such patterns will be acquired in each prior β grain to reliably rebuild the prior β microstructure.

Fortunately, it is possible to calculate the prior β grain structure from room temperature measurements of the α microstructure due to the phase relationship maintained by the two phases through transformation as described in §2.3.3. As the Burgers' orientation relationship (BOR) is maintained, there are 12 distinct α orientations that form within each β grain on cooling through the transus, it is also known that each α lath can only have transformed from 6 possible prior β orientations. Therefore, with the orientations of two or more α variants which are believed to have originated from the same β grain, it is possible to calculate the most likely parent β orientation from the misorientation between them. The extension of this is to take entire EBSD maps of the α phase, where both the orientation and spatial location of the variants is known, and to calculate for each point what the most likely parent β orientation was before it transformed.

In this study β orientation maps are constructed using a procedure developed by Davies and Wynne [163,164], based on earlier work by Humbert et al. [165,166]. This technique is explained fully in ref. [163] and is summarised below.

β reconstruction takes place in 4 distinct steps:

**1. Identification of neighbouring points that belong to the same α variant.**

This is done by defining a maximum misorientation that two neighbouring points can have and still be considered the same variant; this is kept at 2 ° by default.

**2. Calculating possible β transformations for all α variants**

For each α variant, the 6 possible β orientations it could transform to obeying the BOR are calculated.

**3. Identification of neighbouring α variants that transformed from the same β variant.**

As there are only 12 variants that can transform from each β, then there are only 11 set misorientations that can exist between an α variant and another from the same β grain. The misorientation between neighbouring points in different α variants are compared to these 11 misorientations. If the variation is below a threshold value (3° by default), then the boundary is determined to fufuill the BOR, and both α variants are identified as being from the same prior β grain.

**4. Determination of the parent β orientation.**

The misorientation analysis in step 3 will give a maximum of three possible solutions for the parent β orientation, and will most likely have given a unique solution, for each point in the α variant neighbouring another α variant. However, if more than one solution is given then these orientations are also compared to the 6 orientations calculated in step 2, and whichever occurs the most often is assigned as the β parent orientation for those α variants.

Construction of the β map allows for manipulation and analysis of the data as if it had been collected by EBSD directly, such as allowing textural measurements, grain size distributions, and grain boundary misorientations amongst others.

## 3.7. Heating Validation

In order to interpret the in-situ heating experiments it is important to understand the transformation behaviour of the investigated Ti-6Al-4V alloy. In addition to the measurement of the β-transus by change in resistance described in §3.2.2, the transformation with temperature was also measure directly by Differential Scanning Calorimetry (DSC), and predicted by simulation using computational thermodynamic modelling.

### *3.7.1. Differential Scanning Calorimetry*

Differential Scanning Calorimetry (DSC) provides a way to measure physical transformations in a material by measuring their associated change in enthalpies. DSC operates by heating both the sample and a reference at an identical rate. Measurement is made of the amount of energy required to achieve the temperatures, and if more or less heat flow is required to maintain the temperature compared to the reference, then the sample is experiencing an endothermic or exothermic process respectively. For example, the phase change from α → β in titanium is endothermic [167], requiring heat from the surroundings to take place, consequently a greater flow of heat to the sample is required than to the reference during the phase transformation to achieve the same temperature. Therefore in a plot of temperature against energy required to heat the sample (relative to the reference) any change in enthalpy is registered as a peak. From the peak the enthalpy of the transformation can be calculated, as well as the temperature of the onset and completion of the transformation.

Using a high heating rate results in a stronger signal against the background noise and therefore allows for more accurate peak measurements. However, the completion of the transformation is found to be delayed at faster heating rates due to thermal gradients within the sample [168]. This is complicated further in Ti-6Al-4V, where the transformation does not take place at a distinct temperature, as there is β present at room temperature, and the transformation takes place takes over a range of temperatures. It is found that slower heating rates allow more time for diffusion to take place, leading to a greater proportion of β during transformation at any given temperature [169]. Therefore to get a full depiction of the transformation it is necessary to run the DSC on identical samples at several heating rates.

In this study DSC tests were carried out in a Netzsch 404 F1 Pegasus on cylindrical samples cut from the WAAM wall measuring 4.5Ø mm ×1.2 mm thick with an empty alumina crucible as the reference. The tests were run from room temperature to 1100 °C in order to encompass the phase change at ~1000 °C at three different heating rates of 5, 12 and 20 °C/s. Oxidation was prevented by the achieving a vacuum in the DSC chamber and backfilling with argon shielding gas three times before running the experiment and a constant flow of 40 ml/min of shielding gas was maintained over the sample during testing. To further protect against oxidation, a titanium ‘getter’ with a large surface area was also placed in the DSC furnace.

### *3.7.2. JMatPro Phase Alloy Simulation*

JMatPro, by Sente Software, is a powerful piece of simulation software that uses computational thermodynamics and physical and microstructural models in an attempt to predict a range of microstructural characteristics of metallic materials. For the purposes of this study, JMatPro was used to predict the proportion of phases present at any particular temperature in order to correlate with the transformation observed by the in-situ EBSD experiments described in §3.5.3. JMatPro calculates the phases present at a temperature by using the CALPHAD approach. CALPHAD, the CALculation of PHAse Diagrams, has been described extensively elsewhere [170], is concerned with the development of mathematical models that describe the thermodynamic behaviour of phases from experimental observations of binary and ternary systems, that are then used to predict the behaviour of multicomponent systems. A disadvantage of the process (as it is being used here) is that the phase proportions are calculated under equilibrium conditions; i.e. as if given infinite time for diffusion to occur. However, this is not deemed to be too far removed from the situation in the in-situ experiments that involved relatively slow heating rates and several holds at temperature to carry out the mapping. The coefficients of the thermodynamic properties of the possible phases are held within the Thermotech database, and the composition of the alloy was measured directly.

Compositional analysis of the WAAM material was carried out by Timet, Birmingham, England. Metallic compositional analysis was carried out using inductively coupled mass spectrometry on a HORIBA ULTIMA2, and the oxygen and nitrogen content were determined by inert gas fusion with a LECO EF-400.

# 4. Manuscripts

The four paper manuscripts that follow make up the bulk of the work presented in this thesis, along with the supplementary results presented in §5. The manuscripts are not ordered in the order of publication, but in the order that is believed to give a more complete story to the research. The first two manuscripts focus on characterisation of the effect an in-process deformation step has on the microstructure of two different AM processes, where it was observed in both cases that a greatly refined prior β grain structure with a weaker texture was formed, rather than the expected coarse columnar structure described in §2.5.1. The subsequent two manuscripts attempt to explain the origin of the refined β structures that had been observed and described in the previous two.

Each Manuscript includes the same text and figures as the published versions, but they have been reformatted to be in keeping with the rest of this document. A brief introduction is given before each manuscript to summarise and give the context of the work, including attributing the contributions of the named authors to each manuscript.

## 4.1. Integration of Deformation Processing with Additive Manufacture of Ti-6Al-4V Components for Improved β Grain Structure and Texture

This manuscript was the first published work to observe the effect of a deformation process step in combination with an AM technique. The effect of peening on a laser based AM technique on the resultant grain structure and texture was investigated in Ti-6Al-4V samples by EBSD.

This paper was submitted on 11th November 2014 as conference proceedings for TMS:2015, held in Orlando, Florida over the dates 15th-19th of March 2015, where the work was presented by the lead author. The paper underwent peer review and was published in a printed volume on the 16th February 2015, and online on the 27th February 2015.

The contributions of the named authors were as follows:

*University of Manchester*

**Jack Donoghue** – Lead author, all metallographic preparation, SEM analysis and EBSD data analysis.
**Phillip Prangnell** – Supervisor of Jack Donoghue

*BAE Systems*

**Jagjit Sidhu & Andrew Wescott** – Responsible for the manufacturing of the samples only.

# Integration of Deformation Processing with Additive Manufacture of Ti-6Al-4V Components for Improved β Grain Structure and Texture

Jack Donoghue[1], Jagjit Sidhu[2], Andrew Wescott[2], and Phillip Prangnell[1]

[1]Materials Science Centre, University of Manchester, Grosvenor St. Manchester M13 9PL, UK
[2]BAE Systems, Sowerby Research Centre, PO Box 5, Filton, Bristol BS12 7QW, UK

Keywords: Additive Manufacture, Deformation Processing, Microstructural Refinement

## Abstract

With Ti alloys like Ti-6Al-4V, the solidification conditions across virtually all AM platforms lead to strongly textured, coarse columnar, β grain structures. Transformation to α on cooling dilutes the texture, but significant texture is still inherited which contributes to undesirable anisotropy in AM parts. In the work presented a deformation step has been integrated into the manufacture of components produced by the blown powder method, using an Ultrasonic Impact Treatment (UIT), which has the additional benefit of reducing residual stresses. It has been found that the introduction of surface deformation to each layer can lead to a greatly refined grain structure with a more randomised texture. To investigate the origin of this effect, reconstruction of the β grain structure and texture from the α EBSD measurements has been used to characterise the high temperature β microstructure.

## Introduction

There is potential for the aerospace industry to greatly benefit from Additive Manufacture (AM) as it allows the near-net-shape manufacture of components [1–7] and provides more design freedom than traditional manufacturing, which can facilitate substantial weight savings through better design optimisation [1]. Ti-6Al-4V is one of the most widely used titanium aerospace alloys due to its high specific properties [8]. However, optimum performance is traditionally achieved with this material through the thermomechanical processing (TMP) [9]. In contrast, AM is based on the layerwise deposition of material through melting and this can lead to quite different microstructures and textures [2,3].

Of particular concern in aerospace components with alloys like Ti-6Al-4V is that coarse-columnar primary β-grain structures are nearly always observed in AM processes [2,3,7]. Transformation to α on cooling refines the microstructure, however, significant texture is still inherited in the α phase and this can contribute to anisotropy. A coarse β structure develops in AM because there is a steep thermal gradient in the melt pool ahead of the solidification front. When combined with the high partition coefficients of Al and V in Ti [10], this limits the degree of constitutional supercooling that is possible and nucleation ahead of the solidification front becomes very difficult. As a result, homo-epitaxial re-growth takes place within each melted layer, allowing coarse directional grain structures to develop that can grow up through many deposited layers. [2,3,7]. In addition, because of the preferred <001> growth direction in cubic metals, the large columnar grains tend to have a strong β <001> fibre texture parallel to the average solidification direction within a particular AM process [2,3]. Disrupting this columnar structure by metallurgical means is challenging as there are few options for grain refining additions in titanium [11].

In α-β alloys like Ti-6Al-4V, upon rapid cooling below the β transus, the majority of the β phase transforms to fine Widmanstätten α lamellae [9] while the remainder of the parent β is retained as thin layers between the α plates [12]. The texture is weakened by the transformation as there are 12 possible variants of the α phase formed within each β grain, as described by the Burgers orientation relationship [13]; $\{110\}\beta \parallel \{0002\}\alpha$, $\langle 111\rangle\beta \parallel \langle 11\bar{2}0\rangle\alpha$. However, on reheating back to the β phase field, which in AM generally occurs several times within each deposited layer [3], the retained β phase re-grows with its original parent orientation, consuming α, and thus thermal cycling does not lead to any significant texture weakening.

In AM processes a component is built up from multiple tracks with a small moving heat source which can lead to the development of substantial residual stresses and distortion [5]. Similar stresses are accrued with a single track deposition in traditional welds, and have previously been relieved by imparting a compensating plastic strain by treatments such as peening [14] and rolling [15]. However, when a rolling step was introduced into a wire-plasma AM process, in addition to a decrease in residual stresses, a large reduction in the prior β grain size was observed accompanied by a weakening of the β <100> fibre texture [16]. Given the relatively small plastic strains applied in this work, this is quite a surprising result and the mechanism of grain refinement still remains to be fully explored. In the present work, the laser blown powder technique (LBP) has been integrated with Ultrasonic Impact Treatment (UIT) (a form of peening [17]), of the deposited layers to determine if a similar microstructural improvement could be achieved with this higher layer resolution AM process.

# Experimental

## *AM Builds*

Simple linear ~ 250 long, ~15 wide, and ~ 65 mm high walls were built up using a laser blown powder AM system with gas atomised Ti-6Al-4V powder. The power of the Nd-YAG Trumph laser used was 1000W and the deposits were produced with a constant travel speed of 15 mm/s. The powder was blown into the melt pool by an argon carrier gas and oxidation was prevented by containment within an argon filled environment. Deposition occurred on a base plate of similar composition to the powder. 20 tracks of material were deposited to make up each layer and 75 layers were deposited to make each wall, with a layer height of ~0.9mm. The build sequence for each layer was identical, but the raster direction was reversed. Thus below, $x$ is taken to be the direction parallel to the length of the wall and beam travel direction and $z$ is normal to the layers. Three builds were made for comparison purposes; i) a standard build with no deformation, ii) with an Ultrasonic Impact Treatment (UIT) applied every 5 layers, and iii) with UIT applied after every deposited layer. UIT was applied when the material had cooled down uniformly across the top surface of each layer.

## *Characterization and β- Phase reconstruction*

For metallographic examination the walls were sectioned in the $x$-$z$ and $y$-$z$ planes, before being ground and polished. Samples were etched with Kroll's reagent for optical microscopy. Orientation and texture analysis was carried out by Electron Back Scatter Diffraction (EBSD) in a Camscan FEG-SEM. Orientation maps were generated with an Oxford instruments EBSD system, operating Channel 5 software. The textures of the reconstructed high temperature β phase (see below) and room temperature α phase are depicted by pole figures. As the <100> fibre texture was aligned with the columnar grain growth direction, and this was found not to be coincident with the $y$, and $z$ directions in the build geometry. A second reference frame has been used where $x$, $y$, and $z$ have been rotated around the x axis to $x$, $y'$, and $z'$ so that $z'$ is aligned with the dominant grain growth direction, or <100> fibre axis. This procedure has been adopted throughout to produce the IPF coloured orientation maps depicted below (See figure 1).

Because EBSD measurement are made at room temperature, where it is very difficult to resolve the small quantity of retained β phase, reliable orientation date could only be obtained from the α phase. Thus, in order to characterise the primary β-phase, a reconstruction procedure was applied (developed at The University of Sheffield and described elsewhere [18]) which calculates the most probable parent β orientation for any α grain by utilising the Burgers relationship, and comparison of the misorientation between neighbouring α plate variants.

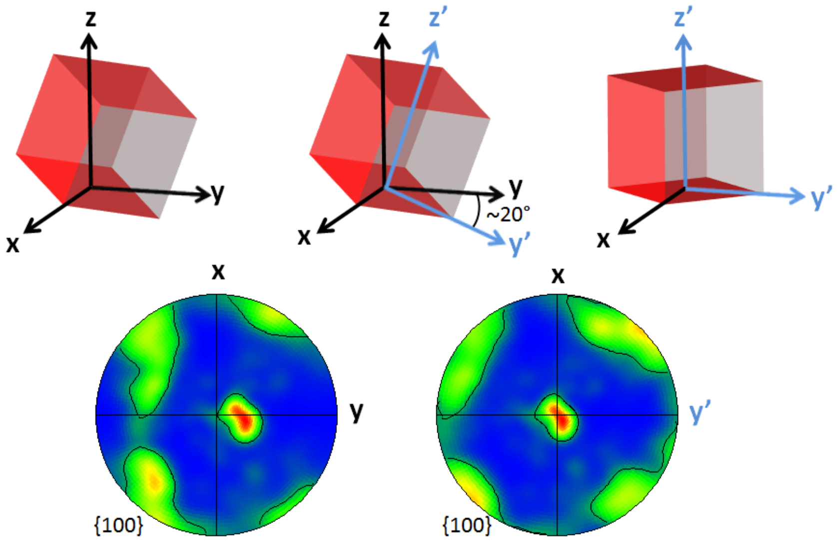

Figure 1. Example of the rotation typically required of ~ 20˚ around the x axis of the build geometry (x, y, z) to (x, y', z') to align z' with the dominant <001> fibre axis of the columnar grain growth direction for the β phase.

## Results and Discussion

Optical images of the conventional LBP build (i) can be seen in figure 2 where it is possible to readily distinguish the coarse columnar prior-β microstructure as well as microstructural banding. Similar banding has been observed in other AM processes [4,19] and is associated with microstructural changes that occur across the β transus [4]. Epitaxial-growth of the prior β columnar grains up through many deposited layers can clearly be observed in figure 2a, where the grains are approximately ~ 0.25 mm wide and over 1 cm in height, some being taller than the field of view. The 'fish-scale' banding morphology in figure 2a is related to the semi-circular cross-section of the weld pool seen when viewed transverse to the direction of travel, (*y*-*z* plane), which is tilted due to overlap with the previously deposited neighbouring track. In comparison, the horizontal banding observed in figure 2b occurs due to the travel of the heat source which, when viewed at steady state in this plane, maintains a constant depth for the isotherm that reaches the β transus temperature.

Also visible in this cross-section is curvature of the grains towards the y direction, caused by them following the maximum thermal gradient at the solidification front from the tilted bowl-shaped melt pool. In comparison the tilt of the grains is very slight in figure 2b, because from this perspective the rapid movement of the laser in *x* elongates the melt pool causing a flatter solidification front. In addition, tilt in *x* is effectively suppressed by the reversal of the beam travel direction with each successive pass which results in the average preferred growth direction being parallel to z [3]. In contrast tilt in *y* in the *y*-*z* plane is reinforced in each successive layer, as regardless of the direction of deposition in *x*, the tracks were stepped across from the same side of the build and thus the curvature of the solidification front was always the same when viewed in this plane.

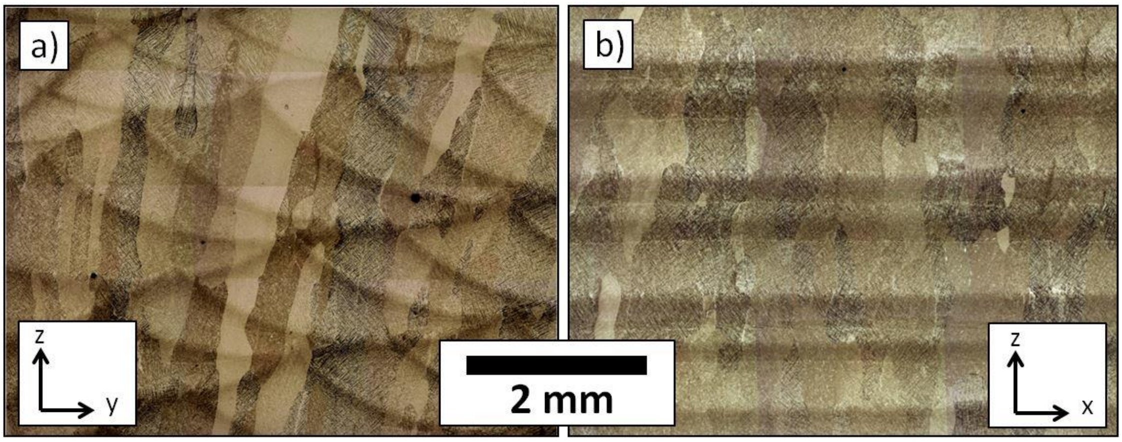

Figure 2. Etched microstructures of the standard wall (no UIT) in the z-y (a), and z-x (b) planes.

### *Effect of UIT on the primary β grain structure*

In figure 3 the primary β grain structures are clearly seen in IPF orientation maps reconstructed from EBSD measurements of the α orientations present at room temperature. Figure 3 includes maps of the three samples produced with and without the UIT treatment, where the data has been rotated as described in figure 1 to align *z′* with the principle <001> fibre direction, which is coloured red.

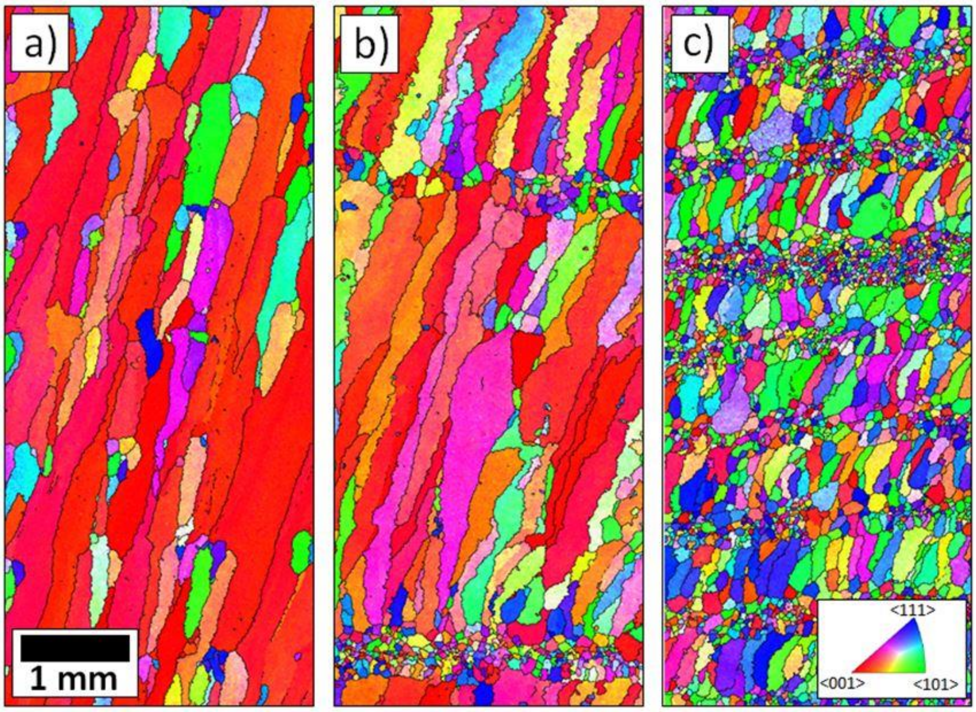

Figure 3. Reconstructed EBSD maps of the y-z plane from (a), the untreated build, (b) with UIT applied every 5 layers and (c), UIT applied every layer.

In the untreated control sample, shown in figure 3a, large columnar grains are again clearly visible and it is evident from their dominant red colour that the grains have a strong <100> preferred growth direction. In the second sample shown in figure 3b the UIT treatment was applied to every fifth deposited layer, and as a result a band of finer equiaxed grains can be observed, breaking up the columnar structure and limiting the height of each columnar band to ~4 mm. The narrow bands of equiaxed grains that have been produced within each deformed layer are much finer than the columnar grains, (~ 50μm in diameter) and have more random orientations. However, too few grains have been sampled to give reliable statistics. In figure 3c the effect of applying the UIT to every layer is also shown, which leads to an alternating structure of fine equiaxed grains and smaller columnar grains. The more frequent application of UIT now limits the columnar grains to a height of only ~0.5mm, leading to a more random texture.

### *Effect of UIT on texture in the LBP process*

As can be seen from the β <001> pole figure in figure 4a, from the standard build without the UIT treatment, there is strong <100> alignment along the columnar grain direction. This confirms that the moving melt pool solidification conditions, combined with layer-by-layer deposition, leads to epitaxial growth of a coarse, preferentially aligned β grain structure in a Ti-6Al-4V alloy. However, although there are statistical concerns as only a relatively small number of grains were sampled (~500), rather than forming a true <100> fibre as has been reported in the literature [20], it appears that the columnar grains are predominantly spread around a cube component that is rotated ~ 45° around $z'$, relative to the laser travel direction. It should also be noted that, as shown in figure 1, the fibre axis was originally tilted around $x$ by 20° away from the layer normal direction ($z$) because of the curvature of the melt pool base and the effect track overlap had on the tilt of the melt pool surface. Cube [3] and 45° rotated cube [2] components have been previously reported in AM builds using an electron beam method [2].

A possible explanation for the cube orientation has been given by Antonysamy et al. whom suggested that a repeated alternating orthogonal raster pattern can encourage alignment of the <100> growth direction with the beam path as well as in the build direction [3]. However, this explanation is not applicable here as the cube texture is orientated at 45° to the travel direction. This behaviour needs further investigation, but in the LBP process it is possible that it is related to the shape of the melt pool where an elliptical, or tear drop shape, would cause grain growth in the $x$-$y$ plane to occur predominately at an angle relative to the beam travel direction.

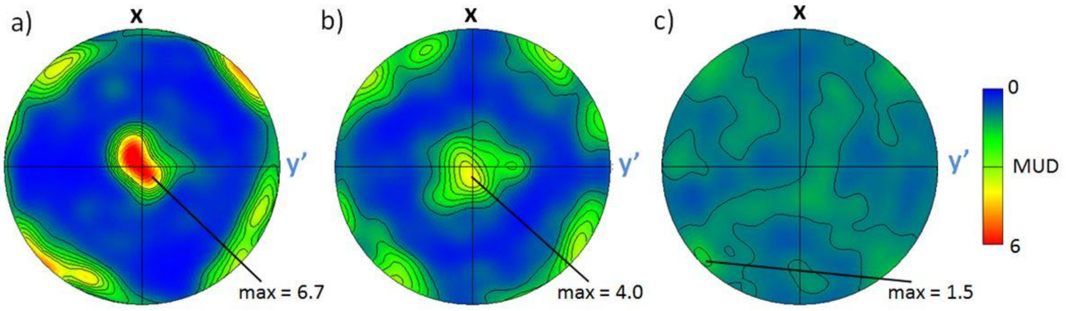

Figure 4. <100> pole figures indicating the β texture strength for (a) the standard untreated build, (b) LBP with UIT applied every 5 layers, and (c) LBP with UIT applied to every layer.

In figure 4b it can be seen that when UIT was applied to every fifth layer the average texture was substantially weakened by a factor of ~40%. As the layers of fine randomly orientated grains produced by this treatment were very thin and did not contribute greatly to the sample volume. The texture weakening has occurred largely as a result of the bands of columnar grains not being able to develop such strong preferred orientations, owing to their growth being repeatedly cut-off by the application of the deformation treatment; i.e. the reduction in texture strength is more related to the length of stable columnar grain growth that is needed to re-establish a strong <100> texture after it is interrupted.

This interpretation can be better demonstrated by separating the textures obtained from the two grain structures, as has been done in figure 5. From these results it can be seen that the main <001>//*z*' component taken from the columnar band data has only a slightly stronger maximum intensity than that seen for the whole volume averaged texture (figure 4b). In addition, it can now be seen that the thin band of refined grains has a very weak texture, which still contains some of the same 45º rotated cube component.

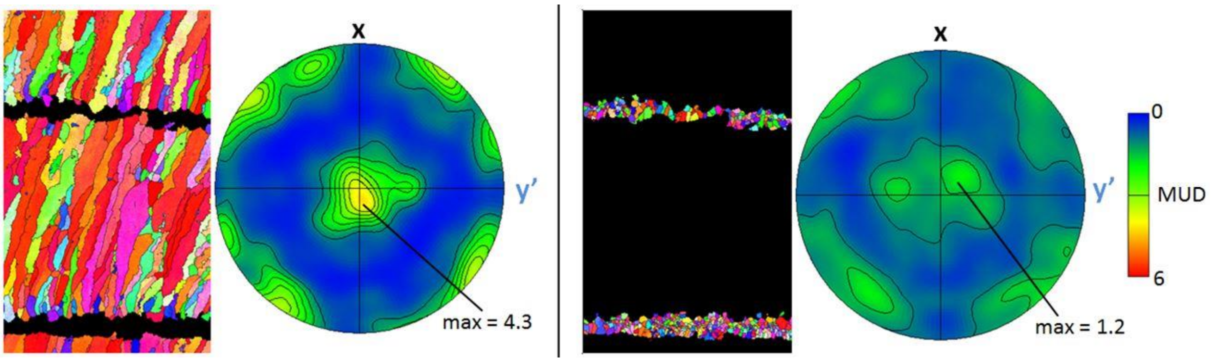

Figure 5. Separation of the textures of the sample deformed every five layers into their columnar and refined regions.

More important than the above results, in terms of understanding the potential for the ultrasonic impact treatment to improve texture in AM, is that when UIT was applied to every deposited layer the β texture became very weak (figure 4c). In fact, from figure 4c it can be seen that when UIT was used repeatedly on every layer the resultant texture of the wall was effectively random.

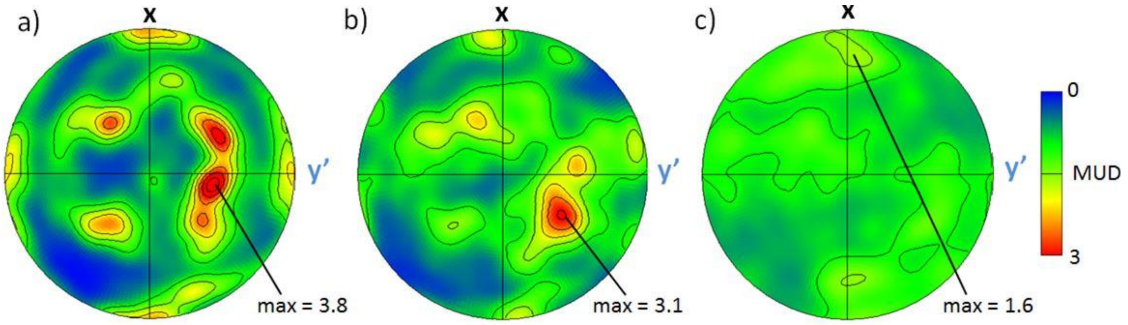

Figure 6. {0002} basal pole figures indicating the room temperature α texture strength of (a) the standard build, (b) with UIT applied every 5 layers and (c) the texture when UIT was applied every layer.

As described in the introduction, owing to the 12 orientations possible from the Burgers relationship, transformation to α at room temperature significantly weakened all the final textures of the AM parts relative to those seen for the primary β grain structures that developed during solidification (figure 6). Thus, the strong β texture seen in the standard wall transformed to a stronger α texture than in the ultrasonic impact treated walls, but in both cases the texture was weakened by the transformation. In contrast, because of the original weakened β texture, in the build that was treated with the UIT process every layer the α texture was effectively eliminated.

### *Origin of the microstructural refinement*

In AM, the effect of the deformation applied to the top surface of a build by the UIT process cannot be interpreted simply as 'recrystallisation' because of the complex thermal cycle the material experiences and the fact that there is a massive α → β phase transformation that occurs on re-heating each layer above the β transus temperature, by subsequent passes of the heat source. In the undeformed standard sample establishment of a columnar microstructure is enabled by the retained β in the room temperature transformation microstructure, which acts as nuclei for the primary β microstructure to re-grow upon re-heating above the β transus. On solidification of a new added layer, epitaxial re-growth then occurs from this re-created β grain structure. It is therefore apparent that deformation of the room temperature microstructure by UIT must result in the development of new β orientations within the retained β phase that then can grow as new grains on reheating in the next pass. Alternatively, intense deformation of the α lamellae, and possibly by processes like twinning, could cause new β orientations to nucleate within the α phase during reheating.

The UIT process itself only introduces local deformation below the surface with a diminishing strain with depth, and it is evident most of this region is lost by re-melting as the next layer is deposited. With the current process parameters the UIT treatment is thus only just successful, because the depth of deformation is just deep enough to survive application of the next layer and provide sufficient deformation to induce refinement of the β phase when it re-grows; i.e. we do not see a graduated microstructure across the refined zones to correspond with the decrease in stored energy with depth, that would be expected from the UIT process. Instead only a thin layer of refined grains is observed with a distinct boundary between the columnar structure underneath, implying that there must be a critical condition to overcome in order for the grain refinement to occur. As in the *y-z* plane the refined zones occur in horizontal bands parallel to the deformed surface, rather than following the fish-scale banding pattern that indicates the temperature profile below each melt track, it can be deduced that this critical condition is strain limited. This refined layer of random β grain orientations then goes on to disrupt the development of columnar growth of the same grain orientations up through many layers. When allowed to continue, this behaviour would normally result in the growth of very large grains that are progressively selected to be more closely aligned with the optimum growth direction and, hence, the UIT treatment also disrupts the development of the strong <001> texture seen in the standard build.

## Conclusions

As has been noted in other AM processes, a coarse columnar prior β grain structure with a strong texture is formed by preferential <100> growth in the standard LBP process. However, a rotated cube component has been observed rather than a <100> fibre texture.

The addition of UIT to every layer is a very effective process step for interrupting columnar growth of the coarse β grain structure normally seen on solidification. This is achieved by producing a band of finer equiaxed prior β grains with a randomised texture.

Although the depth of surface deformation obtained by UIT in this study was not great enough to fully refine the microstructure of each layer, this could be achieved with an AM technique that has a thinner layer height and/or by a deformation process that can impart a greater depth of deformation.

## Acknowledgements

The authors would like to thank Dr. B. Wynne (Sheffield) for provision of the β reconstruction software. J. Donoghue is grateful for financial support provided by LATEST2 (EP/G022402/1) and Airbus, UK. We are also grateful to Prof. S. Williams group at Cranfield for proposing the idea of applying deformation to AM processing and the EPSRC CIM in Laser Based Production Processes (EP/K030884/1).

# References

1. P. Kobryn, N. Ontko, L. Perkins, and J. Tiley, (2006).

2. S. S. Al-Bermani, M. L. Blackmore, W. Zhang, and I. Todd, Metall. Mater. Trans. A 41, 3422 (2010).

3. A. A. Antonysamy, J. Meyer, and P. B. Prangnell, Mater. Charact. (2013).

4. F. Wang, S. Williams, P. Colegrove, and A. a. Antonysamy, Metall. Mater. Trans. A 44, 968 (2012).

5. P. Colegrove, H. E. Coules, J. Fairman, F. Martina, T. Kashoob, H. Mamash, and L. D. Cozzolino, J. Mater. Process. Technol. 213, 1782 (2013).

6. K. Taminger and R. Hafley, NATO AVT (2006).

7. S. Reginster, A. Mertens, H. Paydas, J. Tchuindjang, Q. Contrepois, T. Dormal, O. Lemaire, and J. Lecomte-Beckers, Mater. Sci. Forum 765, 413 (2013).

8. R. R. Boyer, Mater. Sci. Eng. A 213, 103 (1996).

9. G. Lütjering, Mater. Sci. Eng. A 243, 32 (1998).

10. M. J. Bermingham, S. D. McDonald, M. S. Dargusch, and D. H. StJohn, J. Mater. Res. 23, 97 (2011).

11. M. J. Bermingham, S. D. McDonald, K. Nogita, D. H. St. John, and M. S. Dargusch, Scr. Mater. 59, 538 (2008).

12. G. Lütjering and J. C.Williams, Titanium, 2nd ed. (Springer, Berlin, n.d.).

13. W. G. Burgers, Phys. I 561 (1933).

14. L. Hacini, N. Lê, and P. Bocher, Exp. Mech. 49, 775 (2008).

15. D. F. O. Braga, H. E. Coules, T. Pirling, V. Richter-Trummer, P. Colegrove, and P. M. S. T. de Castro, J. Mater. Process. Technol. 213, 2323 (2013).

16. A. A. Antonysamy, Microstructure, Texture and Mechanical Property Evolution during Additive Manufacturing of Ti6Al4V Alloy for Aerospace Applications, University of Manchester, 2012.

17. S. Roy and J. Fisher, Int. J. Steel Struct. (2005).

18. P. S. Davies, An Investigation of Microstructure and Texture Evolution in the Near-A Titanium Alloy Timetal 834, University of Sheffield, 2009.

19. E. Brandl, A. Schoberth, and C. Leyens, Mater. Sci. Eng. A 532, 295 (2012).

20. P. Kobryn and S. Semiatin, J. Mater. Process. Technol. 135, 330 (2003).

## 4.2. The Effectiveness of Combining Rolling Deformation with Wire-Arc Additive Manufacture on β-Grain Refinement and Texture Modification in Ti-6Al-4V.

Similar to **Manuscript 1**, this manuscript uses EBSD extensivly to characterise the effect the addition of an in process deformation step has on the microstructure and texture of Ti-6Al-4V AM builds. In this instance the effect of a rolling step on a wire-arc AM technique are investigated. This study goes into more detail than the previous included manuscript, and attempts to relate the refined grain structure to the strain distribution imparted by the rolling step.

The discussion in this paper makes a brief reference to the subsequent included manuscript, **Manuscript 3**, due to the dates of publication of the papers. However, the choice has been made to include the papers out of chronological order as it is believed by the author that it leads to a more logical reading order to have the two characterisation papers and the two mechanism papers alongside each other.

This paper was submitted on 15th October 2015 to the Journal '*Materials Characterization'*. After peer review a revised version of the manuscript was submitted on the 6th January 2016, which was accepted the following month and made available online on the 8th of February 2016. The article was included in the April 2016 edition of the printed Journal.

The paper is as published, with the exception of figure 14 (and the paragraph discussing it) that were added for this thesis.

The contributions of the named authors were as follows:

*University of Manchester*

**Jack Donoghue** – Lead author, all metallographic preparation, SEM analysis and EBSD data analysis.
**A.A. Antonysamy** – Performed some of the preliminary ground work, and took the macroscopic photograph included in Figure 2.
**P.B. Prangnell** – Drew the schematic diagram in figure 1. Supervisor of Jack Donoghue.

*Cranfield University*

**F. Martina, P.A. Colegrove & S.W. Williams** – Responsible for the manufacturing of the samples.

# The Effectiveness of Combining Rolling Deformation with Wire-Arc Additive Manufacture on β-Grain Refinement and Texture Modification in Ti-6Al-4V

J. Donoghue[1]*, A.A. Antonysamy[1+], F. Martina[2], P.A. Colegrove[2], S.W. Williams[2] and P.B. Prangnell[1]

[1]School of Materials, University of Manchester, Manchester, M13 9PL, UK
[2]The Welding Engineering Research Centre, Cranfield University, Bedfordshire, MK43 0AL, UK
[+] Now at GKN Aerospace, PO Box 500, Golf Course Lane, Filton BS34 9AU, UK.

jack.donoghue@manchester.ac.uk; alphons.antonysamy@gknaerospace.com; f.martina@cranfield.ac.uk; p.colegrove@cranfield.ac.uk; s.williams@cranfield.ac.uk; philip.prangnell@manchester.ac.uk

## Abstract

In Additive Manufacture (AM), with the widely used titanium alloy Ti-6Al-4V, the solidification conditions typically result in undesirable, coarse-columnar, primary β grain structures. This can result in a strong texture and mechanical anisotropy in AM components. Here, we have investigated the efficacy of a new approach to promote β grain refinement in Wire-Arc Additive Manufacture (WAAM) of large scale parts, which combines a rolling step sequentially with layer deposition. It has been found that when applied in-process, to each added layer, only a surprisingly low level of deformation is required to greatly reduce the β grain size. From EBSD analysis of the rolling strain distribution in each layer and reconstruction of the prior β grain structure, it has been demonstrated that the normally coarse centimetre scale columnar β grain structure could be refined down to less than 100 μm. Moreover, in the process both the β and α phase textures were substantially weakened to close to random. It is postulated that the deformation step causes new β orientations to develop, through local heterogeneities in the deformation structure, which act as nuclei during the α→β transformation that occurs as each layer is re-heated by the subsequent deposition pass.

Keywords: Additive Manufacture; titanium; grain structure; texture,

*Corresponding Author; +44 7853385063

# 1. Introduction

Near-net-shape fabrication of metallic components by Additive Manufacture (AM) is an important new technological area with many potential applications in the aerospace industry (e.g. [1–17]). AM involves building parts by sequentially consolidating 2D slices of material that are fused together by a focused heat source [1–3]. A range of AM processes are now available, mainly based on laser or electron beam systems, that use powder or wire feedstock [1–12]. Of these techniques, powder bed methods allow more geometrically complex components to be produced, but the part size is restricted by slow build rates and the limited dimensions of the working chamber [1–4].

Recently, a low cost wire-based AM process that exploits standard welding technology has become of interest to industry [9–11]. In Wire-Arc Additive Manufacture (WAAM) a consumable wire is fed at a controlled rate into an adapted electric arc (or plasma) welding torch that is translated by a robot [9–12]. Material is built up in the form of a weld bead that is overlaid on previously deposited tracks. Shielding can be provided by an inert gas flooded hood, or deposition can take place in an atmospherically controlled chamber. The WAAM process has a much higher deposition rate than most other metal additive manufacturing techniques (up to 10 kg/hr). It also provides better material utilization than powder based methods [9–12], but is restricted to wider wall thicknesses and cannot produce as fine scale features. This low cost process is therefore most suited to producing larger scale parts with less complex geometries.

The α - β titanium alloy, Ti-6Al-4V, is the ‘work horse’ of the aerospace industry and widely used in airframe and aeroengine applications, where the production of near-net shape components by AM can result in significant cost savings. However, a current concern with AM using this alloy is that coarse primary columnar β grain structures are nearly always observed to be produced in the consolidated material. This undesirable grain structure is seen across a wide range of AM platforms [6,9–16]. With wire based AM the primary β grains are often as tall as the build height and with larger components can be tens of centimetres long [9–16]. This strong tendency to form coarse-columnar β grain structures in AM with Ti-6Al-4V is difficult to avoid because it results from a combination of the solidification conditions in a small heated moving melt pool, where there is a steep positive thermal gradient at the solidification front, and the metallurgical characteristics of the alloy itself [13–16]. In particular, the Ti-6Al-4V alloy system does not lend itself to nucleation ahead of the solidification front because of the high partition coefficients of aluminium and vanadium, which are close to one, and the lack of suitable grain refining particles in the melt [17]. These process and metallurgical limitations restrict the degree of constitutional supercooling that can occur so that, when combined with a lack of melt inoculants, nucleation ahead of the solidification front is difficult to achieve [13–16].

Although in AM the β grain structure developed during solidification transforms to a fine α and retained β lamellar structure on cooling below the β-transus temperature, the microstructural memory of the coarse, directional, primary-β microstructure can still have a significant impact on mechanical performance. In particular, directional growth of large primary β grains generally produces a strong <001> fibre texture, which gives rise to a related α transformation texture [13–16] and this can potentially result in texture clustering of aligned α-plates within the β matrix. Such factors are known to be detrimental to fatigue life [18,19] and can contribute to mechanical anisotropy [20–22]. In addition, with a coarse primary β grain structure, grain boundary α can cause premature failure in transverse loading [21,23]. However, to date, little systematic work has been published on the texture found in AM titanium components produced by wire-based techniques like the WAAM process.

Potential methods for refining the poor primary grain structure seen in AM deposits include; i) modification of the solidification conditions in the melt pool, through manipulation of the process variables [10], or ii) altering the alloy chemistry [17,24,25]. However, in AM there is limited scope for changing the process window, because this is dictated by the conditions required to obtain stable part dimensions [9,10]. Furthermore, while trace additions of elements like boron are known to act as growth restrictors in titanium [25] this can have negative consequences through the formation of brittle second phase particles (e.g. TiB).

In the present work an alternative approach has been investigated for improving the large columnar β-grain structures and strong textures typically seen in wire-based AM processes. This has involved the introduction of a small deformation step sequentially with the deposition of each layer. The deformation step was applied using a roller integrated with the AM system, so that each deposited layer could be lightly deformed before adding a new layer of material (Figure 1). Although this set up limits the technique to simpler geometries, the aim of this approach was to see if it was possible to introduce sufficient plastic deformation into each layer so that refinement of the β-grains could occur during re-heating, when the next layer was deposited. It was also hoped that this might generate a weaker texture, which would lead to more isotropic mechanical properties [18,19,26]. Although the introduction of a light rolling step in AM will moderately reduce the rate of build-up of material and causes a slight spreading in the wall width, this can be controlled in an automated manufacturing system and would not be a major issue when building relatively simple component designs. In fact, it has been found that rolling increases the accuracy of the wall dimensions, by correcting variation in the wall width caused by the bead profile [27]. There are also other potential methods available for applying deformation to each layer in AM that are not so restricted by geometry, such as by peening [28]; hence the efficacy of this novel approach is of more general interest.

It should be noted that in this collaborative study the concept of the hybrid WAAM deformation process was developed by Cranfield University Welding Engineering Research Centre [27,29], who have previously published work investigating the effect rolling has on the residual stress within the builds [27], and noting the effect on the refinement of the microstructure [30]. The current work, performed at Manchester University, is complementary in that it investigates the effect the refinement has on the primary β and final α texture, and goes into more detail than the previous work into the mechanism of formation and the distribution of the refined β grain structure.

## 2. Experimental

### *2.1 WAAM samples*

The undeformed and rolled WAAM samples were built using a Ti-6Al-4V alloy welding wire (1.2 mm diameter) with a titanium base plate of the same alloy. The substrate material was a conventional hot rolled and annealed plate that had a recrystallized equiaxed α - β microstructure [18]. The samples studied were produced under identical conditions - as one meter long, 20 layer high, straight, vertical walls, using a pulsed GTAW welding system with an average current of 110 A. Each wall was a single track wide and had a width of ~ 6 mm. Argon shielding was provided by a trailing hood containing a laminar flow device with a high gas flow rate. This resulted in an average oxygen content in the deposited walls of less than 1500 ppm. The deposition parameters employed are given in Table 1 and full details of the WAAM process can be found in ref [9]. To produce the deformed samples, after deposition of each individual layer, a 100 mm diameter roller was run across the top of the walls using a rigid gantry system on which the welding torch was also mounted (see Figure 1). Each layer was rolled after the temperature of the top layer cooled naturally to well below 300 °C (i.e. close to cold deformation conditions, and well into the α – β field). The roller employed contained a 3.6 mm radius semi-circular groove, designed to approximately match the curvature of the bead surface. The compressive load during rolling was controlled using a load cell and was applied directly downwards through the roller bearings to the top of each wall.

Table 1. WAAM deposition parameters used to build the samples investigated.

| Deposition Parameter | Value |
|---|---|
| Travel speed | 270 mm/min |
| Average Arc Voltage | 12 V |
| Average Current | 110 A |
| Wire feed speed | 1.6 m/min |
| Frequency | 10 Hz |
| Trailing shield gas flow rate | 20 l/min |

Five sample conditions were analysed; (i) a control sample built without rolling, as well as two walls to which rolling was applied after adding each layer, with a down-force of (ii) 50 or (iii) 75 kN, and two walls where rolling was only applied to the penultimate layer with the same loads (i.e. (iv) 50 and (v) 75 kN) and the final layer was not deformed.

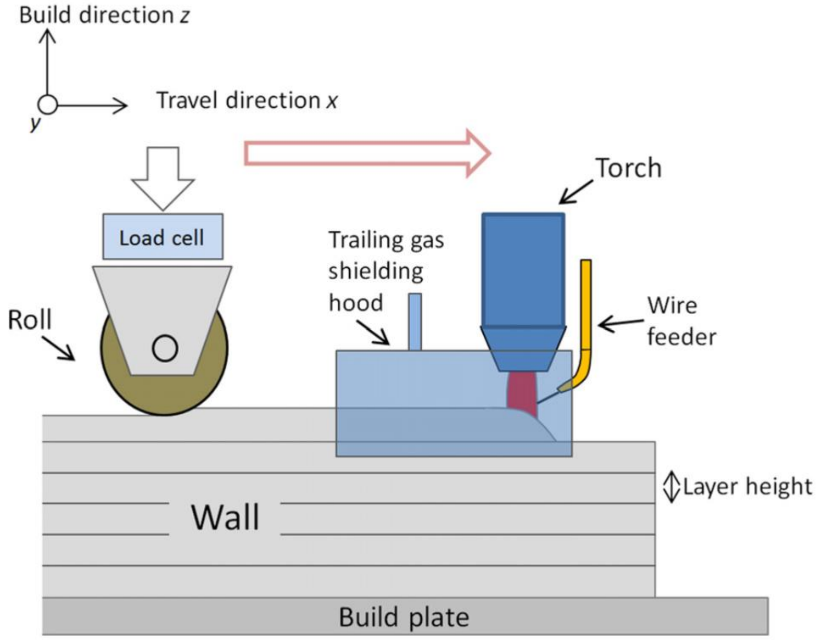

Figure 1. Schematic diagram of the combined WAAM rolling process.

In the results presented, a standard reference frame has been used for the orientation of all the samples where; z is the direction normal to the deposited layers (and parallel to the wall height), x is parallel to the wall length and coincident with both the torch travel and rolling direction, and y is the transverse direction normal to the wall surface (see Figure 1). For the samples rolled every layer the net reduction in wall height is given in Table 2, where it can be seen that the 50 and 75 kN rolling loads resulted in an average compressive strain ($\varepsilon_z$) of 8 and 19% respectively.

Table 2. Change in average layer height and wall width after rolling each added layer in the Ti6Al4V builds, along with the estimated average true principle strains in ND, RD and TD.

| Sample | Layer height | Rolling reduction | Wall Width | Change in Width | $\varepsilon_z$ | $\varepsilon_y$ | $\varepsilon_x$ |
|---|---|---|---|---|---|---|---|
| Control | 1.13 | - | 5.71 | - | - | - | - |
| 50 kN | 1.04 | 0.09 | 6.17 | 0.46 | - 0.083 | 0.077 | 0.006 |
| 75 kN | 0.93 | 0.20 | 6.71 | 1.00 | - 0.19 | 0.16 | 0.03 |
| | (mm) | (mm) | (mm) | (mm) | | | |

## *2.2 Characterisation techniques*

The undeformed and rolled AM samples were characterised in two cross-sections for microstructure and textural analysis; i.e. down their centre line in the vertical x-z plane and ii. in the plane of the layers (x-y), half way up each wall - to observe any microstructural variation vertically and through the thickness. Following standard preparation procedures, etching and optical microscopy was used to reveal the deposits' macrostructures. Metallographyically prepared samples were analysed by scanning electron microscopy and electron back scatter diffraction (EBSD) orientation mapping using a CamScam Maxim FEG-SEM. Orientation maps were collected with an Oxford instruments EBSD system, with Aztec acquisition software. Large area maps of ~ 12 x 6 mm, with a 5 µm step size, were used to obtain average texture data and provide comparative macro-views of the coarse β-grain structure across all samples.

## *2.3 β- phase reconstruction and texture analysis*

In a Ti-6Al-4V alloy with a fine lamellar microstructure it is challenging to index the residual β-phase directly by conventional EBSD because of its small scale and low volume fraction (~ 5-9% [31]). The high temperature parent β phase grain structures and textures that were originally present after solidification, prior to transformation on cooling, were therefore reconstructed from room temperature α orientation data using a procedure developed by Davies and Wynne [32,33], based on earlier work by Humbert et al. [34,35]. Full details of this approach can be found in ref. [32]. The reconstruction procedure uses the Burgers Orientation Relationship (BOR) between the α and β phase to calculate the six possible β parent orientations for each α plate [32–35]; where the BOR is given by:

$$\{110\}_\beta \parallel \{0002\}_\alpha \qquad \langle 111\rangle_\beta \parallel \langle 11\bar{2}0\rangle_\alpha$$

The most probable parent β orientation for each α plate is then selected by comparing the most common solution for the misoreintations between neighbouring data points. Variables within the procedure that can be altered are the misorientations between neighbouring α points, that can be considered the same α variant, and the allowable maximum angular deviation from the ideal BOR [32]. Here, these parameters were kept at 2° and 3°, respectively.

Texture information was extracted from the original measured α EBSD maps and reconstructed β orientation data and is presented in standard pole figures. In all the orientation maps, inverse pole figure (IPF) colouring has been used with the reference axis aligned with the main fibre direction, which is close to z. High angle grain boundaries (HAGBs) >15° in misorientation are depicted by black lines.

### *2.4 Strain distribution in the AM deposits*

In order to relate the plastic deformation to the refined microstructure, it is necessary to map the distribution of the plastic strain as well as the distribution of the grain sizes. Two different approaches were applied to determine the plastic strain distribution in the rolled AM samples using EBSD maps; i) from the pattern quality and ii) the relative effect on the deviation of the misorientation of neighbouring α variants from fulfilling the BOR. If the microscope conditions are kept constant, variation in pattern quality can be attributed to local changes in distortion of the crystal lattice caused by the rolling deformation [36]. The standard measure of pattern quality is Band Contrast (BC), which refers to the brightness of the diffracted bands above background. However, here the Band Slope (BS) was used, which is the gradient of the intensity of signal at the edge of a band (slope of the intensity above back ground). BS was chosen due to the lower sensitivity of the probed volume to crystallographic orientation, compared to BC, which is more strongly affected by how well orientated the crystallographic planes are for diffraction [37]. For method ii) the deviation of misorientations between neighbouring α variants from fulfilling the BOR, within the EBSD data, was determined using the β reconstruction software. In Ti alloys this method is effective because, although there will be local variability between specific α variants, on average the degree of rotation of neighbouring α plates away from the ideal BOR increases with plastic strain [38]. Although neither of the above techniques give direct values for the strain, they both give a reliable qualitative indication of how the strain is relatively distributed within the wall.

## 3. Results

### *3.1 Overview*

Macroscopic optical images of sections through the centre of the WAAM walls (x-z plane) produced with and without deformation applied to each added layer, are shown in Figure 2. The main features that can be noted are the prior β grain structure that developed on solidification, before transformation to an α - β lamellar microstructure on cooling to room temperature, and the regularly spaced horizontal white bands. In the un-rolled wall (Figure 2a) the presence of very large prior columnar β grains can clearly be seen, which run upwards virtually throughout the entire build height. In comparison, when rolling was applied (Figures 2a & b), coarse columnar β-grains are absent and the new grain structure is hard to distinguish at this magnification. However, smaller columnar grains can still be observed in the last added layer, which has not been reheated by subsequent deposition passes.

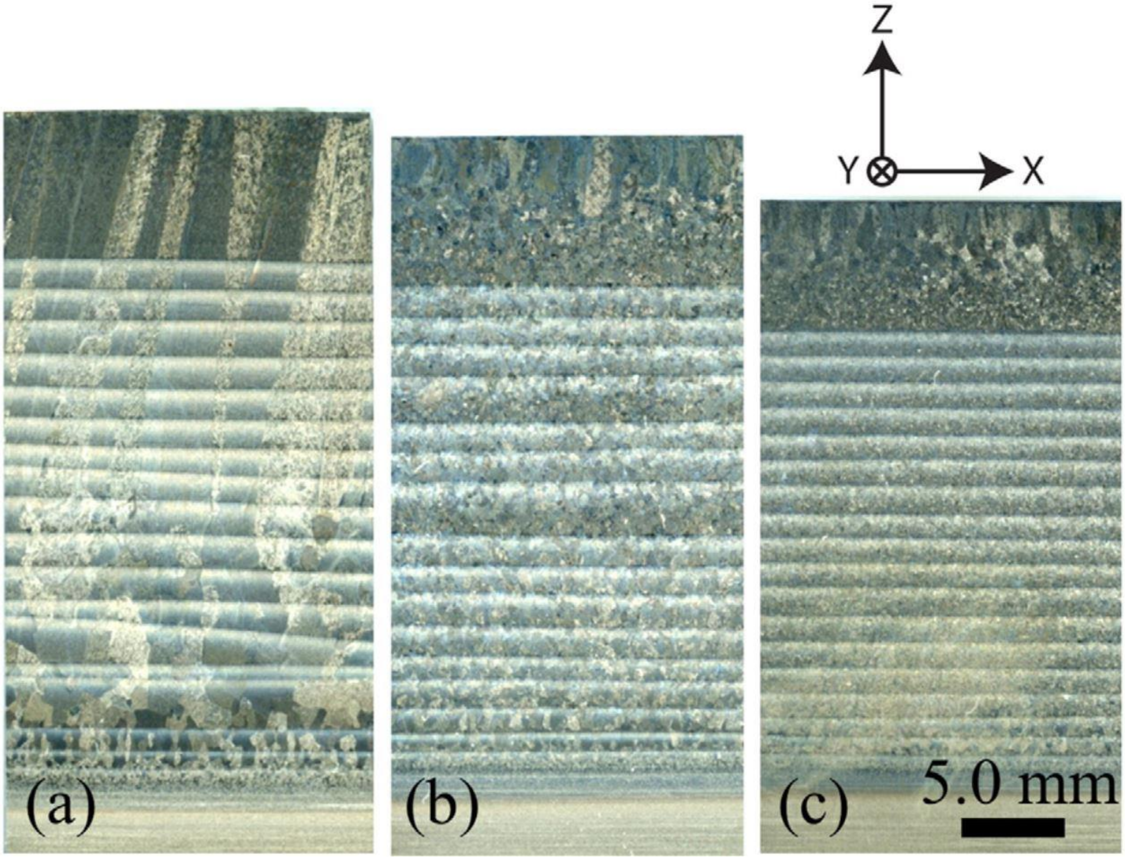

Figure 2. Macroscopic views of sections through the WAAM walls, cut along their centre, x-z, plane produced; (a) without deformation and with an increasing applied rolling load, of (b) 50 kN and (c) 75 kN.

The spacing of the white bands seen in Figure 2 corresponds to the height of each added layer. The bands are formed within the Heat Affected Zone (HAZ) that developed by the moving thermal field below the heat source, as each new layer is deposited [9]. Similar banding has been seen in other AM processes [6,9,12,15] and is thought to occur at a depth where the peak temperature reached was just below the β transus temperature. This has been reported to result in local coarsening of the transformation microstructure [9,12]. In most AM processes the thermal field depth that causes this effect corresponds to three to five added layers, depending on the processing conditions [6,9,11]. With the WAAM process the first white band can be seen to be at a depth of about 8 mm blow the top surface (Fig. 2) and occurred at a depth equivalent to approximately four layers. In the last layer deposited, the newly added and re-melted material solidifies as the β phase and the material within the HAZ of the last pass above the top white band is fully re-heated into the β phase field. This region then transforms directly to α on cooling, although material lower down in the HAZ will have been re-heated and re-transformed between one and three times, depending on the sequential layer number [6]. Hence, the top four layers above the last white band, where deformation was concentrated when each new layer was rolled (see below), had a similar fine lamellar transformation microstructure. This microstructure was relatively uniform and was mainly comprised of a Widmanstätten α morphology, with thin layers of retained β between the lath boundaries (Figure 3). Regardless of being rolled or not, all the samples underwent a very similar cooling rate [30] through the β transus, and therefore the α transformation structure was found to be nearly identical for all build conditions.

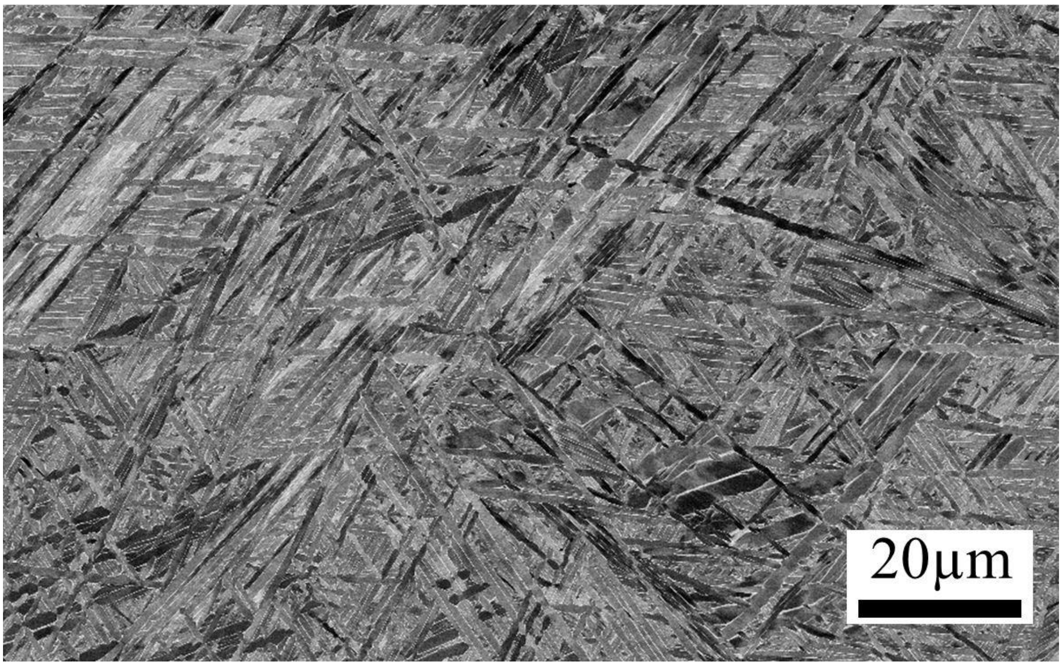

Figure 3. Example of the typical α-β transformation microstructure seen in the WAAM deposits.

### *3.2 Strain distribution*

In Figure 2 the application of a rolling pass to each added layer can be seen to have reduced the overall height of the walls by an amount that increased with the applied load. The average principal (true) strains implied by the net wall shape change are shown in Table 2. It can be seen that the samples rolled with an applied load of 50 and 75 kN had deformed by an average compressive strain in z of 8 and 19%, respectively. The net strain values indicate a decrease in average layer height and an increase in wall width after deformation, while the increase in length of the sample along each wall in the rolling direction was relatively small. This is to be expected because, with a thin wall that is attached to a base plate, there is high constraint along the wall in the rolling direction and less lateral constraint than with a conventional rolling geometry. The net average shape change experienced by the WAAM walls was thus close to plane strain, but with the principal components rotated 90˚ about the build direction, z, (or ND), relative to RD in conventional rolling of a wide plate [39]. However, as will be seen below from the EBSD strain mapping results, the local strain distribution in each layer was found to be highly non-uniform.

The local strain distribution in an individual layer was investigated using the techniques described in §2.4. In Figure 4 the change in EBSD pattern quality determined from the band slope (BS) is plotted with depth down the centre line of the walls rolled with 50 and 75 kN loads. It should first be noted that the periodicity observed in the BS plot deeper in each wall (on the right hand side of the plot) is caused by the microstructural banding in the transformation structure described above (Figure 2). This occurs because local variations in the coarseness of the microstructure within a layer systematically changes the density of α plate boundaries across it, which in turn influences the average value of the BS due to the poorer quality of overlapping diffraction patterns encountered at grain boundaries. In comparison, towards the left side of the graph (i.e. closer to the top wall surface), which is from the region above the last white band seen in each wall, there is little variation in the α microstructure. When this effect is taken into account, the underlying trend in the BS curves can be attributed to the relative plastic strain within the α-phase. For both rolling loads the BS value can be seen to decrease to a minimum below the top wall surface before increasing again to level out at constant value. This behaviour can be interpreted as the plastic strain from rolling being low near the top surface and increasing to a maximum at a depth of between 1.5 and 2.5 mm, before then falling off further down the wall to approach zero at a depth of about 5 and 8 mm, for the 50 and 75 kN loads, respectively. It can be further seen that for the sample produced with a 75 kN rolling load the minimum positon in BS value is both deeper and wider than with a 50 kN load; suggesting that, not only the local strain was larger with a greater rolling load, but that the depth where the greatest plastic strain occurred also penetrated further below the rolled surface (2 as opposed to 1.5 mm, with the 75 and 50 kN loads, respectively).

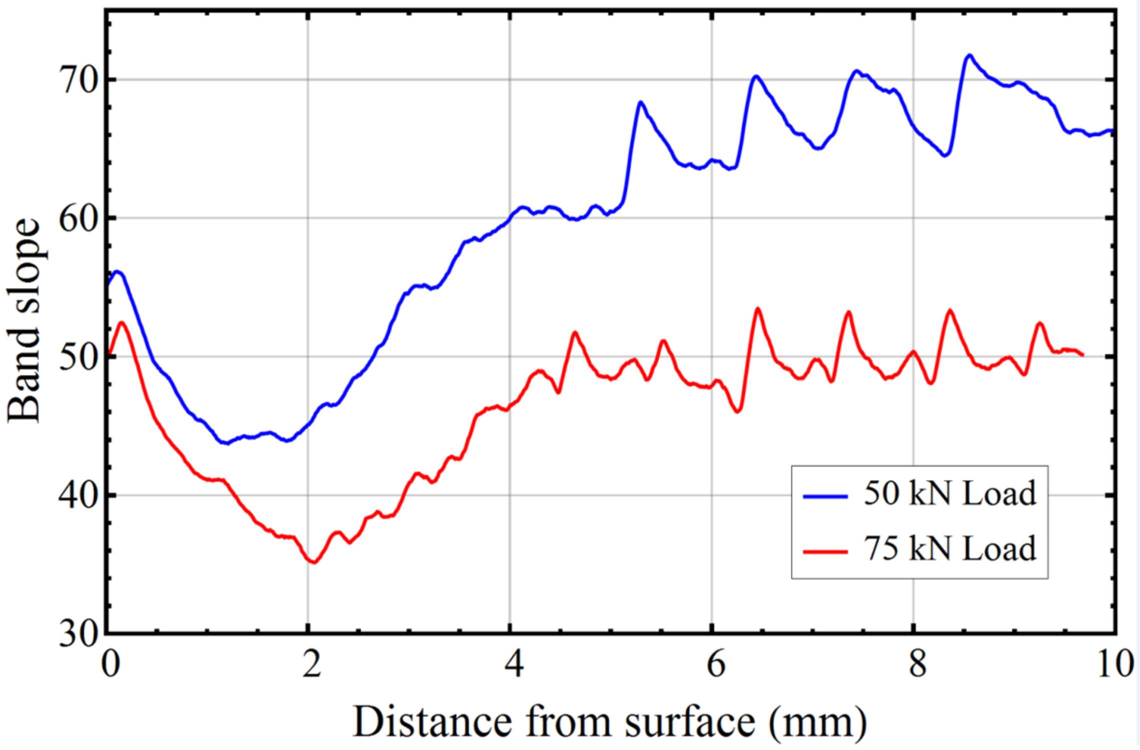

Figure 4. EBSD pattern quality, measured by the relative band slope, for the two rolled walls plotted with vertical distance down their centre from their top surface.

The conclusion that the plastic strain generated by rolling each layer was low at the top surface, and greatest between 1.5 to 2.5 mm deep in each wall, can be attributed to the constraint imposed by the profiled roller. This interpretation can be further corroborated by using the BOR misorientation mapping technique, the results of which are depicted in Figure 5. As well as confirming that the maximum strain was concentrated at a specific depth below the top of each rolled wall, the map in Figure 5 also demonstrates that the strain developed by the grooved roller was not evenly distributed across a walls width, being focused in its centre with respect to the wall's width.

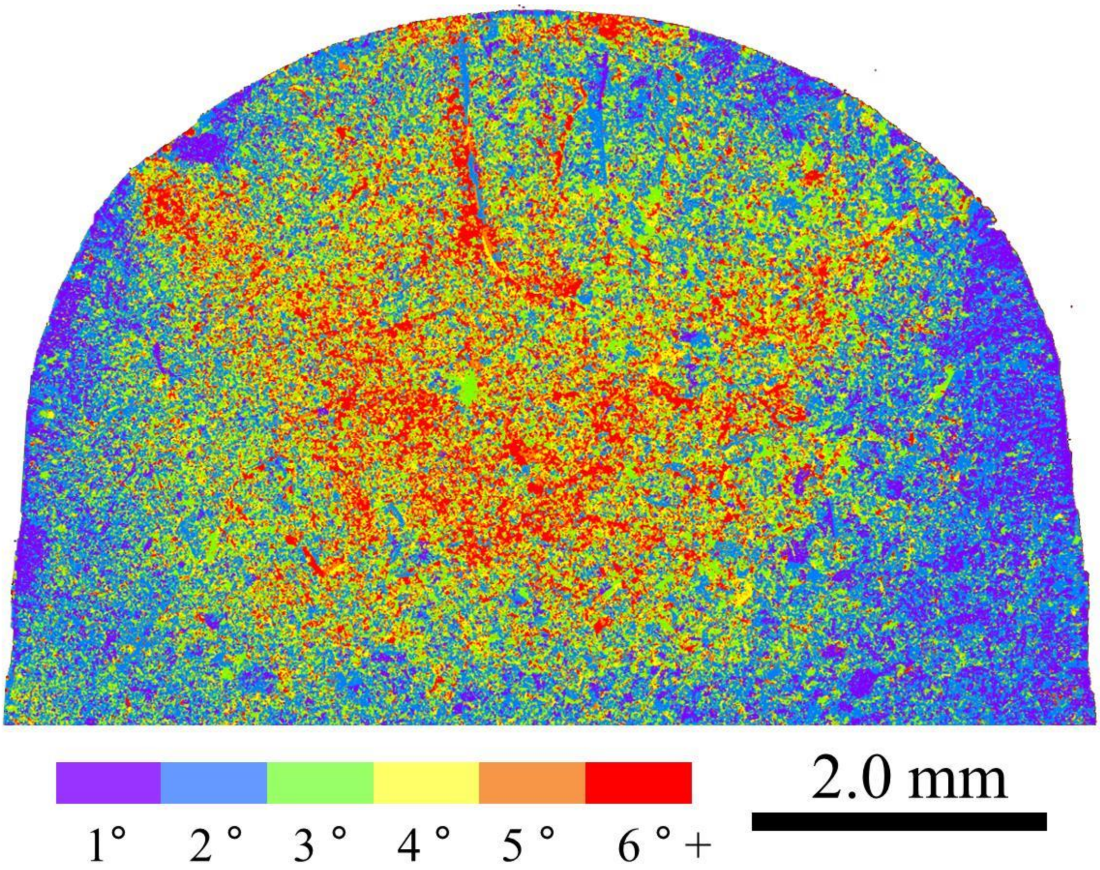

Figure 5. The strain distribution seen in the top section of the 75 kN rolled wall, inferred by plotting the deviation of neighbouring α laths from fulfilling the ideal Burger's orientation relationship.

### *3.3 Effect of rolling on refinement of the primary β-grain structure*

Figure 6 compares EBSD orientation maps of both the α-phase and reconstructed parent β grain structures seen in the un-rolled control and rolled WAAM walls. The maps depicted are x-z centre plane cross-sections taken from the top of each wall to a depth of ~ 10 mm (equivalent to about the last 8 layers). In the α phase EBSD maps (Figures 6a - c) a memory of the parent β grain structure is evident from the texture clustering seen in the α variants, which is particularly obvious in the un-rolled control sample. However, following reconstruction it becomes very apparent that a coarse columnar β grain structure with a strong texture developed in the un-rolled wall before its transformation to α (Figure 6d). The red colouring that dominates the β phase in this IPF map indicates that the columnar grains have strong preferential alignment with a mutual <001> fibre [13–16]. In the undeformed wall it can also be seen that the columnar β grains have a width of approximately 2 mm and their lengths' can be measured in centimetres.

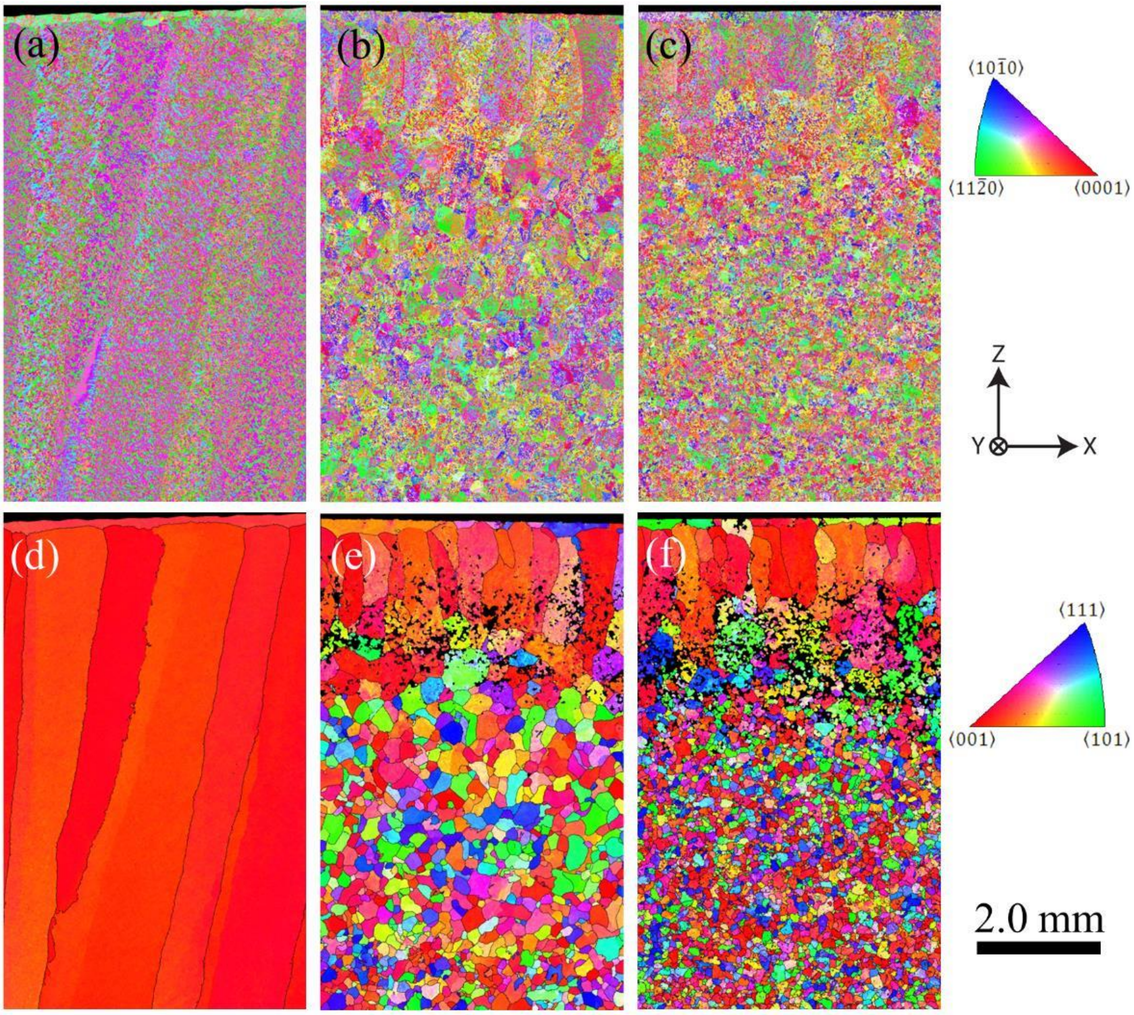

Figure 6. Measured α-phase (a-c) and reconstructed β-parent phase (d-f) IPF orientation coloured EBSD maps from the undeformed control and rolled WAAM walls, produced with rolling loads of 50 and 75 kN, obtained from mid plane, x-z, wall sections.

In contrast, when the rolling step was applied to each deposited layer, a much more refined equiaxed β-grain structure was observed, as well as a weaker texture (Figures 6e & f). Greater grain refinement was also seen in the wall that had received a higher rolling load. In Figures 6(e) & (f) it is further apparent from the grain structure that is formed in the last layer, how quickly a columnar structure is re-established when it has not been refined by rolling and re-heating. Finally, a band can be seen in Figures 6(e) and (f) between a depth of 1 to 4 mm's below the rolled walls top surface's where there are unindexed points in the maps. These missing points result from data being discounted during β reconstruction because it had too great a deviation from the BOR and the depth of this band coincides with the strain distribution generated by rolling the last layer, as described above (Figures 4 and 5).

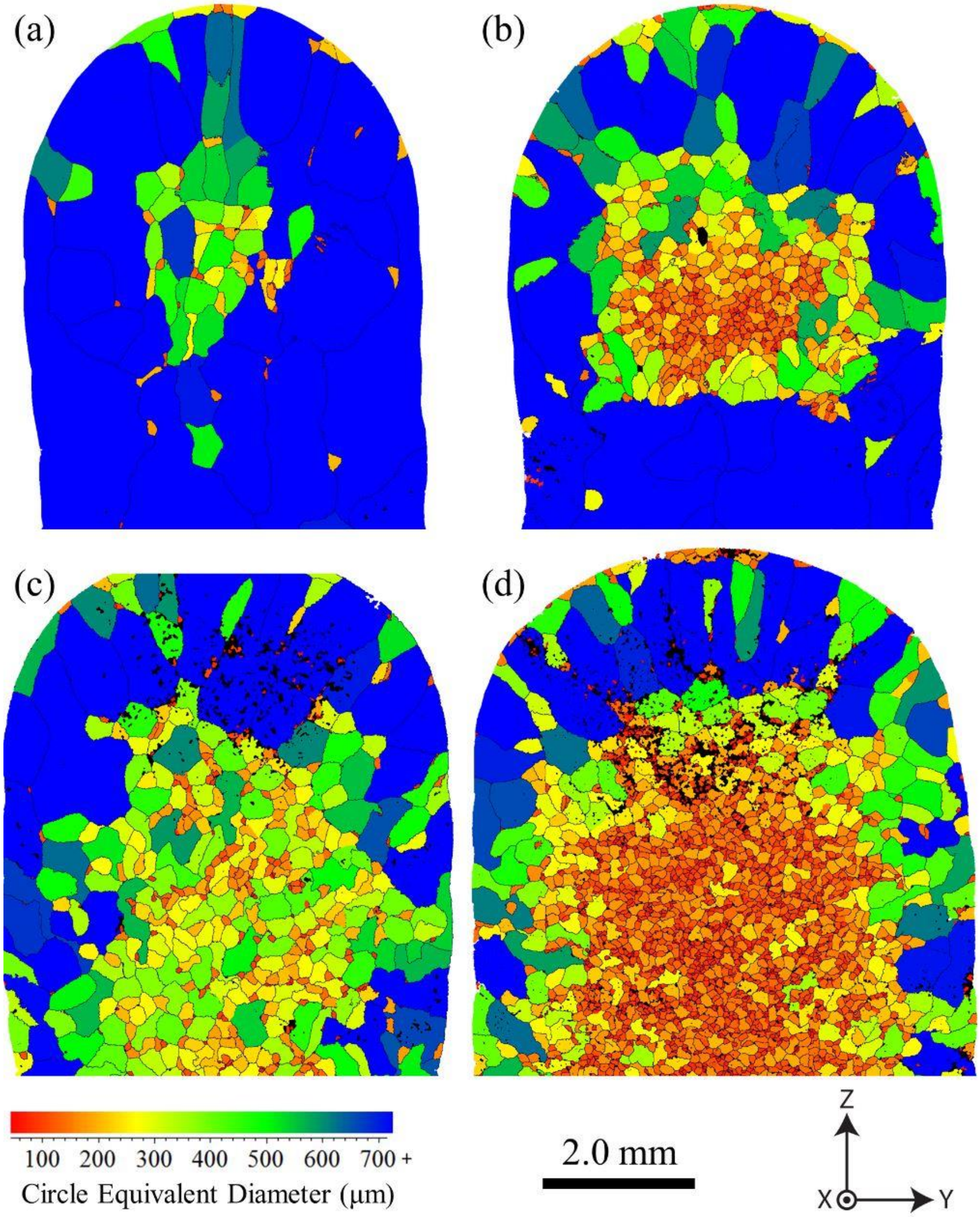

Figure 7. EBSD reconstructed β grain size maps from transverse, y-z, cross-sections near the top of rolled WAAM walls; (a) and (b) with only one rolling pass applied to the penultimate layer and (c) and (d) with a rolling pass applied to every layer, both with rolling loads of 50 kN and 75 kN respectively.

Figure 7 shows EBSD maps from y–z transverse wall cross-sections that have been coloured to highlight the size distribution of the refined β grains. In (a) and (b) rolling was only applied to the penultimate layer, and in (c) and (d), as before, every layer was rolled. The images in Figure 7 (c) and (d), therefore, correspond to the transverse sections from the walls previously described in Figure 6. The grain sizes given are the equivalent circular diameter of the reconstructed β-grains. From Figures 7(a) and (b) it is evident that when a rolling pass was only applied to the penultimate layer, and it was re-heated during depositing the next and final layer, refinement of the β grain structure predominantly occurred below the top surface within a core region in each wall. This region of β refinement can be seen to increase with rolling load and shows good qualitative agreement with the plastic strain distribution inferred from Figure 6.

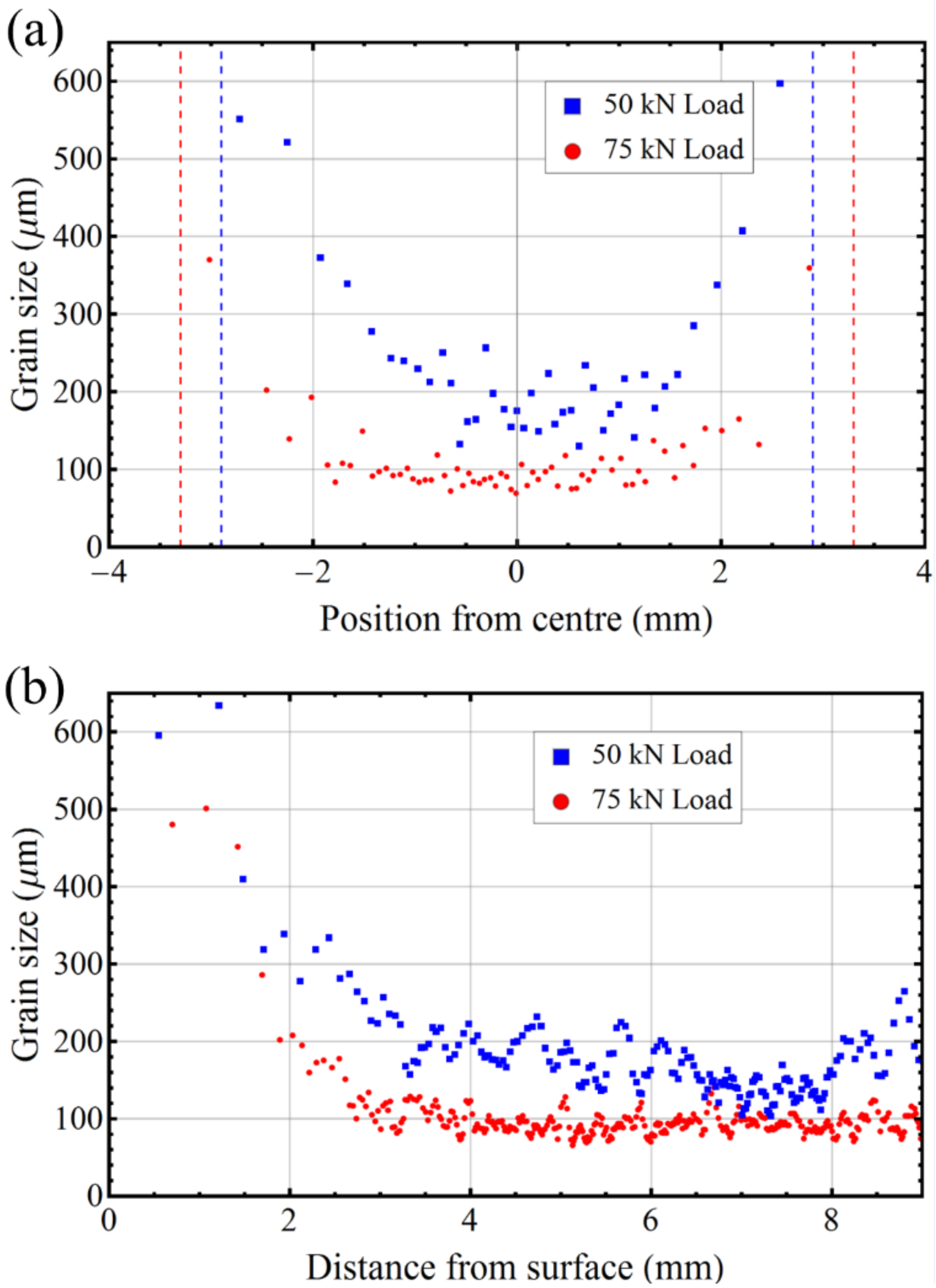

Figure 8. The average β grain size variation seen in walls produced when every layer was rolled after deposition, with a 50 or 75 kN applied load; (a) across the walls over 5 layers below the final white band and (b) as a function of depth down their centre lines. In (a) the dashed lines indicate the outside surfaces of each wall.

When rolling was applied to every added layer (Figures 7c & d) the width of the refined core region increased, relative to the samples where only the penultimate layer was rolled (Figures 7a & b), and extended all the way down each wall. The average grain sizes measured below the top layer across these walls are given in Figure 8(a). With both rolling loads, the grain size can be seen to increase towards each wall's outer surfaces and there is a central plateaus region where the average grain size is refined to a minimum level, which reduces with increasing applied load. In the core region at the centre of the walls the β grain size was reduced to around 140 and 90 μm with rolling loads of 50 and 75 kN, respectively. In addition, with the higher 75 kN load the grain size in the wall core was more uniform and the core region was proportionally wider compared to the wall thickness.

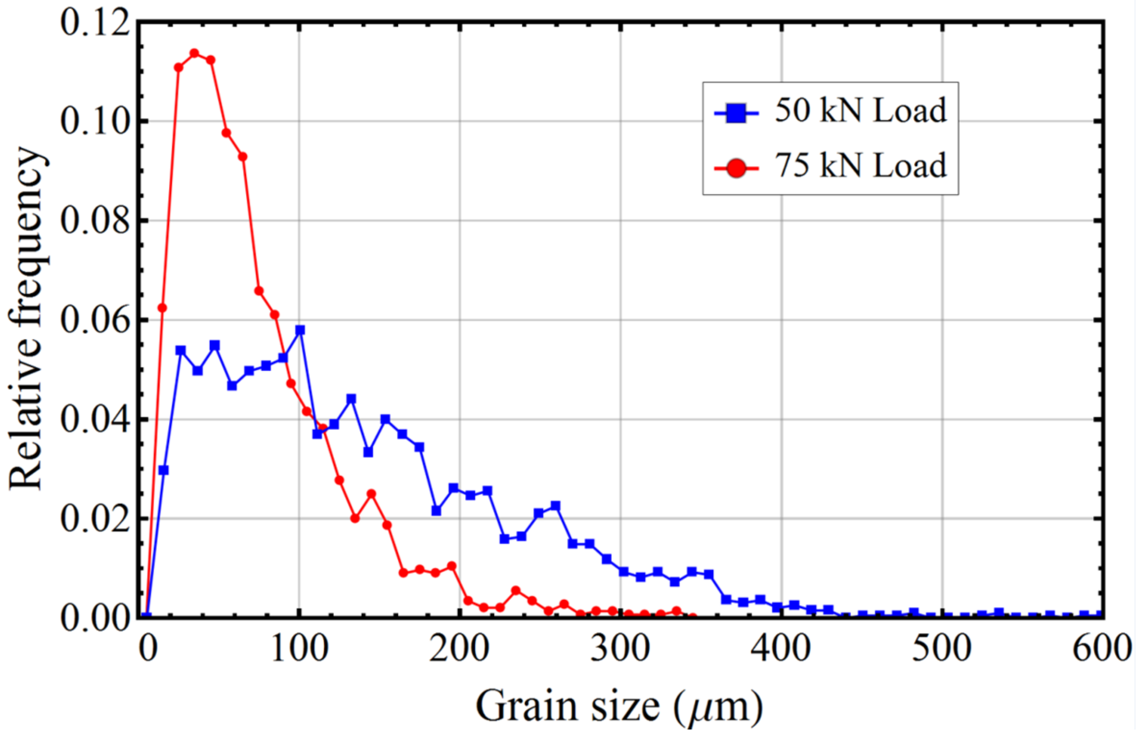

Figure 9. Comparison of the β grain size distributions measured from reconstructed EBSD maps obtained at the centre of the walls rolled with a load of 50kN and 75kN.

An equivalent plot depicting the variation in grain size with vertical position down the centreline of the rolled wall samples is given in Figure 8(b). The grain size data for both rolling loads shows an increase in average diameter at the top of each wall, which corresponds to the re-establishment of a columnar β structure in the final layer to solidify (Figures 6e & f). Below this transition region, rolling each layer refined the grain size to a relatively uniform minimum level with the larger 75 kN rolling load, but when the 50 kN downforce was used there was far more variability. A histogram of the grain sizes in the fully refined core region of this cross-section is given in Figure 9. It should be noted that grain sizes below the reliable measurement limit for the set up used have been excluded (25μm) from the EBSD data. However, the average grain sizes were found to be 130 μm and 94 μm for the 50 kN and 75 kN rolling loads respectively, which corresponds well with measurements made by the line intercept method on optically acquired micrographs in a previous study [30]. In it is also evident from Figure 9 that the β grain size distribution from the refined core regions of the rolled walls was more tightly distributed around the smaller mean value when the larger rolling load was used. For example, with a 50 kN down force the largest grain measured 590 µm) was almost twice the size of the that observed in the 75 kN sample (350 µm).

## *3.4 Effect of rolling on texture in the WAAM process*

Strong crystallographic textures can cause anisotropy in a material's mechanical properties and this can be particularly pronounced in titanium alloys that have hcp crystal structures [18,40,41]. In the un-deformed AM wall the reconstructed EBSD map in Figure 6(d) clearly indicates the presence of a strong β-texture. However, textural changes can also arise from deformation, or its influence on any recrystallization or phase transformation that may occur during subsequent heat treatment [40,41]. It is thus important to compare the texture seen in a un-deformed build with that found when a rolling step was utilised with the WAAM process to refine their coarse primary β grain structures.

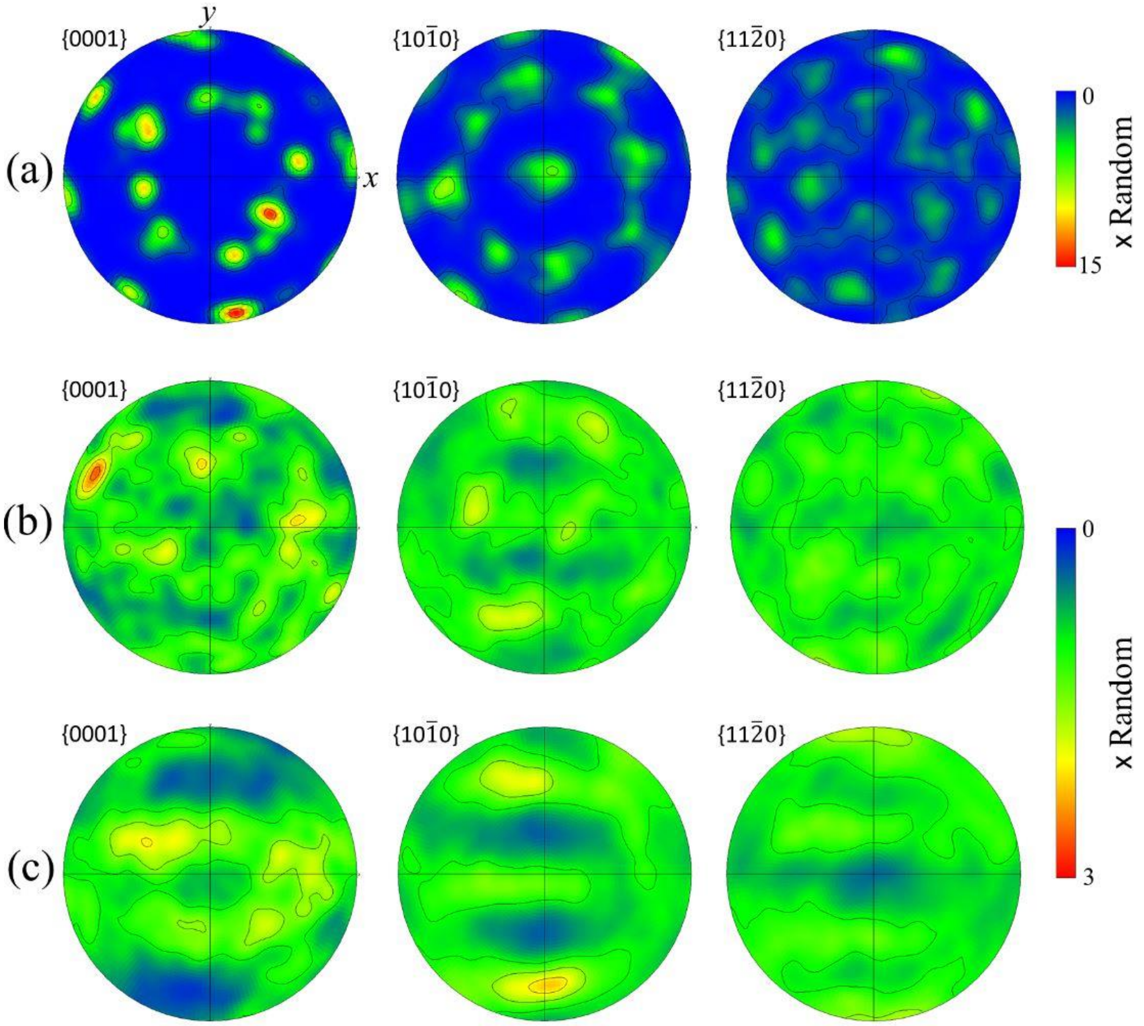

Figure 10. Pole figures obtained from large area EBSD maps depicting α textures measured from the centre of; (a) the un-rolled wall, (b) the wall rolled with a 50 kN load, and (c) the wall rolled with a 75 kN load.

Pole figures obtained from the large area EBSD maps depicting the α-textures and the reconstructed parent β-textures that existed prior to transformation, on cooling down below the β-transus temperature, are provided in Figures 10 and 11. The EBSD maps were taken from the centre, x-z, plane of each wall, and for the rolled walls therefore mainly represent orientations from their more refined core region (Figure 7). The pole figures are orientated with the build direction and compression axis (z) near to normal to the plane of projection and the torch travel direction (x) is aligned vertically. Before presenting these results it should be noted that the sampling statistics for the solidification texture in the un-deformed wall were poor, owing to the large prior-β grain size (only 10 grains were covered in the map area), whereas the statistics for the textures in the rolled samples were more representative because of their more refined grain structure.

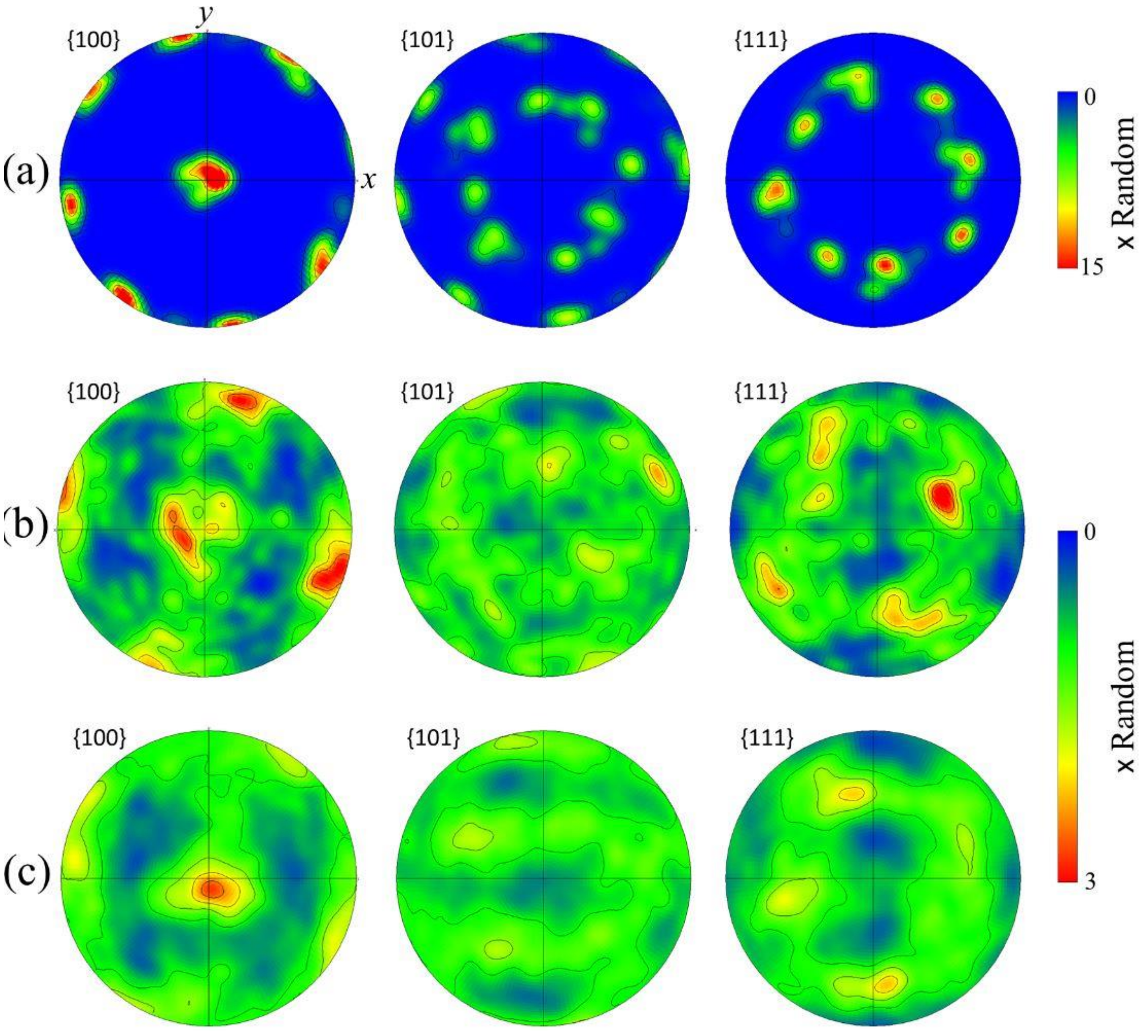

Figure 11. Pole figures obtained from large area EBSD maps depicting the parent phase β textures reconstructed from the centre of; (a) the un-rolled wall, (b) the wall rolled with a 50 kN load, and (c) the wall rolled with a 75 kN load.

Of the α textures, shown in Figure 10, the texture of the un-deformed as-deposited wall is difficult to describe at first sight because of the poor β parent grain sampling statistics. However, it becomes much clearer when β phase reconstruction is performed. From the 100 β phase pole figure in Figure 11a it can be seen that the α phase transformed from β parent grains that had a common <001> direction aligned close to the build direction. The corresponding α-texture seen in Figure 10a is, therefore, an <001> β transformation texture that is poorly defined, partly because of the poor statistics for the parent β grain orientations, but also because it has become weakened by the twelve possible α variant orientations available through the Burgers relationship [42–44].

In comparison to the strong texture seen in the control sample, much weaker α and β textures were found in the rolled walls (Figures. 10 b & c; Figure 11 b & c), which had maximum intensities of less than approximately 3 and 4 times random for the α and β phases, respectively. In both of the rolled walls it was found that the strongest orientations present in their reconstructed β pole figures were consistent with the textures containing residual weakened cube components. As can be seen from Figure 11(b) and (c) both the rolled wall's 100 pole figures have one <001> pole aligned close to the build direction, z, with the other related <001> poles rotated by different amounts about z relative to the deposition direction (e.g. ~10 and 20° in the 50 kN and 75 kN examples shown). These residual <001> fibre orientations were weaker in the wall rolled with a greater down force; the maximum intensity dropping from 3.5 times random for the 50kN rolling load to 2.8 for the 75kN load and this led to a corresponding drop in the strength inherited in the α transformation textures, on applying rolling to each layer, from 2.7 to 2.2 times random.

## 4. Discussion

With titanium alloys, coarse-directional grain structures are of concern in the industrial application of AM processes because of their potential to cause anisotropic properties in aerospace components [13,16,23]. The above results show that the introduction of a rolling deformation stage sequentially within the WAAM build cycle could be a useful technique for refining such undesirable grain structures, as well as for reducing the intensity of the strong textures normally seen in the as-deposited material. Interestingly, the strain required to achieve a high level of β refinement has been found to be relatively low, which makes it practical to apply such a technology when producing components with relatively simple geometries. However, other methods for introducing plastic deformation in AM are also being investigated, such as peening [28], which offers higher compatibility with more complex component designs.

### *4.1 Grain structure development in the conventional WAAM material*

By reconstruction of the parent β phase that forms on solidification, it has been confirmed that in the conventional WAAM process a very coarse primary columnar grain structure is developed as material is built up, by sequentially adding many new layers. This columnar grain structure has a strong preferential <001> β texture. It has been previously noted that the main reason such a coarse grain structure develops is because the high thermal gradient in the melt pool and the alloy chemistry do not allow sufficient constitutional supercooling for nucleation to be possible ahead of the solidification front [17]. Similar to welding, in AM when a layer is added the temperature rapidly increases below the fusion boundary and the material high in the heat affected zone will fully transform back to the β phase, whereupon grain coarsening will occur where the peak temperature reached is significantly above the β transus [11] (Fig. 6d). When solidification of the single β phase subsequently takes place at the rear of the moving melt pool, because nucleation ahead of the growth front is not possible, the coarsened β-grains at the fusion boundary then act as a substrate for epitaxial re-growth back into the liquid following the maximum thermal gradient, which is normal to the solidification front. A columnar structure is thus developed as grains grow following the rear melt pool surface [45].

This process repeats as more layers are added, with the retained β in the transformation microstructure re-growing, each time when it is re-heated in each new cycle to re-create β grains with the same orientation they had in the previous pass. When re-heated above the β transus, the reformed β grains can also potentially coarsen each cycle, before providing the substrate for epitaxial re-growth at each new fusion boundary. Hence, in AM without deformation the same grain orientations re-grow over many layers as each new layer is added. As the β-grains develop, grain growth thus occurs both in the solid state and during solidification where orientations are progressively selected that have a preferred <001> crystallographic direction parallel to the maximum thermal gradient at the solidification front [45], leading to the strong <001> texture seen in the final wall [13–16] (Figs. 5d, 11a). One of the reasons a deformation step is so effective in causing β grain refinement and a weaker texture in AM is thus because it has the potential to disrupt the accumulative ‘ratcheting’ effect of this repeated cyclic behaviour that is inherent in an additive ‘layer’ manufacturing process.

### *4.2 Grain refinement in the rolled WAAM deposits*

In the samples studied, the rolling loads employed led to relatively modest average compressive plastic strains of 8 and 19%. Nevertheless, when each deposited layer was sequentially rolled during the AM process, the original coarse columnar grain structure was found to become greatly refined, giving rise to an equiaxed β-grain structure with an average diameter of less than 100 µm in the core of the wall produced with the 75 kN rolling load. Although the refined β grain size increased towards the surface of the walls, this overall reduction in grain size still compares very favourably to the centimetre-scale columnar grains seen in standard un-deformed samples (Figure 2). In addition, both the parent β and α phase texture strengths was substantially weakened in the rolled samples.

In the samples studied, the refined β grains were formed at temperatures well above the β transus temperature. This is obvious from comparison of Fig. 2 with the refined region in Fig.

7b. In Fig. 2 the top white bands lies just below the β tranus temperature (as has been widely acknowledged [6] and this is at a depth of over 8 mm's below the top surface which is well below the depth where β refinement occurs in Fig. 7b. In addition in a single phase material refinement would not be expected through conventional recrystallization as the driving force is usually insufficient at such low strain levels of below 20% [46]. It can therefore be concluded that the grain refinement seen at these low applied strains is caused by the growth of new β orientations associated with the influence of deformation on the $\alpha \rightarrow \beta$ phase transformation, which occurs during re-heating above the β transus temperature, when the next layer is deposited. This implies rolling creates new β orientations, other than those retained from the parent β grains in the original transformation structure formed during cooling each solidified layer. These orientations can then act as new nuclei that grow on re-heating each layer above the β transus temperature when the next layer is added. This prevents the original β grains simply re-growing the orientations of the substrate during epitaxial solidification of the next layer deposited, which leads to the coarse columnar structures normally seen in undeformed WAAM walls, by the 'ratcheting process' discussed above.

Because the strain applied to each deposited layer was relatively low, the origin of the new β orientations is most probably related to heterogeneities that develop within the deformation of the fine Widmanstätten transformation microstructure found in AM titanium parts. One possible mechanism, already discussed by the current authors in Ref [47], has been observed directly using in-situ heating experiments and involves new β orientations originating from deformation twinning of α laths within the deformed region below the top of a rolled wall. Further related mechanisms, by which new β orientations can be generated by the application of relatively low levels of plastic deformation in AM, also associated with deformation twinning, and from strain concentration at colony boundaries, are still under investigation and will be the subject of a future publication.

EBSD strain mapping has shown that the core wall region where β grain refinement was found to be closely related to the local strain distribution generated in each rolling pass (Figure 5). This is strongly influenced by the shape of the roller which was profiled to match the curvature of the top layer bead profile. With a grooved roller, the top of the wall is highly constrained and cannot spread sideways, which causes a 'dead-zone' near the roll surface and forces the plastic deformation to be concentrated at a greater depth within the wall core. Although this strain distribution was not pre-planned, it is beneficial when trying to combine deformation with AM techniques like the WAAM process that features a large re-melt depth (~1.5 mm) as it means that the majority of useful deformation is not lost by the deformed material being re-melted by the subsequent pass. Other techniques, such as peening, tend to concentrate plastic deformation closer to a surface [48] and would therefore be less suitable for refining the grain structure unless they are combined with an AM technique that has a low re-melt depth [28].

A negative effect of the grooved roller is that the strain introduced is lower near the wall faces, which leads to a more refined core with coarser grains towards each wall edge. However, when rolling was applied to every added layer (Figures. 7c & d) the width of the refined core region was found to increase and the grain size in the less refined skin was still much smaller than in the undeformed wall. The fact that rolling each layer was more effective than rolling a single layer, is discussed further below and can be explained partly by the fact that repeatedly rolling each layer does not allow a coarse β structure to develop, prior to the application of an individual rolling pass, and partly because deformation occurs to a sufficient depth that there is some overlap with the previous layer, which will therefore be deformed and re-heated above the β transus more than once when rolling is applied in every pass.

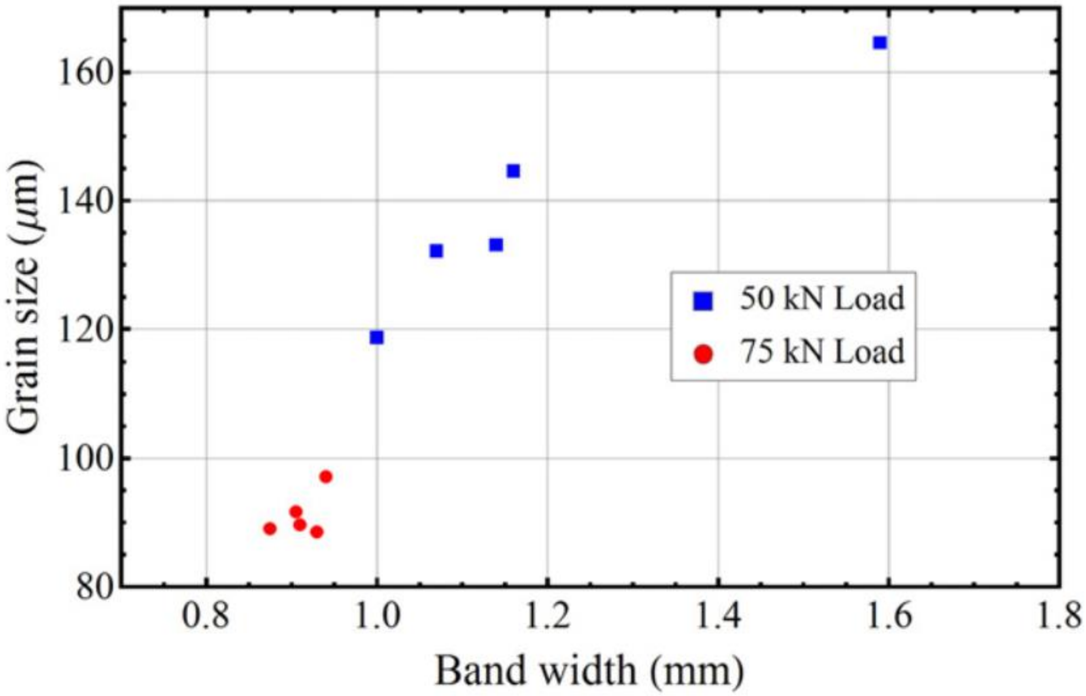

Figure 12. Average grain size plotted against layer height for the two rolling loads.

Apart from in the last added layer, which is not re-heated following deformation, it was found that there was very little variation in grain size with build height for the wall deformed with a 75 kN rolling load every pass. However, more variation was observed in the 50 kN wall (Figure. 8b). The cause of this variation can be related to the lower depth of deformation and greater inconsistency in the deposition conditions that led to more irregularity in the layer height with this sample, as can be observed from the greater unevenness in the vertical spacing of the white bands seen in the 50 kN wall as opposed to the 75 kN sample (Fig. 2). Furthermore, in Figure 12 it can be noted that there is a clear correlation between the white band layer-thickness and the average refined grain size. It is apparent that a lower rolling load is likely to exaggerate such variability, because there is a lower penetration depth of the plastic strain in each layer; i.e. where there is a narrower, or wider, layer separation this will lead to a finer, or coarser, β grain size because of the greater variation in strain overlap between deformation passes with a lower rolling load.

### *Texture development*

The observation of a strong <100> β fibre texture in the un-rolled walls has been discussed above (§4.1) and is consistent with studies performed with other AM techniques [11,14]. In the 100 pole figure in Figure 11(a) the main fibre axis can be seen to have an intensity of 15 times random, although this value should be treated with cautions as, despite the large area mapped (12 by 6 mm), the prior β grain size was so large that sufficient data could not be obtained to develop a full texture description (Figures 10a and 11a). Owing to the poor sampling statistics, an attempt has therefore not been made to evaluate the possibility of variant selection affecting the α-texture. However, it is interesting that in a recent paper Sargent et al. [31] have claimed that transformation strains can cause variant selection within similarly coarse grains found in Ti-6Al-4V castings. Encouragingly, the application of a deformation step to each layer greatly weakened the β parent textures, to 3.5 and 2.8 times random with the 50 kN and 75kN rolling loads, respectively. On transformation this was further diluted leading to extremely weak α textures being seen in the rolled samples of 2.7 and 2.2 times random. Although the maximum intensities were greatly reduced, both of the rolled walls still retained a memory of the original β phase <001> fibre texture that tended to be present as a weaker rotated cube orientations. Overall this suggests that the presence of these components is caused by insufficient sampling statistics, which resulted in a tendency for orientations related to one dominant 'harder' parent β grain, that was more resistant to refinement, to be retained from the original <001> fibre within each EBSD map area.

Finally, the synergistic advantages of applying a rolling step to each layer after it is deposited are highlighted in Figure 13, which compares the grain size and texture strength down the centre of the wall rolled with the higher load, from its top surface, with an enlarged EBSD map of the same region. In the last layer to be added it can be seen that there is a rapid increase in the β grain size and texture strength towards the top surface of the deposit. It can be noted that this is partly caused by β grain growth in the HAZ below the melt pool, and then is further enhanced by <001> growth selection during the development of a columnar structure by directional solidification. However, in this single layer the grain size reached and texture strength are nowhere near as high as that developed in the undeformed wall, where the grain size and intensity of the <001> fibre progressively increase through the 'ratcheting' of these two effects during the addition of further layers as a wall is built. This is because when each layer is sequentially rolled the development of a columnar grain structure and strong fibre texture is disrupted after every layer is deposited, and does not have the same opportunity to develop during multiple repeated cycles.

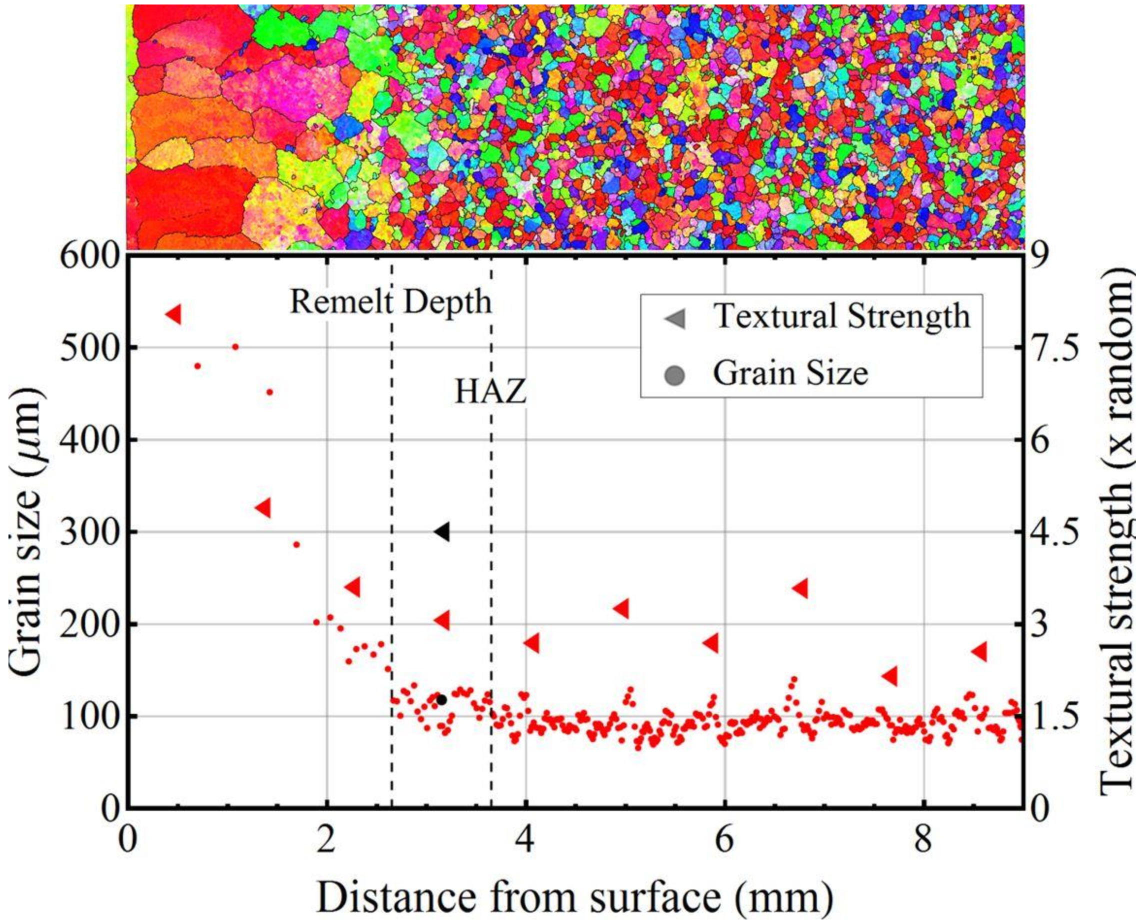

Figure 13. Plot of β textural strength (given by the maximum intensity in the 100 pole figure) and grain size variation with height down the centre line, for the wall rolled with a load of 75 kN applied to every added layer. Also indicated in blue are the values for the corresponding region in the sample produced with only one 75 kN rolling pass applied to the penultimate layer. The magnified insert is of the β grain structure in top 9 layers of the wall.

Of additional significance to the synergistic benefit of rolling every layer is that each layer will have a finer grain size and weaker texture before it is rolled than in an unrolled wall, where the columnar structure is much more developed. The single data points shown in Figure 13, taken from the rolled refined region of the sample where rolling was applied only to the penultimate layer, of an otherwise undeformed wall (figure 7b), demonstrate that, in this case the level of grain refinement in the deformed core region is similar, but the resultant texture is much stronger (4.5 as opposed to 2.7 times random) than when the starting microstructure has been previously refined; i.e. when a single rolling pass was applied to a coarse grained undeformed columnar structure, following re-heating by adding the next layer, the grain size refinement was approximately the same as when you start with a refined grain structure, but the reduction in texture strength was still far less. This is because when you start with a stronger texture, that has been able to develop over many layers of β grain growth in an unrolled wall, it will require a larger rolling strain to reduce it to the same level.

Therefore, the addition of a rolling pass to every layer leads to a weak texture in the wall by both preventing the formation of a strongly textured columnar grain structure, which requires many layers of undisturbed growth to develop, and by this, in turn, ensuring a far weaker texture in the next layer before it is deformed. The combination of these two effects thus greatly decreases the rolling strain required to reduce the texture strength in a WAAM component.

From the β pole figures in Figure 11, it is possible to convince oneself that as the rolling load is increased, that a traditional bcc rolling texture is beginning to develop. This is ostensible from the apparent development of symmetry around the deformation axes, especially in the {101} and {111} pole figures of 75kN compared to 50kN in Figure 11 a & b respectively. As can be seen in the $\varphi_2$=45° ODF slice in Figure 14a when compared to the schematic slice in Figure 14b, there is little evidence of the α-fibre or γ-fibre rolling components that are often observed when rolling bcc metals such as steels [49]. The rotated cube component highlighted in the {100} pole figure in Figure 11 is clearly shown in the ODF slice, as is a contribution from the {011}<011> orientation, which may explain the perceived symmetry in the {101} pole figure. There is no obvious explanation for the origin of this orientation, but it should be stressed that these textures are extremely weak.

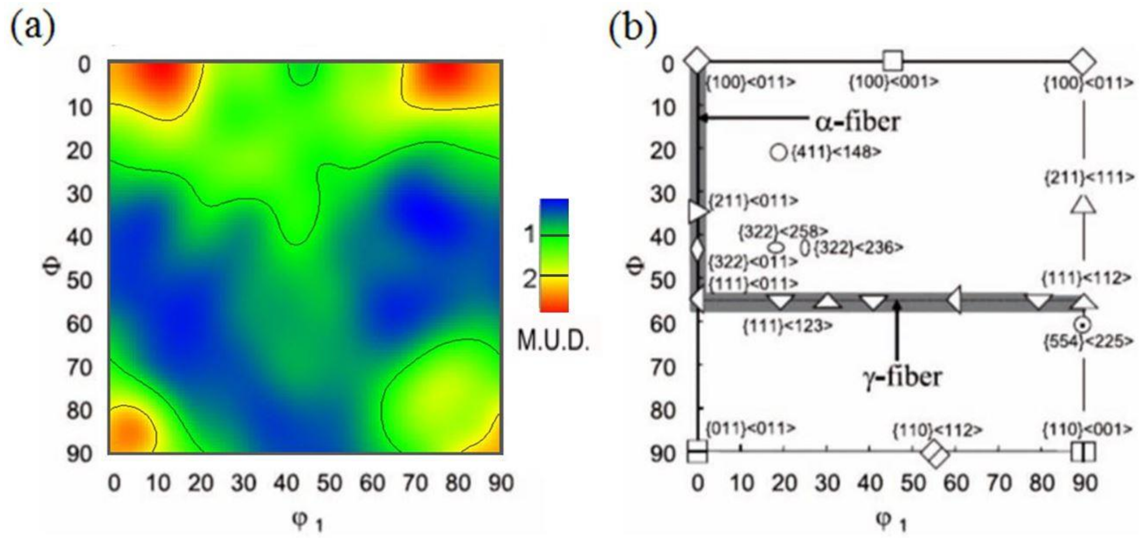

Figure 14. $\varphi_2$=45° ODF slice of the refined prior β grains of the WAAM wall deformed between every layer with a 75kN rolling load (a), accompanied by a schematic slice indicating key orientations and deformation components for bcc metals. (b) adapted from [49].

## 5. Conclusions

The efficacy of a deformation step, on refining the primary β grain structure and texture developed in a Ti-6Al-4V alloy, has been investigated during Wire Arc-Additive Manufacture (WAAM). By reconstruction of the β parent phase, from α phase EBSD maps, it has been confirmed that in the conventional WAAM process the deposited material develops centimetre-scale, coarse-columnar, β grains that grow through the build height with an associated strong <001> β fibre texture. This coarse grain structure results from the retained β in the transformation structure re-growing with the same orientations when heated above the β transus, with the next new layer added. Once reformed, the β grains coarsen and act as a substrate for epitaxial columnar growth during solidification of the new layer.

The application of a rolling step sequentially to each added layer was surprisingly effective, in terms of the low level of strain required, to both refine the β grain size and weaken the primary β and final α textures, which were reduced to close to random by the application of a only modest 8-20% rolling reduction. However, the homogeneity of the refined β grains was found to improve with increased levels of deformation. A profiled roller has also been shown to be advantageous for increasing the depth of deformation in each layer - thus helping the deformed region to survive re-melting in the next addition cycle.

It is postulated that the deformation step causes β grain refinement through promoting twinning, which generates new β orientations that then grow during the α → β transformation as each layer is re-heated by the subsequent deposition pass.

There are synergistic advantages of rolling each layer because this disrupts the establishment of the coarse columnar grain structure that only normally develops over many undisturbed repeated addition cycles. Rolling each layer also ensures that the β grain structure is refined and the texture weaker in each new added layer, before it is deformed, and this decreases the deformation required to obtained a weaker texture.

## Acknowledgements

The authors would like to thank Prof. Brad Wynne (University of Sheffield) for provision of the β reconstruction software. J. Donoghue is grateful for financial support provided by LATEST2 (EP/G022402/1) and Airbus, UK.

## References

[1] I. Gibson, D.W. Rosen, B. Stucker, Additive Manufacturing Technologies, Springer US, Boston, MA, 2010.

[2] J. Kruth, M. Leu, T. Nakagawa, Progress in additive manufacturing and rapid prototyping. CIRP Ann. Technol. 1998; 47: 525–540.

[3] P. Kobryn, N. Ontko, L. Perkins, J. Tiley, Additive manufacturing of aerospace alloys for aircraft structures. 2006; 2–12.

[4] E.O. Ezugwu, Z.M. Wang, Titanium alloys and their machinability - a review. J. Mater. Process. Technol. 1997; 68: 262–274.

[5] X. Wu, J. Liang, J. Mei, C. Mitchell, P.S. Goodwin, W. Voice, Microstructures of laser-deposited Ti–6Al–4V. Mater. Des. 2004; 25: 137–144.

[6] S.M. Kelly, S.L. Kampe, Microstructural Evolution in Laser-Deposited Multilayer Ti-6Al-4V Builds : Part I . Microstructural Characterization. 2004; 35: 1861–1867.

[7] S. Kelly, S. Kampe, Microstructural evolution in laser-deposited multilayer Ti-6Al-4V builds: Part II. Thermal modeling. Metall. Mater. Trans. A. 2004; 35: 1869–1879.

[8] F. Wang, J. Mei, X. Wu, Microstructure study of direct laser fabricated Ti alloys using powder and wire. Appl. Surf. Sci. 2006; 253: 1424–1430.

[9] F. Martina, J. Mehnen, S.W. Williams, P. Colegrove, F. Wang, Investigation of the benefits of plasma deposition for the additive layer manufacture of Ti–6Al–4V. J. Mater. Process. Technol. 2012; 212: 1377–1386.

[10] F. Wang, S. Williams, M. Rush, Morphology investigation on direct current pulsed gas tungsten arc welded additive layer manufactured Ti6Al4V alloy. Int. J. Adv. Manuf. Technol. 2011; 57: 597–603.

[11] F. Wang, S. Williams, P. Colegrove, A. a. Antonysamy, Microstructure and Mechanical Properties of Wire and Arc Additive Manufactured Ti-6Al-4V. Metall. Mater. Trans. A. 2012; 44: 968–977.

[12] E. Brandl, A. Schoberth, C. Leyens, Morphology, microstructure, and hardness of titanium (Ti-6Al-4V) blocks deposited by wire-feed additive layer manufacturing (ALM). Mater. Sci. Eng. A. 2012; 532: 295–307.

[13] A.A. Antonysamy, P.B. Prangnell, J. Meyer, Effect of Wall Thickness Transitions on Texture and Grain Structure in Additive Layer Manufacture (ALM) of Ti-6Al-4V. Mater. Sci. Forum. 2012; 706-709: 205–210.

[14] S.S. Al-Bermani, M.L. Blackmore, W. Zhang, I. Todd, The Origin of Microstructural Diversity, Texture, and Mechanical Properties in Electron Beam Melted Ti-6Al-4V. Metall. Mater. Trans. A. 2010; 41: 3422–3434.

[15] P. Kobryn, S. Semiatin, Microstructure and texture evolution during solidification processing of Ti–6Al–4V. J. Mater. Process. Technol. 2003; 135: 330–339.

[16] A.A. Antonysamy, Microstructure, texture and mechanical property evolution during additive manufacturing of Ti6Al4V alloy for aerospace applications, University of Manchester, 2012.

[17] M.J. Bermingham, S.D. McDonald, M.S. Dargusch, D.H. StJohn, Grain-refinement mechanisms in titanium alloys. J. Mater. Res. 2011; 23: 97–104.

[18] G. Lütjering, J.C. Williams, Titanium, Springer Berlin Heidelberg, Berlin, Heidelberg, 2007.

[19] I. Bantounas, D. Dye, T.C. Lindley, The role of microtexture on the faceted fracture morphology in Ti–6Al–4V subjected to high-cycle fatigue. Acta Mater. 2010; 58: 3908–3918.

[20] T. Vilaro, C. Colin, J.D. Bartout, As-Fabricated and Heat-Treated Microstructures of the Ti-6Al-4V Alloy Processed by Selective Laser Melting. Metall. Mater. Trans. A. 2011; 42: 3190–3199.

[21] H.K. Rafi, N. V. Karthik, H. Gong, T.L. Starr, B.E. Stucker, Microstructures and Mechanical Properties of Ti6Al4V Parts Fabricated by Selective Laser Melting and Electron Beam Melting. J. Mater. Eng. Perform. 2013; 22: 3872–3883.

[22] F. Martina, S.W. Williams, P. Colegrove, Improved microstructure and increased mechanical properties of additive manufacture produced Ti-6Al-4V by interpass cold rolling, in: SFF Symp., 2013: pp. 490–496.

[23] B.E. Carroll, T. a. Palmer, A.M. Beese, Anisotropic tensile behavior of Ti–6Al–4V components fabricated with directed energy deposition additive manufacturing. Acta Mater. 2015; 87: 309–320.

[24] X. Wu, R. Sharman, J. Mei, W. Voice, Microstructure and properties of a laser fabricated burn-resistant Ti alloy. Mater. Des. 2004; 25: 103–109.

[25] M.J. Bermingham, S.D. McDonald, K. Nogita, D.H. St. John, M.S. Dargusch, Effects of boron on microstructure in cast titanium alloys. Scr. Mater. 2008; 59: 538–541.

[26] B. Baufeld, O. van der Biest, Mechanical properties of Ti-6Al-4V specimens produced by shaped metal deposition. Sci. Technol. Adv. Mater. 2009; 10: 015008.

[27] P. Colegrove, H.E. Coules, J. Fairman, F. Martina, T. Kashoob, H. Mamash, et al., Microstructure and residual stress improvement in wire and arc additively manufactured parts through high-pressure rolling. J. Mater. Process. Technol. 2013; 213: 1782–1791.

[28] J. Donoghue, J. Sidhu, A. Wescott, P. Prangnell, Integration of Deformation Processing with Additive Manufacture of Ti-6Al- 4V Components for Improved β Grain Structure and Texture, in: 2015 TMS Annu. Meet. Exhib., Orlando, Florida, 2015.

[29] P. Colegrove, S. Williams, Added Layer Manufacture, GB2491472, 2012.

[30] F. Martina, P. a. Colegrove, S.W. Williams, J. Meyer, Microstructure of Interpass Rolled Wire + Arc Additive Manufacturing Ti-6Al-4V Components. Metall. Mater. Trans. A. 2015; 1.:

[31] G. A. Sargent, K.T. Kinsel, A. L. Pilchak, A. A. Salem, S.L. Semiatin, Variant Selection During Cooling after Beta Annealing of Ti-6Al-4V Ingot Material. Metall. Mater. Trans. A. 2012; 43: 3570–3585.

[32] P.S. Davies, An investigation of microstructure and texture evolution in the Near-α titanium alloy timetal 834, University of Sheffield, 2009.

[33] P.S. Davies, B.P. Wynne, W.M. Rainforth, M.J. Thomas, P.L. Threadgill, Development of Microstructure and Crystallographic Texture during Stationary Shoulder Friction Stir Welding of Ti-6Al-4V. Metall. Mater. Trans. A. 2011; 42: 2278–2289.

[34] M. Humbert, N. Gey, The calculation of a parent grain orientation from inherited variants for approximate (b.c.c.–h.c.p.) orientation relations. J. Appl. Crystallogr. 2002; 35: 401–405.

[35] N. Gey, M. Humbert, Specific analysis of EBSD data to study the texture inheritance due to the β→ α phase transformation. J. Mater. Sci. 2003; 8: 1289–1294.

[36] T. Maitland, S. Sitzman, Scanning Microscopy for Nanotechnology: Techniques and Applications, in: Springer Science & Business Media, 2007.

[37] J.-Y. Kang, S.-J. Park, M.-B. Moon, Phase Analysis on Dual-Phase Steel Using Band Slope of Electron Backscatter Diffraction Pattern. Microsc. Microanal. 2013; 19: 13–16.

[38] T.E. Buchheit, G.W. Wellman, C.C. Battaile, Investigating the limits of polycrystal plasticity modeling. Int. J. Plast. 2005; 21: 221–249.

[39] G. Deiter, Mechanical Metallurgy, 3rd ed., McGraw-Hill Science, New York, 1986.

[40] U.F. Kocks, C.N. Tomé, H.-R. Wenk, Texture and Anisotropy: Preferred Orientations in Polycrystals and their Effect on Materials Properties, Cambridge University Press, Cambridge, 2000.

[41] I. Dillamore, W. Roberts, Preferred orientation in wrought and annealed metals. Metall. Rev. 1965; 10.:

[42] I. Lonardelli, N. Gey, H.-R. Wenk, M. Humbert, S.C. Vogel, L. Lutterotti, In-situ observation of texture evolution during α→β and β→α phase transformations in titanium alloys investigated by neutron diffraction. Acta Mater. 2007; 55: 5718–5727.

[43] A.J.J. van Ginneken, W.G. Burgers, The habit plane of the zirconium transformation. Acta Crystallogr. 1952; 5: 548–549.

[44] G.C. Obasi, S. Birosca, J. Quinta da Fonseca, M. Preuss, Effect of β grain growth on variant selection and texture memory effect during α→β→α phase transformation in Ti–6 Al–4 V. Acta Mater. 2012; 60: 1048–1058.

[45] S. David, J. Vitek, Correlation between solidification parameters and weld microstructures. Int. Mater. Rev. 1989; 34.:

[46] K. Muszka, M. Lopez-Pedrosa, K. Raszka, M. Thomas, W.M. Rainforth, B.P. Wynne, The Impact of Strain Reversal on Microstructure Evolution and Orientation Relationships in Ti-6Al-4V with an Initial Alpha Colony Microstructure. Metall. Mater. Trans. A. 2014; 45: 5997–6007.

[47] J. Donoghue, A. Gholinia, J. Quinta da Fonseca, P.B. Prangnell, In-situ High Temperature EBSD Analysis of the Effect of aDeformation Step on the Alpha to Beta Transition in Additive Manufactured Ti-6Al-4V, in: TMS Titan., San Diago, 2015.

[48] R.K. Nalla, I. Altenberger, U. Noster, G.Y. Liu, B. Scholtes, R.O. Ritchie, On the influence of mechanical surface treatments-deep rolling and laser shock peening-on the fatigue behavior of Ti-6Al-4V at ambient and elevated temperatures. Mater. Sci. Eng. A. 2003; 355: 216–230.

[49] K.A. Annan, C.W. Siyasiya, W.E. Stumpf, Effect of hot rolling conditions on ridging in 16wt% Cr ferritic stainless steel sheet. J. South. African Inst. Min. Metall. 2013; 113: 91–96.

## 4.3. In-situ High Temperature EBSD analysis of the effect of a deformation Step on the Alpha to Beta Transition in Additive Manufactured Ti-6Al-4V

In an attempt to understand the origin of the new prior β grain structures characterised in **Manuscripts 1** and **2**, this manuscript details an in-situ heating experiment that was used to observe a deformed region of a Ti-6Al-4V AM microstructure by EBSD as it is heated to temperatures approaching the β transus. The heating experiment was carried out to observe where in the microstructure the new β orientations originated from, and if there was any associated orientation relationship, in order to better understand the refinement mechanism.

This paper was submitted on 15th May 2015 as conference proceedings for Titanium 2015, held in San Diego, California over the dates 16th-20th of August 2015, where the work was presented by the lead author. The paper underwent peer review and was published in a printed volume in April 2016, and was made available online on the 8th May 2016.

The contributions of the named authors were as follows:

**Jack Donoghue** – Lead author, all metallographic preparation, and EBSD data analysis. SEM analysis carried out in partnership with Ali Gholinia.
**Ali Gholinia** – Assistance with SEM Analysis.
**João Quinta da Fonseca & Philip Prangnell** – Supervisors of Jack Donoghue.

# In-situ High Temperature EBSD Analysis of the Effect of a Deformation Step on the Alpha to Beta Transition in Additive Manufactured Ti-6Al-4V

Jack Donoghue; Ali Gholinia; João Quinta da Fonseca; Philip Prangnell

Materials Science Centre, University of Manchester, Grosvenor St. Manchester M13 9PL, UK

Keywords: Additive Manufacture, Ti-6Al-4V, Alpha to Beta Phase Transformation, In-situ heating

## Abstract

Additive Manufacture (AM) of Ti-6Al-4V generally leads to an undesirable microstructure with a non-random texture. The alpha texture is inherited from large columnar β grains that grow across the deposited layers with a strong preferential <001> growth direction. It has been found in AM that the application of a surprisingly small amount of plastic strain to each layer, by methods such as in-process rolling, can disrupt the columnar growth and produce a more randomly orientated, fine equiaxed β grain structure, and consequently a refined final microstructure and far weaker alpha texture. The origin of this interesting effect was investigated by direct in-situ observation of the formation of new β grain orientations, within the retained deformed beta, and their growth on reheating near to the transus temperature, by EBSD analysis. This analysis has shown that α colonies twin during deformation, which generates new beta orientations during reheating.

# Introduction

The titanium alloy Ti-6Al-4V has long been favored by the aerospace industry, due to its high specific strength and excellent fatigue resistance [1]. The high cost of this material, combined with the inherent difficulty of machining, makes the fabrication of Ti-6Al-4V aerospace components a natural match with the emerging technologies of Additive Manufacture (AM), that are capable of producing near-net-shape parts [2–9]. However, it is widely acknowledged that AM processes produce very different microstructures and textures to those that are traditionally developed through thermo-mechanical processing (TMP) [10], and this can lead to a different property balance in AM components that needs to be better understood.

In AM with Ti alloys large primary columnar β grain structures, with a strong <001> fibre texture, are generally observed to form on solidification that extend over several layers of deposition [2,3,5]. On cooling to room temperature, the primary bcc β grains transform to a fine hcp α lamellar microstructure, the morphology of which is dependent on the cooling rate, with residual β retained in thin layers between the α laths [10]. Due to hcp crystal structures being inherently anisotropic [11], the mechanical properties of Ti-6Al-4V components are thus strongly dependent on the α texture developed in this process [12]. In AM textural weakening by the β → α phase transformation is significant, as the Burgers' orientation relationship ($\{110\}\beta \parallel \{0002\}\alpha$, $\langle 111\rangle\beta \parallel \langle 11\bar{2}0\rangle\alpha$, [13]) allows 12 possible variants to be formed from each β grain and strong variant selection is not generally observed [9]. However, due to the strong original β texture created on solidification, the inherited α texture can still be of sufficient strength to affect property anisotropy in AM parts [8].

The formation of large prior β grains in AM with Ti-6Al-4V is caused partly by the solidification conditions in the moving melt pool and partly by the metallurgy of the alloy itself. In each pass the heat source re-melts a portion of the previously deposited material, as well as reheating the substrate back above the β transus to a depth typically equivalent to that of 3-5 previously deposited layers [9]. In the α → β transformation of the underlying material, the β phase is thought to re-grow with the same orientation from the residual β retained within the transformation microstructure, consuming the surrounding α, and reforming the original prior-β grain structure. Solidification of the molten material then occurs homo-epitaxialy from the β grains at the fusion boundary, which grow following the receding melt pool surface. Nucleation of new grains ahead of the solidification front is prevented by the limited constitutional supercooling that is possible, due to the steep thermal gradients involved in the small melt pool and the high partition coefficients of Al and V in Ti [14], leading to the development of coarse column grain structures. In addition, because of the preferred <001> growth direction, the large columnar grains that develop tend to establish a strong preferential β <001> growth direction perpendicular to the solidification front [2,3]. This undesirable coarse β grain structure has been found to be difficult to avoid in AM by manipulation of the process parameters [6].

It has been recently found that the addition of a light deformation step in AM, when applied to each deposited layer, can be surprisingly effective in refining the β grain structure. For example, peening using an Ultrasonic Impact Treatment (UIT) in Laser Blown Powder AM has been shown to lead to refined, equiaxed, prior-β grains with more randomized orientations (Fig. 1) [7]. The addition of a rolling step to Wire Arc Additive Manufacture (WAAM) has also been found to greatly reduce the prior β grain size and cause a large reduction in texture strength, leading to improved mechanical isotropy [8,9] and this will be discussed in a future publication. Here, the prime interest is in explaining the high level of refinement found when only relatively small plastic strains are applied in the WAAM rolling process, which being of the order of 10% are much lower than would be expected to cause conventional recrystallization in a Ti-6Al-4V alloy [15].

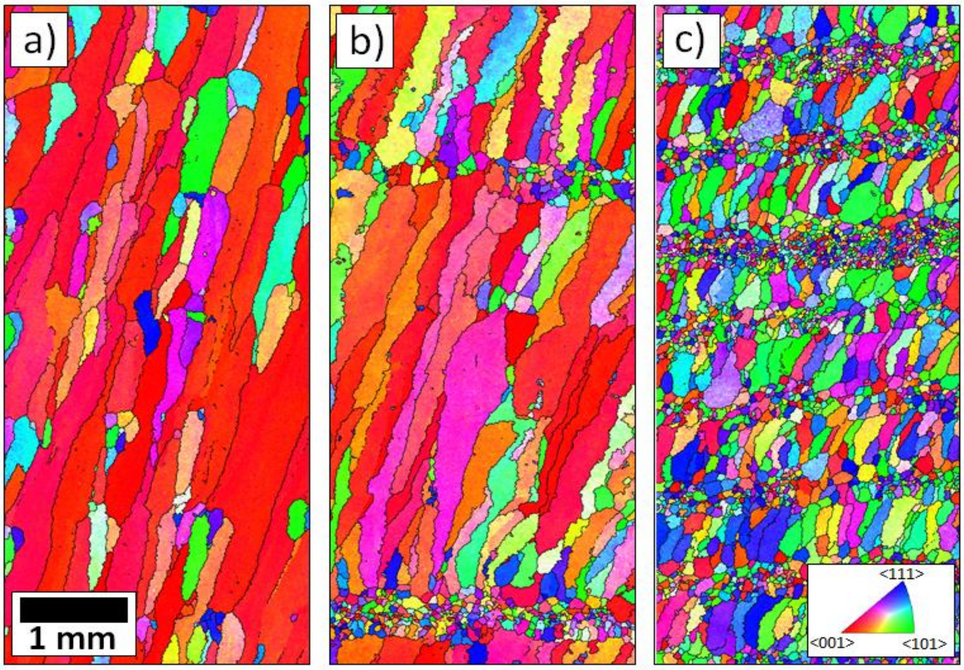

Figure 1. β reconstructed EBSD orientation maps showing: a) typical β columnar microstructure achieved by laser blown powder AM technique, b) the β grain refinement obtained with in-process ultrasonic impact treatment applied every 5 layers, and c) treatment every layer [7].

It was therefore the purpose of this study to investigate the origin of the new, differently orientated β grains that are generated by combining AM with relatively low strain deformation. To achieve this aim, AM material that had been lightly rolled in the WAAM process was studied in-situ, using a high temperature heating stage, while conducting Electron Back Scattered Diffraction (EBSD) orientation mapping at temperatures approaching the alloy's β transus.

# Experimental

## *AM Build*

The rolled WAAM wall investigated was supplied by Cranfield University, Welding Engineering and Laser Processing Centre, and was built using a pulsed GTAW welding system with an average current of 110 A, using 1.2 mm diameter Ti-6Al-4V alloy wire as a feed stock (Fig. 1). The deposition parameters employed are given in table 1 and full details of the WAAM rolling process can be found in ref [4]. A 100 mm diameter roller with a 3.6 mm radius groove, designed to match the curvature of the deposit bead, was run across the top of the wall after deposition of every layer, once the temperature of the last layer had dropped below 300˚C. The compressive rolling load was applied directly downwards through the roller bearings to the top of the wall with a constant downforce of 75kN, controlled using a load cell.

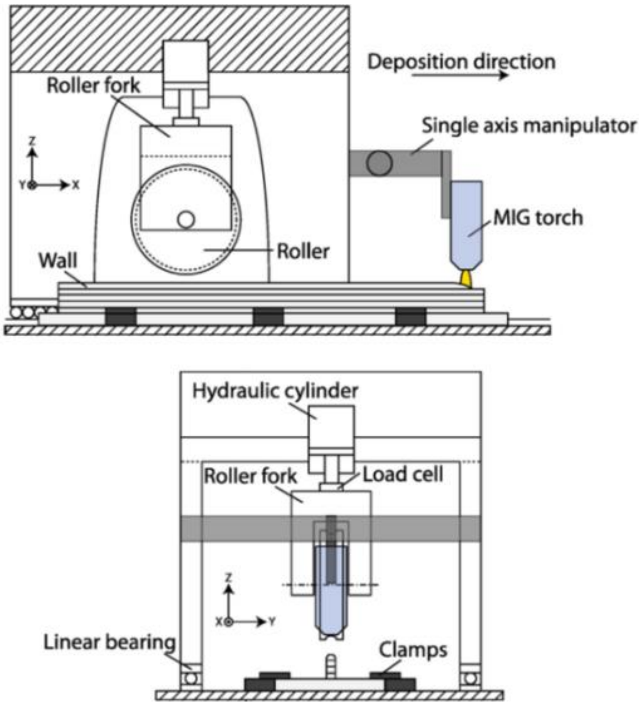

Figure 2. Schematic diagram of the WAAM rolling and deposition equipment, adapted from [4].

Table 1. GTAW Deposition parameters used to build the WAAM wall investigated.

| Deposition Parameter | Value |
|---|---|
| Travel speed | 270 mm/min |
| Average Arc Voltage | 12 V |
| Average Current | 110 A |
| Wire feed speed | 1.6 m/min |
| Frequency | 10 Hz |
| Trailing shield gas flow rate | 20 l/min |

### *Sample Location and Preparation*

A suitable site to carry out the in-situ heating experiment was selected from a region close to the rolled surface, on a cross-section of the built wall, and prepared using standard metallographic techniques. Prior to heating, microstructural investigation of the chosen area was carried out by high resolution EBSD mapping with a step size of 0.05 μm, using an FEI Magellan 400L SEM, fitted with an Oxford Instruments Nordlys EBSD detector. A second high resolution map of the site chosen was also made after completion of the in-situ heating experiments.

### *In-situ Heating*

EBSD Mapping at temperature was carried out within an FEI Nova 600 NanoLab SEM fitted with an Oxford instruments EBSD detector and a Gattan Murano heating stage. The sample was initially rapidly heated to 600°C at a rate of 60 °C/min, with pauses at 200°C and 400°C, to correct for drift due to thermal expansion of the sample. Above 600°C the heating rate was lowered to 10 °C/min to avoid overshooting the target temperatures. EBSD maps were made every 50°C from 700°C, to a maximum temperature of 950°C. This maximum temperature was limited by the capability of the heating stage and is slightly below the β transus. However, calculations under equilibrium conditions by JMATPro [16] predicted transformation to ~ 80% β at this temperature, which is adequate for the observation of the early nucleation and growth of β grains. Parameters for the EBSD maps were chosen to keep the acquisition time to ~30 mins, which was a compromise between acquiring as high a resolution map as possible and avoiding excessive isothermal evolution of the microstructure. The resolution of the maps was, therefore, sacrificed with the step size falling from 0.3 μm at 800°C to 0.5 μm at 950°C. It should also be noted that with increasing temperature there was a decrease in the level of indexing because of a reduction in signal to noise ratio in the EBSD patterns, due to detector wash out by the infrared radiation emitted by the sample. After the completion of the final map, the sample was allowed to cool quickly, dropping to under 500°C in 2 minutes.

### *β- Phase reconstruction*

In order to characterize the prior β grain structure an automated reconstruction procedure was applied (developed at The University of Sheffield and described elsewhere [17]) which calculated the most probable parent β orientation for any α grain by utilising the Burgers relationship and comparison of the misorientations between neighbouring α plate variants.

$\{110\}_\beta \parallel \{0002\}_\alpha \qquad \langle 111\rangle_\beta \parallel \langle 11\bar{2}0\rangle_\alpha$

Unless otherwise stated, The EBSD maps are plotted using IPF colouring with the reference direction being chosen to best highlight the orientations observed, as for this study we were not concerned with the orientations in relation to a specific reference frame.

# Results

## Site Selection

The area of interest chosen for the in-situ heating investigation was selected for two reasons: firstly, to include the presence of twinning, which was commonly noted in the deformation structure within colony α regions, and secondly to encompass a prior β grain boundary. The room temperature microstructure of the location chosen is shown in Fig. 3. Areas with Widmanstätten α plates are clearly visible in the two prior-β grains on the left and right sides of the region imaged, with a band of colony α down the centre. The colony α appears to have grown mainly into the right β grain from a prior β grain boundary. At this high resolution it was possible to index the fine residual β where it was thickest (e.g. at the triple points where the α laths met) as shown in Fig. 4a. Analysis of the residual β detected shows there to be two distinct orientations, confirming the colony has formed on a prior β boundary. The prior β grain structure has also been revealed using β reconstruction software at a higher magnification in Fig. 4b, which clearly shows the presence of two prior β grains and an un-reconstructed region corresponding to a twin, which could not be reconstructed as it has altered the parent phase habit relationship. Fig. 4 also provides {100} pole figures displaying good agreement between the orientations measured from each grain by the small amount of residual β that could be indexed and the data generated by the reconstruction software.

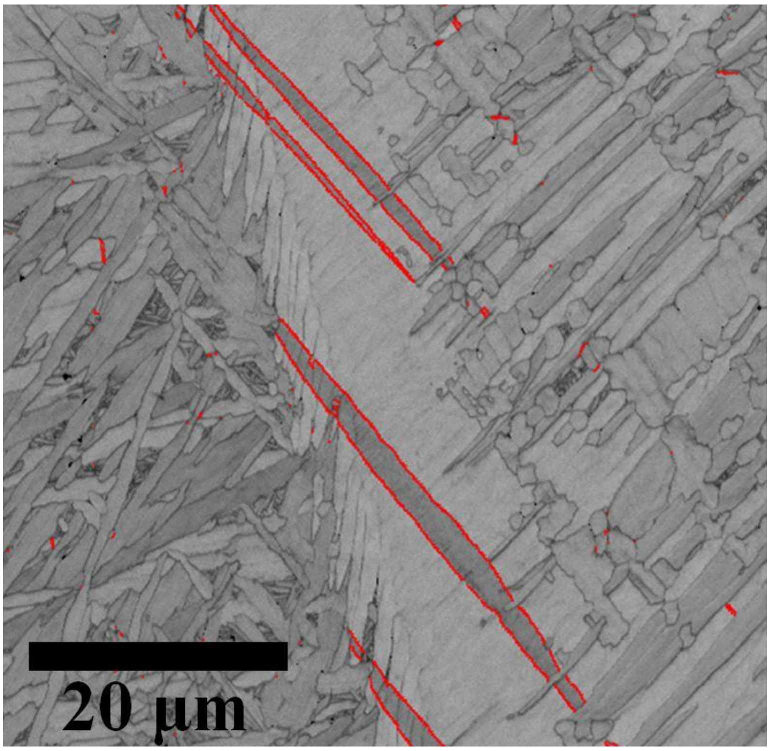

Figure 3. EBSD band contrast map of the chosen site for in-situ heating, with the twin boundaries highlighted in red.

The twin boundaries highlighted in Fig. 3, were found to be from a tensile $\{10\bar{1}2\}$ twin, a common twin in Ti, that has been previolsy observed in deformed Ti-6Al-4V [18], it can be seen that the twinning has occured sympathetically across several of the lath boundaries within the colony α. It can also be inferrd from the ease of β reconstruction that the net strain in this region of the sample was relatively low.

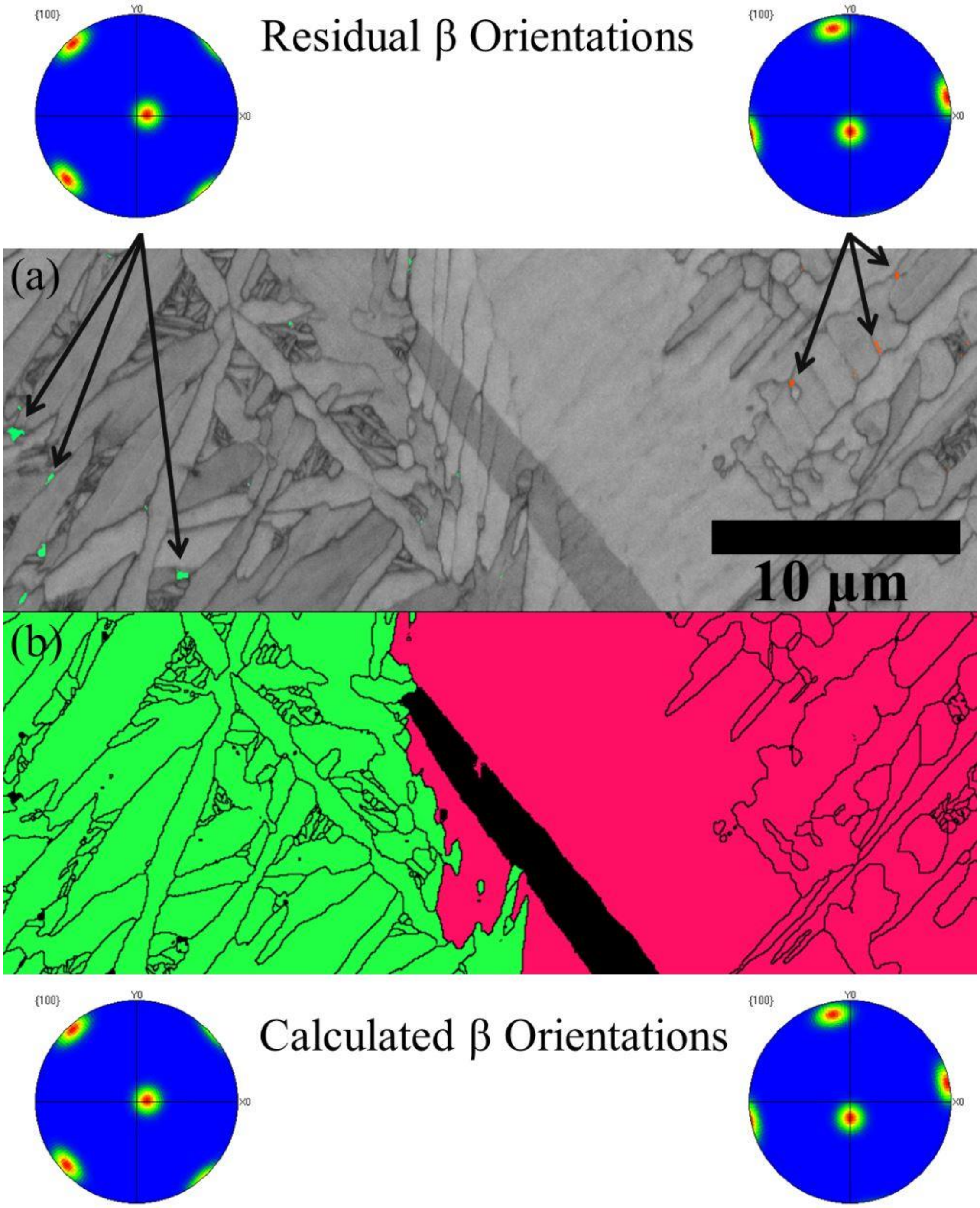

Figure 4. Magnified region of the map in Fig. 3, showing: a) fine residual β indexed between the α laths on either side of the colony (arrowed) and b) the reconstructed β parent grains with the boundaries of the α lathes that formed from them. Also shown are {100} pole figures of the detected and reconstructed β, showing good agreement. Note: the only region that failed to reconstruct is that of the twinned α.

### *Heating Experiments*

During in-situ heating, and despite fastidious attempts to achieve a good vacuum within the SEM chamber, a very thin film developed on the surface of the sample at 700°C, as can be seen in Fig. 5. It is believed that this film developed via a reaction between outgassing from the thermally conductive paste used to mount the sample (despite pre-baking at 200°C) and the sample surface. The presence of this film hampered the ability to carry out EBSD analysis at this temperature, but the enhanced contrast provided by this film on differing underlying orientations allowed for high resolution imaging of the deformation twins, which can be seen to pass though several laths in an α colony with SE imaging in Fig. 5.

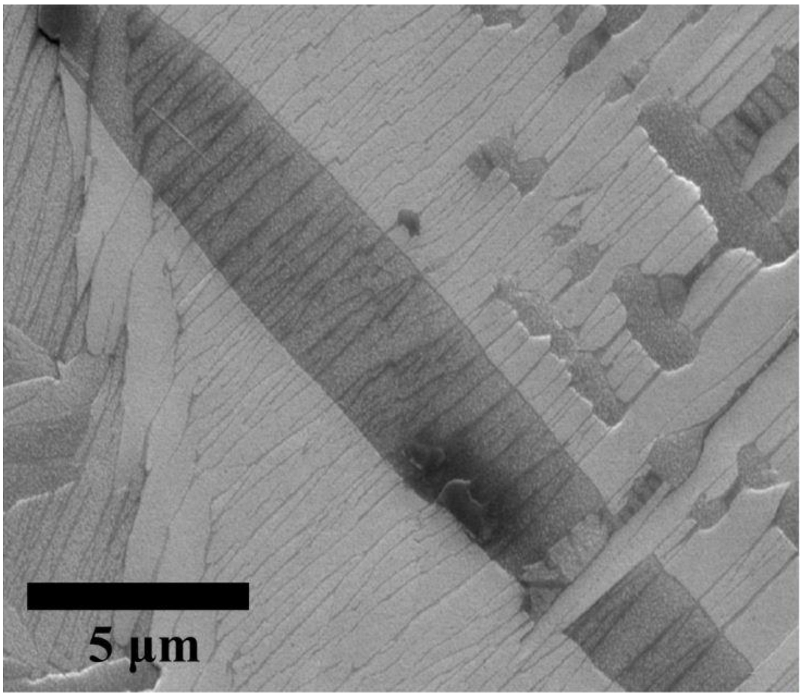

Figure 5. High resolution SE image of a twin crossing laths within the colony α. Image taken at 700°C, contrast given by differences in surface film thickness.

At 800°C the surface film could no longer be discerned and it was possible to again obtain EBSD patterns of the underlying material with reasonable indexing. A concern is therefore that some oxygen or nitrogen may have dissolved into the sample surface, affecting the β transformation temperature. However, the findings below are still self-consistent with the β orientations and twinning behaviour observed in the starting material. When compared to the high resolution map taken at room temperature in Fig. 6a, up to 800°C (Fig. 6b) very little microstructural evolution was observed to take place - that could be detected with the lower EBSD resolution used with the heating stage.

It should be noted that with this lower resolution at this temperature none of the residual β could be indexed, although it was observed at room temperature using higher resolution EBSD mapping (Figs. 4a, 6a).

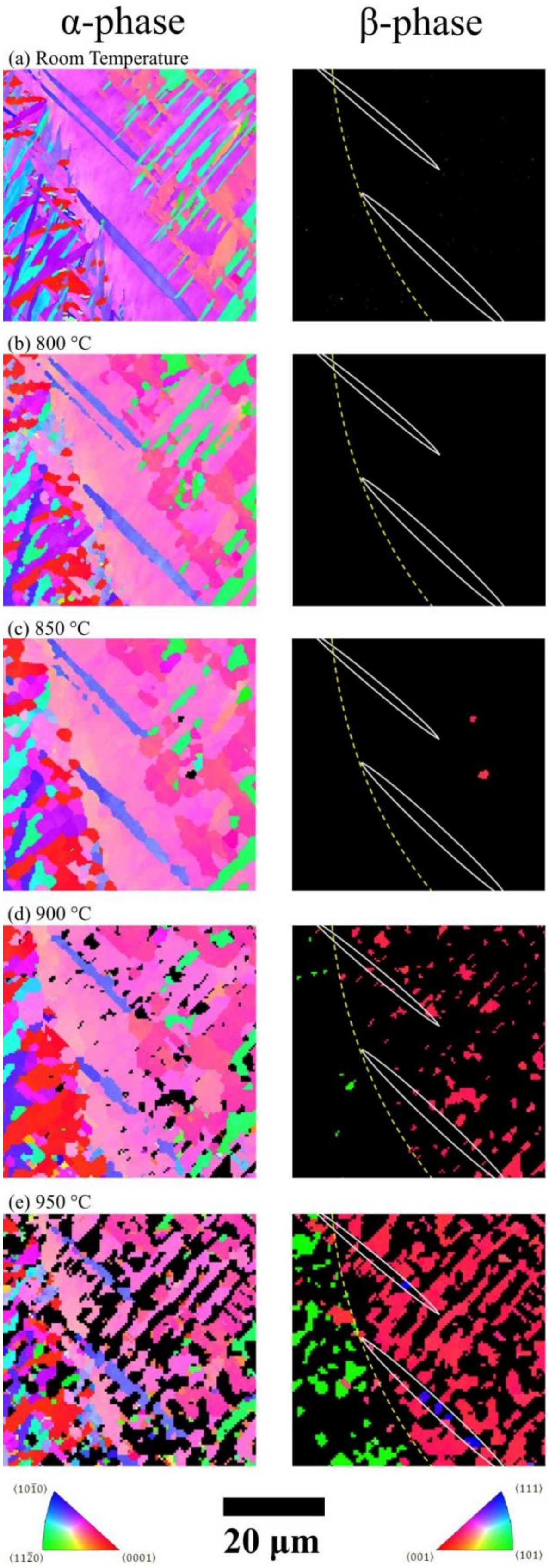

Figure 6. EBSD maps of the region studied by in-situ heating; a) room temperature (high resolution) b) 800°C, c) 850°C, d) 900°C, and e) 950°C (at lower resolution). The left and right maps show the α and β phases at each temperature, with the location of the prior β grain boundary (yellow dashed line) and α twin boundaries (solid white lines) indicated on the β phase map.

At 850°C (Fig. 6c) the β phase started to grow and could be indexed in the right hand grain, with exactly the same orientation as the fine residual β indexed at room temperature in the high resolution data. At 900°C far greater growth of β had occurred in the right-hand original prior-grain and at this temperature some β was also indexed in the left hand prior-β grain, again with the same orientation of the original residual β detected at room temperature. At this stage, the in-situ study therefore revealed only evidence of re-growth of the prior β grain structure from the residual β that originally formed on solidification in the AM sample, reproducing the same parent grain orientations.

In Fig. 6e, at the final temperature mapped of 950°C, which was the maximum that could be reached with the current set-up, the phase transformation had progressed to the point where the β phase made up ~35% of the indexed points. At this stage, on either side of the prior β grain boundary, growth of the residual β had continued retaining its original orientation. However, a third new orientation was now detected located within the region of the α twins. By isolating this new β orientation in the EBSD maps, it was found to be related to the twinned α by the Burgers' orientation relationship.

In Fig. 7 a high magnification, high resolution, EBSD map is shown from the original twinned α colony region, after rapidly cooling down from the in-situ heating experiment. The proportion of indexing was lower in this map (88.7%) compared to before the heating experiment (95.3%), owing to the development of slight topography on the sample surface following the thermal cycle. However, it is still possible to discern a number of interesting features. At room temperature the microstructure has returned to an α transformation structure which greatly resembles the original microstructure observed before the experiment (Fig. 6a). The re-formation of a similar α transformation microstructure is not that

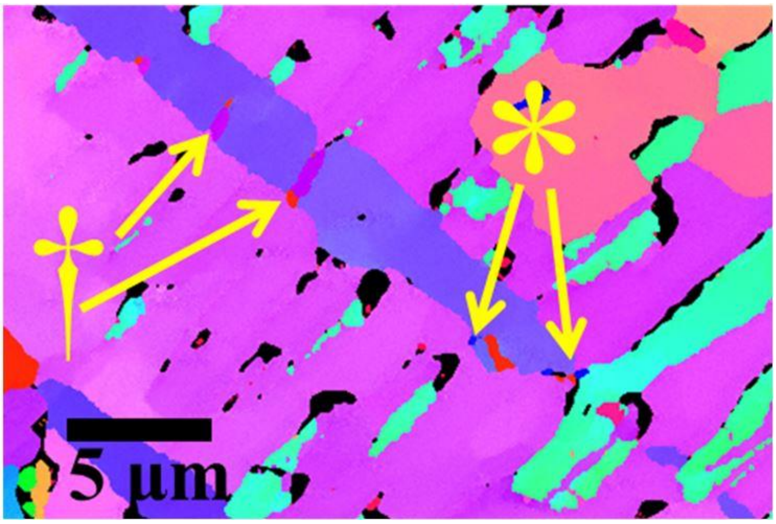

Figure 7. High resolution α and β EBSD map of a twinned region after the heating experiment, with residual β of the new orientation indicated by *, and new α orientations, not observed before the heating experiment indicated by †.

surprising, as at the highest temperature reached of 950°C (Fig. 6e) ~ 65% of the sample indexed was still α, and the α lathes retained will act as growth sites for the transformation back from β → α, reproducing much of the original microstructure. However, also shown in Fig. 7 is residual β with the new orientation observed at high temperatures bordering the twinned α region. Shown in Fig. 7 is the existence of new α orientations that were not identified prior to, or during, the heating experiment. Analysis of these new α variants has revealed that they share a Burgers' orientation relationship with the new β orientation formed within the twined region and, therefore, they nucleated and grew from this new β phase orientation during cooling after the in-situ heating experiment. A final observation from Fig. 7 is that both the residual new β and new α variants are found located on the boundaries between the α laths within the twinned colony, indicating these boundaries as the locations of the initial nucleation and/or growth of the new β orientation during heating.

## Discussion

While the influence of surface effects cannot be ignored, this in-situ study has, for the first time, directly observed the influence of light prior-plastic deformation on the α → β phase transformation, when starting with a fine lamellar microstructure. This has clearly shown that, without deformation, the presence of residual β in the original transformation structure accounts for the regrowth of β grains with the same orientation on re-heating above the β transus in an AM thermal cycle, and this would thus re-create quite closely the original solidification grain structure if further solid state grain growth does not occur in the process. In addition, a new β orientation has been observed to be formed within the prior β grains associated with twinning induced by light deformation of the α phase. Deformation twinning is in itself not widely reported in Ti-6Al-4V, although it has been noted recently to occur under certain deformation conditions [18]. However, it is likely that the fine α structure (lath width ~ 1μm), produced in AM materials owing to the high cooling rate, is more susceptible to deformation twinning because of the higher flow stress in fine grained materials and the associated role this stress is expected to play in twin nucleation [19]. In addition, the colony α structure, where twinning was observed to occur, contained a single α variant. The near identical orientation of the α laths in such a colony region would therefore encourage sympathetic twinning to take place across α lath boundaries, as seen in Figs. 3 – 5. On re-heating it has been shown that within such twinned regions the α transforms to β phase with a distinctly different orientation that is determined by the Burgers' orientation relationship to the twined α phase. The new β orientation was found to grow in several locations, but always originating from the colony boundaries within the twins, and of a single consistent orientation. It is evident from Fig. 6 that this new orientation does not grow until a higher temperature is reached than for the residual β which kept the same original orientation as the parent β grain. This implies there may be a higher energy barrier involved, which is consistent with the mechanism not being as simple as the re-growth of the pre-existing β, which does not require a nucleation stage. The observation of only one β variant nucleating within the twinned regions could be attributed to the associated stress field of the twin-matrix interface [20] and the influence of strain on variant selection in Ti-6Al-4V [21]. An alternate origin for the new β orientation is the possibility that deformation twinning across the α colony would also locally deform the thin residual β layers between the lath boundaries leading to the formation of the new β orientation. Unfortunately, the β layers between the laths in the twinned colony α structure were too thin to resolve by EBSD. The exact nature of the local β deformation structure within the twinned region will therefore require further investigation by TEM.

Irrespective of the exact mechanism, the observation of the growth of new β orientations on re-hearting, due to twinning of the α phase caused by the application of a low applied strain in AM, could in principle contribute to explaining the origin of the refined equiaxed prior-β grain structure and α textural weakening seen when AM is combined with deformation techniques, as described in [7] and [8]. However, there are additional questions that have been raised by this study that will need further future investigation. For example, small grains with a new β orientation would have to compete with a matrix dominated by residual β of the original orientation (Fig. 6e). Competitive growth of different β orientations during coarsening would only occur when the microstructure had fully transformed to β and this unfortunately could not be observed, due to the temperature range limitation of the heating stage in this experiment. It is also likely that the radically higher heating rate seen in the AM process, compared to that used in the in-situ experiment, may affect the result.

Secondly, in the sample studied, the only significant α colony regions were observed near the prior β grain boundaries and it would thus be expected that if β grain refinement was only due to the mechanism discussed above, then it would be expected that the new βorientations would merely form near the original grain boundaries in the prior coarse-columnar β microstructure. However, as shown in Fig. 1 [7], equiaxed β grains are found homogenously throughout the wall, suggesting that other mechanisms of refinement of the normal coarse columnar β grain structure need to be considered. For example, subsequent to this study it has been discovered that the curved profile of the roller constrains the top wall bead immediately below the rolled surface, so that greater plastic strain is experienced within the wall at a larger depth than in the area investigated. Therefore, this greater strain may give rise to alternative mechanisms of β refinement that were not observed in this initial investigation.

Finally, one surprise was the lower than expected level of transformation observed in the heating experiment. For example, it was predicted that for this alloy, at a temperature of 950°C there should have been a transformation to ~80% β, by volume fraction, whereas only ~35% β was indexed by EBSD. A possible cause for this disparity could be an error in the calibration of the thermocouple controlling the heating stage. But, the observation of the surface film at 700°C (Fig. 5), suggests another possibility. It is likely that this film was formed by a reaction between the titanium and gasses outgassed into the chamber, such as oxygen and nitrogen that formed a thin layer of oxide/nitride on the sample surface. If this was the case, then the absence of the film at 800°C implies it dissolved at higher temperatures by diffusion into the sample. As both nitrogen and oxygen stabilise the α phase [11], this could lead to the reduced volume fraction of β observed. This behaviour would also potentially explain why in Fig. 6e, there is an unexpected preferential transformation to β of the right hand compared to the left grain, which could be related to preferential growth of the film on different α orientations, as shown in Fig. 5.

## Summary

A lightly deformed section of an additively manufactured Ti-6Al-4V wall has been successfully studied by EBSD in-situ in an SEM, during heating up to a temperature approaching the β transus of 950°C. This has allowed direct observation of the regrowth of the β phase in the original AM deposit, on re-heating through the α→ β transformation.

It has been found that, in the example studied, the majority of the β phase grew back with the same orientation that it first formed with during solidification, from residual β in the transformation structure, thus largely re-creating the prior β grain structure. However, the light deformation experienced by the sample was observed to give rise to the formation of a specific new β orientation.

This new β orientation has been shown to originate from within twinned α colonies and suggests one new possible mechanism for the β grain structure refinement observed in additive manufacturing processes, when they are combined with an in-process deformation step.

As α colonies are confined to close to the prior β grain boundaries within a coarse-grained AM microstructure, it is suggested that the observed phenomenon is not the only mechanism responsible for producing the β grain refinement seen in AM when it is combined with a deformation step.

## Acknowledgements

The authors would like to thank Prof. S. Williams group at Cranfield University for the manufacture of the rolled WAAM walls. J. Donoghue is grateful for financial support provided by LATEST2 (EP/G022402/1) and Airbus, UK.

## References

[1] R.R. Boyer, An overview on the use of titanium in the aerospace industry, Mater. Sci. Eng. A. 213 (1996) 103–114.

[2] S.S. Al-Bermani, M.L. Blackmore, W. Zhang, I. Todd, The Origin of Microstructural Diversity, Texture, and Mechanical Properties in Electron Beam Melted Ti-6Al-4V, Metall. Mater. Trans. A. 41 (2010) 3422–3434.

[3] A.A. Antonysamy, J. Meyer, P.B. Prangnell, Effect of Build Geometry on the β−Grain Structure and Texture in Additive Manufacture of Ti-6Al-4V by Selective Electron Beam Melting, Mater. Charact. (2013) 153-168.

[4] P. Colegrove, H.E. Coules, J. Fairman, F. Martina, T. Kashoob, H. Mamash, et al., Microstructure and residual stress improvement in wire and arc additively manufactured parts through high-pressure rolling, J. Mater. Process. Technol. 213 (2013) 1782–1791.

[5] S. Reginster, A. Mertens, H. Paydas, J. Tchuindjang, Q. Contrepois, T. Dormal, et al., Processing of Ti Alloys by Additive Manufacturing: A Comparison of the Microstructures Obtained by Laser Cladding, Selective Laser Melting and Electron Beam Melting, Mater. Sci. Forum. 765 (2013) 413–417.

[6] F. Wang, S. Williams, M. Rush, Morphology investigation on direct current pulsed gas tungsten arc welded additive layer manufactured Ti6Al4V alloy, Int. J. Adv. Manuf. Technol. 57 (2011) 597–603.

[7] J. Donoghue, J. Sidhu, A. Wescott, P. Prangnell, Integration of Deformation Processing with Additive Manufacture of Ti-6Al- 4V Components for Improved β Grain Structure and Texture, in: 2015 TMS Annu. Meet. Exhib., Orlando, Florida, 2015.

[8] F. Martina, S.W. Williams, P. Colegrove, Improved microstructure and increased mechanical properties of additive manufacture produced Ti-6Al-4V by interpass cold rolling, SFF Symp. (2013) 490–496.

[9] A.A. Antonysamy, Microstructure, texture and mechanical property evolution during additive manufacturing of Ti6Al4V alloy for aerospace applications, University of Manchester, 2012.

[10] G. Lütjering, Influence of processing on microstructure and mechanical properties of ( α+ β) titanium alloys, Mater. Sci. Eng. A. 243 (1998) 32–45.

[11] G. Lütjering, J. C.Williams, Titanium, 2nd ed., Springer, Berlin, n.d.

[12] J.L.W. Warwick, J. Coakley, S.L. Raghunathan, R.J. Talling, D. Dye, Effect of texture on load partitioning in Ti-6Al-4V, Acta Mater. 60 (2012) 4117–4127.

[13] W.G. Burgers, Cubic-Body-Centered Modification Into The Hexagonal-Close-Packed Modification Of Zirconium, Phys. I. (1933) 561.

[14] M.J. Bermingham, S.D. McDonald, M.S. Dargusch, D.H. StJohn, Grain-refinement mechanisms in titanium alloys, J. Mater. Res. 23 (2011) 97–104.

[15] K. Muszka, M. Lopez-Pedrosa, K. Raszka, M. Thomas, W.M. Rainforth, B.P. Wynne, The Impact of Strain Reversal on Microstructure Evolution and Orientation Relationships in Ti-6Al-4V with an Initial Alpha Colony Microstructure, Metall. Mater. Trans. A. 45 (2014) 5997–6007.

[16] JMatPro, (n.d.).

[17] P.S. Davies, An investigation of microstructure and texture evolution in the Near-α titanium alloy timetal 834, University of Sheffield, 2009.

[18] D.G.L. Prakash, R. Ding, R.J. Moat, I. Jones, P.J. Withers, J.Q. Da Fonseca, et al., Deformation twinning in Ti-6Al-4V during low strain rate deformation to moderate strains at room temperature, Mater. Sci. Eng. A. 527 (2010) 5734–5744.

[19] A. Ghaderi, M.R. Barnett, Sensitivity of deformation twinning to grain size in titanium and magnesium, Acta Mater. 59 (2011) 7824–7839.

[20] J. Christian, S. Mahajan, Deformation twinning, Prog. Mater. Sci. 39 (1995) 1–157.

[21] N. Gey, M. Humbert, M. Philippe, Y. Combres, Investigation of the α-and β-texture evolution of hot rolled Ti-64 products, Mater. Sci. 219 (1996) 80–88.

## 4.4. The Role of Twinning on the β-Grain Size Refinement in Ti-6Al-4V Additive Manufacture Combined with Rolling Deformation

Following on from **Manuscript 3**, this manuscript attempts to more fully explain the mechanism that causes the refinement of prior β grain structures observed in Ti-6Al-4V AM microstructures when a deformation step is integrated into the processes, as observed in **Manuscripts 1** and **2**. In order to better understand the refinement mechanism, the following manuscript details two experiments; the first is a repeat of the in-situ heating experiment detailed in **Manuscript 3**, but on a more heavily deformed region of the microstructure, and the second is a simulation of a single deformation step followed by a deposition pass, as described in §3.2, to relate the orientations of the refined β to the coarse grained prior β microstructure they formed from.

The discussion in this paper is partially focused around orientation rotations due to twinning these rotations are shown schematically in figures 12 and 13 within the paper, however, a more detailed account of the calculations involved can be found in the appendix of this thesis on page 192.

This paper is currently in draft form, and will be submitted to a suitable journal in the near future.

The contributions of the named authors were as follows:

**Jack Donoghue** – Lead author, all metallographic preparation, mechanical testing, SEM analysis and EBSD data analysis.
**João Quinta da Fonseca & Philip Prangnell** – Supervisors of Jack Donoghue.

# The Role of Twinning on β-Grain Refinement in Ti-6Al-4V Additive Manufacture Combined with Rolling Deformation

J. Donoghue*, J. Quinta Da Fonseca, and P.B. Prangnell

jack.donoghue@manchester.ac.uk; joao.fonseca@manchester.ac.uk;
philip.prangnell@manchester.ac.uk

Materials Science Centre, University of Manchester, Manchester M13 9PL, UK

## Abstract

Additive Manufacture (AM) of Ti-6Al-4V generally leads to an undesirable microstructure with a non-random texture. Large columnar β grains grow across deposited layers with a preferential <001> direction. It has been found that the application of surprisingly small amount of plastic strain to each layer, by methods such as in-process rolling, can disrupt the columnar growth and produce a fine equiaxed β grain structure that is more randomly orientated. The origin of this interesting effect has been investigated by direct in-situ SEM observation combined with EBSD analysis of the growth of new β grain orientations, from within the deformed AM microstructure, on reheating near to the transus temperature. Thermo-mechanical simulation of the combined AM and deformation process has also been employed in order to directly relate the texture of the refined β grain structure back to the parent orientation present prior to reheating above the β transus. Analysis of the new orientations formed has shown that they can almost exclusively be related to deformation twinning of the thin residual β present at room temperature, caused by the rolling process.

Keywords: Additive Manufacture; titanium; grain refinement; texture,

*Corresponding Author;

# 1. Introduction

Additive Manufacture (AM) is increasingly being embraced by the aerospace industry due to its potential for near-net shape fabrication of more geometrically optimised components, with a reduced lead time over more established manufacturing techniques. The advantages of AM are particularly significant when a titanium feedstock is used due to both the inherently high material cost, and the difficulty and expense associated with machining components made from traditional forgings [1]. Of all the titanium alloys, Ti-6Al-4V is the most studied in the context of AM [1–12], as this alloy is used extensively in the aerospace industry due to its excellent combination of specific mechanical properties, corrosion and fatigue resistance [1].

However, there are still some hurdles to be overcome before AM technologies can fully realise their potential when producing Ti-6Al-4V components. A recent review by Carroll et al. [2] has highlighted that mechanical anisotropy is observed in many Ti-6Al-4V builds across several AM technologies. In particular a large anisotropy in ductility is reported, with greater elongation to failure occurring in the build direction (the direction normal to the plane of each deposited layer) accompanied by a tendency for a slightly lower tensile strength. Fatigue properties have also been found to be anisotropic, with greater dynamic strength seen normal to the build direction [3]. In both cases this anisotropy has been associated with the directionality of the highly columnar prior β grain structure that is produced via a wide range of AM technologies, including laser [4,5], electron [6,7], and arc [8] heat sources.

The formation of this coarse columnar β microstructure is practically inevitable in AM with Ti-6Al-4V when the solidification conditions of the processes are combined with the metallurgical behaviour of titanium. In all AM techniques the moving heat source not only melts the feedstock to be consolidated, but also re-melts a significant amount of the previous layers. The high temperatures reached also raise the material surrounding the melt pool to significantly above the β transus, which for Ti-6Al-4V is ~1000°C. As the alloying elements in Ti-6Al-4V have a partition coefficient close to one [13], the steep thermal gradients across the melt pool do not allow sufficient constitutional supercooling to develop nucleation ahead of the solidification front [14]. Therefore, solidification occurs by epitaxial regrowth of the retransformed β grains that surround the melt pool at this temperature. As this process is repeated with every layer of deposition, such grains typically grow through multiple added layers, and potentially the entire height of a build. Due to the <100> direction being the preferential solidification direction for bcc metals [15], growth selection leads to a strong <100> texture in the direction of the columnar growth [9,10,16]. In their review, Carroll et al. [2] have dismissed the idea that the strong prior β texture can lead to the tensile property anisotropy observed in AM parts, as the texture is greatly weakened by each β grain transforming to a fine α lath structure when cooled below the β transus with only a thin layer of residual β remaining (~5-10%) between the α laths. The α → β transformation weakens the texture as each α lath can in principle adopt any one of the 12 distinct orientations dictated by the Burgers orientation relationship (BOR). Instead Carroll et al. argue that the anisotropy is largely caused by the presence of large α colonies that form at prior β grain boundaries that allow a preferential path for damage accumulation. Refining the prior β grain structure can in principle minimize this effect.

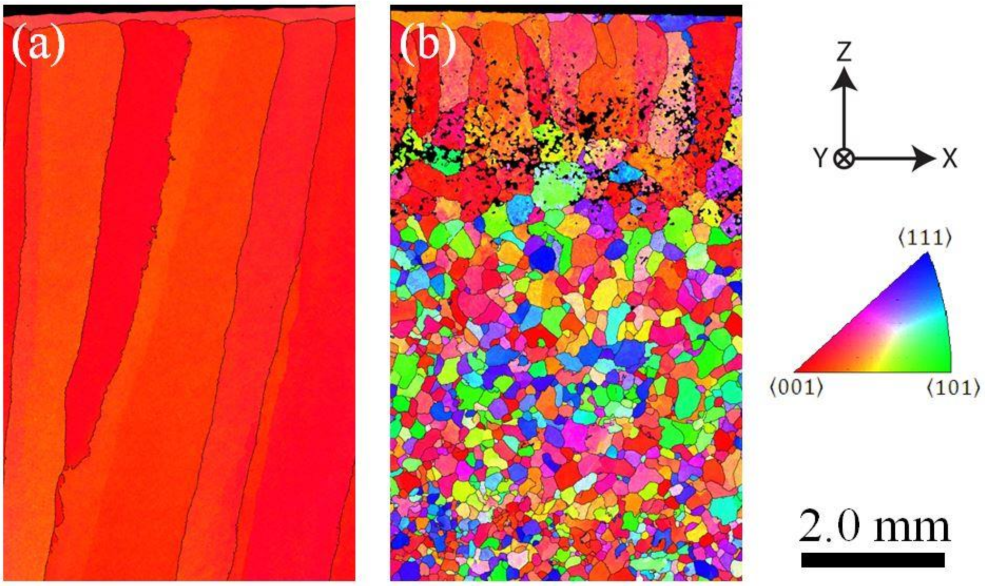

Figure 1. Orientation maps of the prior β grain microstructure of WAAM at the top of a single pass wide wall over multiple added layers showing (a) the highly textured, coarse columnar microstructure formed under standard deposition, and (b), the refinement achieved when rolling has been applied between every layer; adapted from [11].

A reduction in the β grain size, and therefore the limiting of α colony size, in Ti-6Al-4V can be achieved by both alloy manipulation and by thermomechanical processing. Alloy additions that have low solubility in titanium and partition ahead of the solidification front, such as boron, have been added to titanium alloys and have been successful in reducing the prior β grain size [17,18]. However, the TiB precipitates that form as a consequence of this alloying addition are found to crack at relatively small strains [19] and could act as initiation sites for fatigue cracks under cyclic loading. In contrast, traditional thermomechanical processing of Ti-6Al-4V involves forging above the β transus in order to break up the coarse as-cast prior β structure by dynamic recrystallization [20], and it is found that high monotonic strains in excess of ~0.5 are required to break up the β microstructure if the deformation is carried out in the α-β phase field [21]. Both processing approaches would be impractical to integrate with an AM technique. However, it has recently been observed that a surprisingly high degree of β microstructural and textural refinement can be achieved in an AM process by cold working to relatively moderate strains of less than 0.1 [11,12]. For example in a Wire and Arc based AM technique (WAAM) where a roller is lightly passed over the build between every deposition pass [11,12,22], the prior β grain size can be reduced from the order of mm's to ~100 μm, as shown in Figure 1. In addition, samples produced with this more refined prior β microstructure have more isotropic tensile properties in both tensile strength and elongation [22].

Obtaining this high degree of refinement after such a modest cold working is surprising as the mechanism does not appear to correspond with that typically observed with the thermomechanical treatment of α-β titanium alloys [11,12]. It has been suggested by Martina et al. that the refinement takes place due to a static recrystallization mechanism below the β transus, as evidenced by a direct measurement of the temperature at the point of refinement by an inserting a thermocouple into the AM build process that suggested the point of refinement took place at ~780°C [12]. However, subsequent research by Donoghue et al. has found that the α variants within each refined prior β all share Burgers' Orientation Relationship (BOR) with a parent β grain and therefore must have formed upon cooling from above the β transus [11]. It is therefore likely that the formation of the refined prior β microstructure is related to the α to β phase transformation. This research has also shown that the region where β refinement occurs correlates more closely to the strain distribution imparted by the rolling pass than the temperature field, with refinement only occurring in the region fully transformed to β by exposure to the thermal field of the subsequent deposition pass.

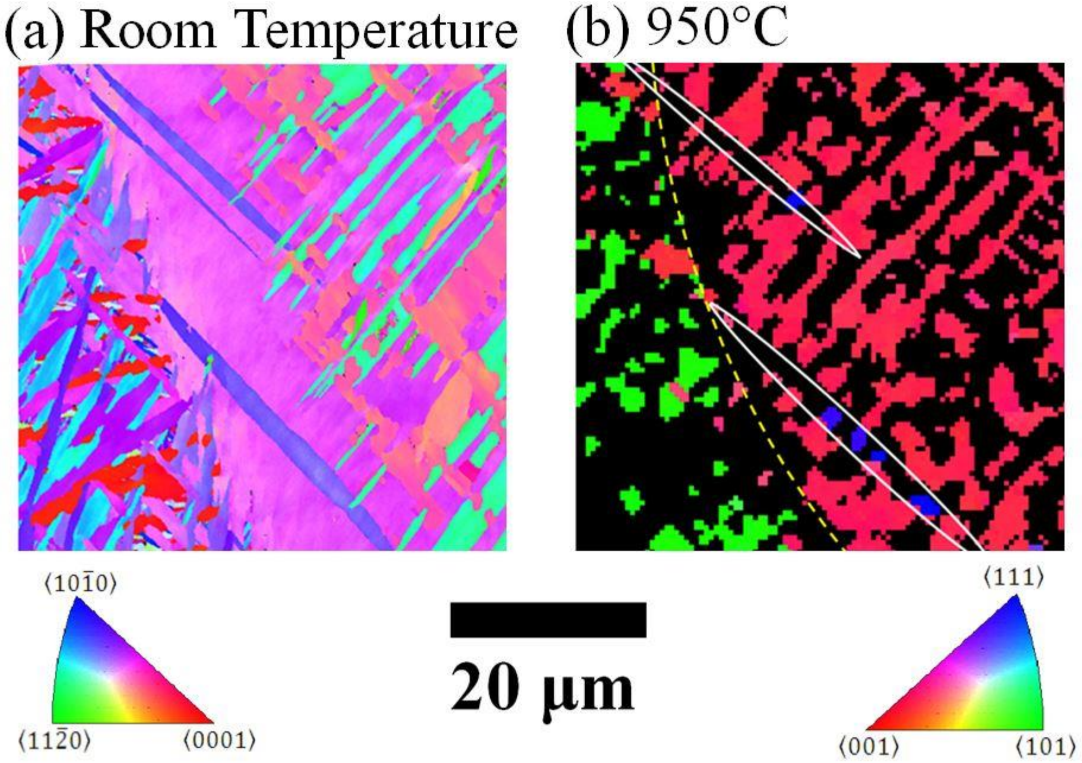

Figure 2. EBSD maps of the deformed region studied by in-situ heating in Ref [10]; (a) room temperature α map, and (b), a β phase map of the same region at 950°C where significant phase transformation has taken place. The location of the prior β grain boundary (yellow dashed line) and α twin boundaries (solid white lines) are indicated on the β phase map.

Recently, we studied the annealing of a deformed WAAM build heated to close to the β transus, in-situ by EBSD [10]. The outcome of this experiment is summarised in Figure 2. As expected, we found that the majority of the α laths returned to their original parent β orientation on heating as the residual β trapped between the laths grew to consume them. In addition we saw that a new beta orientation grew from a twinned α colony, giving a potential source for new β orientations observed in the refined microstructure. However, in this work it was not clear whether these new β orientations could lead to the level of refinement observed because α colony twinning was rare, and it was therefore difficult to see how these new orientations could compete with the majority of the matrix which re-grows from residual β. Furthermore, it was subsequently discovered that these results may not be representative since the region studied was close to the rolled surface of the WAAM wall, where plastic deformation was constrained by the contoured roller; the maximum strain actually occurred 2-3 mm from the top surface into the build [11].

With AM being increasingly investigated as a processing route for Ti-6Al-4V, the unexpected improvement to the microstructure and mechanical properties obtained by a light in-process deformation step could lead to a whole family of new processes being developed. Thus, it is important to understand the mechanism by which this refinement occurs so that it can be better exploited. Furthermore, identification of a new approach to refine the prior β microstructure of Ti-6Al-4V could have consequences beyond additive manufacture, for example, breaking down the coarse prior β microstructure of castings. Therefore, to better understand the origin of the refined β structure found in the WAAM process when combined with light rolling, we have repeated the previous in-situ study using EBSD in the region of maximum strain. In parallel, we have also simulated both the rolling step and the subsequent rapid thermal cycle re-heating above the β transus experienced during the process, using a sample produced by WAAM containing a few large prior β grains of known orientation.

## 2. Experimental

### *2.1 WAAM Samples*

In the WAAM process, a pulsed GTAW welding system melts and ‘adds’ layers of material fed into the arc heat source using a wire feeding system. The set up used has been described in detail elsewhere [12,23]. For this study, walls were built with a 1.2 mm diameter Ti-6Al-4V alloy welding wire, with an average welding current of 110 A, to give a single track wide wall with a thickness of ~ 6 mm. The material was deposited onto a rolled Ti-6Al-4V baseplate with an equiaxed bimodal α - β microstructure. Oxidation was prevented by the use of a trailing hood that provided a high laminar flow of argon shielding gas. Two walls were investigated in this study, one where no deformation was applied, and a second where deformation was applied after every layer of deposition. In this second wall, each deposited layer was deformed by running a roller across the top of the walls using a rigid gantry system. The 100 mm roller had a 3.6 mm radius semi-circular groove to mirror the bead profile of the top of the wall, and a controlled compressive load of 75 kN was applied after every layer of deposition, once the temperature of the top layer had cooled naturally to room temperature.

The microstructure of the two walls and was found to be radically different, as characterised in [11] and shown in Figure 1. The undeformed wall had a very coarse, columnar prior β structure with a preferential <100> growth direction with the columnar grains extending over several deposited layers, and potentially across the entire height of the build, whereas the wall with deformation applied, had an equiaxed prior β grain structure, refined to ~ 90 μm grain size, with a much weaker texture. Despite the radically different prior β structures, the room temperature α + β transformation microstructure was very similar for both samples [12]. This was expected because the cooling rate through the β transus is approximately the same in each case. Both samples had a fine Widmanstätten transformation microstructure, with < 1 μm residual β layer between the α laths and a tendency to form colonies of the same α variant at prior β boundaries, as shown in Figure 3.

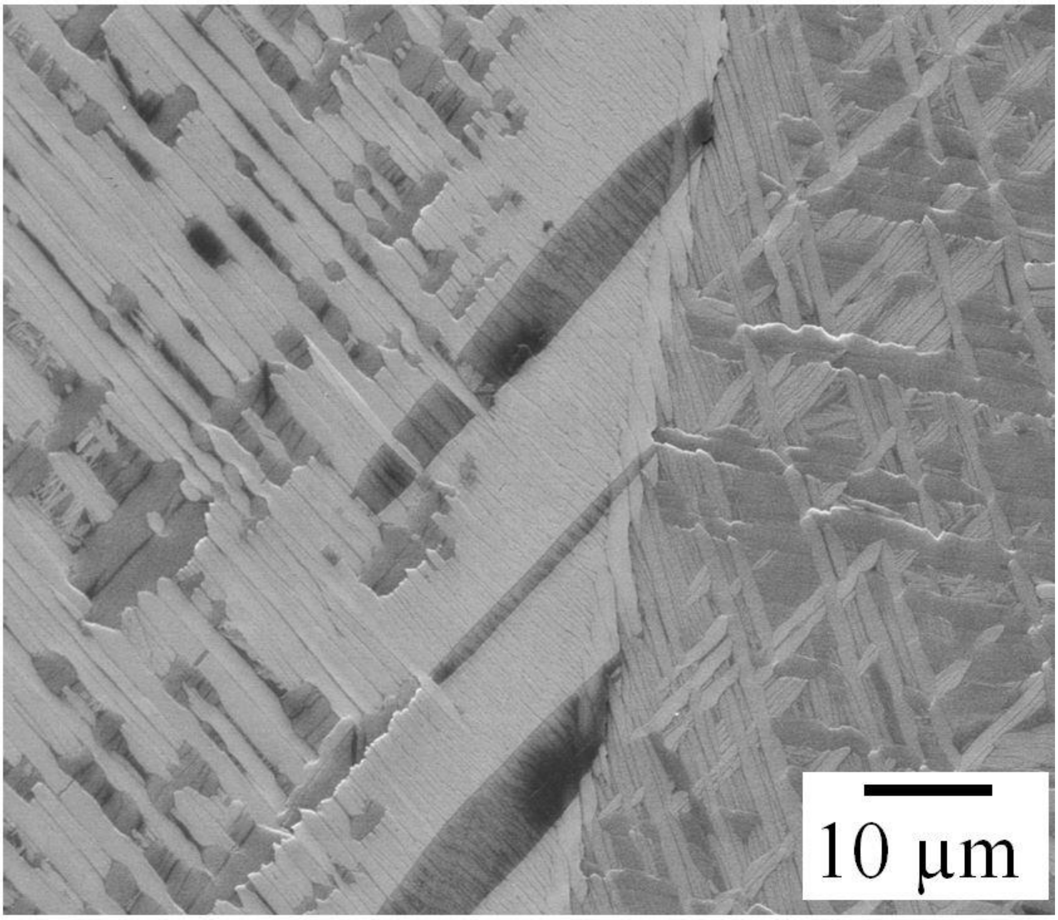

Figure 3. High magnification SE micrograph of the typical α + β microstructure found in WAAM Ti-6Al-4V builds showing an α colony on a prior β grain boundary in the centre of the image, with a basket weave Widmanstätten microstructure present further into the interior of the grain.

The regions of interest selected within each of the WAAM walls are shown in Figure 4. The in-situ EBSD experiment aimed to identify the possible origin of new β orientation within the rolled WAAM microstructure and therefore the sample was taken from the most deformed region [11]. This is ~ 2 mm from the rolled surface, along the centreline of the wall, as shown in Figure 4a. For the simulation of the rolling and β reheating process steps, the ‘matchstick’ samples were EDM machined with the sample’s long direction approximately parallel to the direction of columnar growth to maximise the volume included of individual columnar prior β grains within the sample, as shown in Figure 4b.

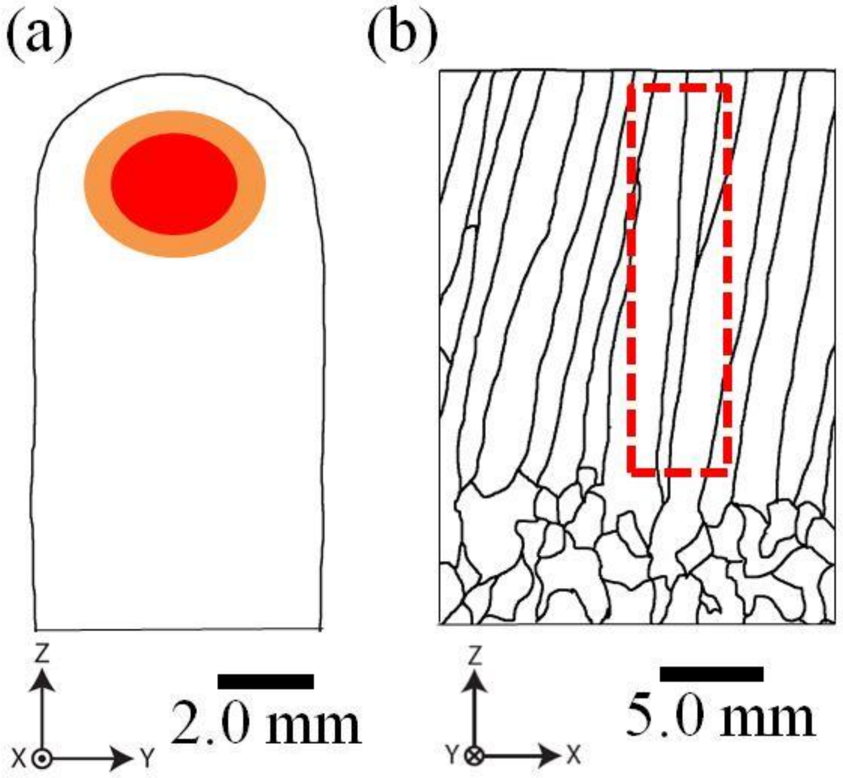

Figure 4. Schematic diagram indicating the locations within the WAAM walls from which the samples were taken; (a) indicates the region most highly strained by the contoured roller (as found in [11]) used for the in-situ EBSD heating experiment. (b) indicates the location in an undeformed wall with respect to the columnar grain orientations that deformation and reheating simulations were carried out on.

### 2.2 In-situ heating experiment

Following standard metallographic preparation, a sample of dimensions 2 × 2 × 1 mm was attached to a Gatan Murano heating stage using a water based, thermally conductive, carbon paste. The EBSD mapping at temperature was carried out within an FEI Nova 600 NanoLab SEM, fitted with an Oxford instruments Nordlys EBSD detector with Aztec acquisition software. Initially, the sample was rapidly heated to 550°C at a rate of 40 °C/min, with pauses at 200°C and 400°C, to correct for translation of the region of interest due to thermal expansion. Above 550°C the heating rate was lowered to 10 °C/min to avoid overshooting the target temperatures. EBSD maps were attempted every 50°C from 700°C, up to a maximum temperature of 950°C. This maximum temperature was limited by the capability of the heating stage and is slightly below the β transus. Previous experiments found that at this temperature transformation had proceeded to a ~35 % β phase content, which is a sufficient volume fraction to observe the early transformation to β and subsequent growth of β grains, but less than would be predicted for this alloy at this temperature [152]. The partial suppression of the α → β transformation in the previous in-situ study was thought to be likely due to absorption into the sample surface of remnant gases within the SEM chamber that stabilise the α phase [10]. The parameters for the EBSD maps were chosen to keep the acquisition time to ~15 mins, a compromise between EBSD map resolution and avoiding excessive isothermal evolution of the microstructure. A step size of 0.15 μm was therefore used, except for an initial high-resolution map, using a step size of 0.05 μm, to map the residual β between the α laths at room temperature. Once the final map had been acquired, the sample was allowed to cool quickly, dropping to under 500°C in 2 minutes.

## *2.3 Process simulation*

### Rolling Simulation

Rolling along the length ($x$) of a thin tall wall produces mainly an increase in the width ($y$) with negligible elongation along the length of the wall. Therefore deformation occurs in plane strain and:

$\varepsilon_y \approx -\varepsilon_z$ and $\varepsilon_x \sim 0$

This is different from conventional rolling where there is elongation along the rolling direction and negligible strain in the transverse direction.

In order to replicate plane strain conditions, a channel die compression rig was designed with a 5 mm channel, as shown in Figure 5a, to constrain a sample of dimensions 5 × 5 × 20 mm cut from the undeformed wall as shown in Figure 4b. The sample was strained at room temperature at a fixed cross head speed of 30 mm/s to a target reduction of 15% using a graphite based lubricant.

### Thermal Cycle Simulation

An Instron® ETMT8800 Electrothermal Mechanical Testing System (ETMT) was used to replicate the temperature cycle experienced by the WAAM material as it is heated above the β transus temperature by the deposition of the next layer. The ETMT allows controlled resistive heating in miniature samples where the temperature is measured with a type-R thermocouple spot-welded to the sample, which also provides the feedback for the temperature control [24]. The ETMT sample was cut from the centre of the plane strain compressed sample by electrical discharge machining (to minimise surface deformation and thermal input) down to a cross section of 1.9 × 1.9 mm. The gauge length between the water-cooled grips was held at 15 mm, leaving 4 mm at each end of the sample to be gripped and ensure good electrical contact as shown in Figure 5c. The heating rate used was based on previous work where thermocouples were inserted into the melt pool during the WAAM process and it was found that the peak temperature was reached within 2 s upon the subsequent pass of the deposition [12]. The peak temperature at the centre of the sample was targeted to be 1100°C, to ensure that a significant section of the 15 mm gauge length was taken above the β transus of ~1000°C, but low enough to avoid rapid grain growth. Rapid cooling occurred by conduction to the water cooled grips, with the temperature dropping below 1000°C after 1 s and below 500°C in a further 8 s. The test was undertaken under load control in the ETMT, to allow free thermal expansion and contraction of the sample without generating significant stresses and unwanted deformation. Oxidation was prevented by maintaining a constant flow of argon shielding gas over the sample.

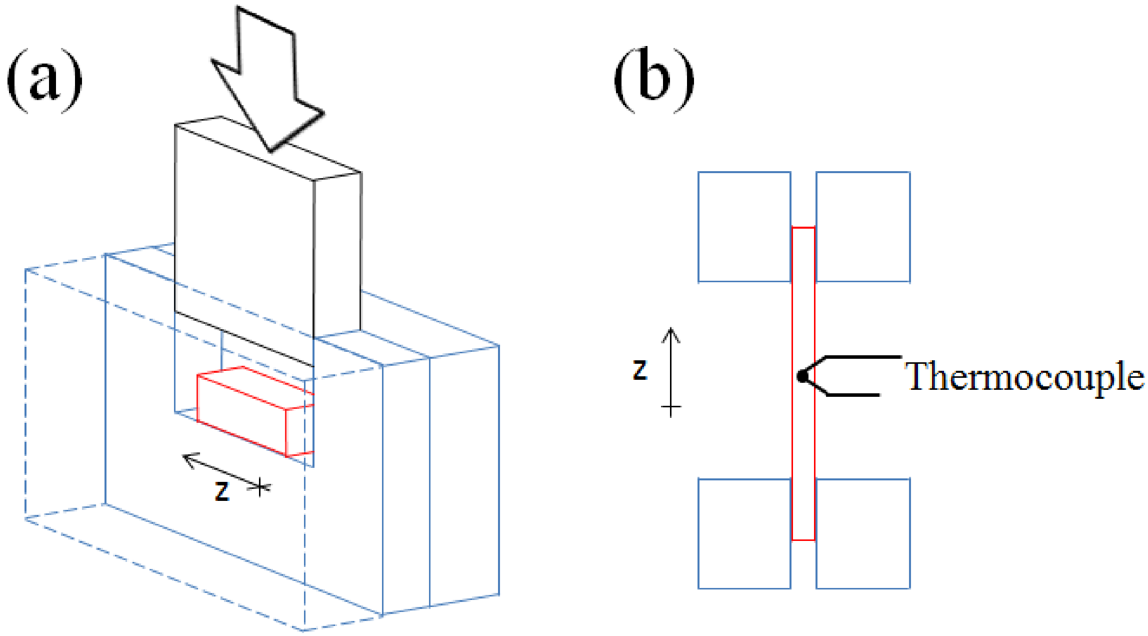

Figure 5. Schematic diagrams of the two main steps used to simulate the deformation and heating conditions in the WAAM process with the original build direction (and therefore columnar structure) of the AM samples indicated; (a) plane strain compression of the sample cut from the undeformed WAAM wall, and (b) ETMT experimental setup.

Following metallographic preparation of the ETMT samples, orientation analysis was carried out by EBSD mapping with a step size of 2 μm using a CamScam Maxim FEG-SEM. Orientation maps were collected with an Oxford instruments EBSD system, with Aztec acquisition software. A large, 13.0 × 1.9 mm area map encompassing half of the heated region of the ETMT sample was mapped, covering the region taken above the β transus as well as the region held below the transus temperature by the ETMT grips.

### *2.4 β phase reconstruction*

Due to the low volume fraction of residual β at room temperature in Ti-6Al-4V (~ 5-9% [25]), and the fact it is finely distributed between the α laths, it is difficult to directly map the β phase within AM samples and then infer the high temperature β structure, especially when mapping large areas. However, as there are only 12 possible α orientation variants that can be formed from each β grain upon transformation, it is possible to calculate orientation of the parent β phase data using a procedure developed by Davies and Wynne [26,27], based on earlier work by Humbert et al. [28,29]. This technique is explained fully in ref. [26] and involves comparing all the possible β orientations for neighbouring α variants and assigning the most common solution, allowing a prior β orientation map to be built up. During the reconstruction procedure, α points determined to belong to the same α variant were defined as those within 2° misorientation of each other, and only values diverging by less than 3° from the BOR are accepted for α variants to be considered part of the same prior β grain.

## 3.0 Results

### *3.1 In-situ heating*

**Region Selection**

The criteria for selecting a region of interest were the same used in the previous study [10]: to cover a prior β grain boundary, so the transformation could be observed in more than one grain; and to include the presence of α twinning deformation structures, as they have been found by the previous study to be the source of new β orientations during re-heating. The room temperature microstructure of the location chosen is shown in Figure 6a. The microstructure at room temperature largely consists of α plates that have formed in a colony microstructure on a prior β grain boundary through the centre of the region, as well as a Widmanstätten basketweave morphology further into each grain. At this higher resolution it was possible to index the fine residual β phase where it was at its thickest (e.g. at the triple points where the α laths meet). These measurements validated the β reconstruction procedure, giving identical orientations (Figure 6b), and confirmed the colony structures had formed on a prior β boundary. The black regions identifiable in Figure 6b are α orientations that have failed to reconstruct, due to reorientation caused by α twinning induced by rolling. Through boundary misorientation analysis, it was found that the twins were of the $\{10\bar{1}\bar{2}\}$ tensile mode, with a characteristic misorientation of 85° around $\langle 11\bar{2}0\rangle$ as highlighted in red in Figure 6c. From Figure 6b and 6c it is evident that the deformation twins continue across the prior β grain boundary. This occurred because although the two prior β grains are misorientated by ~40°, the two β grains had a common α variant, which in turn was only misorientated by ~10° with respect to the variants that make up the colonies either side of the prior β grain boundary. This misorientation was thus low enough to allow the twin to propagate across the boundary. It should be noted that the slight variation of colour within the prior β grains of the IPF coloured β reconstructed maps is a result of lattice rotation due to slip during rolling, which causes the orientation of the α variants to locally deviate away from exactly fulfilling the BOR.

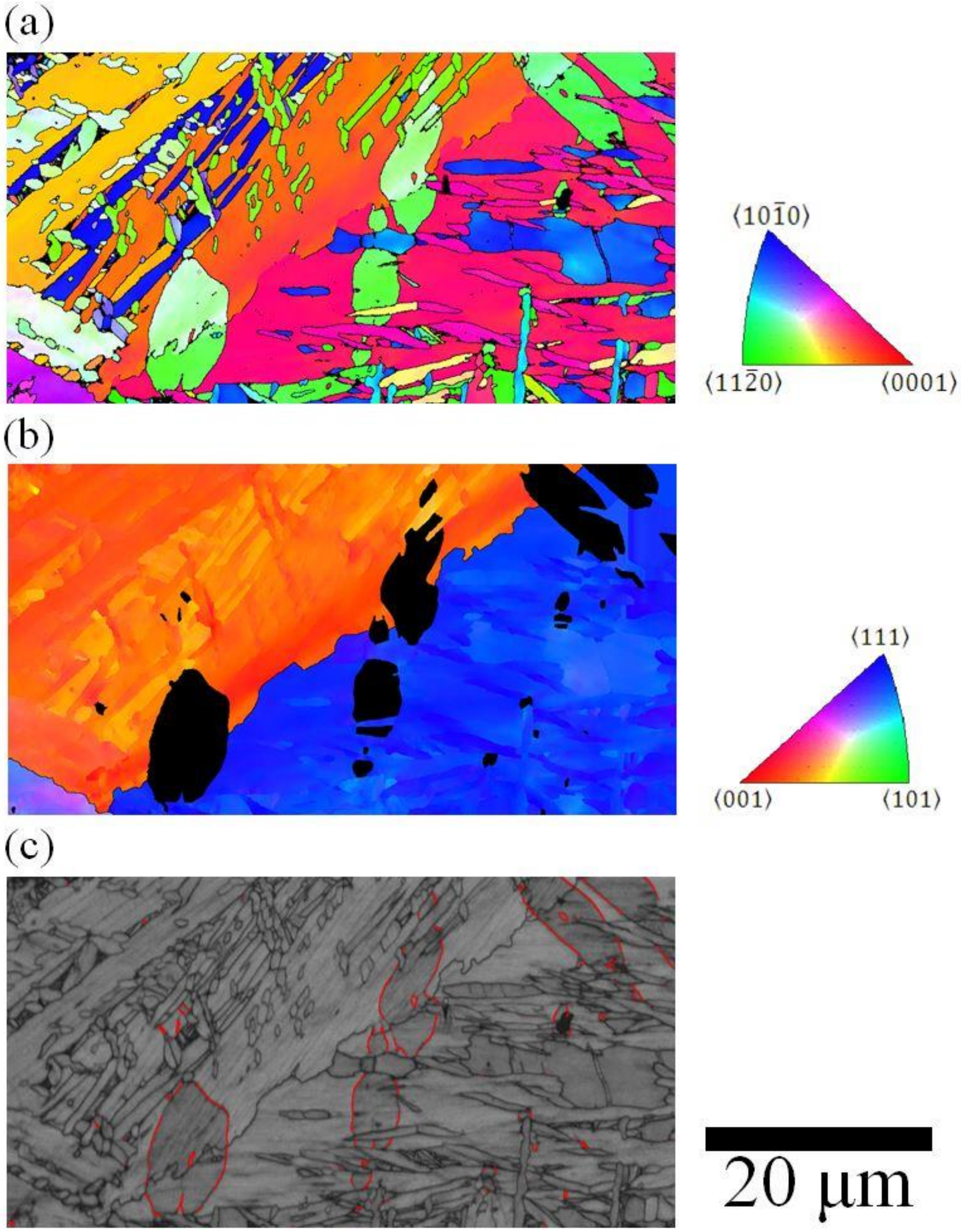

Figure 6. High resolution orientation maps from the region chosen for the in-situ heating experiment encompassing a prior β grain boundary. (a) measured α + β orientations in IPF colouring, (b) α twin boundaries highlighted on a band contrast map, and (c) a reconstructed β orientation map in IPF colouring.

**Heating Experiment**

Figure 7 shows the development of the selected region with temperature, observed by EBSD, with maps from the α and β phases shown separately in order to better appreciate the transformation process. Despite extensive efforts to achieve a high vacuum within the SEM chamber a thin film formed on the surface of the samples at 700°C, preventing the indexing of titanium EBSD patterns. The film remained on the sample surface until 800°C. When the sample reached a temperature of 850°C the majority of the film had disappeared, allowing EBSD analysis of the titanium to again take place (Figure 7b). However, a portion of this film was still present, as can be seen in Figure 7b, where there are a large number of points that are neither indexed as α or β phase. Despite this difficulty, the regions that did index well show a high degree of agreement with the room temperature map, suggesting that the microstructure is essentially stable up to this temperature.

When heated to 900°C and (Figure 7c) the entire area indexed well, with non-indexed points in the α map corresponding to regions indexed in the β map, indicating the total loss of the surface film that was previously affecting EBSD indexing. At this temperature, significant β transformation had taken place, with β growth occurring throughout the microstructure. As seen previously, new β orientations are observed growing from within the twinned α colonies, that share the BOR with the twinned α. However, unlike in the previous study, where β growth throughout the rest of the microstructure was limited to regrowth of the residual β orientations, several new β orientations were observed growing throughout the prior β grains, away from the twinned α colonies present at the grain boundaries. At least two additional β orientations other than the residual parent β orientation are observed growing within each of the prior β grains in the region studied. Further increasing the temperature to 950°C increased the amount of transformed β (Figure 7d), up to 35% of the indexed points, without generating new orientations.

### *3.2 Process Simulation*

The dimensions of the WAAM sample before and after deformation to simulate the rolling in the plane strain compression rig deformation are given in Table 1, as well as the resultant plastic strains. There was little expansion in the constrained direction indicating that deformation was close to the plane strain conditions experienced by the added layer when rolled. The plastic strain of ~13% is similar to those reached during the in-process rolling, which ranged from of 8 - 19% [11]. The heating rate achieved by the ETMT closely matched that recorded during processing, as can be seen in Figure 8. The peak temperature recorded at the centre of the sample was 1080°C, and therefore comfortably above the β transus.

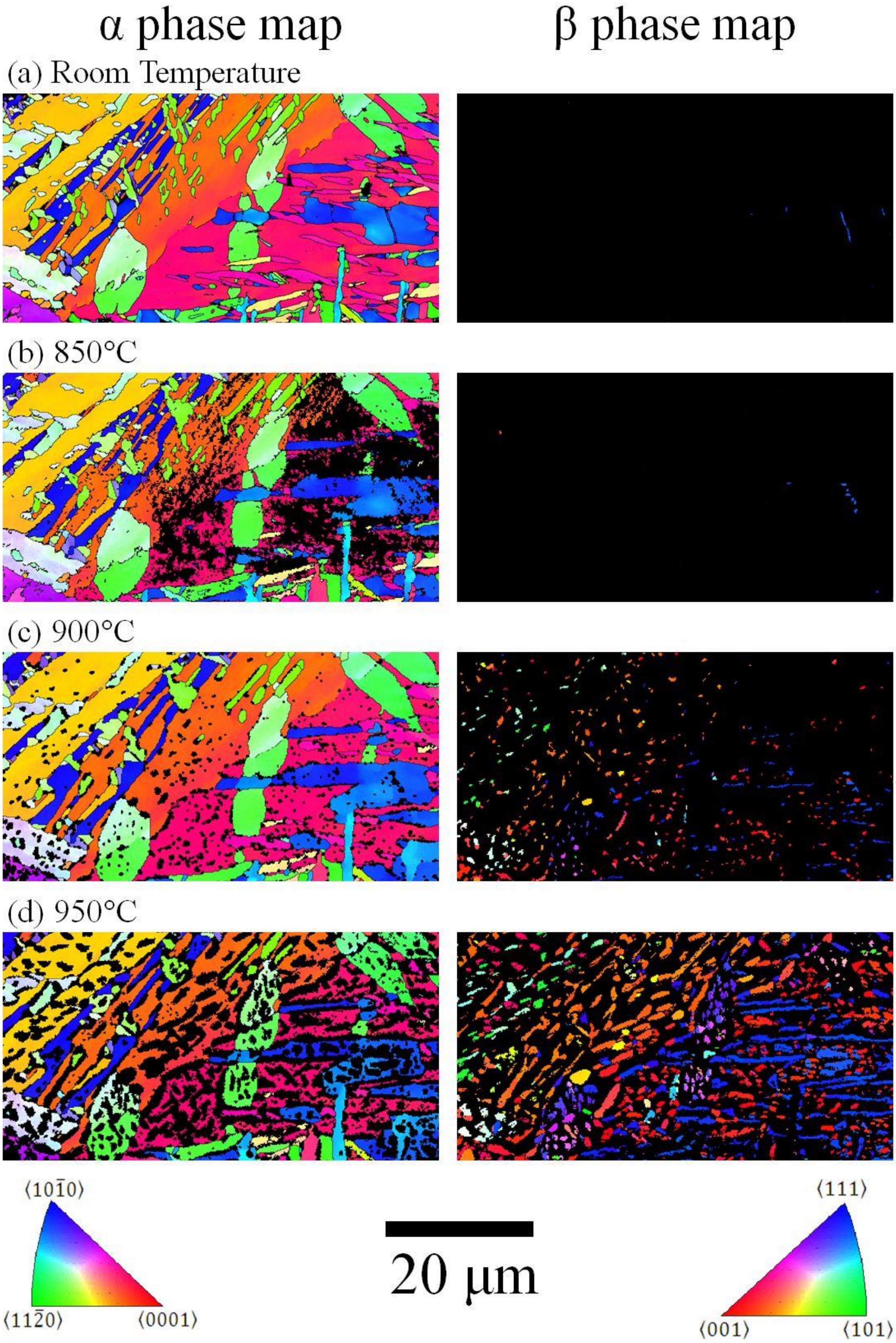

Figure 7. IPF coloured EBSD maps of the region studied by in-situ heating; a) room temperature (high resolution) b) 900°C, c) 925°C, and d) 950°C. The left and right maps show the α and β phases at each temperature.

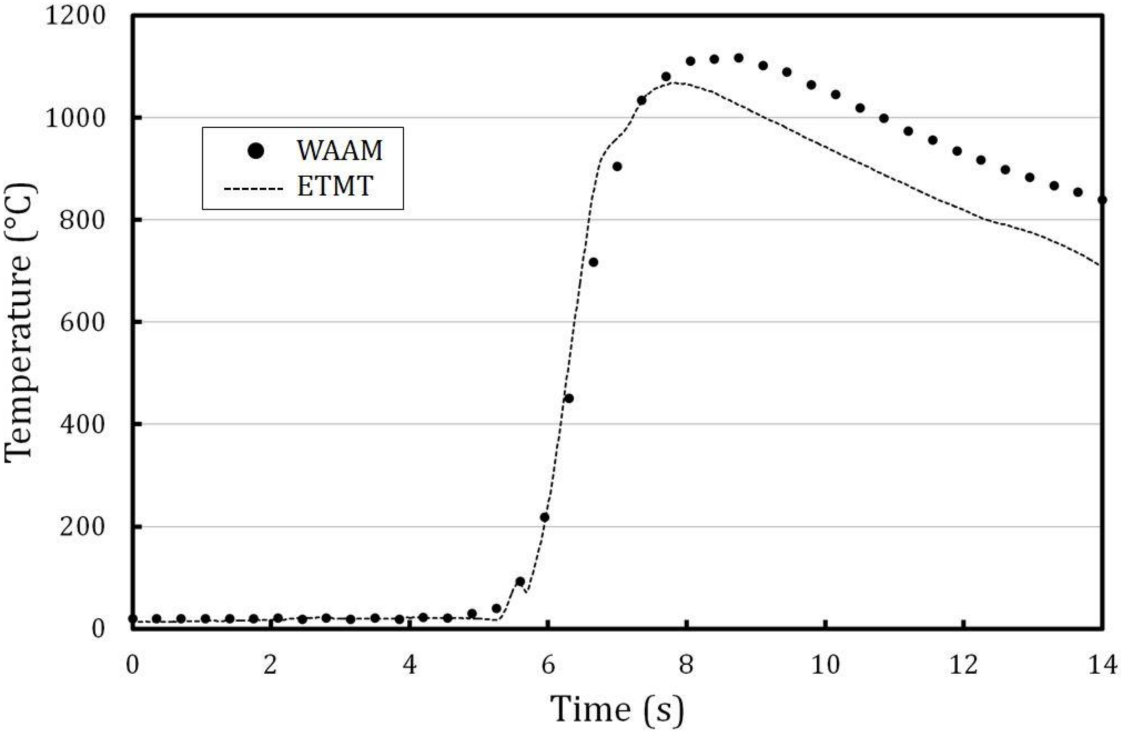

Figure 8. ETMT heating profile compared to that measured in the WAAM process in Ref[12].

A reconstructed β orientation map of half of the region studied is shown in Figure 9a. In the upper section the map successful refinement of the coarse columnar β structure has taken place, leading to an equiaxed β structure of refined grains of ~ 50μm. In contrast, in the lower section of Figure 9a no β refinement has occurred. Since the plastic strain across the length of the sample is constant, the lack of refinement implies that the maximum temperature in this region remained below the β transus temperature due to the influence of the cooled grips.

Table 1. Dimensions and plastic strains of WAAM block before and after plane strain compression.

| | Height (mm) | Length (mm) | Width (mm) | $\varepsilon_h$ | $\varepsilon_l$ | $\varepsilon_w$ |
|---|---|---|---|---|---|---|
| Before | 4.99 | 20.59 | 4.99 | - | - | - |
| After | 4.28 | 23.24 | 5.05 | - 0.142 | 0.129 | 0.012 |

The orientation map in Figure 9a is coloured using IPF colouring in the long direction of the sample, which is nearly parallel to the original columnar growth (see Figure 4b). In the refined region there is not only a significant reduction in β grain size, but also a wide range of new β orientations. However, within the IPF map it is possible to identify distinct regions within the refined zone of preference for grains of similar alignment. For example, there is a region in the upper right of the map where there is a prevalence of blue grains, which have a <111> direction parallel to the z direction. The boundaries of these regions are highlighted in Figure 9b.From the shape of these boundaries it is apparent that these regions probably correspond to different columnar β grains present prior to refinement. This theory is reinforced by the 001 pole figures included in Figure 9b that correspond to these regions. The contoured pole figures from each region in all cases consist of a four lobed spread of orientations symmetrically arranged around (an absent) single cube orientation. As each region has a distinct, and related, texture, this strongly suggests that the boundaries identified in Figure 9b correspond to the columnar prior β grain structure.

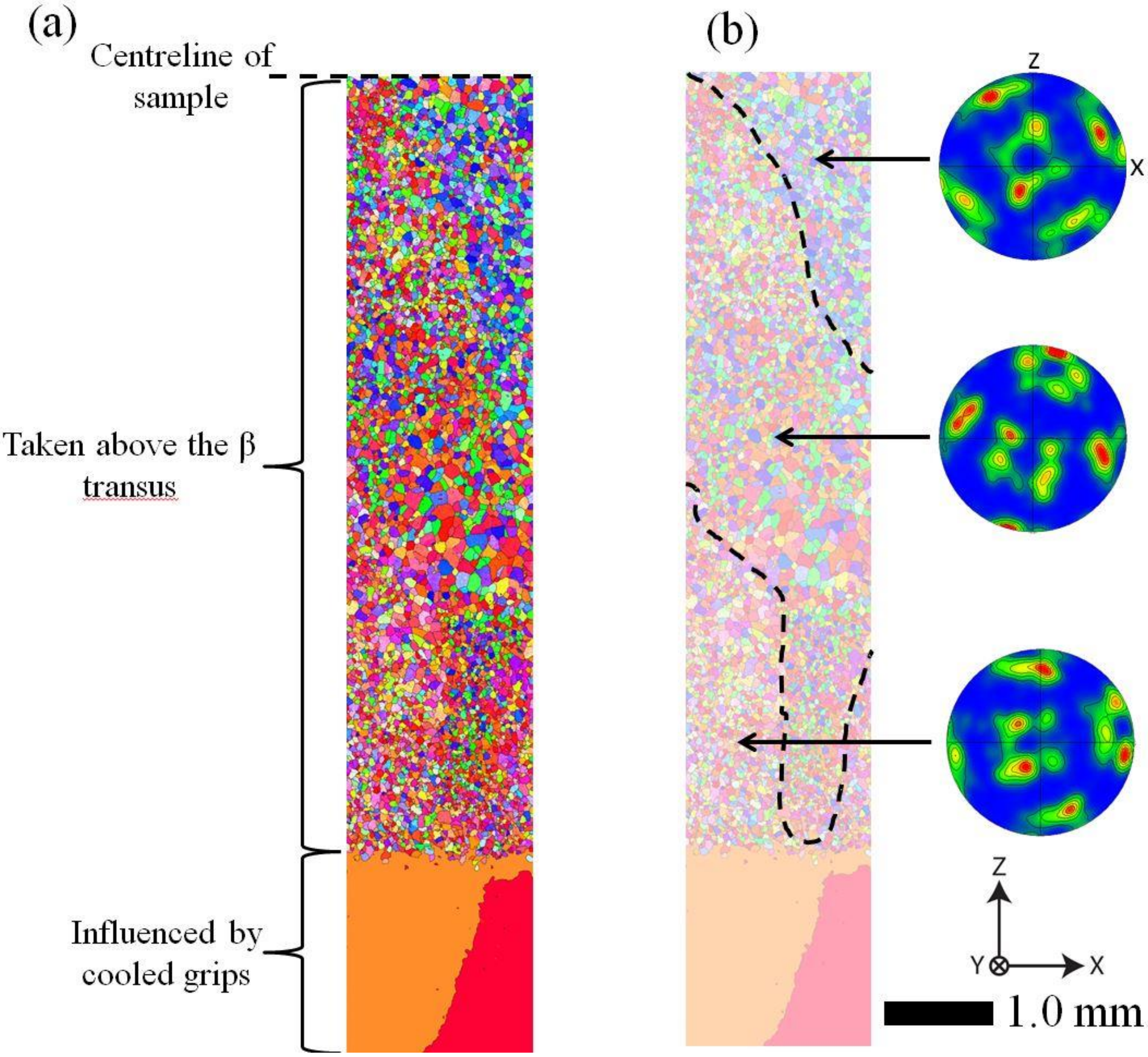

Figure 9. Reconstructed β orientation map of the deformed and reheated simulation sample with (a) the relevant locations on the sample marked, and (b) incorporating {100} pole figures of highlighted regions.

From Figure 10 it can also be appreciated in that there is an orientation relationship between grains in the refined microstructure to the β they refined from. This can be seen where the refined grains border the remainder of the coarse prior β grain they originated from, as the grain was not entirely heated above the β transus. The 001 pole figures in Figure 10 show that there is a clear relationship between the original β orientation and the resultant refined β texture, with the four lobed texture of the refined grains aligning symmetrically about the {001} poles of the prior β orientation.

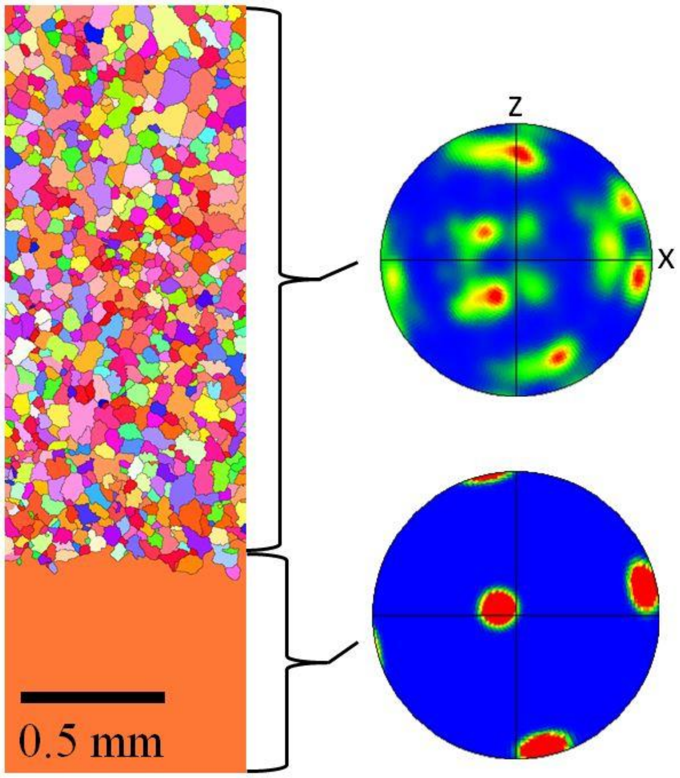

Figure 10. Magnified region of reconstructed β orientation map in Figure 9a, across a single β parent grain that only the top half of has been heated above the β transus and has transformed to the refined grain structure. {100} pole figures of both the parent grain and the refined region are provided.

## 4.0 Discussion

Simulation of both the rolling step and rapidly heating above the β transus has successfully replicated the prior β refinement observed in the WAAM process [11,12]. During previous WAAM trials, cold rolling strains of 8-19% led to an average refined prior β grain size of 90 - 140 μm, whereas in the simulated process an applied plastic strain of 13% produced a smaller average β grain size of 50 μm. This disparity can be explained by the difference in peak temperature reached during the simulation and in the process. In the simulated thermal cycle this was 1080°C, just above the β transus, whereas in the WAAM process the majority of the refined zone would have to be heated to a higher temperature and held above the β transus for longer, which promotes grain coarsening.

A possible explanation for the origin of the new grain orientations observed in the rolled samples and process simulation is given by the observation of the formation of new β orientations in the in-situ heating experiment in Figure 7. Unlike in the previous study [10] (summarised in Figure 2), that only found new β orientations developing from twinned α colonies, here we observed new β orientations growing throughout each original prior β grain interior.

Analysis of the α – β grain boundaries between the new β orientations and the deformed alpha finds that each new β orientation shares the Burgers' orientation relationship with one of the neighbouring deformed α grains. Therefore, it is conceivable that rather than the β growing from residual β in the structure, new β orientations are transforming directly from the deformed α. However, it is considerably more energetically favourable for a phase transformation to occur growing from material already of the high temperature phase rather than spontaneous transformation [14]. Therefore it would be expected that β would grow form the residual β in the microstructure in preference to directly from the α, particularly so far below the transus temperature. In addition, if each deformed α variant (12 in each prior β grain) had the capability to transform to β according to the Burgers' relationship (6 potential orientations), then it would be expected that each prior β grain would transform to a maximum of 72 orientations (although found to be slightly fewer due to crystallographic symmetry). This is a far greater number than observed in the in-situ heating experiment (where only a few distinct new β orientations were observed), and would lead to a far greater textural randomness than observed in the process simulated sample, where a reasonably strong, well defined texture was observed.

A further potential explanation for the origin of the new β orientations is indicated by misorientation analysis of the β – β grain boundaries in the sample heated to 950°C, where it is found that the majority of the boundaries correspond to bcc deformation twins.

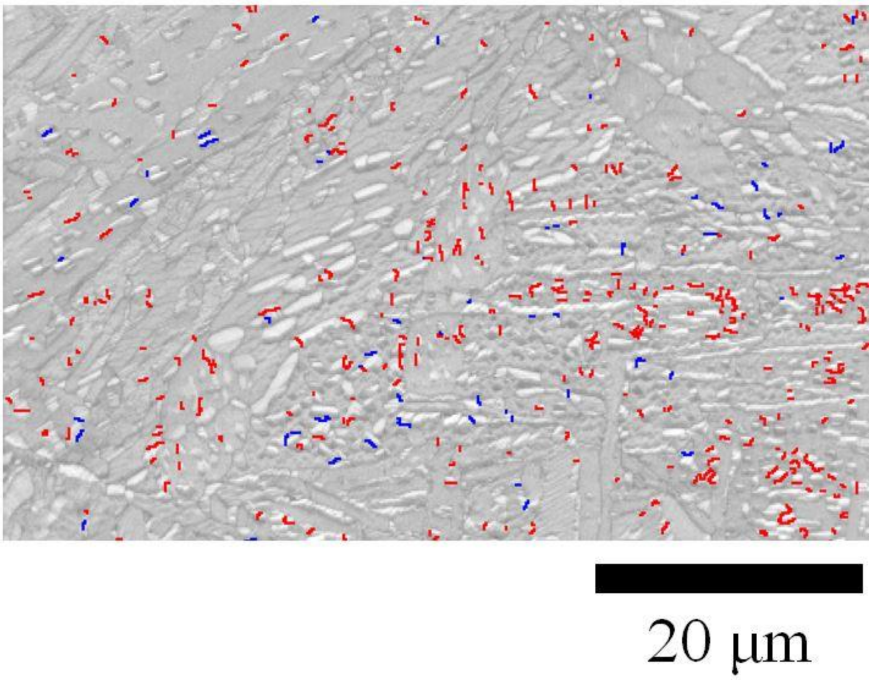

Figure 11. EBSD band contrast map taken at 950°C. Highlighted in red and blue are β-β grain boundaries corresponding to 60° around ⟨111⟩ and 51° around ⟨110⟩ respectively.

Figure 11 shows the band contrast image corresponding to the 950°C high temperature EBSD map in Figure 7d, on which specific β – β grain boundary misorientations have been highlighted. By far the most prevalent misorientation between neighbouring β is 60° around <111>, which corresponds to the bcc twinning system {112}<111>. Also present is a number of misorientated boundaries of 51° around <100>, a misorientation that corresponds to the twinning system {332}<113>. Both of these twinning systems have been observed occurring in metastable β titanium alloys [30–32] but have not to the authors knowledge been observed in the deformation of Ti-6Al-4V. Twinning is understood not to be favourable in the β phase in Ti-6Al-4V, as its composition does not favour the formation of ω phase that supposedly facilitates twinning in metastable β alloys [32]. However, it is possible that twinning of the β phase occurs in AM builds is due to the fine microstructure generated as a result of the rapid cooling rates involved in the process. For example, it has been found in other materials that below a certain grain size the critical stress needed to activate deformation twinning drops dramatically [33–35]. This is believed to be due to the reduced probability of the presence of defects in a nanoscale-volume of material to act as a dislocation sources in grain interiors. This makes deformation dominated by dislocation emission from grain boundaries, where the emission of partial dislocations for twinning have been found, to be easier than that of perfect dislocations [33]. This behaviour has most commonly been observed in fcc materials [33,35], although it has also recently been confirmed to occur in bcc structures [34]. It has been found that the emission of partial dislocations over perfect dislocations is preferred in nanowires of several bcc materials due to the increased influence the surface has on the energy to form dislocations [36]. The symmetrical positioning of the {001} poles of the refined grains from each of the prior coarse columnar grains in Figure 9b is also indicative of twinning.

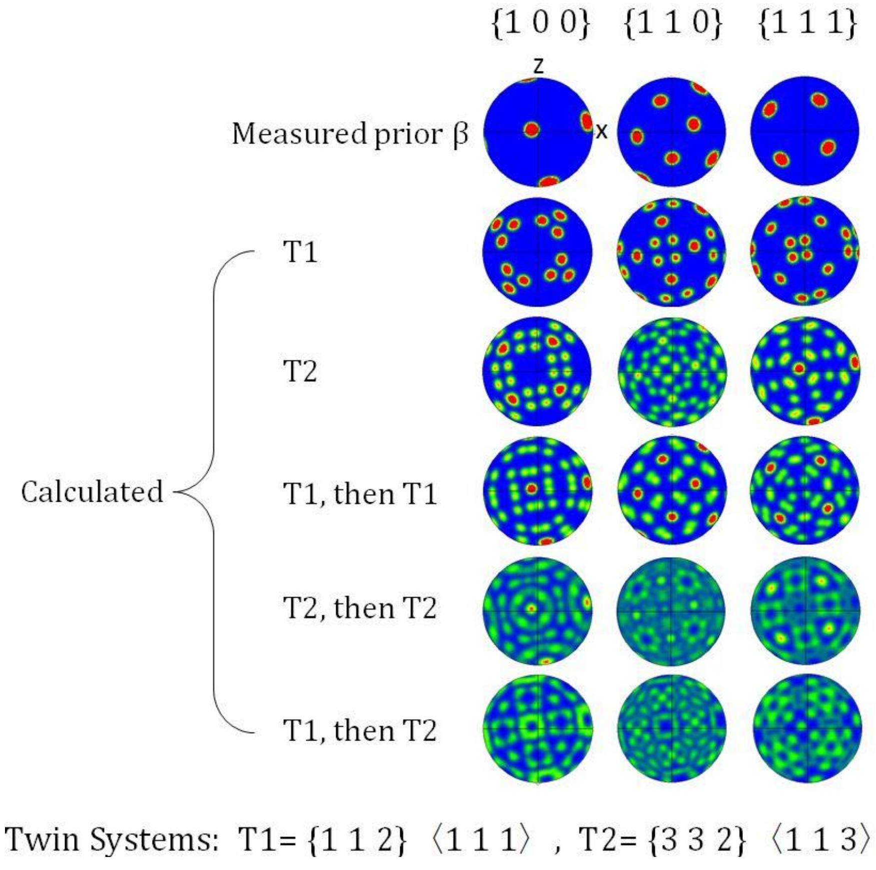

Figure 12. Resultant {100} pole figures of the orientations present after twinning a single orientation by the bcc twinning systems {112}<111> and {332}<113>, assuming all twinning systems are activated.

In order to see if the β twinning could have led to the new orientations of the refined β (Figure 9), we calculated the ideal orientations that are produced by different twinning operations from a single β parent orientation. The resultant simulated orientations are shown in Figure 12 using the parent orientation from the region highlighted in Figure 10. This specific orientation was chosen as the resultant orientations of the refined grains from this parent orientation were also known. From comparing Figure 10 and Figure 12, it is apparent that the twinning operation that most closely resembles the refined grain structure, is achieved when the original parent orientation is twinned by the {112}<111> system twice. This twinning operation results in 12 unique orientations that coincide closely with the positions observed in the pole figures in Figure 9. These new calculated twinned orientations and their correspondence to the refined region in the sample used to simulate the WAAM-rolling cycle are highlighted in Figure 13, where the same colouring is used to denote the twinned variants in the calculated pole figure, the measured pole figure from the reconstructed β grains, and the orientation map of the same region. There is a significant spread in the orientations of each variant, but with an allowed deviation of 7.5° from a central value, that 12 variants account for ~85% of the refined grains (Figure 13b & c) with certain variants appearing more prevalently than others. However, it was also found that although the simulated orientations agree well, that the majority of the measured refined grains were systematically orientated slightly closer (by ~5°) to the original parent orientation than predicted by the twinning reorientation alone. This difference can be seen by comparison of Figure 13a & b.

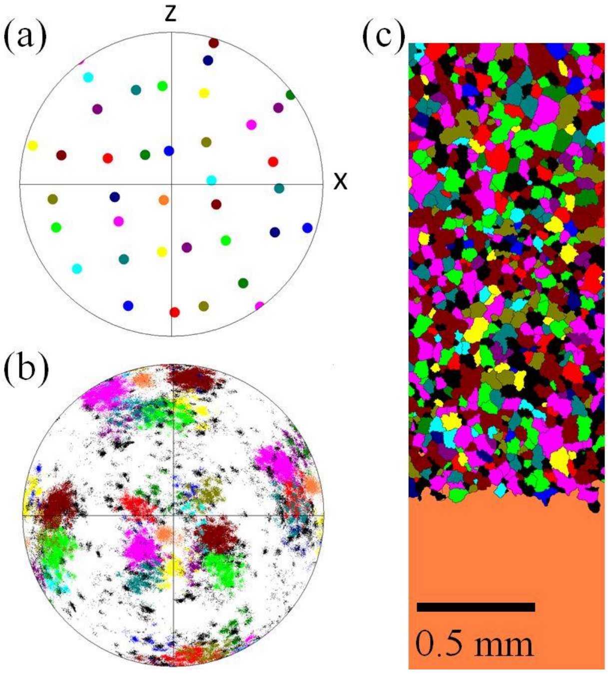

Figure 13. (a) Calculated pole figure showing the 12 independent orientations achieved by twinning the parent β orientation highlighted in Figure 10 by the ⟨111⟩ twinning system twice. The twinning systems are coloured individually and the colouring is continued into (b) and (c) where the non-contoured pole figure and reconstructed β orientation map of the region are given respectively.

Both this systematic shift and orientation spread can be accounted for by slip occurring in the α phase simultaneously to the β twinning during the room temperature deformation. The orientation spread between individual refined β grains from the same twin variant can be accounted for by the various constraining conditions on the residual β throughout the prior β grain due to the transformation microstructure. Prior to deformation all of the fine residual β between the α laths in a single prior β grain will be of the same initial orientation, however, the transformation microstructure of an interwoven basket weave structure of 12 different α variants ensures that the thin β is constrained in numerous different ways throughout the grain. The assortment of α variants locally surrounding residual β, combined with their orientation with respect to the loading direction, will determine the activation of the slip systems within them, and govern their shape change. Therefore, the rotation of the β away from a single orientation for each variant can be accounted for by the rigid body rotation of the twinned inter-lath β by the surrounding deforming α laths. This conjecture is supported by the observation of a similar orientation spread in the α variants from a single prior β grain in the deformed microstructure (a single α variant shown in Figure 14) as observed for a refined β variant (Figure 13b). The perceived rotation towards the parent orientation may instead be a rotation towards the deformation direction, as the cube orientation of the prior columnar β grains indicated in Figure 9 are found to be well aligned with the sample directions (that are in turn aligned with the deformation directions).

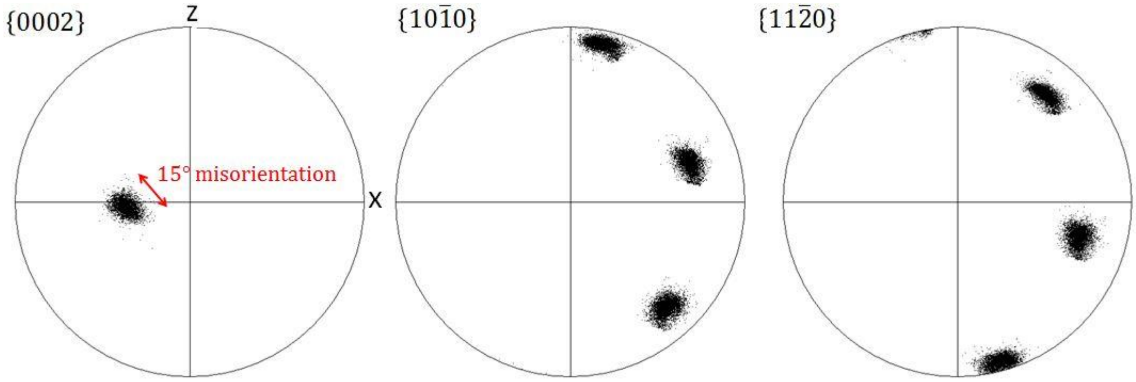

Figure 14. Hexagonal pole figures highlighting the orientation spread of an α variant from a single columnar grain after deformation.

The differing constraints experienced by the β micro-twins can also help explain why all 12 twinned variants are present rather than the more limited number of systems that would be predicted to be activated, by Schmidt factor analysis alone. Schmidt factor analysis would essentially compare the direction of twinning shear for each twinning system and select the system to be activated as the one that would best accommodate the stress relative to the direction of applied force.Therefore, for a single grain orientation it would always be predicted that the same twinning system would be activated for an applied stress (or two twinning systems if the Schmid factors are close). However, Schmidt factor analysis does not take into account constraint of neighbouring grains that may be orientated in a hard direction, or are an intrinsically harder phase, as α is in Ti-6Al-4V [37]. Therefore, it is feasible that within one prior β grain, similarly orientated residual β have twinned by different twinning systems dependent on local constraint. This may give rise to the observed microstructure where all 12 twin variants are present, albeit with differing prevalence.

Figure 13 indicates that 85% of the grains in the refined region can be directly related to twinning of their parent β orientation. The 15% of grains unaccounted for by the β twinning, described above appear black in the pole figure in Figure 13b, and their orientations appear to be almost randomly distributed. However, the small number of these grains makes it difficult to infer their origin. It is possible that these additional orientations could be the result of the second twinning system observed in the in-situ heating experiment, or have originated by the mechanism described in the previous heating experiment [10] with the new β orientations originating from, and sharing the Burgers' orientation relationship with, twinned α.

The one β orientation that is noticeably missing from the refined β microstructure is that of the parent β. It is known that in the deformed microstructure that there a considerable quantity of untwinned residual β of the parent orientation present in the microstructure, as measured by EBSD where it is thickest (eg. triple points at grain boundaries). It would therefore be expected that upon reheating above the β transus that the parent β would compete with the twinned orientations during transformation and growth, and be observed in the final refined microstructure. This is indeed what we observed during the in-situ heating experiment in Figure 7d.

A further difference between the in-situ heating experiment and the process simulation is that the double twinning of the {112}<111> system closely resembles the texture of the refined grains in the process simulated sample, whereas in the in–situ experiment, only growth from a single twinning of the residual β was observed. It is possible that these inconsistencies arise out of differences in the deformation conditions as direct measurement of the local strain within the rolled wall has not been made, only a global measurement of the entire wall. However, the strain used of 13% fell well within the process range of 8-19% that have been shown to result in similar refinement [11]. A larger difference between the two samples is the markedly different heating rates used, with the simulated sample mirroring the process with a heating rate of ~500 K/s, while the in-situ heating experiment only achieved a maximum heating rate of 0.70 K/s which fell away to less than 0.17 K/s at higher temperatures. These radically slower heating rates, combined with the isothermal holds at temperature to allow completion of the EBSD maps may have encouraged the growth, or survival, of β orientations that may otherwise have been suppressed under the rapid heating conditions (and vice versa). In addition, in the in-situ study the volume fraction of β observed did not exceed 35% and therefore competitive growth between orientations was not observed to occur.

It should also be noted that the in-situ experiment was carried out on a free surface. Not only does the free surface result in different constraint on the grains from those in the bulk, it was also affected by the formation of a thin surface film which we believe can be associated with an increase in the β transus temperature. For example, at 950°C, only 35% of indexed points were indexed as β phase, far below the level of transformation expected under equilibrium conditions of ~80% [11]. This suppression of the transformation can be attributed to the absorption of α stabilising oxygen or nitrogen into the sample surface at temperature, which is consistent with the formation of a surface contamination layer observed up to a temperature of ~800°C. If this layer disappeared at higher temperatures by adsorption into the surface, the increase in the interstitial content of the alloy, could account for the suppressed phase transformation and might also have affect other aspects of the transformation behaviour, such as the relative growth rates of the twinned β orientations.

Both the in-situ heating experiment and the process simulation suggest that twinning of the fine inter-lath residual β during cold working leads to the grain refinement observed in the AM techniques combined with deformation. However, we have not been able to detect these twins in the deformed microstructure at room temperature, only during in-situ heating. Since the β deformation twinning was limited to the thinnest β regions that cannot be indexed using EBSD, it is possible that such nanometre sized twins have simply escaped detection due to the ultimate resolution of the technique. Therefore, alternative characterisation techniques will be persued to directly measure and confirm that these β deformation structures exist in the deformed WAAM microstructure.

## 5.0 Conclusions

A high level of β grain refinement and textural weakening has been observed in wire based additive manufacture when an integrated rolling step is introduced to the process. This occurs for relatively low applied rolling reductions. To explain the origin of this effect we have successfully replicated the refined microstructure by simulating the deformation and the temperature profile of an added layer in an AM microstructure. A series of EBSD maps were also taken in-situ at increasing temperatures approaching the β transus from the roll deformed region of the WAAM wall in order to observe the growth of new β orientations, and their relation to the deformed microstructure.

The process simulation resulted in a similar refined equiaxed prior β grain structure with an average grain size of ~50µm, and with a greatly weakened texture, although it was found that the refined β grains bore an orientation relationship to the prior coarse β parent grain. The resultant refined microstructure texture could be related back to the original parent grain by double twinning via the {112}<111> β twinning system. Twins of this type were also observed in the rolled AM microstructure upon β growth when reheating close to the β transus in-situ by EBSD mapping. Therefore, overall the results strongly suggest that deformation β twinning gives rise to the new β orientations that act as nuclei for β regrowth, and hence grain refinement when a new layer is added. It is proposed that the unexpected twinning of the β is due to the fine microstructure generated in additive manufacture as a result of the rapid cooling rates involved, which leads to a very thin residual β layer between α laths.

Traditionally deformation processing of Ti-6Al-4V is carried out at high temperatures due to the high flow stresses and perceived large strains required to break up the large prior β structure formed on casting. The discovery of a new mechanism for β refinement requiring small strains could have far reaching consequences. However, this mechanism is potentially only limited to exploitation in small volume production of Ti-6Al-4V, as both the cooling rates required to generate the fine microstructure, and the forces required to plastically deform the material at room temperature would be prohibitively difficult to achieve in a large billet. Additive Manufacture is particularly suited to taking advantage of this mechanism since although large parts can still be built, the forces are kept low by only deforming small volumes at a time, and the necessary rapid heating and cooling rates required to limit β grain growth and form a fine transformation microstructure are inherent to the process.

## Acknowledgements

The authors would like to thank Prof. S. Williams group at Cranfield University for the manufacture of the rolled WAAM walls and provision of build temperature measurements. Thanks also to Prof. Brad Wynne (University of Sheffield) for provision of the β reconstruction software. J. Donoghue is grateful for financial support provided by LATEST2 (EP/G022402/1) and Airbus, UK.

## References

[1] J. Allen, An Investigation into the Comparative Costs of Additive Manufacture vs. Machine from Solid for Aero Engine Parts. Cost Eff. Manuf. via Net-Shape Process. 2006; 1–10.

[2] B.E. Carroll, T. a. Palmer, A.M. Beese, Anisotropic tensile behavior of Ti–6Al–4V components fabricated with directed energy deposition additive manufacturing. Acta Mater. 2015; 87: 309–320.

[3] E. Brandl, B. Baufeld, C. Leyens, R. Gault, Additive manufactured Ti-6Al-4V using welding wire: comparison of laser and arc beam deposition and evaluation with respect to aerospace material specifications. Phys. Procedia. 2010; 5: 595–606.

[4] P. Kobryn, S. Semiatin, The laser additive manufacture of Ti-6Al-4V. JOM. 2001; 40–42.

[5] H.K. Rafi, N. V. Karthik, H. Gong, T.L. Starr, B.E. Stucker, Microstructures and Mechanical Properties of Ti6Al4V Parts Fabricated by Selective Laser Melting and Electron Beam Melting. J. Mater. Eng. Perform. 2013; 22: 3872–3883.

[6] A.A. Antonysamy, P.B. Prangnell, J. Meyer, Effect of Wall Thickness Transitions on Texture and Grain Structure in Additive Layer Manufacture (ALM) of Ti-6Al-4V. Mater. Sci. Forum. 2012; 706-709: 205–210.

[7] P. Edwards, A. O'Conner, M. Ramulu, Electron Beam Additive Manufacturing of Titanium Components: Properties and Performance. J. Manuf. Sci. Eng. 2013; 135: 061016.

[8] B. Baufeld, O. Van Der Biest, R. Gault, Additive manufacturing of Ti–6Al–4V components by shaped metal deposition: Microstructure and mechanical properties. Mater. Des. 2010; 31: S106–S111.

[9] A.A. Antonysamy, J. Meyer, P.B. Prangnell, Effect of Build Geometry on the β−Grain Structure and Texture in Additive Manufacture of Ti-6Al-4V by Selective Electron Beam Melting. Mater. Charact. 2013;

[10] J. Donoghue, A. Gholinia, J. Quinta da Fonseca, P.B. Prangnell, In-situ High Temperature EBSD Analysis of the Effect of aDeformation Step on the Alpha to Beta Transition in Additive Manufactured Ti-6Al-4V, in: TMS Titan., San Diago, 2015.

[11] J. Donoghue, A.A. Antonysamy, F. Martina, P.A. Colegrove, S.W. Williams, P.B. Prangnell, The effectiveness of combining rolling deformation with Wire–Arc Additive Manufacture on β-grain refinement and texture modification in Ti–6Al–4V. Mater. Charact. 2016; 114: 103–114.

[12] F. Martina, P. A. Colegrove, S.W. Williams, J. Meyer, Microstructure of Interpass Rolled Wire + Arc Additive Manufacturing Ti-6Al-4V Components. Metall. Mater. Trans. A. 2015; 46: 6103–6118.

[13] M.J. Bermingham, S.D. McDonald, M.S. Dargusch, D.H. StJohn, Grain-refinement mechanisms in titanium alloys. J. Mater. Res. 2011; 23: 97–104.

[14] D.A. Porter, K.E. Easterling, M.Y. Sherif, Phase Transformations in Metals and Alloys, Taylor & Francis Group, 2009.

[15] M. Rappaz, S.A. David, J.M. Vitek, L.A. Boatner, Analysis of solidification microstructures in Fe-Ni-Cr single-crystal welds. Metall. Trans. A. 1990; 21: 1767–1782.

[16] S.S. Al-Bermani, M.L. Blackmore, W. Zhang, I. Todd, The Origin of Microstructural Diversity, Texture, and Mechanical Properties in Electron Beam Melted Ti-6Al-4V. Metall. Mater. Trans. A. 2010; 41: 3422–3434.

[17] M.J. Bermingham, S.D. McDonald, K. Nogita, D.H. St. John, M.S. Dargusch, Effects of boron on microstructure in cast titanium alloys. Scr. Mater. 2008; 59: 538–541.

[18] S. Tamirisakandala, R.B. Bhat, J.S. Tiley, D.B. Miracle, Grain refinement of cast titanium alloys via trace boron addition. Scr. Mater. 2005; 53: 1421–1426.

[19] S. Gorsse, D. Miracle, Mechanical properties of Ti-6Al-4V/TiB composites with randomly oriented and aligned TiB reinforcements. Acta Mater. 2003; 51: 2427–2442.

[20] S.L. Semiatin, V. Seetharaman, I. Weiss, The thermomechanical processing of alpha/beta titanium alloys. Jom. 1997; 49: 33–39.

[21] K. Muszka, M. Lopez-Pedrosa, K. Raszka, M. Thomas, W.M. Rainforth, B.P. Wynne, The Impact of Strain Reversal on Microstructure Evolution and Orientation Relationships in Ti-6Al-4V with an Initial Alpha Colony Microstructure. Metall. Mater. Trans. A. 2014; 45: 5997–6007.

[22] F. Martina, S.W. Williams, P. Colegrove, Improved microstructure and increased mechanical properties of additive manufacture produced Ti-6Al-4V by interpass cold rolling, in: SFF Symp., 2013: pp. 490–496.

[23] P. Colegrove, H.E. Coules, J. Fairman, F. Martina, T. Kashoob, H. Mamash, et al., Microstructure and residual stress improvement in wire and arc additively manufactured parts through high-pressure rolling. J. Mater. Process. Technol. 2013; 213: 1782–1791.

[24] B. Roebuck, D.C. Cox, R.C. Reed, An Innovative Device for the Mechanical Testing of Miniature Specimens of Superalloys. Superalloys 2004 (Tenth Int. Symp. 2004; 523–528.

[25] G. A. Sargent, K.T. Kinsel, A. L. Pilchak, A. A. Salem, S.L. Semiatin, Variant Selection During Cooling after Beta Annealing of Ti-6Al-4V Ingot Material. Metall. Mater. Trans. A. 2012; 43: 3570–3585.

[26] P.S. Davies, An investigation of microstructure and texture evolution in the Near-α titanium alloy timetal 834, University of Sheffield, 2009.

[27] P.S. Davies, B.P. Wynne, W.M. Rainforth, M.J. Thomas, P.L. Threadgill, Development of Microstructure and Crystallographic Texture during Stationary Shoulder Friction Stir Welding of Ti-6Al-4V. Metall. Mater. Trans. A. 2011; 42: 2278–2289.

[28] M. Humbert, N. Gey, The calculation of a parent grain orientation from inherited variants for approximate (b.c.c.–h.c.p.) orientation relations. J. Appl. Crystallogr. 2002; 35: 401–405.

[29] N. Gey, M. Humbert, Specific analysis of EBSD data to study the texture inheritance due to the β→ α phase transformation. J. Mater. Sci. 2003; 8: 1289–1294.

[30] Y. Yang, G.P. Li, G.M. Cheng, H. Wang, M. Zhang, F. Xu, et al., Stress-introduced α″ martensite and twinning in a multifunctional titanium alloy. Scr. Mater. 2008; 58: 9–12.

[31] E. Bertrand, P. Castany, I. Péron, T. Gloriant, Twinning system selection in a metastable β-titanium alloy by Schmid factor analysis. Scr. Mater. 2011; 64: 1110–1113.

[32] S. Hanada, O. Izumi, Transmission electron microscopic observations of mechanical twinning in metastable beta titanium alloys. Metall. Trans. A. 1986; 17: 1409–1420.

[33] Y.T. Zhu, X.Z. Liao, X.L. Wu, J. Narayan, Grain size effect on deformation twinning and detwinning. J. Mater. Sci. 2013; 48: 4467–4475.

[34] J. Wang, Z. Zeng, C.R. Weinberger, Z. Zhang, T. Zhu, S.X. Mao, In-situ atomic-scale observation of twinning-dominated deformation in nanoscale body-centred cubic tungsten. Nat. Mater. 2015; 14: 594–600.

[35] H.S. Park, K. Gall, J.A. Zimmerman, Deformation of FCC nanowires by twinning and slip. J. Mech. Phys. Solids. 2006; 54: 1862–1881.

[36] S. Li, X. Ding, J. Deng, T. Lookman, J. Li, X. Ren, et al., Superelasticity in bcc nanowires by a reversible twinning mechanism. Phys. Rev. B - Condens. Matter Mater. Phys. 2010; 82: 1–12.

[37] A.M. Stapleton, S.L. Raghunathan, I. Bantounas, H.J. Stone, T.C. Lindley, D. Dye, Evolution of lattice strain in Ti-6Al-4V during tensile loading at room temperature. Acta Mater. 2008; 56: 6186–6196.

# 5. Corroborative Experiments

This chapter contains and discusses additional experiments designed to further substantiate some of the results of the included in the paper manuscripts, and to validate some of the experimental methods used. The first section reports on attempts to observe in the room temperature deformed WAAM microstructure the β twins that were observed growing during the α → β phase transformation by the in-situ high temperature EBSD experiment in **Manuscript 4**. The second section attempts to understand the disparity between the volume transformed to β from that predicted by thermodynamic calculations, to that observed experimentally in both of the in-situ experiments in in **Manuscripts 3** and **4**.

## 5.1. High Resolution Orientation Mapping

It was suggested in **Manuscript 4** that the refined β grains observed in AM builds that were combined with a deformation step could have originated from twins in the residual β. These twins were only observed at high temperature, where phase transformation had increased the volume fraction of β phase, and individual β grains had grown to a size that allowed identification by EBSD. However, it was theorised that these β twins were formed under deformation of the AM material at room temperature, where β twinning was encouraged due to the fine constrained volumes of residual β between the α laths. The probed volume of a typical SEM beam that leads to the diffraction patterns for EBSD analysis is generally larger than the volume of β between trapped between α laths. All of the direct measurements of residual β by EBSD in **Manuscript 3** and **Manuscript 4** were therefore made where the residual β was thickest, i.e. at triple points where α laths meet. Therefore, in an attempt to identify β twins in the room temperature deformed microstructure, two high resolution orientation mapping techniques were used, Transmission Kikuchi Diffraction (TKD) and automated crystal orientation mapping within the TEM.

### *5.1.1. Transmission Kikuchi Diffraction*

A sample was taken from a WAAM wall where the final process step was a pass of the roller with a 75kN load. The thin sample required for TKD was extracted and thinned by FIB (See §3.3.2) and was taken from the region identified in **Manuscript 2** as the volume that had undergone the highest plastic strain, as shown in Figure 5:1.

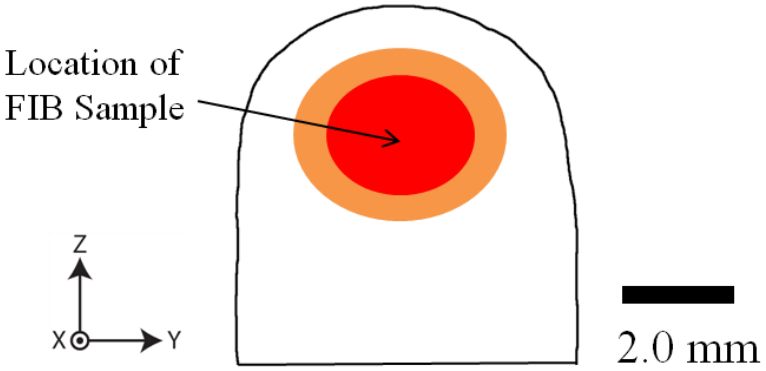

Figure 5:1. Schematic of the cross-section of a rolled wall with the region most highly strained highlighted and the location of sample prepared by FIB for TKD.

The beam settings and experimental setup were those as described in §3.5.2. The resultant TKD map is shown in Figure 5:2.

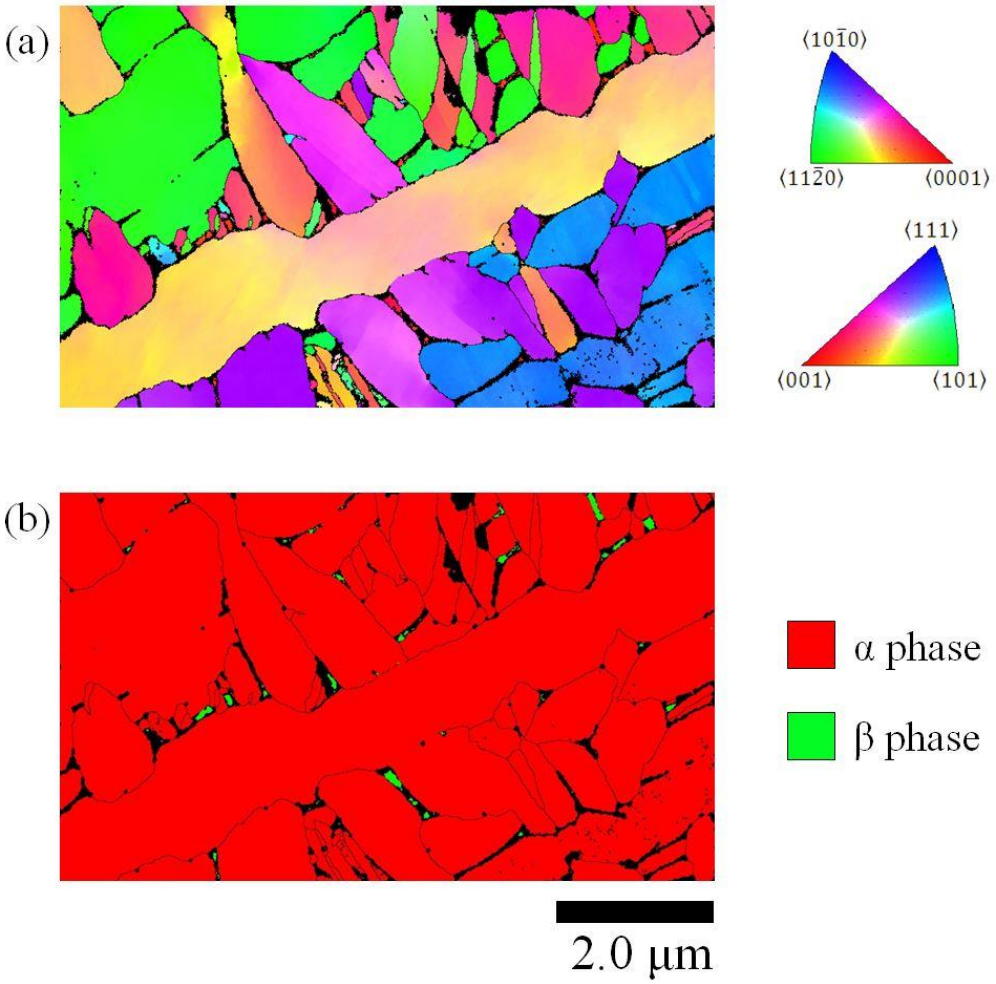

Figure 5:2. TKD map displayed in (a), IPF colouring with respect to the build direction, and (b) coloured by phase.

Of the indexed points, only 0.50% were indexed as β phase. A β phase content of 0.50% is an order of magnitude higher than the 0.08% indexed in the high resolution EBSD map presented in **Manuscript 3** achieved with the FEI Magellan in the bulk material, but is considerably lower than would be expected at this temperature (See §5.2). The orientation of the residual β throughout the map was found to be a single orientation and was consistent with that calculated by the β reconstruction software from the indexed α variants, as shown in Figure 5:3. Therefore, no evidence could be found of the β twins observed at temperature in **Manuscript 4**. However, 8% of the region investigated by TKD remained unindexed, and as can be seen from Figure 5:2, the majority of these unindexed points exist at α grain boundaries that are likely to be α – β – α phase boundaries. These points remained unindexed due to multiple crystals interacting with the electron beam at these phase boundaries, as a consequence of the size of the probed volume relative to the very fine nature of the retained β, resulting in composite overlapping and indistinct Kikuchi patterns as each grain diffracts.

As it is believed that twinning of the β is most likely to occur where the β is thinnest, the inability to index orientations by TKD in these regions means that TKD analysis could not be used to state categorically whether the twins exist in the deformed microstructure or not. The non-indexing is due to the resolution limit of TKD. Therefore, the next step in searching for the twins was to attempt an even higher spatial resolution orientation mapping technique using automated orientation mapping in the TEM.

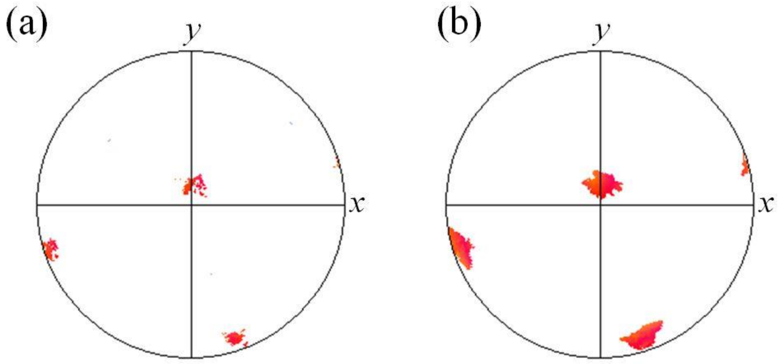

Figure 5:3. {100} pole figures of: (a), the residual β indexed by TKD, and (b), calculated by reconstruction from the α orientations indexed in the same map.

### *5.1.2. Automated Crystal Orientation Mapping in the TEM*

Automated orientation mapping in the TEM (henceforth referred to ASTAR after the acquisition software) sacrifices angular resolution for a reduced probe size, and therefore improved spatial resolution. However, as the features of interest are β twins with a large misorientation (e.g. the observed bcc twinning system is associated with a 60° rotation of the crystal lattice around the <111> axis relative to the parent), the reduction in angular resolution compared to TKD is not critical. The automated orientation mapping equipment used in this study was ASTAR as described in §3.5.2, where the microscope operating conditions are also given. It has previously been found that the interaction volume using this technique falls from ~12 nm in TKD to ~3 nm for automated orientation mapping in the TEM [160].

The sample investigated by TEM was the same sample as used in the TKD study in the previous section, §5.1.1. The 0.72 × 3.80 µm region of interest was selected based on the TKD orientation maps. The selected region is highlighted on the TKD maps in Figure 5:4 a &b, and was chosen due to the number of fine α boundaries that it encompassed, as well as it including an α twin (α twin boundaries highlighted in red in Figure 5:4b) that crosses an α colony boundary. The nature of the deformation of the β between the α laths within a twinned α colony was of interest due to the situation observed in the first in-situ heating experiment in **Manuscript 3**, where a new β orientation was observed growing from a twinned α colony with the Burgers' orientation relationship maintained with the twinned α grain.

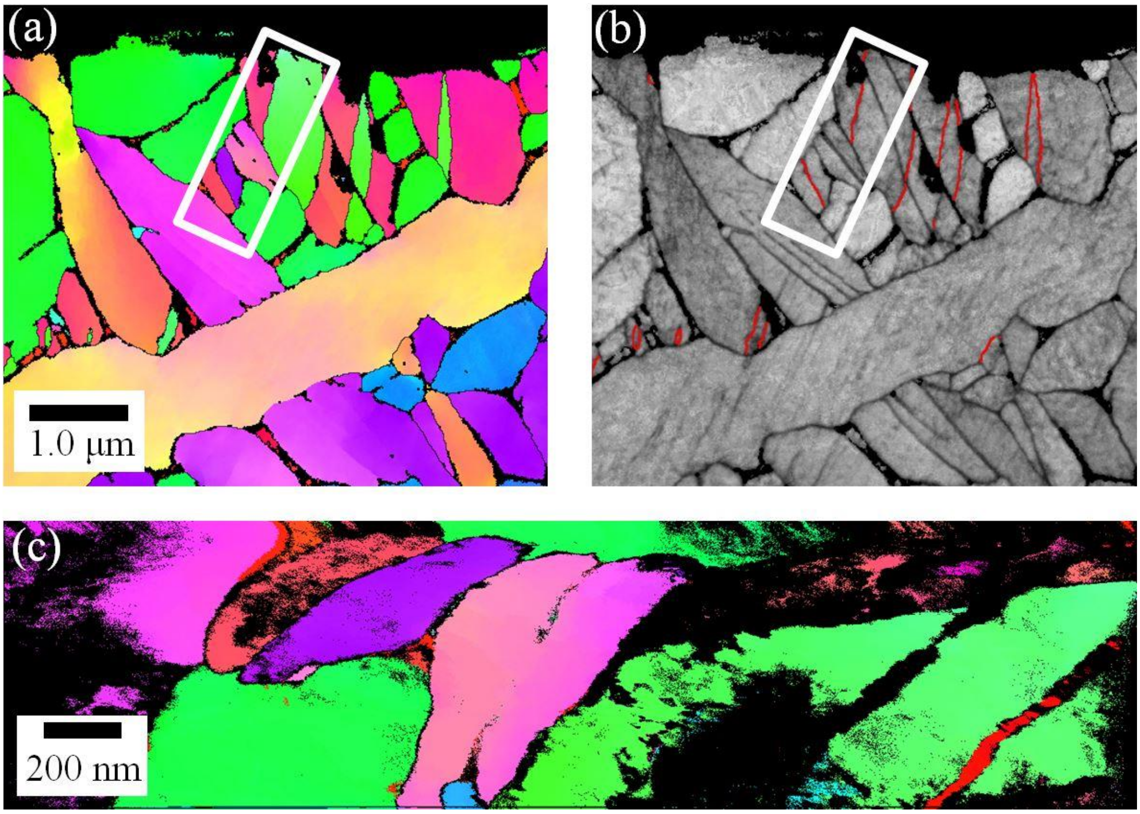

Figure 5:4. (a) reproduction of the orientation map acquired by TKD in Figure 5:2a, highlighting the region mapped in the TEM. The region selected is also highlighted in (b), a band contrast map of the TKD patterns with misorientations of 85° around $\langle 11\bar{2}0\rangle$ indicated in red. (c) the orientation map acquired by ASTAR of the selected region in the same IPF colouring of the TKD map.

There are several differences that can be noted when comparison is made between the two high resolution orientation maps of the region by TKD and ASTAR in Figure 5:4a & c respectively. The first thing of note in Figure 5:4 is the distortion in the shape of the grains in the ASTAR map compared to those observed by TKD, due to drift of the sample relative to the beam, most likely as a consequence of temperature changes during the long scan and sample movement due to thermal expansion. Secondly, it is evident from the IPF colouring that there are several additional orientations indexed in the ASTAR map. However, by eye it is apparent that some of these orientations may be due to misindexing, due to their speckled appearance throughout grains of known orientation from the TKD data. Misindexing was confirmed by analysis of the diffraction patterns in one of these regions as shown in figure Figure 5:5. Despite the similar appearance of the diffraction patterns, one is indexed as the hexagonal crystal structure and the other as cubic. The majority of points in this region are indexed as a hexagonal phase, and this is assumed to be correct due to correspondence with the measurement by TKD. The misindexing of the cubic phase in this case is possibly due a small difference in the tilt of the crystal relative to the incident beam in different locations, leading to different spots diffracting more strongly than others, as can be seen in the diffraction patterns of Figure 5:5b compared to Figure 5:5c. Although these diffraction patterns are similar, the differing relative intensity of the spots in Figure 5:5b leads the indexing software to incorrectly assign the β phase as the correct solution. This error could be reduced with stronger diffraction patterns so more outer spots are visible. Weak diffraction patterns can be caused by numerous factors, including the thickness of the sample, imperfections in the crystal lattice, and the beam interacting with more than one crystal system through the thickness.

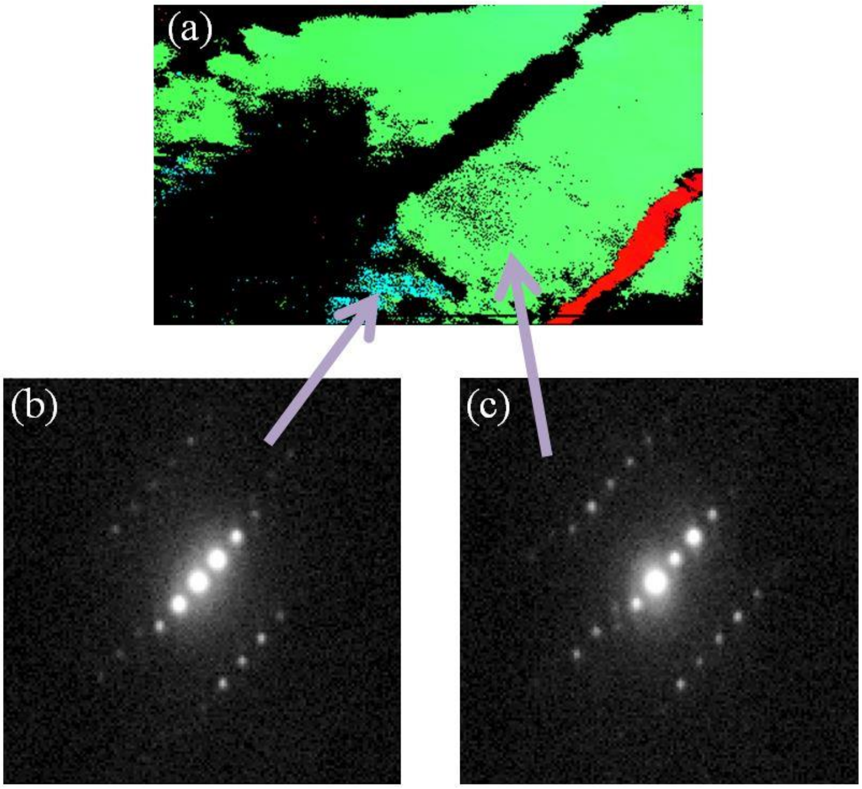

Figure 5:5. A magnified region of the ASTAR map in Figure 5:4 c, with locations of diffraction patterns that were indexed as cubic and hexagonal in (b) and (c) respectively.

It is evident that the high resolution mapping using ASTAR in the TEM has been able to index the residual β successfully where TKD was not able to. For example, in the thin layers of β between α laths of the same colony on the right hand side of Figure 5:4 c. The indexed β phase (after discounting obvious misindexing highlighted in Figure 5:5) is shown without the α phase in Figure 5:6.

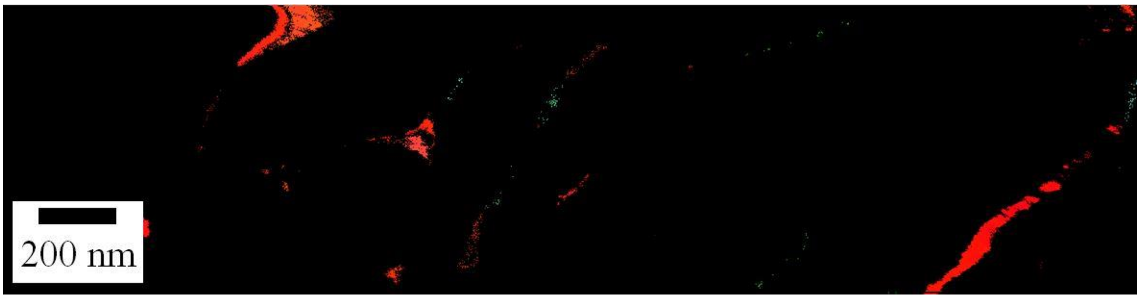

Figure 5:6. Orientation map of the β phase as indexed by ASTAR.

It is apparent that the majority of the indexed β is of a single orientation, and this orientation is consistent as that measured by TKD and calculated by β reconstruction in Figure 5:3. Therefore the majority of the β indexed is residual of the transformation from the β transus. However, a small quantity of a second β orientation was found in the ASTAR mapping (coloured green in Figure 5:3). Unfortunately, further analysis indicated similar misindexing to that shown in Figure 5:5, though this time at a location between two α laths where one would expect to find β, as shown in Figure 5:7.

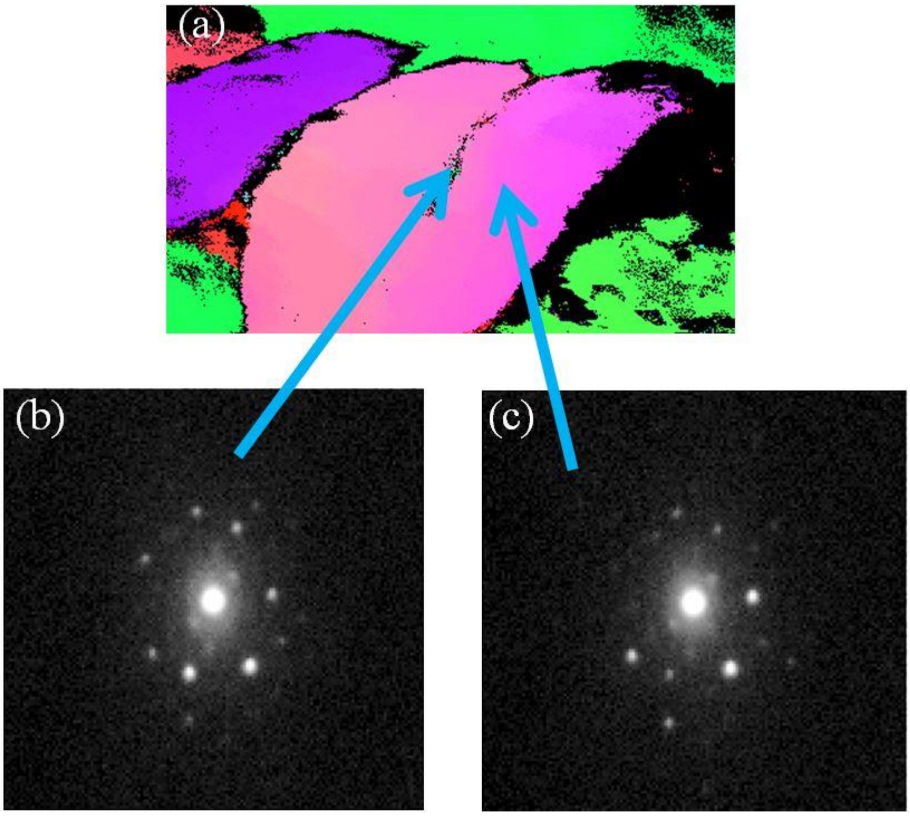

Figure 5:7. A magnified region of the ASTAR map in Figure 5:4 c, with locations of diffraction patterns that were indexed as cubic and hexagonal in (b) and (c) respectively.

As with the case in Figure 5:5, this misindexing is likely due to a small lattice rotation leading to different intensities in the diffraction pattern, causing the indexing software to mistakenly an incorrect solution. However in this case the location is between two α laths, where one would expect to find β, the weak diffraction pattern could be due to the beam interacting with at least two crystal systems, and likely a second phase, as it passes through the sample as shown schematically in Figure 5:8.

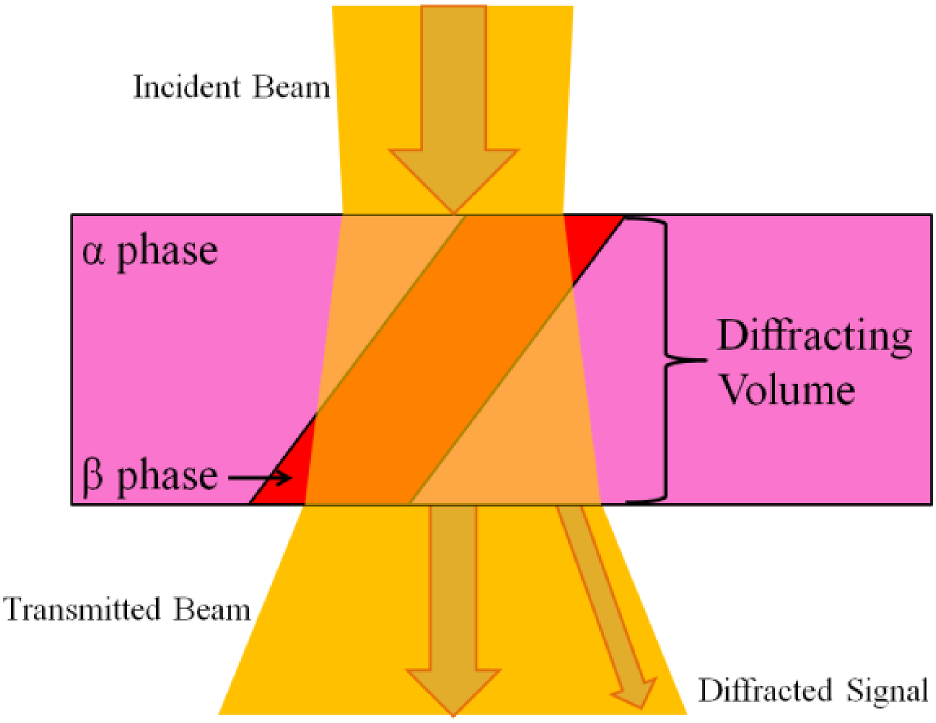

Figure 5:8. Schematic diagram showing the interaction between an incident e-beam and a two phase system.

Therefore as with the orientation map acquired by TKD, no twins of the residual β phase were observed in the deformed WAAM structure.

### Summary

Neither of the high resolution orientation mapping techniques were able to confirm that the β twinned structures observed growing with temperature in **Manuscript 4** are present in the room temperature deformed structure. However, as neither technique was able to resolve the β where it was finest does not rule out that the β twinned structures do not exist, as it is in these regions that the twins are believed to be most likely to exist. In both cases the study was also hampered by the small volumes of material investigated, this was especially true in the case of the TEM ASTAR map where only a few phase boundaries could be investigated within a reasonable time frame.

One of the limits holding back the ability to resolve fine features with the ASTAR technique is the thickness of the prepared samples leading to weaker diffraction patterns that are too easily misindexed, and the potential issue of overlapping patterns at grain boundaries highlighted schematically in Figure 5:8. However, preparation by FIB has been found to be problematic with the sample deforming and eventually tearing if thinned too far. It is also possible that the fine β twins may be prone to detwinning upon the constraint relaxation imparted from the creation of two free surfaces during preparation of the thin sample, especially as detwinning has been observed readily occurring in the deformation of bcc nanowires[172] .

A further possibility exists that the twins do not exist in the room temperature deformed microstructure and that the β twinned structures observed in the in-situ heating experiment have formed as a result of the heating itself, perhaps due to annealing. Annealing twins are rarely observed in bcc materials due to their high stacking fault energy, but have been recently observed in a β-stabilised titanium alloy [173]. However, as the β-stabilised titanium alloy was severely cold deformed to 90% reduction and only observed a small fraction of annealing twins, the two situations are not readily comparable.

## 5.2. In-situ Heating Validation

Both of the in-situ heating experiments presented in the **Manuscripts 3** and **4** observed a lower than expected volume transformation to β at temperatures approaching the β transus than suggested by the literature [169]. The transus temperature for alloys classified as Ti6-Al-4V can vary greatly as the composition window for each element in Ti6-Al-4V is quite large [142], and there is a strong dependence on the concentration of α and β stabilising elements on the transus temperature (§2.3.2). Therefore, to better understand the observed phase change in the in-situ experiments, it is necessary to know the β transus temperature of the material deposited by the WAAM process. The β transus was investigated by three techniques: direct measurements by both Differential Scanning Calorimetry (DSC) and resistivity measurements during heating, and prediction by thermodynamic modelling of the alloy's measured composition.

### *5.2.1. Direct β-transus observation*

#### **Differential Scanning Calorimetry**

In an attempt to determine the β transus of the deposited WAAM material a Differential Scanning Calorimetry (DSC) experiment was carried out, as described in §3.7.1, on identical samples over three heating rates to account for kinematic effects and to minimise the effects of thermal gradients within the sample. The DSC curves of the three heating rates are shown in Figure 5:9.

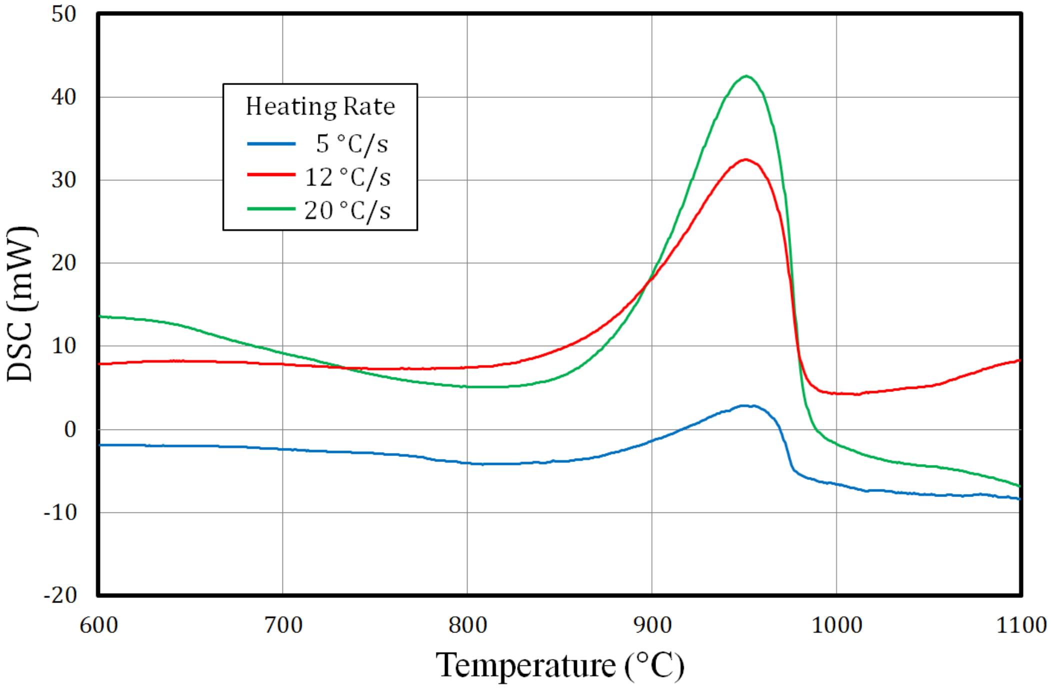

Figure 5:9.DSC curves of Ti-6Al-4V deposited by the WAAM process at three different heating rates.

For each heating rate, the temperature at which the transformation was completed was determined by peak analysis carried out with tools included in the Netzsch Proteus DSC acquisition software. The temperature that the material became entirely β phase is plotted against heating rate in Figure 5:10.

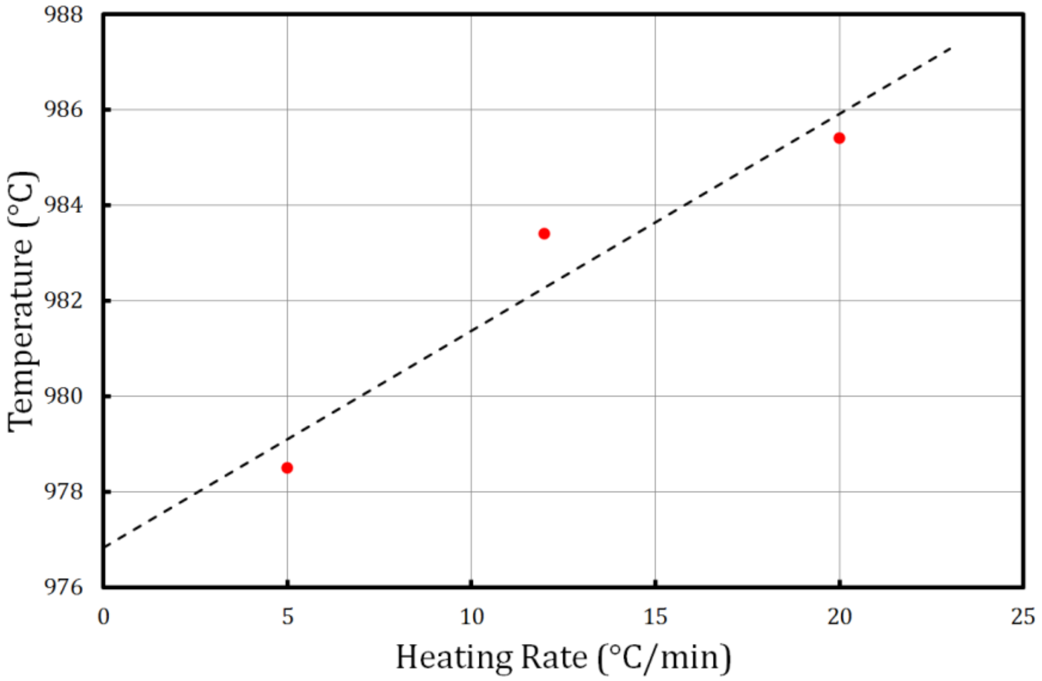

Figure 5:10. β transus temperatures as determined by DSC for several heating rates.

For the heating rates tested from 5 °C/min to 20 °C/min it is found that the β transus varies from 978.5 °C to 984.5 °C. The delay in transformation with higher heating rates echoes what has been seen by others, and is due to the slower heating rates leading to lower thermal gradients within the sample, ensuring a more homogenous temperature and therefore crisper exothermic transformation peak [168]. The effect of thermal gradients cannot be minimised further by the use of slower heating rates, as a consequence of the signal to noise ratio also dropping with decreased heating rates (this can be seen by the lack of peak definition at a heating rate of 5 °C/min in Figure 5:9). However, a crude extrapolation from the heating rates tested suggests a β-transus temperature of ~977°C.

### Change in resistance with heating

As described in §2.3.1, the difference in electrical conductivity of the two titanium phases allows the phase transformation to be measured directly by measuring the change in electrical conductivity of a sample during heating.

The resistivity was measured during an ETMT heating cycle as described in §3.2.2 on a sample cut from an undeformed WAAM wall. The ETMT resistive heating experiment was carried out under similar conditions as the experiment described in **Manuscript 4** where the sample was rapidly heated above the β transus in under 2 s.

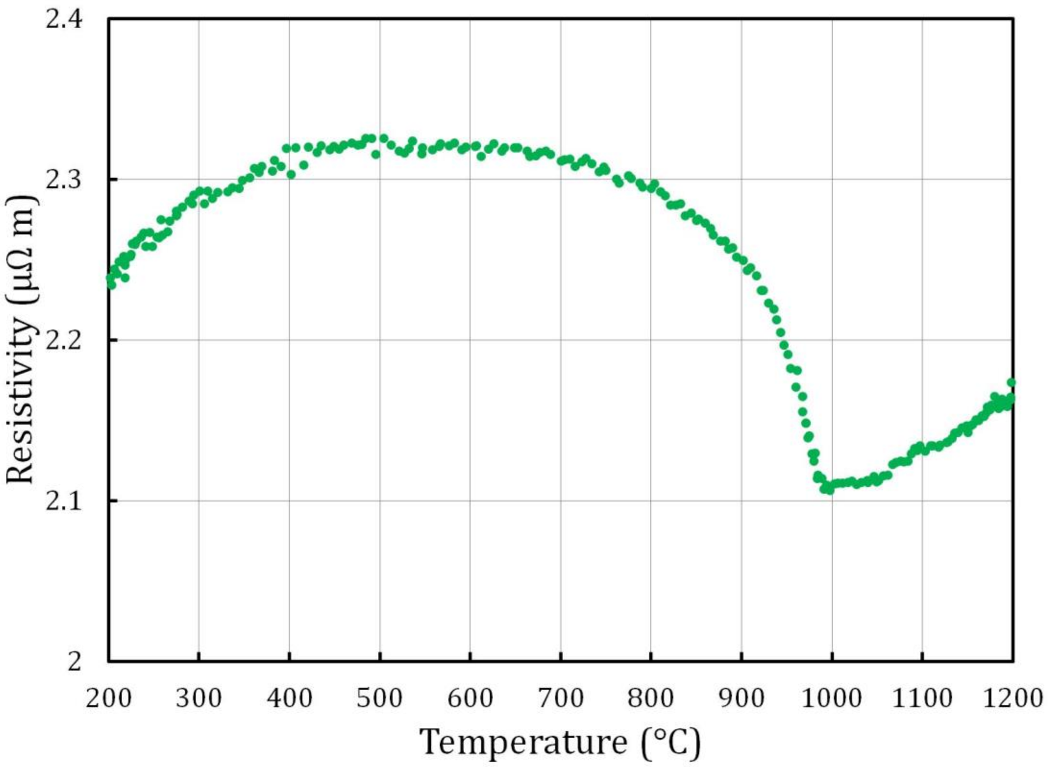

Figure 5:11. A plot of resistivity versus temperature of Ti-6Al-4V WAAM material heated rapidly by resistive heating.

The resistivity of the sample at each temperature tested is plotted in Figure 5:11. It is found that initially the resistance of the sample steadily increases with increasing temperature due to the greater lattice vibrations. As temperature is further increased, the resistivity change plateus and then begins to drop, as a greater volume of the material transforms to the more electrically conductive β phase. An abrupt change in behaviour is observed at 985°C, associated with the completion of the phase transformation to β, before the linear increase of resistivity with temperature resumes as atomic vibrations again become the dominant factor in the resistivity of the sample.

The measured β-transus temperature of 985°C shows good agreement with the DSC measurements ranging from 978.5 °C to 984.5 °C. As described in the previous section, the extrapolated β transus temperature of 977 °C from DSC gives a lower limit of the β-transus, therefore the measurement by resistivity measurement is slightly higher than by DSC. A small overestimate of the β transus is to be expected when determined by change in resistance with this experimental set-up due to the slight temperature profile across the sample during heating. The temperature is measured in the centre of the sample where it is hottest, whereas the resistivity is calculated between two points either side of this (see Figure 3:7 in §3.2.2). Therefore the inflection in the resistivity curve in Figure 5:11 signifying the completion of phase transformation will be recorded at a slightly higher temperature than it is occurring.

Regardless of the exact value of the β-transus temperature, both the direct measurements support the statement that for this Ti-6Al-4V alloy, the β-transus temperature is significantly below the ~1000°C that is often quoted as the β-transus for all Ti-6-Al4V in the literature [4,44,164]. Therefore the lower than expected transformation volume fraction the in-situ heating experiments in **Manuscripts 3** and **4**) are not due to the WAAM material having a higher than expected β-transus.

### *5.2.2. JMat ProPhase Alloy Simulation*

JMat Pro was used to predict the equilibrium level of transformation based on the composition of the alloy. Although the composition of the feedstock wire was stated by the manufacturer, it was decided to analyse the composition of material directly from the WAAM wall, as it was known that the argon shrouding was unlikely to be perfect and so it was expected that there would be an increase in the oxygen content of the wall. The alloy composition was measured by TIMET on material taken from a WAAM wall by the techniques listed in §3.7.2. The measured constituents of the alloy are given in Table 5:1 alongside the specification for the wire feedstock supplied by the feedstock manufacturer.

Table 5:1. Chemical composition of the Ti-6Al-4V used in this study in wt%.

| Heat Source | Al | V | Fe | C | O | N |
|---|---|---|---|---|---|---|
| Wire specification | 6.08 | 4.00 | 0.180 | 0.035 | 0.160 | 0.011 |
| Wall measurement | 6.24 | 3.96 | 0.053 | - | 0.055 | 0.013 |

The alloy composition in the WAAM wall was significantly different to that stated by the feedstock manufacturer, with oxygen content found to be substantially lower. This variation is most likely due to poor quality control of the feedstock rather than chemical variations occurring as a result of processing. As explained above, during processing you would only expect the oxygen content to increase due to the high affinity for oxygen titanium has at the processing temperatures. In addition, if the aluminium content were to vary, it would be expected to decrease rather than increase, as aluminium evaporates preferentially to titanium from the melt [174]. However, confirmation of this would require further analysis of the feedstock wire.

For the JMat Pro calculation, the measured composition of the WAAM wall was used to predict the phase transformation behaviour, as this was representative of the material used in the in-situ tests. However, no measurement was made of the carbon content of the WAAM wall, therefore for the calculation, the content of the wire specification of 0.035 wt% was used as a guideline, but a large variation was also calculated of ±0.015 wt% to determine the limits of the effect the carbon content has on the phase transformation. The predicted volume transformed to β with temperature is shown in Figure 5:12, with the variation in carbon content indicated by the dashed lines.

For the composition of the WAAM wall given in Table 5:1, it is predicted that the alloy under equilibrium conditions has a β transus temperature range of 977 – 991 °C for a respective carbon content of 0.2 – 0.6 wt%. The lower carbon content estimate transformation range agrees well with the 977°C extrapolated from the DSC data to equilibrium conditions in Figure 5:10.

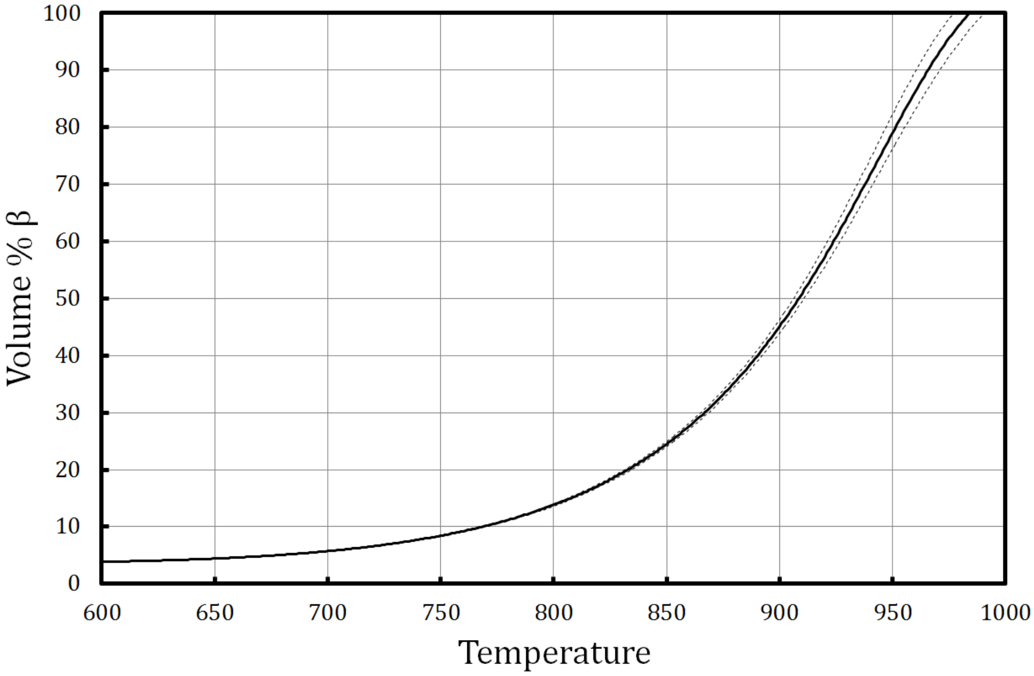

Figure 5:12. Phase transformation to β as calculated by JMat Pro with the dashed lines indicating the influence of ±0.015 wt% carbon content.

For comparative purposes the percentage of EBSD patterns indexed as β at temperature in each of the in-situ experiments carried out (including those in **Manuscripts 3** and **4**) and is plotted alongside the transformation curve calculated above in Figure 5:13. From this plot it can be seen that the transformation to β is delayed by ~50 °C in the in-situ heating experiments compared to what is predicted.

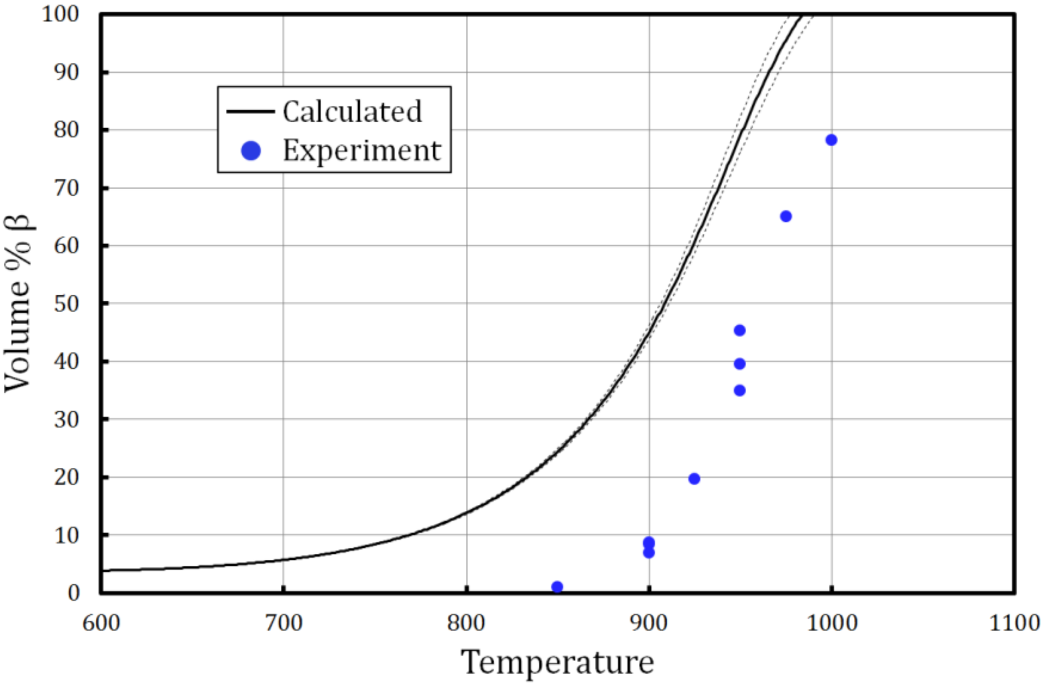

Figure 5:13.Transformation to β observed experimentally by in-situ EBSD and as calculated by JMat Pro.

It is expected that the β content would be underrepresented at low volume fractions due to the previously mentioned difficulty of obtaining diffraction patterns from a fine phase, due to the size of the volume probed by from the electron beam (see §3.5.2). It is also expected that the transformation would take place at a slightly higher temperature than predicted by JMat Pro, as JMat pro calculates the phase content under equilibrium conditions, i.e. as if diffusion had been given an infinite amount of time to take place. However, the heating rates obtained in the SEM at high temperatures were very slow at ~2 °C/min, and as shown by the DSC experiments in Figure 5:10, this has very little effect on the transformation temperature. Therefore the ~50 °C disagreement is either down to an issue with the temperature measurement by the thermocouple (thought to be unlikely, as had been previously calibrated against the melting points of pure metals), or a process occurring during heating in the SEM that supresses the β transformation, such as the surface film observed in in **Manuscripts 3** and **4** that prevented the indexing of titanium up to ~850°C.

### *5.2.3. Surface Layer EBSD Analysis*

In both of the in-situ EBSD heating experiments in in **Manuscripts 3** and **4,** a layer suspected of being an oxide was observed to begin forming on the surface of the samples at ~400 °C. This layer appeared to form with different thicknesses dependent on the α variant beneath allowing for high contrast images to be taken in secondary electron mode at high temperature (**Manuscript 3**, Figure 5.). The film also prevented the indexing of titanium diffraction patterns until its disappearance at ~850 °C. However, as shown from the band contrast map in Figure 5:14, the diffraction patterns from the unindexed region were actually stronger than the diffracting titanium metal beneath it. The patterns were saved to be analysed later to confirm whether the thin film was indeed an oxide.

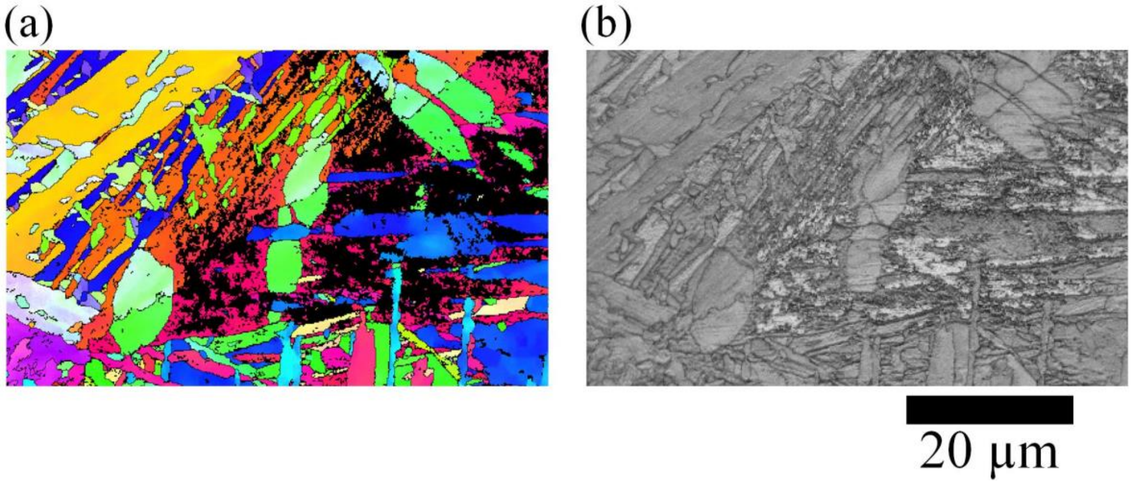

Figure 5:14. (a) A reproduction of Figure from **Manuscript 4** of an EBSD map taken at 850 °C, alongside a band contrast map of the same region in (b).

An example diffraction pattern from the surface layer is given in Figure 5:15a. The diffraction pattern of the surface layer was found to index well as the cubic titanium oxide TiO, as shown in Figure 5:15b, the lattice parameters of which are given in Table 5:2. The most commonly observed oxides growing on Ti-6Al-4V are $TiO_2$ in three different crystalline forms, two tetragonal and one orthorhombic, as these are the most thermodynamically stable oxides in a standard atmosphere [175]. However, the observation of TiO is not without precedent, Lu et al. [176] studied the formation of oxides on pure titanium in near vacuum conditions by X-ray photo-electron spectroscopy, and found that by 850 °C all other oxides had reduced to TiO. Unfortunately, patterns were not saved at lower temperatures to confirm whether other oxides formed initially in the in-situ experiments.

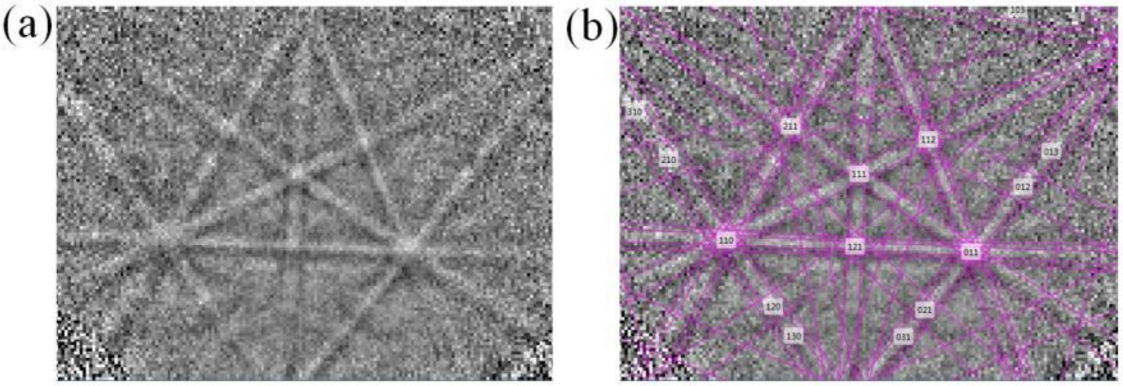

Figure 5:15. EBSD diffraction pattern measured at 800 °C from the surface layer, and (b) the same pattern indexed as TiO.

Table 5:2. Crystal parameters of titanium oxide TiO.

| Name | Crystal system | Laue group | Space group | Unit Cell | | Reference |
|---|---|---|---|---|---|---|
| | | | | $a=b=c$ | $\alpha=\beta=\gamma$ | |
| TiO | Cubic | $m\bar{3}m$ | $Fm\bar{3}m$ | 4.2043 Å | 90° | ICSD[56612] |

The maps in Figure 5:16 are constructed from the same diffraction patterns as those that were used to construct the maps in **Manuscript 4** Figure 7, but have been reanalysed to take account of the TiO phase. Comparison between the equivalent maps of Figure 5:14b and Figure 5:16b show good agreement between the points indexed as TiO, and the regions of high band contrast that remained unindexed.

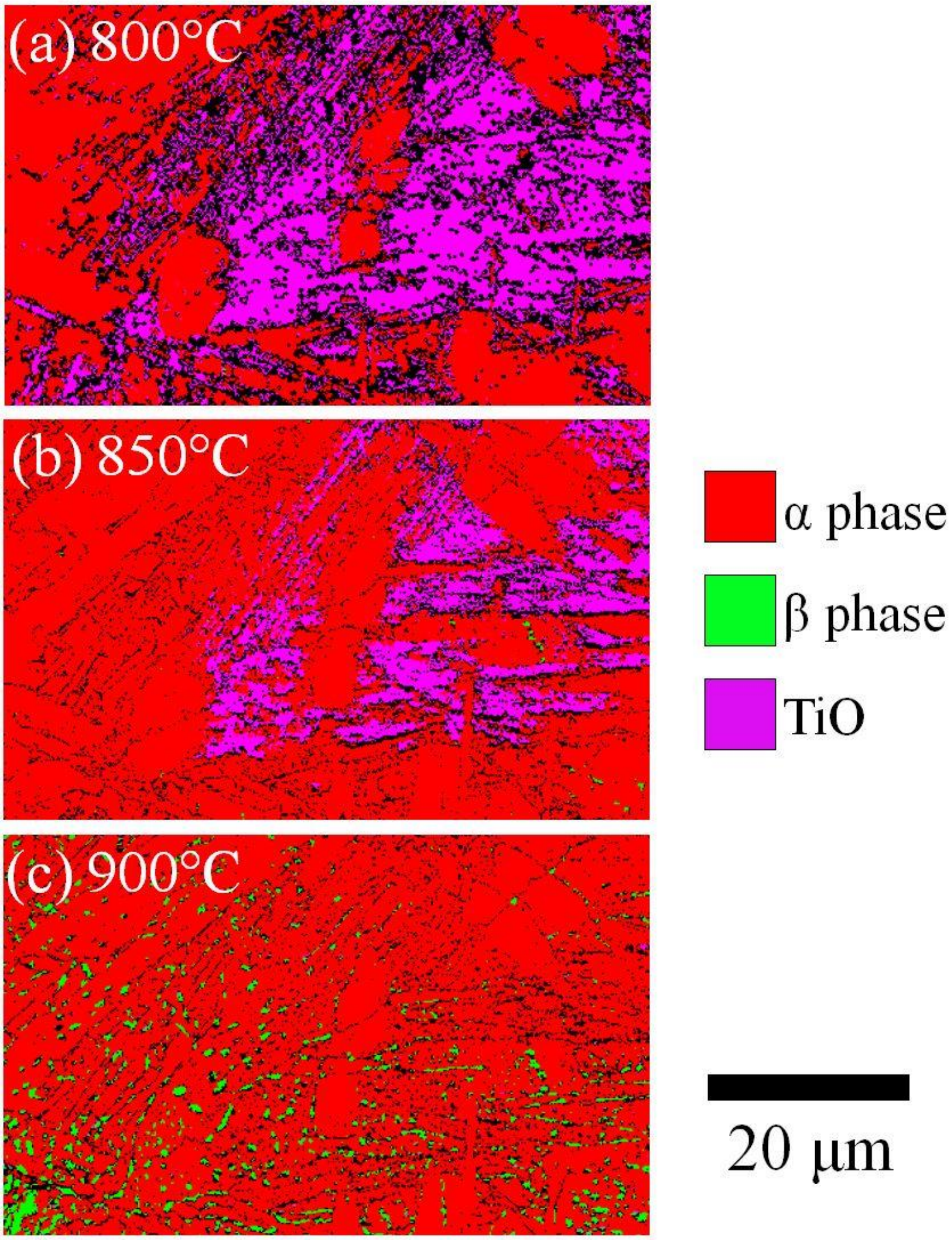

Figure 5:16. Phase maps of in-situ EBSD experiment described in **Manuscript 4**, re-indexed to include the TiO phase, and coloured to show the phase of each indexed pattern.

It was found that from 800 °C to 850 °C that the number of points indexed as TiO decreased dramatically. This mirrors what was observed by Lu et al. [176] where at 850 °C they found very little of any oxide remaining, their belief being that the disappearance of the oxide was due to decomposition of the oxide and either diffusion into the bulk titanium, or desorption from the surface and being removed by the vacuum pump. Desorption may too have been occurring in the in-situ experiment, but it is the diffusion of the oxygen into the bulk titanium sample that is of interest due to the oxygen potentially stabilising the α phase and delaying the β transformation. There is evidence of diffusion from the oxide to the bulk occurring in Figure 5:16; the thickness of the oxide layer is inhomogeneous and appears to grow preferentially on certain underlying α orientations, as evidenced by the prevalence of the oxide in the top right-hand section of Figure 5:16 a & b, it is also evident that in the higher temperature map of the same region in Figure 5:16c, that the top right-hand section is the region that is least transformed to β. Although there is only one small area mapped, with too few α orientations to draw definitive conclusions, it seems likely that diffusion of oxygen into the sample at high temperature has taken place.

### *5.2.4. In-situ Heating Experiment on an Undeformed WAAM Sample*

In addition to the heating experiments covered in **Manuscripts 3** and **4**, a further in-situ heating experiment was carried out on an undeformed WAAM wall. The purpose of this test was to confirm that with no deformation within the microstructure that the original prior β structure is regained upon heating though the β transus, thus reinforcing the understanding of how columnar microstructures are formed within AM, and simultaneously corroborating the observations in the previous experiments.

The methodology of the experimental set-up was the same as described in §3.5.3, but due to the coarse grain structure of the undeformed WAAM microstructure, a larger area EBSD map was required to ensure coverage of several prior β grains. To ensure that the mapping time was kept below 20 minutes (similar to the other in-situ heating experiments) a larger step size of 2 µm was used. Figure 5:17 repeats the depiction of the heating experiments in **Manuscripts 3** and **4**, in that it shows two orientation maps for each temperature, one for each phase, with the indexed points coloured in IPF colouring in the direction of columnar growth.

As with the previous heating experiments, it is observed in Figure 5:17 that with increasing temperature there is increased transformation to β from a predominantly α microstructure. However, unlike the previous in-situ heating experiments on deformed WAAM material, where there were new β orientations observed growing either from twinned α colonies (**Manuscript 3**) or from twinned inter-lath residual β (**Manuscript 4**), all of the β observed at high temperature in the undeformed material in this experiment is of the orientation expected to be grown from the residual β of the prior high temperature grain structure from the previous β → α transformation.

3

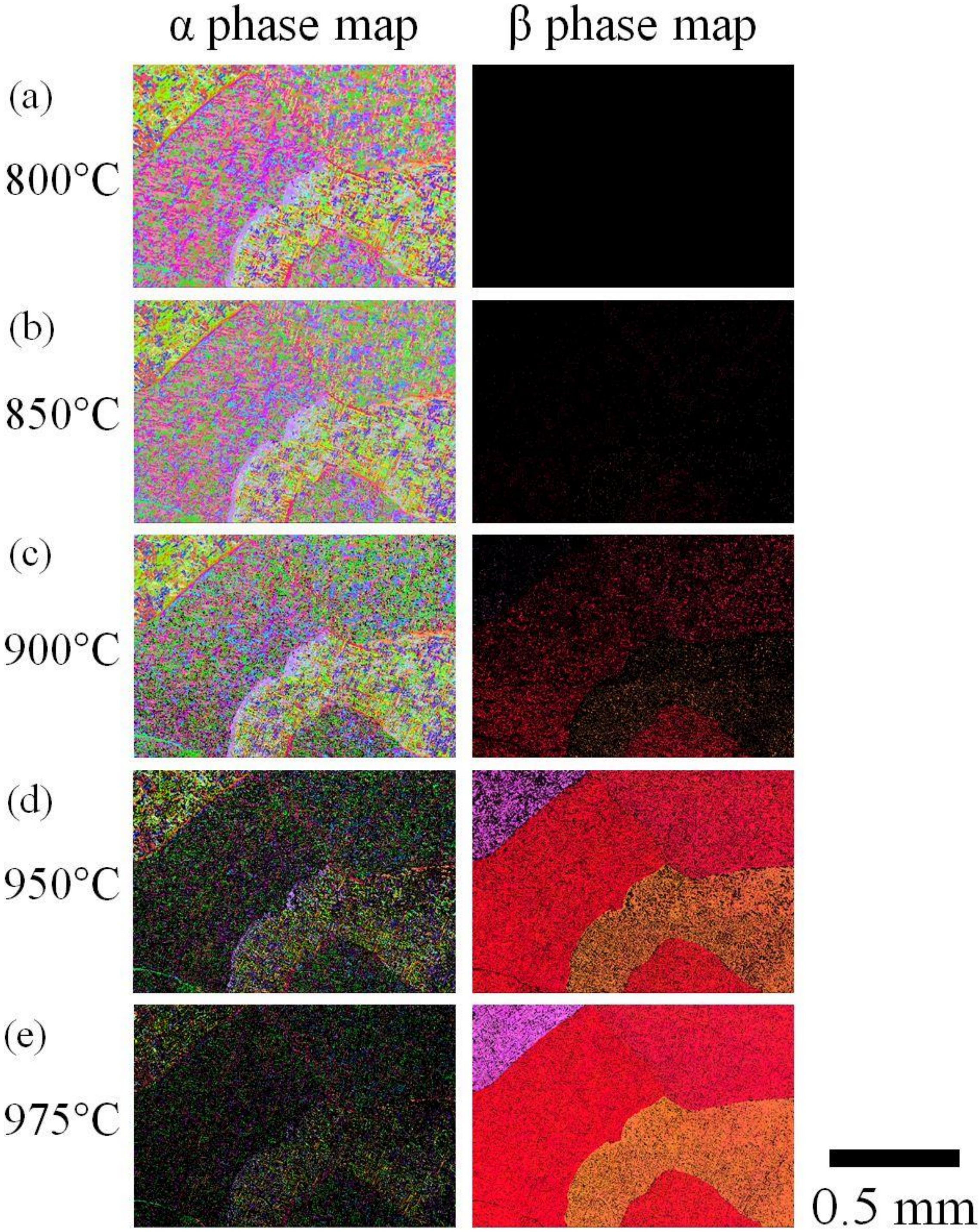

Figure 5:17. EBSD maps of the region studied by in-situ heating at temperatures stated on the figure. The left and right maps show the α and β phases at each temperature in IPF colouring with respect to the build direction.

The almost exact regeneration of the previous high temperature grain structure is confirmed by the comparison of the high temperature β map at 975°C and a β reconstruction from the room temperature α variants in Figure 5:18. The observation of the recreation of the prior β structure helps confirms the ‘ratcheting’ process that is often used to describe the creation of the columnar structure that is observed to exist in Ti-6Al-4V AM builds. As described in §2.5.1, the formation of the columnar microstructure is believed to occur because each additional pass of the melt pool heats the surrounding material above the β transus. When cooling, the molten material solidifies and grows epitaxially upon the underlying grains, since solidification ahead of the solidification front is discouraged by the metallurgy of titanium (§2.4.3). Figure 5:18 confirms that in the absence of deformation, AM Ti-6Al-4V will return to its prior grain structure and orientation under heating, therefore allowing for the directional continuation of grains by the epitaxial solidification upon them.

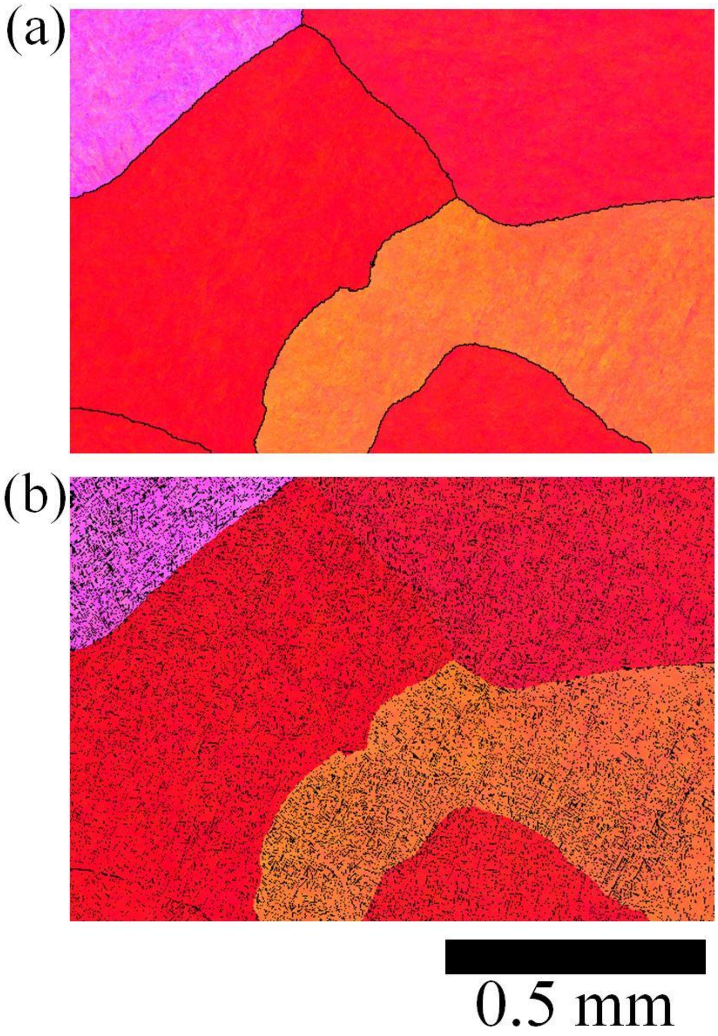

Figure 5:18. β orientation maps of the same region. (a) calculated from α variants present at room temperature, and (b) β measured directly at 975° C.

After heating to 975°C the sample was rapidly cooled, dropping to under 500°C in 2 minutes, and remapped when the sample was approximately at room temperature. A comparison of the region before and after heating to the peak temperature is given in Figure 5:19. Despite being heated to a temperature where only 14% of the structure was indexed as α phase, it can be seen that room temperature α structures are accurately reproduced, with it possible to pick out many lath structures that are present in both maps. Therefore, it appears logical that just as β grain structures are reproduced when heating to the transus temperature by growing from the fine residual β trapped between α laths; that residual α remnant at temperatures approaching the β transus will preferentially regrow to consume the β, on cooling from the transus, rather than nucleating new α grains, recreating the prior grain structure.

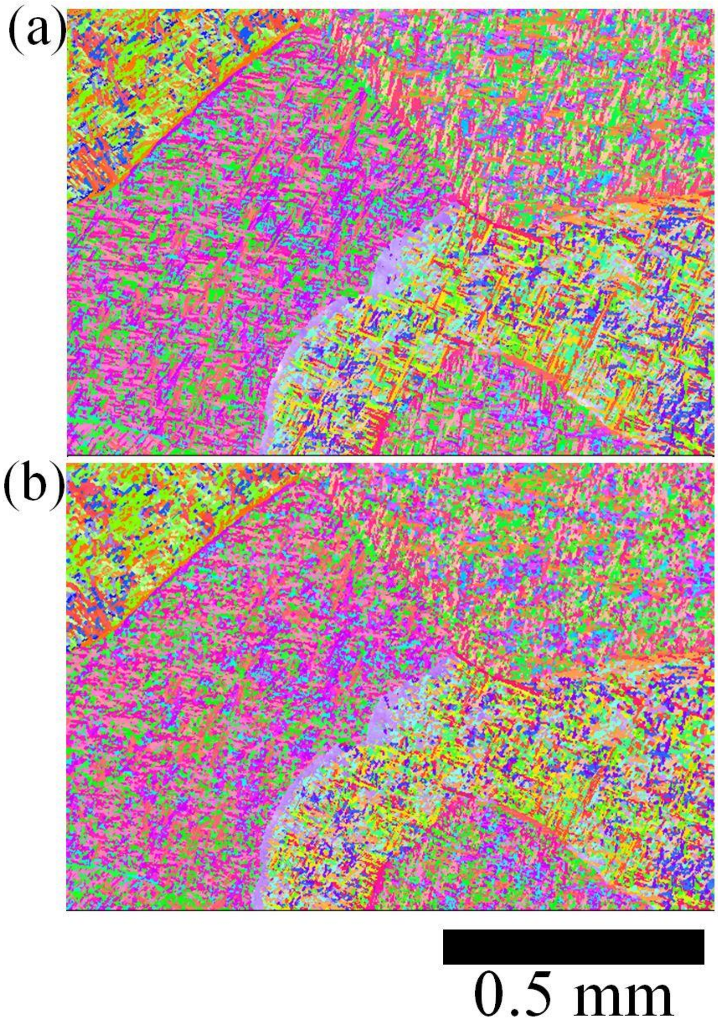

Figure 5:19. Room temperature EBSD maps of region before (a) and after (b) taking to 975° C and into the β phase.

Far greater transformation is observed at each temperature than was observed in the previous in-situ heating experiments as shown in Figure 5:20, where it is also shown that the phase transformation observed is far closer to that predicted for the alloy by JMatPro in §5.2.2. This sample does differ from the previous experiments in that it has not been rolled, however, this is not believed to be the cause of the greater transformation. As previously stated in **Manuscript 4**, the previous in-situ experiments took place over a range of strains from the rolled profile, none of which were particularly high, and all showed consistent heating behaviour. In the previous experiments, the lower than expected phase transformation was put down to the absorption of oxygen from a surface oxide layer at ~800°C that stabilised the α phase, and thus lowered the transformed volume of α to β (as described in the previous section, §5.2.3). As the surface oxide layer also prevented the indexing of titanium EBSD patterns, no EBSD maps were attempted until 800°C in the in-situ heating experiment on the undeformed WAAM experiment. At the first mapping temperature of 800°C no influence of the oxide layer on the EBSD patterns was observed, therefore it is possible that the oxide layer did not form in this experiment, perhaps giving an explanation why the phase transformation to β was closer to what was predicted by JMatPro, but it is not obvious why the oxide should not form in this case as the experimental procedures in all experiments were very similar. Before the in-situ heating, all of the mounted samples were baked at 180°C for in excess of 30 mins to allow volatiles to evaporate from the sample prior to insertion into the microscope. For every heating experiment the chamber was repeatedly backfilled with nitrogen gas in an attempt to eliminate contaminate molecules from the air. In addition, in all tests the chamber pressure was closely monitored for degassing at high temperature, with the chamber left to re-achieve a high vacuum if any increase in pressure was registered.

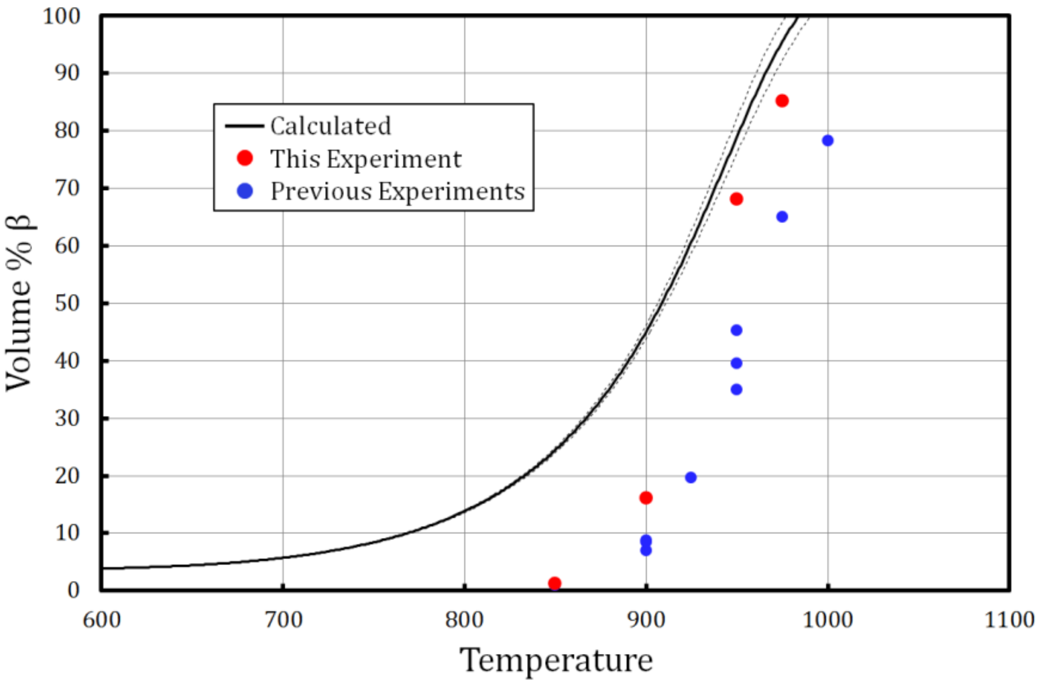

Figure 5:20. Reproduction of Figure 5:13 showing the transformation to β observed experimentally by in-situ EBSD and as calculated by JMat Pro incorporating the in-situ heating experiment of an undeformed sample.

As previously stated, one difference between this heating experiment and those made previously was that no attempts at EBSD mapping were made before 800°C. As the previous in-situ heating experiments on the deformed samples involved an attempt at EBSD mapping at regular intervals from room temperature to the peak temperatures, it is possible that the difference in mapping routine could have led to the difference in volume transformation to β highlighted in Figure 5:20. One outcome of the increased number of EBSD maps at lower temperatures is that samples regularly held at temperature for mapping will undergo a slower overall heating rate over this temperature range taking ~2 hrs to heat to 800°C opposed to ~30 mins with no mapping. However, this difference in heating rates is unlikely to significantly affect the α→β transformation, as little evolution of the microstructure was observed up to this temperature at the mapping resolutions. The transformation is observed to commence above 800°C, where the heating rates for all experiments were similar. A further effect of not mapping at lower temperatures is limiting of beam induced contamination of the region of interest of the sample surface. Beam induced contamination occurs when the electron beam interacts with hydrocarbon contamination on the surface of the sample, leading to a carbon rich deposit [177]. As can be seen in Figure 5:21, beam induced deposition was taking place as a result of the EBSD mapping during experiments. As this deposit is believed to be carbon rich, it is unlikely to be directly responsible for the formation of the oxide observed in §5.2.3, but it is possible that it may influence its formation. In addition, carbon diffusion into the sample will raise the β transus as shown in Figure 5:12.

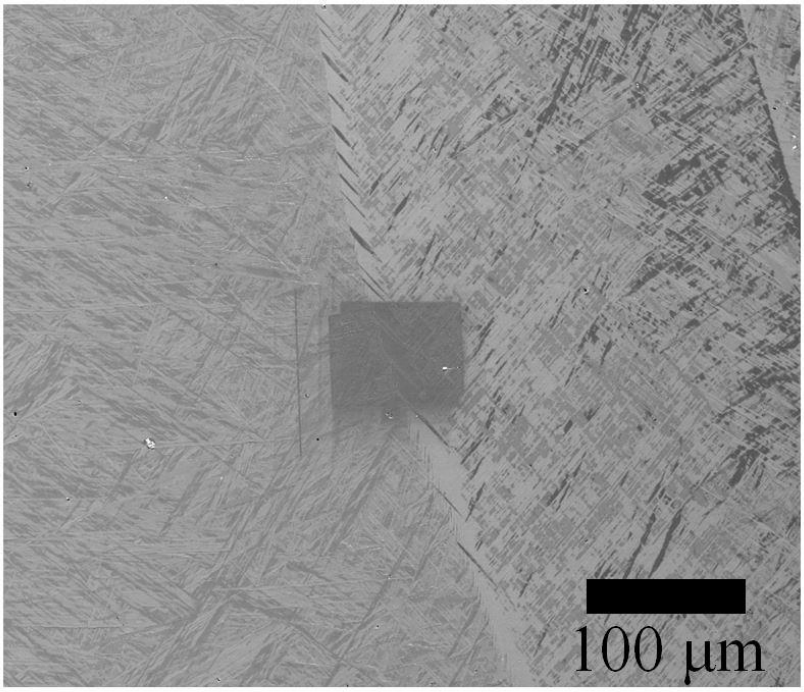

Figure 5:21. SE micrograph taken a 700°C during the heating experiment in **Manuscript 3**, highlighting the beam induced contamination from EBSD mapping

One final difference between the two sets of heating experiments that may explain the discrepancy in transformation behaviour, highlighted in Figure 5:20, was the use of different sample sizes in the two experiments. In the samples of deformed WAAM material where the transformation to β was supressed compared to what was expected took place on a cuboid sample measuring ~2mm x 2mm x 1mm, opposed to a cylindrical sample of the undeformed material measuring 1mm x 4.5 Ø mm. Therefore, the larger sample of the undeformed material had a considerably larger surface area of ~40 $mm^2$ compared to ~16 $mm^2$ for the samples where less transformation to β was observed. If it is assumed that the levels of contamination were similar in all cases, then it can be expected that the oxide layer formed on a larger sample would be thinner and therefore have less of an influence on the α→β transformation when adsorbed into the sample surface at higher temperatures.

# 6. Summary, Conclusions, and Further Work

This final chapter attempts to combine and summarise the findings of the four included manuscripts along with the additional results provided in Chapter 5 of corroborative experiments. The summary is followed by concluding remarks that state the outcomes of this work in the context of how knowledge in this field has been expanded by the study taking place. Finally, a brief discussion is given on the potential avenues that the research could continue down to further the work started in this thesis.

## 6.1. Summary

**Manuscripts 1** and **2** were both concerned with characterising the resultant microstructure and texture of additive manufacture of Ti-6-Al-4V when incorporated with deformation processing steps. **Manuscript 1** investigated the effect Ultrasonic Impact Treatment (UIT), a form of peening, had on a Laser Blown Powder (LBP) AM technique, and **Manuscript 2** focused on the effect of rolling on Wire-Arc Additive Manufacture WAAM. In both cases it was found that rather than the strongly textured prior β columnar grains that are typically formed in Ti-6Al-4V AM, refined equiaxed prior β grains with a more random texture are formed. These findings are summarised in Figure 6:1.

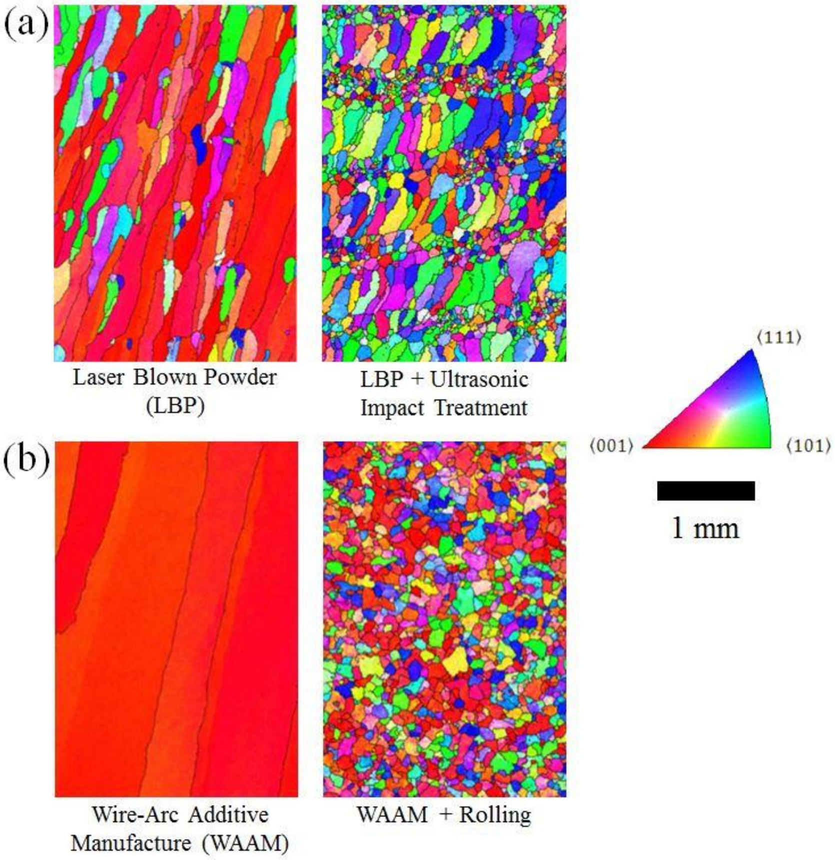

Figure 6:1. The effect on the microstructure and texture of the two investigated deformation processes on the two AM techniques. a and b are adapted from figures in **Manuscript 1**, and **Manuscript 2** respectively.

It was demonstrated in **Manuscript 2** that the region of refined grains corresponds well with the strain distribution from the deformation step, and that the new grains are formed when the deformed region is taken above the β-transus.

It was found that the combination of the depth of the deformation zone and the thermal profile of the melt pool are the determining factors in dictating the region of refinement. With the peening discussed in **Manuscript 1** the deformation was concentrated at the surface, so the majority of useful work put into the build was lost by re-melting upon the addition of the subsequent layer. Fortunately, the re-melt depth of the LBP process was fairly small, so enough of the sufficiently deformed material was not re-melted, and this led to the refined β grains seen upon being reheated back above the β transus. As the depth of the zone of sufficient deformation was not greater than an added layers thickness, it led to alternating bands of refined grains and the columnar grain structure re-establishing itself in each layer as can be seen in Figure 6:1a. The re-melt depth of the WAAM process discussed in **Manuscript 2** was significantly larger than the LBP. However, it was also found that, due to the constraint imparted by the rolling conditions, that the deformation was focused to an even greater depth than this. This higher depth of the deformation, being greater that the thickness of an added layer, ensured that the entire build was refined.

In order to ascertain where in the microstructure the new β orientations were growing from during transformation, and to understand their orientation relationship to the deformed microstructure, samples of AM Ti-6Al-4V were analysed in-situ by EBSD at temperature. It has been confirmed that in the absence of deformation that β grows from the residual β in the room temperature microstructure to return the microstructure to its previous high temperature state during the α→β transformation (§5.2.4). **Manuscripts 3** and **4** discussed in-situ heating experiments on deformed regions of the WAAM microstructure. **Manuscript 3** focused on α twins that had formed across α colony structures at a prior β boundaries, and found that at temperatures approaching the β-transus that new β orientations form within the α colony that share the Burgers' orientation relationship with the twinned α. However, it was not apparent how new grains of this origin could account for the level of refinement observed. The in-situ heating experiment in **Manuscript 4** focused on a more highly deformed region of the microstructure and found that new β orientations were found to grow throughout the prior β grains. The majority of the new β orientations were found to relate to the residual β by the {112}<111> bcc twinning system.

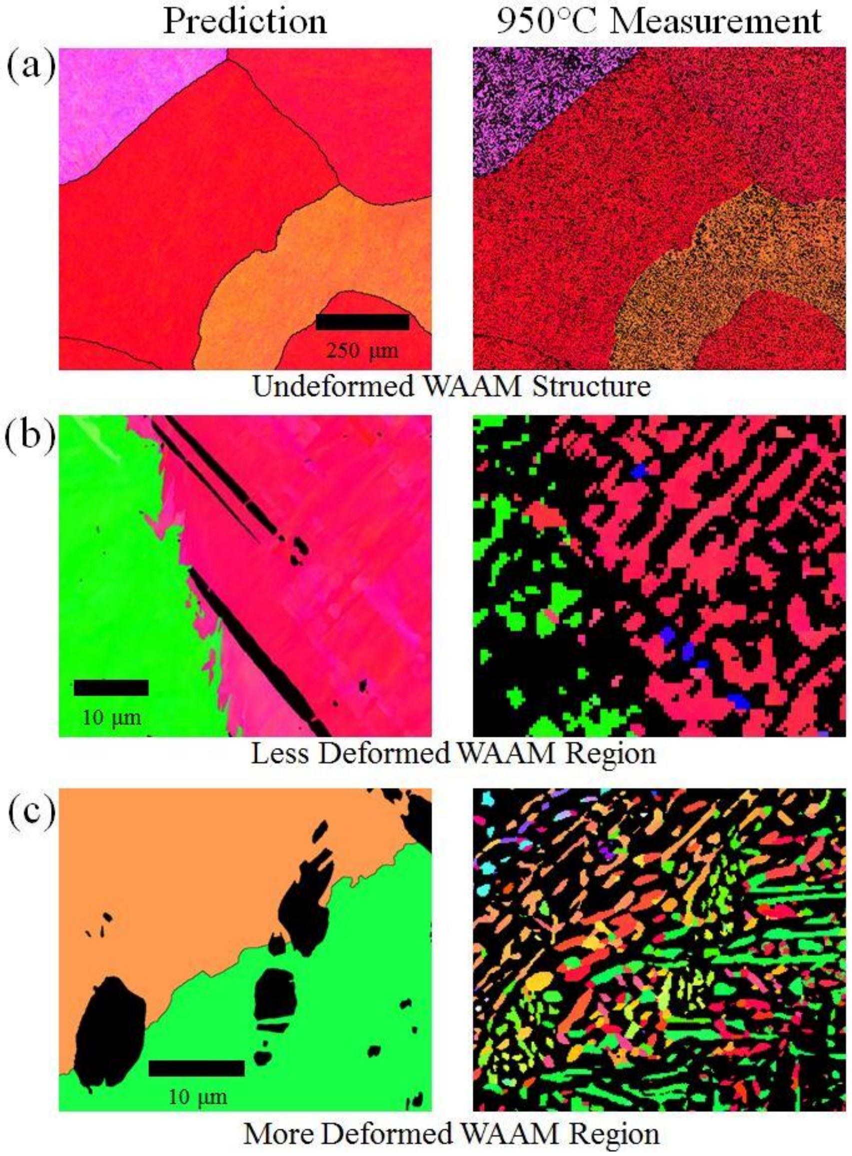

Figure 6:2. Direct measurements compared with predictions (from β reconstruction) of the high temperature β structure of three WAAM microstructures with differing levels of plastic strain. a, b and c are adapted from figures in §5.2.4, **Manuscript 3**, and **Manuscript 4** respectively.

In addition to the in-situ heating experiment, **Manuscript 4** also simulated a single deformation pass and layer addition process step and found that the new orientations formed could be traced back to the same twinning system. Although twinning of the β phase has not previously been reported in Ti-6Al-4V, it was proposed that the β twinning had occurred in this case due to the very fine morphology of the residual β found in the AM builds facilitating the twinning.

Two high spatial resolution orientation mapping techniques were employed in an attempt to confirm the presence of the β twins in the room temperature deformed microstructure in §5.1.1 and §5.1.2. Neither of the mapping techniques were able to confirm the presence of the β twins at room temperature; however, neither technique was able to resolve the β where it was thinnest, despite the high resolution nature of the techniques.

## 6.2. Conclusions

- The direct observation of β re-growing from the residual β from the previous β→α phase transformation when heating back above the β transus supports the mechanism proposed in the literature that leads to the coarse columnar prior-β grain structure with a <100> preferential growth observed in Ti-6Al-4V AM builds.
- Refinement of the coarse prior-β grain structure can be achieved with a surprisingly modest plastic strain, and could therefore be potentially applied to a wide range of deformation processing techniques. However, it has been found that the plastic strain has to be over a certain threshold and that in AM the depth of the deformation must therefore be greater than the re-melt depth to see any refinement. The depth of the deformation should ideally be at least as great as an added layer's thickness to see refinement across the entire build.
- The texture of the refined grains is related to the texture of the grains they are refined from. Therefore, to achieve as weak a texture as possible in the final build, it is beneficial to overlap the refined zones with each pass and prevent the <100> growth from re-establishing.
- The refined structure is generated by new β orientations out competing growth from the residual β from the previous β→α phase transformation when heated back above the β transus. New β orientations have been directly observed growing from twinned α colonies in the deformed microstructure, as well as growing from between α laths with orientations sharing β twinning relationships with the residual β.
- Simulation of both the deformation step and thermal cycle of the Wire Arc Additive Manufacture + Rolling successfully reproduced the refined prior-β grain structure observed in process. Analysis of the refined grains from individual coarse prior-β grains suggests that β twinning may be the mechanism by which the orientations of the refined grains are formed.

## 6.3. Further Work

This section includes both upcoming planned experiments and potential new avenues for the research to be continued.

### Synchrotron Experiment

It was suggested in **Manuscript 4** that twins in the room temperature β phase grow to form the refined grain structure found in the finished builds. The observation of the bcc twins was made by EBSD at temperature. However, despite extensive efforts to observe the twins in the room temperature structure in §5.1, no evidence of their existence was found. This could be due to the resolution limits of the techniques used. Therefore a repeat of the simulation experiment in **Manuscript 4** is to take place at a Synchrotron X-Ray Diffraction Facility (SXRD) in February 2017 on the I12: Joint Engineering, Environmental, and Processing (JEEP) beamline of the Diamond Light Source.

For the SXRD experiment, a piece of WAAM material will be deformed in plane strain conditions beforehand, and then rapidly heated up in-line at the synchrotron using the Electro-Thermal Mechanical Testing system (ETMT). As with the previous simulated sample, the experiment will be focused on just a few of the large prior β grains, but in this case with information on the grain structures being collected in-situ, in real-time via diffraction patterns. The high intensity of the X-ray source should be able to overcome the suspected minimal volume fraction of the β twins, to categorically confirm or disprove their existence. Regardless of the detection of the β twins, the experiment should further understanding of the development of the refined grain structure, and explain how the new grain orientations come to dominate the structure at the expense of the parent β orientation.

### Extension of Simulation Studies

The work within this thesis has demonstrated that the prior-β grain refinement observed in additive manufacture of Ti-6Al-4V can be successfully replicated in laboratory conditions by both simulation of the deformation pass and the thermal cycle of the subsequent deposition pass. There therefore now exists the framework to carry out more systematic studies of both the influence of both strain, and the thermal history on the refinement.

The success of the simulated sample also allows for the effect of other variables to be tested out on the small scale without the expense and complication of building several walls by AM. For example, the expected effect of the technique on different alloys can be more rapidly tested than by finding the build parameters by trial and error.

### Progression of WAAM technology

Cranfield University, the originators of the WAAM process, are looking to develop the technology and commercialise it. Along with increasing the scope to more alloys as discussed above, Cranfield are in the process of developing a rolling system that rolls the sides of the AM walls as shown in Figure 6:3 that they are calling ‘pinch rolling’ to cope with alternative build geometries. Initial trials of the technique have been promising with regards to the reductions in residual stresses, but the technique also shows promise for prior-β grain refinement as well. The ability to alter both the width of the rollers in addition to the height at which the wall is rolled means that greater control over the region of the wall that is deformed can be achieved. Greater control of the deformed region could lead to better build efficiency that is when considered in conjunction with the thermal influence of the subsequent deposition pass, as the deformation need only be applied over the region that is known to be taken above the β transus, but not remelted.

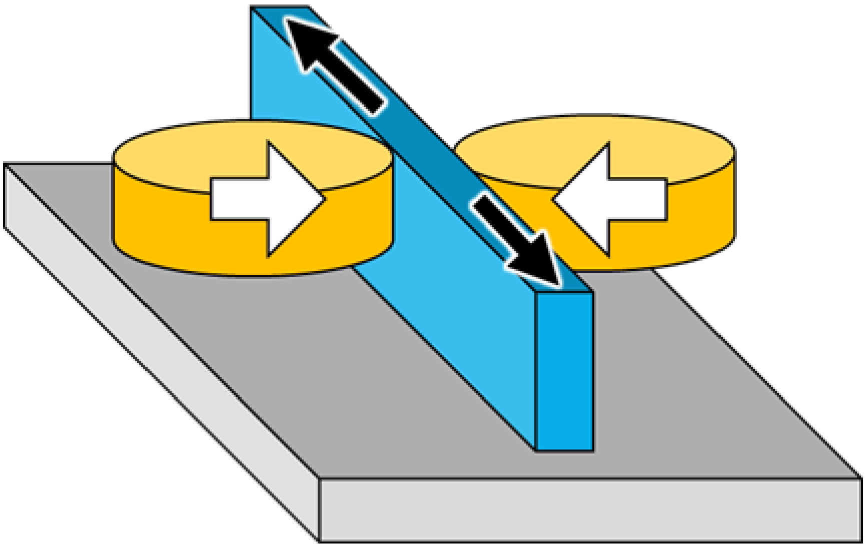

Figure 6:3. Schematic of new WAAM side-rolling technique being developed by Cranfield University [178].

# Appendix – Twinned β Orientation Calculation

In **Manuscript 4** calculated pole figures were presented in figures 12 and 13 of the orientations that twins could have when both the parent orientation and twinning systems were known. This section gives a brief summary of how the orientations of the twins were calculated.

The orientation of any crystal in space can be expressed as a three dimensional rotation from a standard reference frame. Therefore both a crystal orientation, and a reorientation due to twinning, can be expressed as a rotation matrix. It then follows that the twinned volumes orientation ($O_{twin}$) can then easily be calculated from the dot product of the orientation of the parent ($O_{parent}$), and the rotation due to twinning ($R_{twin}$), as demonstrated in Equation 5.

$$O_{twin} = O_{Parent} \cdot R_{twin}$$

Equation 5

As in **Manuscript 4** the twinning reorientation is being calculated from a measured orientation by EBSD, it is necessary to consider the orientation notation used by the acquisition software. Although orientations can be stored as rotation matrices, it is more common for EBSD software to store the information in Euler angles as in this way the orientation is defined by three angles rather than array of nine numbers and therefore takes less computer memory. Euler angles define an orientation by three intrinsic rotations about the axes of a rotating coordinate system. The most common set of rotations for EBSD data is the Bunge notation consisting of a rotation of $\varphi_1$ around the *z* axis, followed by a rotation of $\Phi$ around the new *x'* axis, before a final rotation of $\varphi_1$ around the resultant *z''* axis [154]. Therefore the rotation matrix that defines the orientation of a crystal, $O_{Parent}$, can be calculated by the dot product of these three rotations, and is given in Equation 6 .

$$O_{parent} = \begin{pmatrix} \cos\varphi_1\cos\varphi_2 - \cos\Phi\sin\varphi_1\sin\varphi_2 & -\cos\Phi\cos\varphi_2\sin\varphi_1 - \cos\varphi_1\sin\varphi_2 & \sin\Phi\sin\varphi_1 \\ \cos\varphi_2\sin\varphi_1 + \cos\Phi\cos\varphi_1\sin\varphi_2 & \cos\Phi\cos\varphi_1\cos\varphi_2 - \sin\varphi_1\sin\varphi_2 & -\cos\varphi_1\sin\Phi \\ \sin\Phi\sin\varphi_2 & \cos\varphi_2\sin\Phi & \cos\Phi \end{pmatrix}$$

Equation 6

Twins are often described by the crystallographic geometry they occur in. For example the β twinning system discussed in **Manuscript 4**, is labelled as {112}<111> where {112} is the family of planes that the twinning occurs on, and <111> are the directions that the twinning shear can be accommodated in. Twins can also be described by an angle axis pair that also describes the misorientation, in this case 60° around the <111> axis. As the twinning in this case is of a cubic β phase, the rotation matrix corresponding to a twin system, $R_{twin}$, can be calculated from the angle-axis pair that defines the twin system by the Rodriguez rotation formula given in Equation 7, the full derivation of which is given in reference [179].

$$R_{twin} = \begin{pmatrix} \cos\theta + {\omega_h}^2(1-\cos\theta) & \omega_h\omega_k(1-\cos\theta) - \omega_l\sin\theta & \omega_h\omega_l(1-\cos\theta) + \omega_k\sin\theta \\ \omega_k\omega_h(1-\cos\theta) + \omega_l\sin\theta & \cos\theta + {\omega_k}^2(1-\cos\theta) & \omega_k\omega_l(1-\cos\theta) - \omega_h\sin\theta \\ \omega_l\omega_h(1-\cos\theta) - \omega_k\sin\theta & \omega_l\omega_k(1-\cos\theta) + \omega_h\sin\theta & \cos\theta + {\omega_l}^2(1-\cos\theta) \end{pmatrix}$$

Equation 7

Where a rotation of angle $\theta$ takes place around a crystallographic axis specified by the unit vector $\widehat{\omega} = (\omega_h, \omega_k, \omega_l)$.

In order to be plotted in pole figures and EBSD maps by Orientation analysis software, Bunge notation Euler angles can be extracted from $O_{twin}$ by consideration of the components of the matrix in Equation 5.

# References

[1] R.R. Boyer, An overview on the use of titanium in the aerospace industry. Mater. Sci. Eng. A. 1996; 213: 103–114.

[2] S.W. Williams, WAAM Technology Overview, in: WAAMMat Idustry Day, Cranfield, 2015.

[3] S.S. Al-Bermani, M.L. Blackmore, W. Zhang, I. Todd, The Origin of Microstructural Diversity, Texture, and Mechanical Properties in Electron Beam Melted Ti-6Al-4V. Metall. Mater. Trans. A. 2010; 41: 3422–3434.

[4] B.E. Carroll, T.A. Palmer, A.M. Beese, Anisotropic tensile behavior of Ti–6Al–4V components fabricated with directed energy deposition additive manufacturing. Acta Mater. 2015; 87: 309–320.

[5] J. Donoghue, J. Sidhu, A. Wescott, P. Prangnell, Integration of Deformation Processing with Additive Manufacture of Ti-6Al- 4V Components for Improved β Grain Structure and Texture, in: 2015 TMS Annu. Meet. Exhib., Orlando, Florida, 2015.

[6] F. Martina, P.A. Colegrove, S.W. Williams, J. Meyer, Microstructure of Interpass Rolled Wire + Arc Additive Manufacturing Ti-6Al-4V Components. Metall. Mater. Trans. A. 2015; 46: 6103–6118.

[7] W.U.H. Syed, A.J. Pinkerton, L. Li, A comparative study of wire feeding and powder feeding in direct diode laser deposition for rapid prototyping. Appl. Surf. Sci. 2005; 247: 268–276.

[8] A.A. Antonysamy, P.B. Prangnell, J. Meyer, Effect of Wall Thickness Transitions on Texture and Grain Structure in Additive Layer Manufacture (ALM) of Ti-6Al-4V. Mater. Sci. Forum. 2012; 706-709: 205–210.

[9] I. Gibson, D. Robinson, B. Stucker, D.W. Rosen, B. Stucker, Additive Manufacturing Technologies, Springer, Boston, MA, 2012.

[10] C.X.F. Lam, X.M. Mo, S.H. Teoh, D.W. Hutmacher, Scaffold development using 3D printing with a starch-based polymer. Mater. Sci. Eng. C. 2002; 20: 49–56.

[11] H. Seitz, W. Rieder, S. Irsen, B. Leukers, C. Tille, Three-dimensional printing of porous ceramic scaffolds for bone tissue engineering. J. Biomed. Mater. Res. B. Appl. Biomater. 2005; 74: 782–788.

[12] G. V. Salmoria, R.A. Paggi, A. Lago, V.E. Beal, Microstructural and mechanical characterization of PA12/MWCNTs nanocomposite manufactured by selective laser sintering. Polym. Test. 2011; 30: 611–615.

[13] E. Brandl, F. Palm, V. Michailov, B. Viehweger, C. Leyens, Mechanical properties of additive manufactured titanium (Ti–6Al–4V) blocks deposited by a solid-state laser and wire. Mater. Des. 2011; 32: 4665–4675.

[14] T. Allard, M. Sitchon, Use of hand-held laser scanning and 3D printing for creation of a museum exhibit, in: 6th Int. Symp. Virtual Reality, Archaeol. Cult. Herit., 2005.

[15] M. Vatani, A. Rahimi, F. Brazandeh, An enhanced slicing algorithm using nearest distance analysis for layer manufacturing. Proceeding World Acad. Sci. Eng. Technol. 2009; 3: 721–726.

[16] S. Roy, S. Suwas, S. Tamirisakandala, D.B. Miracle, R. Srinivasan, Development of solidification microstructure in boron-modified alloy Ti–6Al–4V–0.1B. Acta Mater. 2011; 59: 5494–5510.

[17] K.M.B. Taminger, R.A. Hafley, Electron beam freeform fabrication: a rapid metal deposition process, in: Proc. 3rd Annu. Automot. Compos. Conf., Troy, MI, 2003.

[18] B. Vrancken, L. Thijs, J. Kruth, J. Van Humbeeck, Heat treatment of Ti6Al4V produced by Selective Laser Melting: Microstructure and mechanical properties. J. Alloys Compd. 2012; 541: 177–185.

[19] J. Allen, An Investigation into the Comparative Costs of Additive Manufacture vs. Machine from Solid for Aero Engine Parts. Cost Eff. Manuf. via Net-Shape Process. 2006; 1–10.

[20] E. Atzeni, A. Salmi, Economics of additive manufacturing for end-usable metal parts. Int. J. Adv. Manuf. Technol. 2012; 62: 1147–1155.

[21] P. Heinl, a. Rottmair, C. Körner, R.F. Singer, Cellular Titanium by Selective Electron Beam Melting. Adv. Eng. Mater. 2007; 9: 360–364.

[22] J. Parthasarathy, B. Starly, S. Raman, A design for the additive manufacture of functionally graded porous structures with

tailored mechanical properties for biomedical applications. J. Manuf. Process. 2011; 13: 160–170.

[23] M.S. Domack, J.M. Baughman, Development of nickel-titanium graded composition components. Rapid Prototyp. J. 2005; 11: 41–51.

[24] E. Yasa, J.P. Kruth, Microstructural investigation of selective laser melting 316L stainless steel parts exposed to laser re-melting, in: Procedia Eng., 2011: pp. 389–395.

[25] M. Griffith, D. Keicher, Free form fabrication of metallic components using laser engineered net shaping (LENS), in: Time-Compression Technol., Texus, 1996: pp. 125–132.

[26] P. Kobryn, S. Semiatin, The laser additive manufacture of Ti-6Al-4V. JOM. 2001; 40–42.

[27] D. Locke, Laser metal deposition defined. Ind. Laser Solut. 2010;

[28] J. Kummailil, C. Sammarco, D. Skinner, C.A. Brown, K. Rong, Effect of Select LENS$^{TM}$ Processing Parameters on the Deposition of Ti-6Al-4V. J. Manuf. Process. 2005; 7: 42–50.

[29] D.D. Gu, W. Meiners, K. Wissenbach, R. Poprawe, Laser additive manufacturing of metallic components: materials, processes and mechanisms. Int. Mater. Rev. 2012; 57: 133–164.

[30] J. Laeng, J. Stewart, F. Liou, Laser metal forming processes for rapid prototyping-a review. Int. J. Prod. Res. 2010; 37–41.

[31] B. Baufeld, O. Van Der Biest, R. Gault, Additive manufacturing of Ti–6Al–4V components by shaped metal deposition: Microstructure and mechanical properties. Mater. Des. 2010; 31: S106–S111.

[32] D. Clark, M.R. Bache, M.T. Whittaker, Shaped metal deposition of a nickel alloy for aero engine applications. J. Mater. Process. Technol. 2008; 203: 439–448.

[33] P. Colegrove, H.E. Coules, J. Fairman, F. Martina, T. Kashoob, H. Mamash, et al., Microstructure and residual stress improvement in wire and arc additively manufactured parts through high-pressure rolling. J. Mater. Process. Technol. 2013; 213: 1782–1791.

[34] A.A. Antonysamy, Microstructure, texture and mechanical property evolution during additive manufacturing of Ti6Al4V alloy for aerospace applications, University of Manchester, 2012.

[35] Arcam AB, Arcam A2X - Product Catalogue. n.d.;

[36] Arcam AB, Arcam Q20 - Product Catalogue. n.d.;

[37] K. Taminger, R. Hafley, Electron beam freeform fabrication for cost effective near-net shape manufacturing. NATO AVT. 2006;

[38] H.K. Rafi, N. V. Karthik, H. Gong, T.L. Starr, B.E. Stucker, Microstructures and Mechanical Properties of Ti6Al4V Parts Fabricated by Selective Laser Melting and Electron Beam Melting. J. Mater. Eng. Perform. 2013; 22: 3872–3883.

[39] RealLizer, Selective Laser Melting - ReaLizer - Product Catalogue. n.d.;

[40] GmbH SLM Solutions, SLM 500HL - Product Catalogue. n.d.;

[41] Optomec, LENS 850-R Datasheet. 2014;

[42] F. Martina, S.W. Williams, P. Colegrove, Improved microstructure and increased mechanical properties of additive manufacture produced Ti-6Al-4V by interpass cold rolling, in: SFF Symp., 2013: pp. 490–496.

[43] F. Martina, Investigation of Methods to Manipulate Geometry, Microstructure and Mechanical Properties in Titanium Large Scale Wire+Arc Additive Manufacturing, Cranfield University, 2014.

[44] W.E. Frazier, Metal Additive Manufacturing: A Review. J. Mater. Eng. Perform. 2014; 23: 1917–1928.

[45] S.M. Gaytan, L.E. Murr, F. Medina, E. Martinez, M.I. Lopez, R.B. Wicker, Advanced metal powder based manufacturing of complex components by electron beam melting. Mater. Technol. Adv. Perform. Mater. 2009; 24: 180–190.

[46] A. Gasser, G. Backes, I. Kelbassa, A. Weisheit, K. Wissenbach, Laser additive manufacturing: laser metal deposition (LMD) and selective laser melting (SLM) in turbo-engine applications. Laser Mater. Process. 2010; 58–63.

[47] D.F.O. Braga, H.E. Coules, T. Pirling, V. Richter-Trummer, P. Colegrove, P.M.S.T. de Castro, Assessment of residual stress of welded structural steel plates with or without post weld rolling using the contour method and neutron diffraction.

J. Mater. Process. Technol. 2013; 213: 2323–2328.

[48] J. Altenkirch, A. Steuwer, P.J. Withers, S.W. Williams, M. Poad, S.W. Wen, Residual stress engineering in friction stir welds by roller tensioning. Sci. Technol. Weld. Join. 2009; 14: 185–192.

[49] Y. Xie, H. Zhang, F. Zhou, Improvement in geometrical accuracy and mechanical property for arc-based additive manufacturing using metamorphic rolling mechanism. J. Manuf. Sci. Eng. 2015;

[50] E. Statnikov, Physics and mechanism of ultrasonic impact treatment. Int. Inst. Weld. 2004; XIII.:

[51] E. Statnikov, V. Muktepavel, A. Blomqvist, Comparison of ultrasonic impact treatment (UIT) and other fatigue life improvement methods. Weld. World. 2002; 46: 20–32.

[52] S. Roy, J. Fisher, Enhancing fatigue strength by ultrasonic impact treatment. Int. J. Steel Struct. 2005;

[53] B.N. Mordyuk, G.I. Prokopenko, Ultrasonic impact peening for the surface properties' management. J. Sound Vib. 2007; 308: 855–866.

[54] Alcoa, Alcoa Process Diagram. Twitter. 2016;

[55] R. Brooks, Alcoa Details Research, Process Strategy to Maximize 3DP. Forging. 2015;

[56] R.W.K. Honecombe, The Plastic Deformation of Metals, 2nd ed., Butler & Tanner, London, 1984.

[57] D. Hull, D.J. Bacon, Introduction to Dislocations, 3rd ed., Pergamon Press, Oxford, 1984.

[58] E. Schmid, W. Boas, Kristallplastizitaet, (Plasticity of crystals). Transl. 1950. 1935;

[59] R. Mises, Mechanik der plastischen Formänderung von Kristallen. Zeitschrift Für Angew. Math. Und Mech. 1928; 8: 162–185.

[60] E.O. Hall, Twinning and diffusionless transformations in metals, Butterworths Scientific Publications, London, 1954.

[61] J. Christian, S. Mahajan, Deformation twinning. Prog. Mater. Sci. 1995; 39: 1–157.

[62] D. Eylon, J.A. Hall, Fatigue behaviour of beta processed titanum alloy IMI 685. Metall. Trans. A. 1977; 8: 981–990.

[63] J.L. Sun, P.W. Trimby, F.K. Yan, X.Z. Liao, N.R. Tao, J.T. Wang, Grain size effect on deformation twinning propensity in ultrafine-grained hexagonal close-packed titanium. Scr. Mater. 2013; 69: 428–431.

[64] Y.T. Zhu, X.Z. Liao, X.L. Wu, J. Narayan, Grain size effect on deformation twinning and detwinning. J. Mater. Sci. 2013; 48: 4467–4475.

[65] J. Wang, Z. Zeng, C.R. Weinberger, Z. Zhang, T. Zhu, S.X. Mao, In situ atomic-scale observation of twinning-dominated deformation in nanoscale body-centred cubic tungsten. Nat. Mater. 2015; 14: 594–600.

[66] H.S. Park, K. Gall, J.A. Zimmerman, Deformation of FCC nanowires by twinning and slip. J. Mech. Phys. Solids. 2006; 54: 1862–1881.

[67] V. Randle, O. Engler, Introduction to Texture Analysis: Macrotexture, Microtexture and Orientation Mapping, CRC Press, Boca Raton, 2000.

[68] U.F. Kocks, C.N. Tomé, H.-R. Wenk, Texture and Anisotropy: Preferred Orientations in Polycrystals and their Effect on Materials Properties, Cambridge University Press, Cambridge, 2000.

[69] F. Humphreys, M. Hatherly, Recrystallization and Related Annealing Phenomena, 2nd ed., Pergamon, 2004.

[70] M. Zhao, J.C. Li, Q. Jiang, Hall–Petch relationship in nanometer size range. J. Alloys Compd. 2003; 361: 160–164.

[71] G. Chen, D. Fray, T. Farthing, Direct electrochemical reduction of titanium dioxide to titanium in molten calcium chloride. Nature. 2000; 407: 361–364.

[72] R. Cole, E. Bateh, J. Potter, Fasteners for composite structures. Composites. 1982; 5: 233–240.

[73] I. Polmear, Light Alloys: From Traditional Alloys to Nanocrystals, Butterworth-Heinemann, 2005.

[74] G. Lütjering, J. C.Williams, Titanium, 2nd ed., Springer, Berlin, 2007.

[75] E.A. Bel'skaya, E.Y. Kulyamina, Electrical resistivity of titanium in the temperature range from 290 to 1800 K. High Temp. 2007; 45: 785–796.

[76] F.C. Campbell, Elements of Metallurgy and Engineering Alloys, ASM International, 2008.

[77] W.G. Burgers, Cubic-Body-Centered Modification Into The Hexagonal-Close-Packed Modification Of Zirconium. Phys. I. 1933; 561–586.

[78] T. Karthikeyan, S. Saroja, M. Vijayalakshmi, Evaluation of misorientation angle-axis set between variants during transformation of bcc to hcp phase obeying Burgers orientation relation. Scr. Mater. 2006; 55: 771–774.

[79] M.R. Daymond, R.A. Holt, S. Cai, P. Mosbrucker, S.C. Vogel, Texture inheritance and variant selection through an hcp–bcc–hcp phase transformation. Acta Mater. 2010; 58: 4053–4066.

[80] N. Gey, M. Humbert, M. Philippe, Y. Combres, Investigation of the α-and β-texture evolution of hot rolled Ti-64 products. Mater. Sci. Eng. A. 1996; 219: 80–88.

[81] G.C. Obasi, S. Birosca, J. Quinta da Fonseca, M. Preuss, Effect of β grain growth on variant selection and texture memory effect during α→β→α phase transformation in Ti–6 Al–4 V. Acta Mater. 2012; 60: 1048–1058.

[82] R. Shi, Y. Wang, Variant selection during α precipitation in Ti-6Al-4V under the influence of local stress - A simulation study. Acta Mater. 2013; 61: 6006–6024.

[83] D. Bhattacharyya, G.B. Viswanathan, R. Denkenberger, D. Furrer, H.L. Fraser, The role of crystallographic and geometrical relationships between α and β phases in an α/β titanium alloy. Acta Mater. 2003; 51: 4679–4691.

[84] D.A. Porter, K.E. Easterling, M.Y. Sherif, Phase Transformations in Metals and Alloys, Taylor & Francis Group, 2009.

[85] I. Lonardelli, N. Gey, H.R. Wenk, M. Humbert, S.C. Vogel, L. Lutterotti, In situ observation of texture evolution during α→β and β→α phase transformations in titanium alloys investigated by neutron diffraction. Acta Mater. 2007; 55: 5718–5727.

[86] Argus Media, MetalPrices.com. 2016;

[87] E.O. Ezugwu, Z.M. Wang, Titanium alloys and their machinability - a review. J. Mater. Process. Technol. 1997; 68: 262–274.

[88] R. Komanduri, Some clarifications on the mechanics when machining titanium alloys of chip formation. Wear. 1982; 76: 15–34.

[89] C.R. Dandekar, Y.C. Shin, J. Barnes, Machinability improvement of titanium alloy (Ti–6Al–4V) via LAM and hybrid machining. Int. J. Mach. Tools Manuf. 2010; 50: 174–182.

[90] ASTM, Standard Specification for Titanium-6Aluminum-4Vanadium Alloy Castings for Surgical Implants (UNS R56406). 2004; F1108.

[91] R. Pederson, Microstructure and Phase Transformation of Ti-6Al-4V, Lulea University of Technology, 2002.

[92] C. Loier, G. Thauvin, A. Hazotte, A. Simon, Influence of Deformation Kinetics of Ti-6wt.%Al-4wt.%V. J. Less Common Met. 1985; 108: 295–312.

[93] T.R. Bieler, R.M. Trevino, L. Zeng, Alloys: Titanium, in: Encycl. Condens. Matter Phys., Elsevier, 2005: pp. 65–76.

[94] F. Wang, S. Williams, P. Colegrove, A.A. Antonysamy, Microstructure and Mechanical Properties of Wire and Arc Additive Manufactured Ti-6Al-4V. Metall. Mater. Trans. A. 2012; 44: 968–977.

[95] M. Simonelli, Y.Y. Tse, C. Tuck, On the Texture Formation of Selective Laser Melted Ti-6Al-4V. Metall. Mater. Trans. A. 2014; 45: 2863–2872.

[96] T. Furuhara, B. Poorganji, H. Abe, T. Maki, Dynamic recovery and recrystallization in titanium alloys by hot deformation. Jom. 2007; 59: 64–67.

[97] R. Ding, Z.X. Guo, Microstructural evolution of a Ti–6Al–4V alloy during β-phase processing: experimental and simulative investigations. Mater. Sci. Eng. A. 2004; 365: 172–179.

[98] E.I. Poliak, J.J. Jonas, Initiation of Dynamic Recrystallization in Constant Strain Rate Hot Deformation. ISIJ Int. 2003; 43: 684–691.

[99] P. Honarmandi, M. Aghaie-Khafri, Hot Deformation Behavior of Ti–6Al–4V Alloy in β Phase Field and Low Strain Rate. Metallogr. Microstruct. Anal. 2012; 2: 13–20.

[100] A. Pilchak, A. Bhattacharjee, The Effect of Microstructure on Fatigue Crack Initiation in Ti-6Al-4V, in: ICF12, Ottawa 2012, 2013: pp. 1–10.

[101] K. Muszka, M. Lopez-Pedrosa, K. Raszka, M. Thomas, W.M. Rainforth, B.P. Wynne, The Impact of Strain Reversal on Microstructure Evolution and Orientation Relationships in Ti-6Al-4V with an Initial Alpha Colony Microstructure. Metall. Mater. Trans. A. 2014; 45: 5997–6007.

[102] S.. Semiatin, V. Seetharaman, I. Weiss, Flow behavior and globularization kinetics during hot working of Ti–6Al–4V with a colony alpha microstructure. Mater. Sci. Eng. A. 1999; 263: 257–271.

[103] I. Weiss, F.H. Froes, D. Eylon, G.E. Welsch, Modification of alpha morphology in Ti-6Al-4V by thermomechanical processing. Metall. Trans. A. 1986; 17: 1935–1947.

[104] E.B. Shell, S.L. Semiatin, Effect of initial microstructure on plastic flow and dynamic globularization during hot working of Ti-6Al-4V. Metall. Mater. Trans. A. 1999; 30: 3219–3229.

[105] I. Weiss, F.H. Froes, D. Eylon, G.E. Welsch, Modification of alpha morphology in Ti-6Al-4V by thermomechanical processing. Metall. Trans. A. 1986; 17: 1935–1947.

[106] G. Lütjering, Influence of processing on microstructure and mechanical properties of ( α+ β) titanium alloys. Mater. Sci. Eng. A. 1998; 243: 32–45.

[107] R.K. Nalla, B.L. Boyce, J.P. Campbell, J.O. Peters, R.O. Ritchie, Influence of microstructure on high-cycle fatigue of Ti-6Al-4V: Bimodal vs. lamellar structures. Metall. Mater. Trans. A. 2002; 33: 899–918.

[108] M.J. Bermingham, S.D. McDonald, M.S. Dargusch, D.H. St. John, Grain-refinement mechanisms in titanium alloys. J. Mater. Res. 2011; 23: 97–104.

[109] C.R. Whitsett, S.M.L. Sastry, J.E. O'Neal, R.J. Lederich, Influence of Rare-Earth Additions on Properties of Titanium Alloys. Room-Temperature Tensile Properties and Fracture Toughness of Ti-6Al-4V with Erbium, Yttrium, and Yttria Additions, 1978.

[110] G.R.E. M.C. Nordin D.L. Olson, The Influence of Yttrium Microadditions on Titanium Weld Metal Cracking Susceptibility and Grain Morphology. Weld. Res. Suppl. 1987; 342–352.

[111] M.J. Bermingham, S.D. McDonald, K. Nogita, D.H. St. John, M.S. Dargusch, Effects of boron on microstructure in cast titanium alloys. Scr. Mater. 2008; 59: 538–541.

[112] S. Tamirisakandala, R.B. Bhat, J.S. Tiley, D.B. Miracle, Grain refinement of cast titanium alloys via trace boron addition. Scr. Mater. 2005; 53: 1421–1426.

[113] M.J. Bermingham, S.D. Mcdonald, M.S. Dargusch, D.H. Stjohn, Microstructure of cast Titanium alloys. Mater. Forum. 2007; 31: 84–89.

[114] S. Mitzner, S. Liu, M. Domack, R. Hafley, Grain Refinement of Freeform Fabricated Ti-6Al-4V Alloy Using Beam/Arc Modulation. 23rd Annu. Int. Solid Free. Fabr. Symp. 6-8 Aug 2012; Austin, TX; United States. 2012; 536–555.

[115] N. Kishore Babu, S. Ganesh Sundara Raman, R. Mythili, S. Saroja, Correlation of microstructure with mechanical properties of TIG weldments of Ti-6Al-4V made with and without current pulsing. Mater. Charact. 2007; 58: 581–587.

[116] S. Sundaresan, G.D.J. Ram, Use of magnetic arc oscillation for grain refinement of gas tungsten arc welds in <I>α–β</I> titanium alloys. Sci. Technol. Weld. Join. 1999; 4: 151–160.

[117] M. Donachie, Titanium: A Technical Guide, 2nd ed., ASM International, 2000.

[118] S. Gorsse, D.B. Miracle, Mechanical properties of Ti-6Al-4V/TiB composites with randomly oriented and aligned TiB reinforcements. Acta Mater. 2003; 51: 2427–2442.

[119] S. Zaefferer, A study of active deformation systems in titanium alloys: dependence on alloy composition and correlation with deformation texture. Mater. Sci. Eng. A. 2003; 344: 20–30.

[120] G.G. Yapici, I. Karaman, Z. Luo, Mechanical twinning and texture evolution in severely deformed Ti–6Al–4V at high temperatures. Acta Mater. 2006; 54: 3755–3771.

[121] R.J. McCabe, E.K. Cerreta, A. Misra, G.C. Kaschner, C.N. Tomé, Effects of texture, temperature and strain on the deformation modes of zirconium. Philos. Mag. 2006; 86: 3595–3611.

[122] S. Semiatin, T. Bieler, Effect of texture and slip mode on the anisotropy of plastic flow and flow softening during hot working of Ti-6Al-4V. Metall. Mater. Trans. A. 2001; 32.:

[123] D.G.L. Prakash, R. Ding, R.J. Moat, I. Jones, P.J. Withers, J.Q. Da Fonseca, et al., Deformation twinning in Ti-6Al-4V during low strain rate deformation to moderate strains at room temperature. Mater. Sci. Eng. A. 2010; 527: 5734–5744.

[124] I. Karaman, G.G. Yapici, Y.I. Chumlyakov, I.V. Kireeva, Deformation twinning in difficult-to-work alloys during severe plastic deformation. Mater. Sci. Eng. A. 2005; 410-411: 243–247.

[125] M. Matsuda, S. Ii, Y. Kawamura, Y. Ikuhara, M. Nishida, Interaction between long period stacking order phase and deformation twin in rapidly solidified Mg97Zn1Y2 alloy. Mater. Sci. Eng. A. 2004; 386: 447–452.

[126] C. Leyens, M. Peters, Titanium and Titanium Alloys: Fundamentals and Applications, Wiley, 2003.

[127] Y. Yang, G.P. Li, G.M. Cheng, H. Wang, M. Zhang, F. Xu, et al., Stress-introduced α″ martensite and twinning in a multifunctional titanium alloy. Scr. Mater. 2008; 58: 9–12.

[128] E. Bertrand, P. Castany, I. Péron, T. Gloriant, Twinning system selection in a metastable β-titanium alloy by Schmid factor analysis. Scr. Mater. 2011; 64: 1110–1113.

[129] S. Hanada, O. Izumi, Transmission electron microscopic observations of mechanical twinning in metastable beta titanium alloys. Metall. Trans. A. 1986; 17: 1409–1420.

[130] S. Suri, G.B. Viswanathan, T. Neeraj, D.H. Hou, M.J. Mills, Room temperature deformation and mechanisms of slip transmission in oriented single-colony crystals of an α/β titanium alloy. Acta Mater. 1999; 47: 1019–1034.

[131] A.A. Salem, S.L. Semiatin, Anisotropy of the hot plastic deformation of Ti–6Al–4V single-colony samples. Mater. Sci. Eng. A. 2009; 508: 114–120.

[132] S. Mironov, M. Murzinova, S. Zherebtsov, G. a. Salishchev, S.L. Semiatin, Microstructure evolution during warm working of Ti-6Al-4V with a colony-alpha microstructure. Acta Mater. 2009; 57: 2470–2481.

[133] S. Mironov, M. Murzinova, S. Zherebtsov, G. a. Salishchev, S.L. Semiatin, Microstructure evolution during warm working of Ti-6Al-4V with a colony-alpha microstructure. Acta Mater. 2009; 57: 2470–2481.

[134] A. Jaworski, S. Ankem, Influence of the second phase on the room-temperature tensile and creep deformation mechanisms of alpha-beta titanium alloys: Part I. Tensile deformation. Metall. Mater. Trans. A. 2006; 37: 2739–2754.

[135] P. Edwards, A. O’Conner, M. Ramulu, Electron Beam Additive Manufacturing of Titanium Components: Properties and Performance. J. Manuf. Sci. Eng. 2013; 135.:

[136] A.A. Antonysamy, J. Meyer, P.B. Prangnell, Effect of Build Geometry on the β−Grain Structure and Texture in Additive Manufacture of Ti-6Al-4V by Selective Electron Beam Melting. Mater. Charact. 2013; 8: 153–168.

[137] M. Rappaz, S.A. David, J.M. Vitek, L.A. Boatner, Analysis of solidification microstructures in Fe-Ni-Cr single-crystal welds. Metall. Trans. A. 1990; 21: 1767–1782.

[138] N. Hrabe, T. Quinn, Effects of processing on microstructure and mechanical properties of a titanium alloy (Ti–6Al–4V) fabricated using electron beam melting (EBM), Part 2: Energy input, orientation, and location. Mater. Sci. Eng. A. 2013; 573: 271–277.

[139] S. Kelly, S. Kampe, Microstructural Evolution in Laser-Deposited Multilayer Ti-6Al-4V Builds : Part I . Microstructural Characterization. Metall. Mater. Trans. A. 2004; 35: 1861–1867.

[140] J.W. Elmer, T.A. Palmer, S.S. Babu, W. Zhang, T. DebRoy, Phase transformation dynamics during welding of Ti-6Al-4V. J. Appl. Phys. 2004; 95: 8327–8339.

[141] P. Kobryn, S. Semiatin, Microstructure and texture evolution during solidification processing of Ti–6Al–4V. J. Mater. Process. Technol. 2003; 135: 330–339.

[142] ASTM, Standard Specification for Wrought Titanium-6Aluminum-4Vanadium Alloy for Surgical Implant Applications (UNS R56400). 2008; F1472.

[143] E. Amsterdam, G. Kool, High Cycle Fatigue of Laser Beam Deposited Ti-6Al-4V and Inconel 718, in: Int. Comm. Aeronaut. Fatigue, Rotterdam, The Netherlands, 2009: pp. 1261–1274.

[144] T. Vilaro, C. Colin, J.D. Bartout, As-Fabricated and Heat-Treated Microstructures of the Ti-6Al-4V Alloy Processed by Selective Laser Melting. Metall. Mater. Trans. A. 2011; 42: 3190–3199.

[145] E. Brandl, B. Baufeld, C. Leyens, R. Gault, Additive manufactured Ti-6Al-4V using welding wire: comparison of laser and arc beam deposition and evaluation with respect to aerospace material specifications. Phys. Procedia. 2010; 5: 595–606.

[146] W.A. Backofen, Deformation Processing, Addison-Wesley Publishing Company, 1972.

[147] S. Kelly, S. Kampe, Microstructural evolution in laser-deposited multilayer Ti-6Al-4V builds: Part II. Thermal modeling. Metall. Mater. Trans. A. 2004; 35: 1869–1879.

[148] B. Roebuck, D.C. Cox, R.C. Reed, An Innovative Device for the Mechanical Testing of Miniature Specimens of Superalloys, in: TMS 2004, Charlotte, North Carolina, 2004: pp. 523–528.

[149] S.Y. Chiu, Y.L. Wang, C.P. Liu, J.K. Lan, C. Ay, M.S. Feng, et al., The application of electrochemical metrologies for investigating chemical mechanical polishing of Al with a Ti barrier layer. Mater. Chem. Phys. 2003; 82: 444–451.

[150] L.A. Giannuzzi, F.A. Stevie, A review of focused ion beam milling techniques for TEM specimen preparation. Micron. 1999; 30: 197–204.

[151] P.J. Goodhew, J. Humphreys, R. Beanland, Electron Microscopy and Analysis, Third Edit, CRC Press, 2000.

[152] R. Rinaldi, X. Llovet, Electron Probe Microanalysis: A Review of the Past, Present, and Future. Microsc. Microanal. 2015; 21: 1053–1069.

[153] S. Nishhikawa, S. Kikuchi, The Diffraction of Cathode Rays by Calcite. Proc. Imp. Acad. 1928; 4: 475–477.

[154] Adam J. Schwartz, Electron Backscatter Diffraction in Materials Science, Springer US, Boston, MA, 2009.

[155] S. Zaefferer, A critical review of orientation microscopy in SEM and TEM. Cryst. Res. Technol. 2011; 46: 607–628.

[156] F.J. Humphreys, Grain and subgrain characterisation by electron backscatter diffraction. J. Mater. Sci. 2001; 36: 3833–3854.

[157] J.Y. Kang, S.J. Park, M.B. Moon, Phase Analysis on Dual-Phase Steel Using Band Slope of Electron Backscatter Diffraction Pattern. Microsc. Microanal. 2013; 19: 13–16.

[158] R.R. Keller, R.H. Geiss, Transmission EBSD from 10 nm domains in a scanning electron microscope. J. Microsc. 2012; 245: 245–251.

[159] S. Suzuki, Features of transmission EBSD and its application. JOM. 2013; 65: 1254–1263.

[160] A.J.W. Garner, Investigating The effect of Oxide Texture on the CorrosionPerformance of Zirconium Alloys, University of Manchester, 2015.

[161] R. Vincent, P.A. Midgley, Double conical beam-rocking system for measurement of integrated electron diffraction intensities. Ultramicroscopy. 1994; 53: 271–282.

[162] Gatan, Murano Heating Stage Data Sheet. 2015;

[163] P.S. Davies, An investigation of microstructure and texture evolution in the Near-α titanium alloy timetal 834, University of Sheffield, 2009.

[164] P.S. Davies, B.P. Wynne, W.M. Rainforth, M.J. Thomas, P.L. Threadgill, Development of Microstructure and Crystallographic Texture during Stationary Shoulder Friction Stir Welding of Ti-6Al-4V. Metall. Mater. Trans. A. 2011; 42: 2278–2289.

[165] M. Humbert, N. Gey, The calculation of a parent grain orientation from inherited variants for approximate (b.c.c.–h.c.p.) orientation relations. J. Appl. Crystallogr. 2002; 35: 401–405.

[166] N. Gey, M. Humbert, Specific analysis of EBSD data to study the texture inheritance due to the β→ α phase transformation. J. Mater. Sci. 2003; 8: 1289–1294.

[167] P. Homporová, F. Warchomicka, Dynamic phase evolution in titanium alloy Ti-6Al-4V, in: 11th World Conf. Titan., Beijing, China, 2011.

[168] R.M. Saeed, J.P. Schlegel, C. Castano, R. Sawafta, Uncertainty of Thermal Characterization of Phase Change Material by

Differential Scanning Calorimetry Analysis. Int. J. Eng. Res. Technol. 2016; 5: 405–412.

[169] J.W. Elmer, T.A. Palmer, S.S. Babu, E.D. Specht, In situ observations of lattice expansion and transformation rates of α and β phases in Ti-6Al-4V. Mater. Sci. Eng. A. 2005; 391: 104–113.

[170] N. Saunders, A.P. Midownik, CALPHAD-Calculation of Phase Diagrams, Pergamon, 1998.

[171] K.A. Annan, C.W. Siyasiya, W.E. Stumpf, Effect of hot rolling conditions on ridging in 16wt% Cr ferritic stainless steel sheet. J. South. African Inst. Min. Metall. 2013; 113: 91–96.

[172] S. Li, X. Ding, J. Deng, T. Lookman, J. Li, X. Ren, et al., Superelasticity in bcc nanowires by a reversible twinning mechanism. Phys. Rev. B - Condens. Matter Mater. Phys. 2010; 82: 1–12.

[173] W.Y. Guo, J. Sun, Annealing twins in a multifunctional beta Ti-Nb-Ta-Zr-O alloy. Bull. Mater. Sci. 2012; 34: 1435–1438.

[174] V. Juechter, T. Scharowsky, R.F. Singer, C. Körner, Processing window and evaporation phenomena for Ti-6Al-4V produced by selective electron beam melting. Acta Mater. 2014; 76: 252–258.

[175] D. Velten, V. Biehl, F. Aubertin, B. Valeske, W. Possart, J. Breme, Preparation of TiO2 layers on cp-Ti and Ti6Al4V by thermal and anodic oxidation and by sol-gel coating techniques and their characterization. J. Biomed. Mater. Res. 2002; 59: 18–28.

[176] G. Lu, S.L. Bernasek, J. Schwartz, Oxidation of a polycrystalline titanium surface by oxygen and water. Surf. Sci. 2000; 458: 80–90.

[177] R.F. Egerton, P. Li, M. Malac, Radiation damage in the TEM and SEM, in: Micron, 2004: pp. 399–409.

[178] J. Hoennige, Rolling and Peening – Techniques to control residual stress, distortion and mechanical properties in WAAM, in: Airbus PhD Day, Airbus, Bristol, 2016.

[179] T. Bajd, M. Mihelj, M. Munih, Rotation and Orientation, in: Introd. to Robot., Springer, 2013.